Scintillator performance investigation for MSL/RAD

Dissertation
zur Erlangung des Doktorgrades
der Mathematisch-Naturwissenschaftlichen Fakultät
der Christian-Albrechts-Universität zu Kiel

vorgelegt von
Onno Kortmann

Kiel im Mai 2010

Referent: Prof. Dr. R. F. Wimmer-Schweingruber

Korreferent: Prof Dr. W. J. Duschl

Tag der mündlichen Prüfung: 12. Juli 2010

Zum Druck genehmigt: 12. Juli 2010

Der Dekan

Abstract

The Mars Science Laboratory (MSL) mission is a NASA Mars rover mission planned to be launched in 2011. One of the instruments onboard MSL is the Radiation Assessment Detector (RAD), a comprehensive particle measurement sensor. The instrument is divided into a RAD Sensor Head (RSH) and a RAD Electronics Box (REB). The sensor head consists of a silicon detector telescope stack, placed in front of a cesium-iodide scintillator calorimeter, followed by an additional tissue-equivalent plastic scintillator, designed to measure the Martian neutral particle field. An Anti-Coincidence (AC) scintillator surrounds both scintillators. To save mass and power, photo multiplier tubes are avoided in the instrument and all scintillators are read out using multiple, independent photo diodes. The unavoidable low signal-to-noise ratios of the photo diode readout of the plastic scintillators pose a challenge for calibration and verification of the instrument's working principles.

The scope of this work is to obtain information about the physical details of the scintillator readout and its implications and limits for RAD's performance. To this aim, an optical Monte-Carlo model of each scintillator is set up. After demonstrating that it adequately explains the major effects seen in RAD's scintillators, further analyses are performed based on this model. It is used for quantitative exploration of noise limits and onboard energy reconstruction methods for the scintillation detectors. Further, it is integrated with a variant of a preexisting particle physics model of the sensor head. In addition, the electronic readout is modeled, too, to finally provide a sequential model explaining all major effects in RAD. This model, supplied with suitable parameters from measurements, is then used to forecast the instrument's behaviour in Martian conditions, especially the behaviour of the AC. To complete the picture, initial results on neutral particle modeling are analyzed and compared to measurements to check the analysis path for neutral particle measurements on Mars. As a byproduct, the analysis yields insights into possible ways of processing data from MSL/RAD and further a set of data analysis tools. Parts of those tools are already in use for investigations regarding other, future missions.

Zusammenfassung

Mars Science Laboratory (MSL) ist ein Marsrover der NASA, welcher 2011 starten wird. Eines der Instrumente an Bord ist der Radiation Assessment Detector (RAD), ein universeller Teilchensensor. Der Sensor ist aufgeteilt in den Sensorkopf und die Elektronikbox, wobei der Sensorkopf aus einem Teilchenteleskop vor einem Cäsium-Jodid Szintillator-Kalorimeter gefolgt von einem gewebeäquivalenten Plastikszintillator zur Neutralteilchenmessung auf dem Mars besteht. Eine Antikoinzidenz (AC) umschließt diese beiden Szintillatoren. Um Masse und Energieverbrauch zu reduzieren, werden Photomultiplier vermieden und alle Szintillatoren des Instruments mittels jeweils mehrerer unabhängiger Fotodioden ausgelesen. Der niedrige Signal-zu-Rausch-Verhältnis dieser Auslesemethode stellt eine Herausforderung für die Kalibration und Verifikation des Instruments dar. Ziel dieser Arbeit ist ein Verständnis der Einzelheiten der Szintillatorauslese und die sich ergebenden Folgerungen und Grenzen für die Fähigkeiten von RAD. Ein optisches Monte-Carlo Modell wird entwickelt. Nachdem gezeigt wurde, daß es die größeren Effekte in den Szintillatoren von RAD hinreichend erklärt, wird es für weitere Analysen herangezogen. Auflösungsgrenzen der Szintillatoren sowie Eigenschaften der onboard-Energierekonstruktion werden quantitativ untersucht. Weiterhin wird es mit einer Variante des bereits existierenden Teilchenphysikmodells von RAD sowie einem Modell der elektronischen Auslese integriert um ein sequentielles Modell zur vollständigen Erklärung der Haupteffekte in RAD zu erhalten. Dieses sequentielle Modell mit einem passenden Parametersatz wird sodann herangezogen um Voraussagen über das Verhalten von RAD auf der Marsoberfläche zu erhalten, insbesondere der AC. Um das Bild zu vervollständigen werden erste Resultate der Modellierung der Neutronenantwort des Instruments mit vorhandenen Messungen verglichen. Als Nebenprodukt dieser Arbeit sind Einsichten in mögliche Verfahren zur Analyse der Daten von RAD enstanden und ein Satz von Werkzeugen um obige Analysen durchzuführen. Teile dieser Werkzeuge werden bereits für andere Missionen verwendet.

Contents

List of Figures

List of Tables

Chapter 1

Introduction

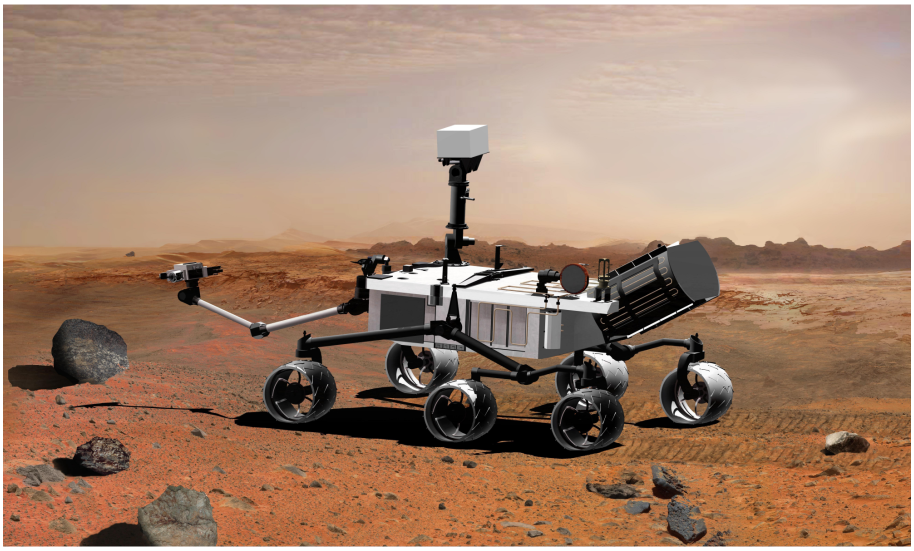

Figure 1.1: Artist's conception of the MSL rover on the Martian surface. Taken from *NASA photo journal*.

In this work, the Radiation Assessment Detector (RAD) instrument, designed to work as a part of the National Aeronautics and Space Administration (NASA) Mars Science Laboratory (MSL) mission, is modeled and its behaviour analyzed for a specific subset of its functionality. In the following, a short description of the MSL mission and the RAD instrument is given. The scope of this work in relation to the RAD instrument is presented.

1.1 Mars Science Laboratory Mission

MSL (Fig. 1.1) is a NASA mission planned to launch in 2011. The mission consists of a surface rover (now named *Curiosity*) along with support hardware, well-equipped with a number of specialized experiments and instruments. It is conceived as a general purpose rover not constrained to a climatic region on Mars so its landing area has not been selected yet.

Similar to the vehicles *Spirit* and *Opportunity* that make up NASA's current Mars Exploration Rover (MER) mission, the rover uses separately steerable wheels and a mast-cam on top of the rover's deck for navigation. Like these two existing rovers, MSL also has the capabilities to communicate without relay with ground stations on Earth.

But in contrast to MER, MSL includes a far greater number of experiments and has the capability to do night journeys by the use of a Radioisotope Thermoelectric Generator (RTG) for power generation and more automated navigation [*NASA Mars Science Laboratory web site*, 2006-2010].

1.1.1 Goals

One of the main goals of MSL is to evaluate Mars' habitability for possible micro-organisms and to search for possible signs of past or present biological activity. New engineering concepts are also tested, such as a 'sky crane' to place the rover onto the surface from a hovering platform and a new semi-autonomous navigation system. In particular, the summarized science goals of the MSL mission are, in this order:

- **Determine whether life ever arose on Mars.** Amongst others, the amount of elements essential for life (carbon, hydrogen, nitrogen, oxygen, phosphorus and sulfur) as well as the amount, distribution and temporal evolution of water will be determined.
- **Characterize the climate of Mars.** This includes in-situ measurements of the Martian weather, the isotopic composition of the Martian atmosphere and the composition and intensity of surface radiation.
- **Characterize the geology of Mars.** MSL is designed to study the rock and soil and to look for rocks which may have formed in the presence of water.
- **Prepare for human exploration.** Landing a large and heavy payload on the Martian surface is the first step to send the heavy equipment and infrastructure required to support a human exploration mission on Mars.

Figure 1.2: The finished RAD sensor heads placed on a clean-room bench. The label FM1 denotes the flight-spare whereas FM2 marks the actual instrument that will be landed on Mars. The sensor heads will be attached to the RAD electronics boxes (not shown here) with their feet. The scale of the instruments in the picture is about 0.5×. The red items on top of the instruments are protective covers that will be removed before flight.

1.2 Radiation Assessment Detector

One of the instruments selected for the MSL mission is RAD, the Radiation Assessment Detector (Fig. 1.2). It was developed, designed and built in a collaboration between the Christian-Albrechts-Universität zu Kiel (CAU) and the Southwest Research Institute (SwRI) in San Antonio, Texas, overseen by Deutsches Zentrum für Luft- und Raumfahrt (DLR) and NASA, respectively. This work is supported by Grant #50QM0501 from DLR.

1.2.1 Goals and Requirements

According to the *RAD Proposal* [2006], RAD's task during the MSL mission is to "characterize fully the broad spectrum of radiation at the surface of Mars". This includes characterization of cosmic radiation on Mars, search for radiation produced by radioactive isotopes on the surface and dosimetry to assess the radiation risks on the Martian surface in preparation for possible future manned missions to Mars.
Overall, the RAD science objectives and observational requirements are:

1. **Characterize the energetic particle spectrum** incident on the surface of Mars, including direct and indirect radiation, created both in the atmosphere as well as in the regolith.

2. **Determine** radiation **dose rate** and equivalent dose rate for humans on the surface of Mars.

3. **Validate Mars Atmospheric Transmission Models and Radiation Transport Codes**.

4. **Determine** the radiation hazard and mutagenic **influences on life**, past and present, at and beneath the Martian surface.

5. **Determine the geochemistry and the chemical and isotopic effects** of energetic particles on the Martian surface and atmosphere.

This list translates into a set of more detailed measurement requirements which also form the **motivation of this work**:

1. **Measure the flux of protons and ions with atomic number $z \leq 26$ and energy $E \leq 100$MeV and separate the ion measurements into groups of ions with similar z.** This demands a high dynamic range for energy measurements in the instrument. The total energy of incoming particles is mainly measured in a scintillation crystal which is read out using a set of photo diodes. In order to reconstruct energy and estimate noise, the read out of this crystal needs to be understood in detail.

2. Neutrons are an important factor for dose rate measurements. Beside a silicon telescope for dosimetry, RAD shall measure the flux of neutrons up to 100 MeV and the dose rate in tissue-equivalent material. Neutral particles are detected with a scintillator surrounded by an active Anti-Coincidence (AC). The AC is a complex shaped plastic scintillator which is read out with an unfortunate, but unavoidable, low signal-to-noise ratio. A good estimate of its performance needs to be available in order to calculate dose rates and neutral particle spectra.

3. **Compare the measured doses and particle spectra to transport models for the Martian atmosphere and regolith and use them to project and compare to radiation environments on past Mars.** As a first step into this direction, a model covering all major aspects of RAD's behaviour is needed.

1.2.2 The Instrument

The RAD instrument mainly consists of two parts, the electronics box (RAD Electronics Box - REB) and the sensor head (RAD Sensor Head - RSH). The first has been built by SwRI while the latter has been developed, designed and manufactured by CAU Kiel and assembled with the help of Kayser-Threde GmbH (KT) in Munich.

The sensor head, as schematically shown in Fig. 1.3, consists of a number of detectors. Detectors A, B and C form a charged particle telescope. The detector D is mainly used to detect γ-rays and the E detector is used as a neutron detector. The detector stack D, E is shielded by a common AC consisting of C, parts of B, F1, and F2 against charged particles. The sensor head includes all electronics to do the initial preamplification of the detector signals, as the preamplifiers should be placed as close as possible to the detectors to minimize noise. More details on the design of the sensor head are given in Sec. 2.3.

The electronics box contains the full signal path after preamplification, i.e. everything that is needed to obtain Pulse Height Analysis (PHA) data or count rates. It also contains various forms of digital storage and a microcontroller processing all PHA data to form histograms for different coincidence configurations, compressing data using Look-Up Tables (LUT) and interfacing with the spacecraft's communication bus to send the gathered data to the ground stations on Earth.

Due to power constraints, an elaborate powering scheme is devised for RAD. It is planned to have a duty cycle with a 15 min observation period every hour.

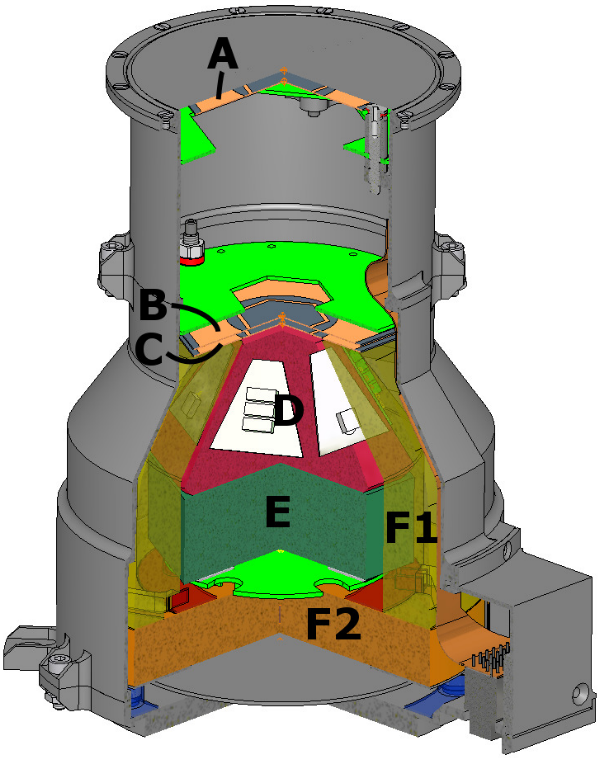

Figure 1.3: Cutaway view (from CAD data) of the RAD sensor head. Approximately 0.75× scale. By L. Seimetz.

1.3 Scope of this work

After this introduction, the first part of this thesis covers all aspects of the basic design of the RAD experiment. The main design goals of RAD, as outlined in the *RAD Proposal* [2006], are related to their implementation in the existing RAD instrument and a top-level view of the full measurement chain is given. The performance of the sensor head in all important measurement ranges is described, referring whenever possible to the large amount of existing technical documentation covering certain aspects of the instrument. This is followed by a brief look at the calibration points available for the RAD instrument, pointing out the available calibrations, missing parts as well as their relation to the modeling efforts.

The third, major part of this work describes the optical modeling effort done for RAD. This part starts with a detailed description of the optical model that has been implemented in the course of this work. The model has been developed as a building block for understanding the complex signals out of RAD's scintillation detectors.

For the D scintillator, the model is then compared to experimental data. To be able to do this, the optical model is extended with the necessary additional parts covering the straggling energy loss in the scintillator as well as the electronic noise behaviour of the photo diode readout detectors. The energy resolution, as provided by the model, is compared to the actual performance of the D scintillator and the overall validity of the model in regard to the D scintillator is checked. The in-flight energy reconstruction parameters are estimated using a more detailed noise model which has been included in App. A.

This is followed by a look at the most complex detector in the RAD instrument, the AC. After describing its performance parameters, a simple first, purely empirical model to describe its performance is discussed. To have a more detailed look, constraints on the parameter set for the optical model of the anti-coincidence are made by comparing the AC behaviour to measurements. For this, a full chain of particle physics and optical model, as well as an electronic readout model is set up. This sequential model is then verified to approximate the AC scintillator behaviour and subsequently used to do initial forecasts of the AC performance in Martian conditions.

To complete the picture, the available calibration data from neutron fields is presented and compared to simulations built on the results from the earlier Chapters. This incorporates the results on the D, E and the AC scintillators, as well as the results by *Böhm and Martin* [2008].

Finally, the analysis of the instrument is summarized and the most important findings for the expected in-flight performance of the instrument are given. As an outlook, possible areas for future applications of this work as well as possible refinements are pointed out. Remaining gaps in the modeling and data analysis efforts for RAD are noted and possible directions for further exploration are given.

In the appendix, one can find a set of the most important plots, elementary processing algorithms, references to and descriptions of important data files as well as a short set of descriptions of "dead-ends" that have been looked at in the course of this work.

Chapter 2

The Measurement Chain

In the following, the complete measurement physics as well as the electronics chain of RAD are presented in an overview. This reaches from the principles of radiation detection, as employed on RAD, up to the data products that will be made available on Earth. Details are only given for those parts which are further discussed in this work, but some important caveats are given for those places where one is easily confused when analyzing RAD's data.

2.1 Radiation detection

The detection principles for high energy particles, as used for RAD, can be classified into those for charged and those for neutral particles. The final measurement of ionization (directly or through optical photons) is done using silicon detectors.

2.1.1 Charged particles

When passing through matter, fast charged particles will gradually lose energy in a process that has been first satisfactorily explained by Bethe and Bloch. Their law states that the energy $-dE$, lost in a given length dx of target material, $-\frac{dE}{dx}$ is (as also given in e.g. *Leo* [1987, 1994])

$$-\frac{dE}{dx} = 2\pi N_a r_e^2 m_e c^2 \rho \frac{Z}{A} \frac{z^2}{\beta^2} \left[\log\left(\frac{2 m_e \gamma^2 v^2 W_{\mathrm{max}}}{I^2} \right) - 2\beta^2 - \delta - 2\frac{C}{Z} \right] \tag{2.1}$$

with the following symbol meanings:

E, z	Energy and charge number of the incident particle
A, Z	Mass and charge number of the absorbing matter (for mixtures etc., see *Leo* [1987, 1994])
ρ	Density of the absorbing matter
r_e, m_e	Classical electron radius and electron mass
N_a	Avogadro's number
I	Mean excitation potential, δ density correction and W_{max} maximum single-collision energy transfer. For details on the density and shell corrections, see *Leo* [1987, 1994].
$\beta := v/c$	Speed in units of c of the incident particle and Lorentz factor $\gamma := \frac{1}{\sqrt{1-\beta^2}}$.

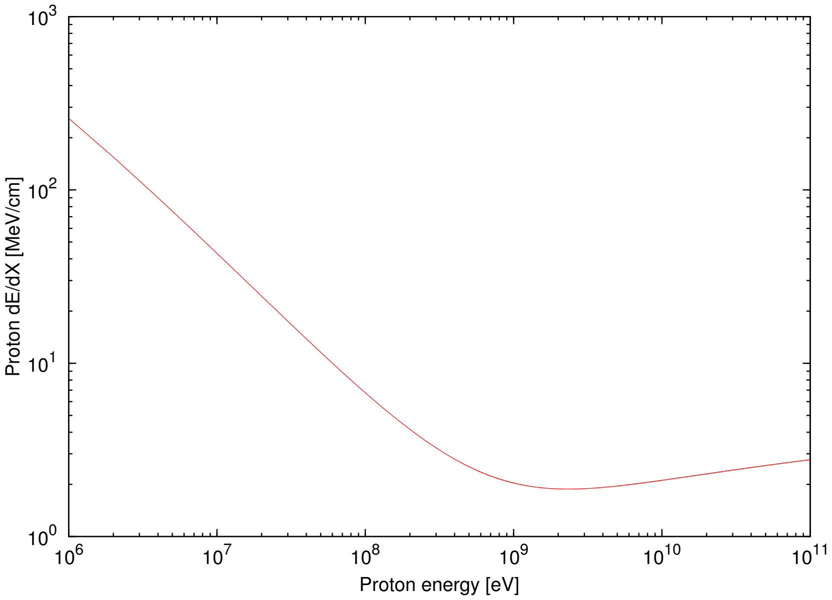

Figure 2.1: Sample evaluation of the Bethe-Bloch formula for protons crossing a carbon material with $\rho = 1\,\mathrm{g\,cm^{-3}}$. Note that there is already a departure from the measured behaviour in the left part ($\sim$ MeV range) of the curve.

This formula can be simplified to give a few basic rules of thumb for most practical cases [*Leo*, 1987, 1994]. Although applicable to a wide range of particle energies, it will break down at lower energies. This is not a problem in the case of RAD, which is designed to look for high-energy particles.

The energy loss ΔE by a charged particle that passed through a slab of matter Δx will cause ionization in the material. This ionization may be converted e.g. into optical photons or phonons (and thus heat). The effects of this ionization, which can usually be assumed to be proportional to ΔE, is then used to estimate the energy loss.

The energy loss function described by Eq. 2.1 has a single minimum when going along the energy axis, as it can be seen exemplarily in Fig. 2.1. Particles with lowest energy loss in this way are called Minimum Ionizing Particles (MIPs). As the $\frac{dE}{dx}$ of particles with energies above the minimum raises only very slightly, particles with even higher energies are quasi minimum ionizing, too. The mean energy loss for a singly charged MIP is about 105 keV in a slab of 300 µm silicon, which is the thickness of each of RAD's silicon detectors.

It should be noted, that, in the context of RAD, this gradual process of energy loss is not an exact description when looking at the microscopic details of a track with low energy loss in thin slabs along the direction of energy loss. Rather, in the case of RAD's detectors and for low ionization densities, energy loss happens in discrete collisions as *energy loss straggling* for which the energy loss is described by a statistical energy loss probability density function (pdf). Only the mean energy loss value is given by Bethe-Bloch. The details of these energy loss straggling distributions and methods for their numerical calculation are given in *Moyal* [1955]; *Isaev and Popov* [1970]; *Bichsel and Saxon* [1975]; *Bichsel* [1988]; *Schorr* [1973]; *Needham* [2003], among others. For a straight crossing of silicon with fittingly 300µm thickness and various energies and particle types, a good set of reference data is given in *Hancock et al.* [1983b]. Some details on this energy loss straggling are used for the discussion in Sec. 3.4.1. The common case of a MIP in 300 µm silicon is well approximated with the

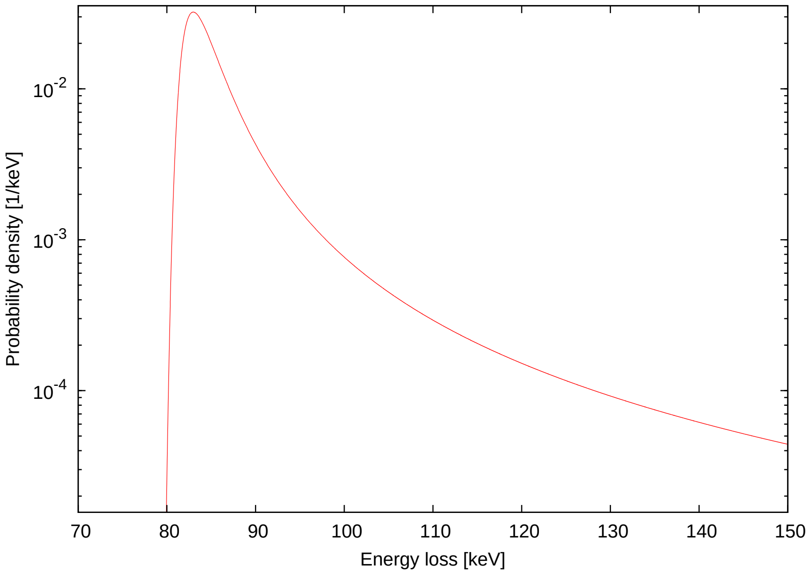

Figure 2.2: Energy loss straggling for relativistic protons in a slab of 300 μm silicon. The shown LANDAU distribution has been plotted using the values for protons with a momentum of 115 GeV c^{-1}, from *Hancock et al.* [1983b].

LANDAU distribution, which is exemplarily shown in Fig. 2.2.

2.1.2 Neutral particles

Neutral particles interact with matter in processes that will produce secondary particles. The charged fraction of those secondary particles will then lose energy in a scintillator which can in turn be detected and quantified. In RAD, γ-photons will produce secondary electrons in the D scintillator whereas neutrons will be detected mostly by their elastic recoil protons. Details of the various γ-interactions are given in *Leo* [1987, 1994] and the specifics for MSL/RAD are detailed in *Gooß* [2006].

Recoil protons may be produced through elastic scattering in the hydrogen-rich plastic material of the E detector. The energy loss response for a monoenergetic neutron field in the energy range accessible to RAD (mostly 1 . . . 100 MeV) can be described by the recoil protons having a flat pdf up to the energy of the incoming neutron. This behaviour can be clearly seen for example in the simulated data in Sec. 7.5, Fig. 7.3. The exact shape may, depending on neutron energy, be much more complicated due to the partial escape of recoil protons. More complicated processes (inelastic scattering) are expected to happen, too. They are not expected to be visible in the RAD scintillators, though, due to limitations in its energy resolution.

2.1.3 Silicon detectors

To be able to further process and analyze the energy losses in any of RAD's detectors, the energy deposits in the various detector subsystems have to be converted into electrical signals. In RAD, silicon Positive-Intrinsic-Negative (PIN) diodes are used for this purpose and are the first part of the frontend of the electronics chain. They are employed in two different

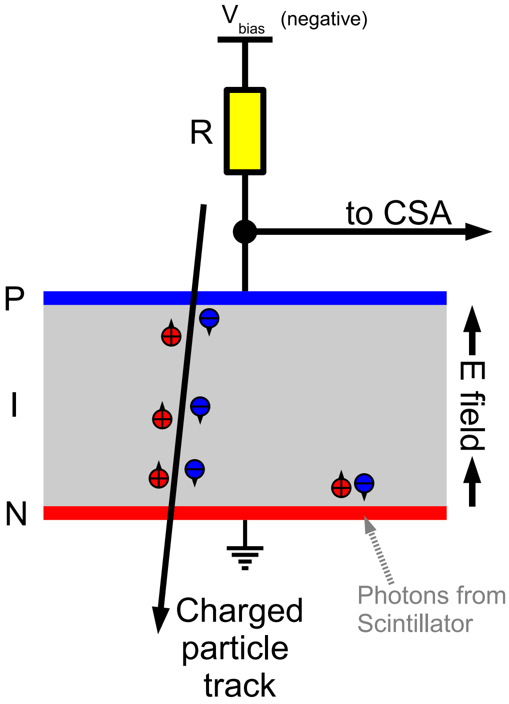

Figure 2.3: Schematic view of PIN diode operation, with biasing as in RAD.

operating modes

- Directly detecting the energy loss caused by the ionization in their intrinsic silicon layer. Any direct particle interaction with the silicon material will be called a *silicon hit* from now on.

- Detection of optical photons produced in any of the scintillation detectors (see below), by acting as a very sensitive photo diode. Depending on the geometry of the particle track in respect to RAD's detectors, it may happen that the optical readout signal is combined with an additional silicon hit.

In both cases, pairs of charge carriers (usually named electrons and holes) are produced in the silicon material through excitation by either the photons or the ionizing energy loss of the charged particle. In the case of photons, the production of charge carriers happens in the very outer surface layer of the material, whereas for interactions with charged particles, the charge carriers are generated across the whole particle track. Fig. 2.3 illustrates this concept.

Except for very high ionization densities (which are not encountered in RAD's operating environment), the amount of charge production is directly proportional to the amount of photons impinging on the surface of the diode and the energy loss of a particle passing through the detector.

An electric field is generated in the bulk of the diode by applying a reverse *bias voltage* between its two electrodes. In RAD this voltage has a nominal value of $-70\,\mathrm{V}$. When an energy deposit happens, this causes the generated carriers to separate and accelerate towards the electrodes. This in turn will cause a short current pulse (due to the separated charges) that is then processed by the very first part of the amplifier chain, the Charge Sensitive (Pre-)Amplifier

(CSA).
Without any bias voltage, the charge carriers would mostly recombine inside the diode material. As usual, the amount of additional electronic noise on an amplified charge pulse is mainly dependent on the behaviour of the first amplification stage(s). For more details refer e.g. to *Leo* [1987, 1994] and see App. A. The amount of ionization energy loss to produce an electron-hole pair has been estimated to be about 3.6 eV at room temperature[1] [*Leo*, 1987, 1994].

The silicon detectors have several intrinsic sources of noise. Impurities in the undoped bulk material of the detector as well as thermally generated charge pairs will cause a small flow of *leakage current*. The amount of thermally generated charge pairs rises exponentially with temperature and the leakage current will appear as an additional source of noise in the detector [*Leo*, 1987, 1994]. The RAD detectors have been selected for low leakage current. As the border regions of silicon slab, where mechanical cuts etc. have been made, are mostly affected by the non-thermal leakage current, a *guard ring* segment surrounds the active detector area. This guard ring, photochemically etched into the silicon substrate, is separately biased and takes most of the leakage current and therefore further reduces the amount of noise seen.

2.1.4 Scintillators

Several reasons constrain the use of pure silicon detectors in every area of RAD:

1. Silicon is not a very good material to directly detect γ-rays. The absorption probability for γ-rays, per unit length of material, is roughly $\sim Z^2$ (atomic number) and for silicon it is only $Z = 14$. For stopping high-energy particles, a longer path length in silicon is needed compared to materials with higher Z.

2. Silicon detectors are only available in thin slabs. To have more silicon material in the particle path requires multiple stacked silicon detectors and/or thicker detectors, complicating wiring and thermal stress issues and introducing the need for increased bias voltages. The Martian atmosphere consists mostly of CO_2 at a pressure of approx. 6 mbar and is therefore prone to dielectric breakdown and forming a gas discharge at high voltages. This problem also makes photo multiplier tubes hard to use.

3. A tissue-equivalent material is favourable for dosimetry. To measure the equivalent dose in biological material, a material that has a density and composition more similar to a material that approximates water as the main component of the human body, has to be used.

4. Cost. This would be a major factor e.g. for the amount of silicon needed to replace the large anti-coincidence detector.

For these reasons, *scintillation detectors* are additionally used to form several core parts of the instrument. A scintillator produces light when it experiences ionizing energy loss. This light is guided to a photosensitive detector which then converts the light pulse as described into a energy-proportional electrical signal. The guiding to the photo detector happens with the help of total reflection, reflective surface coatings or wrappings and by shaping the scintillator appropriately. All scintillators in RAD are read out using silicon PIN detectors [*Canberra*, 2007-7] as photo diodes, fabricated with the same process as those used for detecting direct charged particle interactions.

---

[1] Any changes with temperature are not covered in this work.

An additional process that produces light in transparent materials is Cherenkov radiation [*Leo*, 1987, 1994]. In RAD's scintillators, the amount thus produced is much smaller than that through the scintillation processes and is thus not detectable by the attached photo diodes.

Two different scintillators are used on RAD. The D scintillator is made out of a clear, dense ($\approx 4.5\,\mathrm{g\,cm^{-3}}$) inorganic salt (CsI), whereas the E and F scintillators are made out of a yellowish transparent polymer material with a density very close to water. The two scintillator materials differ in many of their physical properties, but the main distinction that has driven the selection of the materials is the density and the atomic number Z of its constituents.

The plastic scintillator is based on a commercially available formula called BC430 with a long history of being used for aerospace experiments in Kiel [*Pauls*, 1998; *Burmeister*, 2006]. A special modification of that material, denoted BC432M[2] by the vendor, has been produced specifically for RAD. This modification has a slightly lower ($\sim 10\%$) light output but survives the extended temperature range that may be encountered by RAD on MSL in Martian conditions.

The CsI material has a very high light output (per energy deposited) and a slow decay of its light production after being hit ($\sim$ µs). The plastic scintillator has comparatively low light output but a very fast response ($\sim$ ns) instead.

Inherent to both is an additive (different for CsI and plastic(=BC430)), which converts higher energy optical photons (blue … ultraviolet) into the red spectral range, where the photo diode is most sensitive. Additionally, this *wavelength shifter* is used to reduce the effect of self-absorption by the reversal of the optical de-excitation process in the scintillators.

The readout diodes are attached using a transparent, flexible silicon glue to the scintillators [*Dow Corning*, 2005] which serves a secondary purpose of relieving thermally induced mechanical stresses between diode and scintillator.

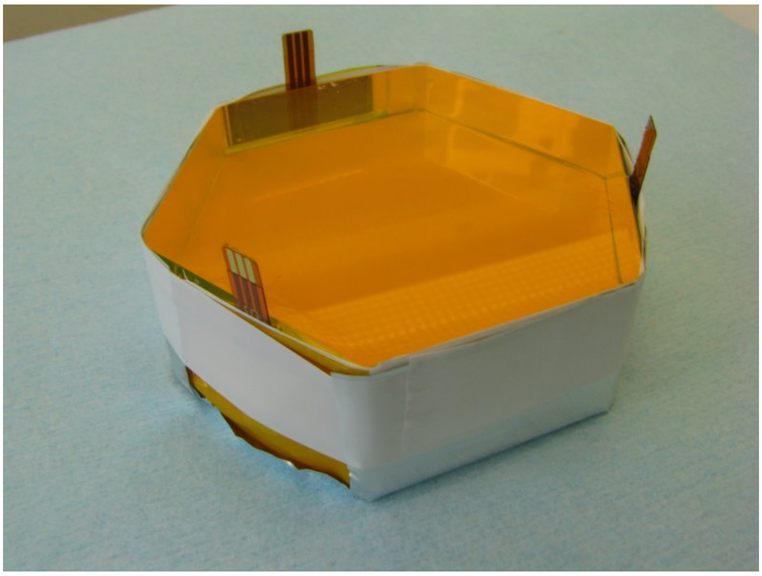

Figure 2.4: Partially wrapped E plastic scintillator piece. The three readout photo diodes are attached and the flex-board cables connecting GND, the guard ring segment and the main anode can be seen. Reflector filter paper has been put onto the bottom side of the scintillator.

---

[2] And yet another material called BC430M exists as an intermediate product. It has been used for some parts of the PF RSH (see Sec. 2.5) and also slightly differs from the other two formulations.

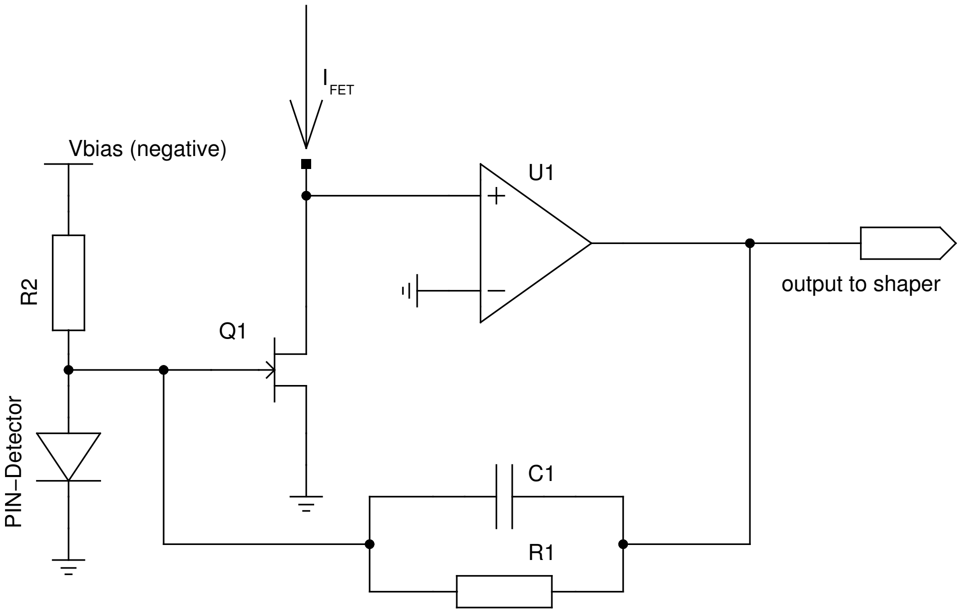

Figure 2.5: Simplified schematic of a CSA. All power supply filtering and biasing parts (except for the diode input resistor) have been left out.

The assembled scintillators are wrapped in a brittle, white material [*Millipore Corporation*, 2005] which is valued here for its high reflectivity, but is originally a chemical filter material. The filter paper wrapping is fixed and further wrapped with high reflectivity PolyTetraFluoroEthylene (PTFE) tape onto the scintillators. Additional layers of aluminium foil are used to shield against light crosstalk between different scintillators. An exemplary picture for this preparation process is shown in Fig. 2.4.

2.2 Signal processing electronics

What is simply marked as '`to CSA`' in Fig. 2.3 is actually the start of a long chain of signal processing electronics which finally yields digitally sampled and processed pulse height analysis data or energy spectra (histograms). The major pieces of this chain are, as implemented on RAD, given below in the order of information flow. Modifications of these stages may exist for other instruments.

CSA The overall working principle of the CSA is shown in Fig. 2.5. The bias voltage $\mathrm{V_{bias}}$ is supplied to each PIN diode using an individual large ($\sim 10\,\mathrm{M\Omega}$) resistor R2. The charge produced by an energy hit will be diverted to the input of the corresponding CSA, which acts as a low impedance load and thus collects this charge from the diode. The input stage is formed with a discrete, sensitive Junction Field Effect Transistor (JFET) Q1 and a further amplification stage U1, coupled in a feedback loop through a *feedback capacitor* C1 back to the gate of the JFET. The JFET is biased with a current $\mathrm{I_{FET}}$ from a voltage source V_{FET} using an additional resistor that is not shown. The feedback causes the low impedance of the input stage and is the signal that is connected as the output of the CSA to the shaping stage. The output of a CSA are voltage steps with a step height proportional to the charge seen and anti-proportional to the value of C1. To avoid saturation of the output due to an accumulation of such voltage steps, a feedback resistor R1 is connected in parallel to the feedback capacitor to cause a decay of the CSA output with a sufficiently long time constant $\tau = \mathrm{R1} \cdot \mathrm{C1}$ to keep the influence of the decay on the following, differentiating stages low. CSAs may be indirectly coupled by having an additional capacitor in front of the JFET gate.

Shaper The second stage of the electrical amplification, the *shaping stage*, forms the voltage step into an approximately GAUSSian voltage pulse. This shaping is usually done by using a combination of a CR high- and a RC lowpass filter [*Leo*, 1987, 1994]. The purpose of this step is a further amplification of the still small signal and signal conditioning, in order to optimize noise perfomance and to ease processing in the following Analog to Digital Converter (ADC) stages.

Triggering and Digitization Although a set of further amplification stages exists in the RAD readout Application Specific Integrated Circuit (ASIC) (see below), the next logical step is the digitization of the signal. The signal path splits up and a *trigger logic* and the *digitization* stage are both fed with the amplified, shaped pulses.

Trigger logic The trigger logic initially decides which energy deposits are worthwhile to further process. For the signals of interest to the trigger logic, a comparator with an adjustable threshold is looking for pulse heights exceeding a selectable value. This value corresponds to a minimum energy deposit, below which the instrument will not be sensitive. The firing of the comparators may be (as it is the case for RAD) fed into another chain of logic that checks for custom patterns on the set of comparator outputs. The trigger logic may then decide to start digitization.

Digitization Digitization of the voltage peak heights on the available set of channels is done by first acquiring the maximum voltage level for each channel in question through a *peak detector*. A certain time will be waited for this peaking to occur. The set of channel voltage levels is isolated in sample-and-hold circuits and prepared to be digitized by the ADC. The ADC, usually with the help of a multiplexer to reduce complexity, digitizes the set of channels that are deemed to be of interest and sends them as PHA data to the onboard processing unit.

Onboard processing The above set of steps is implemented in hardware as it is either handling analogue signals or needs to be fast. The onboard processing unit that receives the digitized PHA data will do further and more complex reduction and packaging of the data. It usually also covers the control and measurement of other instrument parameters (voltages, temperatures etc.) and has the responsibility to send the preprocessed data to the spacecraft bus. The steps that are further done in the onboard processor are mainly driven by data reduction, as the amount of PHA data is way too high to be sent from deep space back to earth completely and the very short time structure of the data is mostly irrelevant. Configurable pulse height histograms are calculated from the incoming pulse height data.

2.3 The RAD Sensor Head

Except for the scintillator readout photo diodes, all active elements of the sensor head are displayed schematically in Fig. 2.6. Additionally, three exemplary charged particle tracks (1, 2, 3) are drawn. These tracks cover most of the sensor head working principles for charged particles. For neutral particles, a simplistic view is to assume interactions in a single detector only. This is not an entirely realistic description, esp. for neutrons; see Chapter 7.

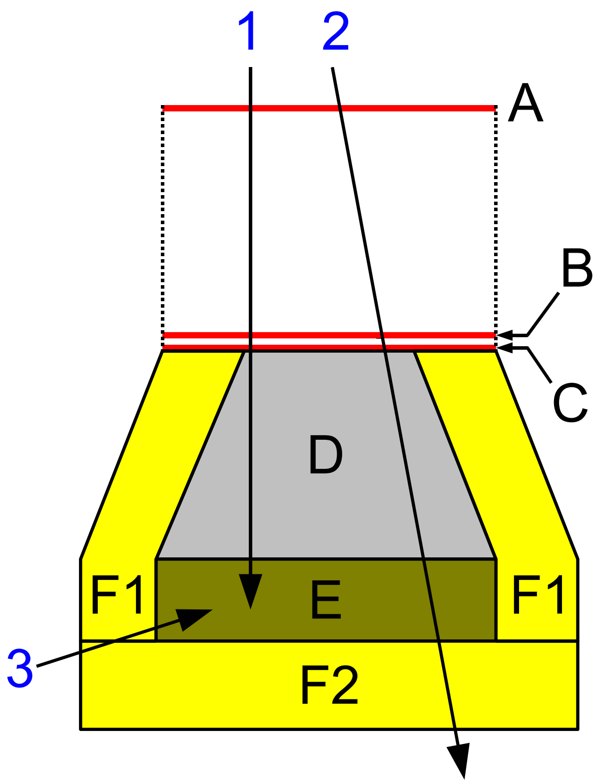

Figure 2.6: Schematic side view of the RSH, with all detectors (except scintillator readout) visible. Three example particle tracks 1, 2, 3 are drawn. For comparison, see also Fig. 1.3.

A, B, C. The A, B, C detectors are segmented silicon detectors with a hexagonal outer shape, bonded onto ceramic carriers. They have all been produced using an identical chip mask (See App. H, Figs. H.1, H.2 for details). The electrical wiring of the individual segments forms a larger set of logical detectors out of these three physical detectors. The set of selected logical detectors is comprehensively described in *Böttcher* [2008]. Most important are the following uses of the ABC detectors:

Charged particle telescope The A detector is separated into an outer segment A1 and an inner[3] segment A2. Together with the inner part of the B and the inner part of the C detector, it forms the main charged particle telescope part of RAD, covering tracks such as 1, 2. By selecting different segments, the telescope full opening angle can be changed between approx. 15° and approx. 30°. Selecting hits in A, B, and C, and not D picks low energy charged particles stopping in C. Note that there is a small amount of absorbing material between C and D.

Optical readout of the F1 AC The outer part of the C detector is optically coupled to the F1 AC scintillator and is the top readout of the AC. To reduce noise, each part of the outer azimuthally segmented area of the C detector is read out with an individual CSA that is then fed additively into a common shaper.

---

[3] Note that this order switched during the design of the instrument. It is reversed for the Pathfinder (see Sec. 2.5) RSH. Analysis of the amount of noise in A1 and A2 in a given run file sorts the segments. The segment with more noise is the outer (larger) one.

Silicon part of the AC A small part of C overlapping both F1 and D is used, together with parts in B overlapping the guard rings of C in projection, to form C2, the top part of the AC for the D/E scintillator.

The first stages of the electronics for the A,B and C detectors are placed on Printed Circuit Boards (PCBs) inside the telescope tube between B/C and A, shaped to stay outside of the charged particle beam cone. To extend the dynamic range, two different gain scale amplification chains exist for the inner and outer part of the A, and for the inner part of the B and the C detector. The gains are appropriately named high and low for those detectors.

D The D scintillator, the CsI-crystal, as visible in Fig. 1.3, is shaped like a capped pyramid with an approximately hexagonal base and a height of 28 mm. Three independent readout diodes with an active area of approx. $2\,\mathrm{cm}^2$ each are attached to its sides, each connected to an individual CSA, also attached to the crystal but with a reflective layer beneath. The D amplification stages are built to have different gains to cover the anticipated high dynamic range of energy loss in the D scintillator. The individual signals out of the D scintillator are named DH, DM and DL, for the **h**igh, **m**edium and **l**ow gain amplification chain, respectively. A corresponding naming scheme applies to the E scintillator.

The D crystal sits below the C detector and is the heart of the instrument. It is designed to stop ions with energies of up to 100 MeV/nuc and is used in conjunction with the A, B, C telescope to characterize the charged particle spectrum. Stopping charged particles in D can be identified by an AC on the E signal below D. By looking at the differential energy loss in A,B,C vs. total energy including D, ion species can be separated into groups. The $\frac{dE}{dx}$ (as measured in A,B,C) and the total energy loss in D (plus maybe the E detector, track 1) give a unique relation for each different z of the incoming particle. As a single detector with C, C2, F in AC, it responds to neutral particles (mostly γ-photons).

A lot of work has been done mainly by E. Böhm and C. Martin on the charged particle identification and processing in RAD and is documented in detail in a series of internal unpublished reports [*Martin and Böhm*, 2008; *Martin et al.*, 2008a; *Martin*, 2008a,b].

As the D scintillator has the highest light yield and as it has a comparatively simple shape, it is used for the first test of the optical model as it is discussed in the next chapter. The dynamic range extension using separate readout diodes implies a trade-off between dynamic range and energy resolution. The limits on energy reconstruction are given by findings from the optical model developed in this work. Validation of the energy reconstruction for the D scintillator is discussed in Sec. 3.4 and following.

E The E plastic scintillator, as visible in Fig. 1.3 and close-up in Fig. 2.4 is the tissue-equivalent dosimetry and neutron detector of RAD. Its shape is approximately a hexagonal prism with a height of 18 mm. Like the D scintillator, it is read out using three independent PIN diodes, again having an active area of approx. $2\,\mathrm{cm}^2$, attached to three sides to the prism and again connected to amplification stages with different gains, for the same reason as in the case of the D scintillator. It should be noted that the E scintillator, contrary to the D scintillator, has no mirror symmetry planes and therefore two readout pairs are only comparable if they are in the same rotational order, see Fig. 2.7. The CSAs and shaper parts of the amplification chain are placed in a compartment that is between the E detector and the bottom plate of the F scintillator. As already described, its high hydrogen content makes it a detection element suitable for neutrons.

No explicit discussion of the optical effects in the E scintillator is performed, but the overall results from the D scintillator checks and the results on the F-AC with its same

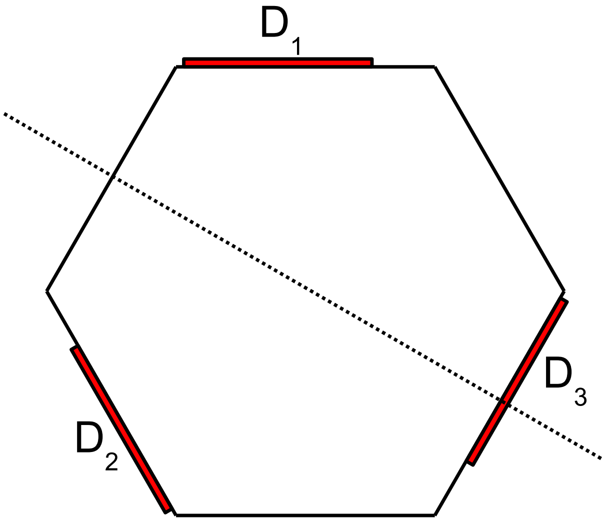

Figure 2.7: Schematic view of the slight offset of the diodes attached to E. The drawing is not to scale and the offset is exaggerated in this drawing. This missing mirror symmetry (e.g. at the dashed line) may cause an asymmetry in the readout. For example, a spatially uniform distribution of energy losses in the E scintillator give a different read out spectrum for selecting $\frac{D_1}{D_1+D_2}$ compared to $\frac{D_2}{D_1+D_2}$. Ignoring this effect may lead to confusion when looking at and comparing individual scintillator channels.

material finally give acceptable estimates of its optical performance, too. This is visible in the neutron discussion (Chapter 7).

F For neutral particle detection (γ-rays and neutrons in the context of RAD), it is of utmost importance to suppress the large expected amount of charged particles hitting the neutral channels. This suppression is achieved by an active AC which gives a veto signal when a charged particle has crossed it. The veto is generated for a selected threshold energy deposit value in each of the AC detectors or a linear combination of F1 and F2. To be effective against charged particles which may come from all directions, it is necessary to completely surround the D/E stack with such an active AC. Besides having the top silicon detectors C and C2 in AC for the D/E neutral detection, the largest part of the AC is formed by the F scintillator surrounding D and E. It is the most heavy single mechanical piece in the RSH.

It is assembled from two pieces, the top cone F1, being read out by the outer C segments as described above, and the approximately cylindrical bottom part F2, which is transparently glued to the top part after the D/E stack is inserted. The same glue as is used for attaching the silicon diodes to the scintillators is used for this. The average wall thickness of the AC is 12 mm and it is made, like the E scintillator, out of the BC432M material for the flight parts. An additional set of three readout diodes (active area again approx. 2 cm^2 each) with individual CSAs is attached to three sides of the bottom part, with a 120° angle between each two diodes. The analogue signal of the three bottom read out CSAs is (like for the outer C segments) added and a single bottom F2 signal results, thus in total two distinct electrical signals F1 and F2 for the F-AC are available at the RSH electrical connector.

The readout of the F-AC is subject to a relatively high amount of electronic noise. This makes the selection of a proper threshold for this detector difficult. Considerable effort has been spent on simulating the physics chain of light generation, light collection and electrical readout of the F scintillator in order to give insights into the efficiency of the AC in regard to charged particle suppression. The details for this are given in Sec. 4 and the following chapters, with the main results on this available in Sec. 6.8.1.

The sensor head is enclosed in a housing out of an magnesium alloy which has the connector to the REB on the bottom side. Additionally, a purge connector is available to keep the internals (esp. the slightly hygroscopic CsI crystal) dry before launch.

2.4 RSH and REB units

During the course of designing and building the final RAD flight model, a prototype sensor head, and prototype as well as support electronics have been built. In the following, an overview over the available set of RSHs and REBs is given, before proceeding with a more detailed description of the electronics options. Measurements have been made with a multitude of combinations of readout electronics as well as sensor heads. As each sensor head and each readout electronics has its very own sets of quirks, data analysis has to be done very carefully when comparing the results of different measurements originating from different sensor head and/or electronics. The Digital Readout Electronics for Nuclear Applications (DIRENA), which is extensively used for prototyping, is roughly described in the detailed electronics section following thereafter.

2.5 Status of RAD Sensor Heads

A total of three MSL/RAD sensors have been built by CAU Kiel. These units are designated as PathFinder (**PF**), Flight Model I (**FM1**) and Flight Model II (**FM2**).

The flight units are two equal units which have been assembled mostly in parallel at Kayser-Threde GmbH in Munich. The detectors and electronics for FM2 have been selected to be slightly better in their performance than those used for FM1, as FM2 is planned to be put onto MSL as the final flight model. The criteria for detector selection were the measured detector bias current and the related detector noise. The electronics boards have mostly been selected according to additional rework that has been done.

The detector for the D-medium-gain (DM) channel of FM1 is unusable as it failed, probably due to excess mechanical stress, during transport. It has been removed from the power distribution circuit, but the CSA and shaping stage are still connected. The glue between the two parts of the AC separated in FM1 during curing. Therefore, some additional total reflectivity is assumed to exist at the interface between the top and the bottom AC of FM1.

The Pathfinder is the prototype unit built to demonstrate the basic working principle of the instrument. It has also been used during a set of particle beam campaigns to get a good understanding of the instrument. Though very similar overall, there are several construction differences between the Pathfinder and the flight units. Apart from different board layouts, surface finishes, alloys for the housing and cabling inside the sensor head, the following major differences exist when compared to the flight models:

- The AC scintillation detector is made of a different material (BC430M) than in the flight model (BC432M).

- The outer anti-coincidence part (F1) of the Pathfinder is 1 mm shorter than in the flight models. The anti-coincidence has been shortened at the bottom of the cylindrical section.

2.6 Status of RAD Electronics Boxes

Three different REBs have been used during the various calibration campaigns done with the sensor heads and additional flight units have been built at SwRI. The initial prototype unit has been used for Proton/Iron testing at Brookhaven National Laboratory (BNL) as well as for the neutron test at iThemba. It is called the **EM-REB**.

Two other units, the so-called **Kiel-** and **Jet Propulsion Laboratory (JPL)**-REB have been used in the late phases of the assembly of the flight models. The Kiel-REB has some parts of the older EM-REB incorporated. Additionally, the EM-REB was changed in its mechanical configuration (from the so-called **FLAT-RAD**[4] state to a flight-like configuration), which affected readout performance.

Finally, a single **flight REB** has been built. The unit lately attached to FM1 is called the **CalRAD**.

2.7 The REB

In addition to the general description of the electronics in Sec. 2.2, for reference and to support the following sections, a few more details need to be given on the electronics as it is implemented in RAD.

To keep signal lines short and therefore reduce noise, crosstalk and Electromagnetic Interference (EMI), the sensor head contains all preamplifiers and all first shaping amplifier stages in its housing. This part, the detectors, CSAs and shapers in RSH, are called the Frontend Electronics (FEE).

A multi-pin connector on the RSH directly couples to its counterpart on the REB. For a lot of early measurements and a lot of accelerator runs, an additional cable has been inserted between RSH and REB. This cable adds considerably to the crosstalk between channels, as well as catching additional EMI, and all electronic analyses should be considered final only when they have been done with the FM2 in flight configuration (RSH attached to REB without cable).

The parts mainly of concern to a physicist in the REB are the so called Voltage Input Readout Electronics for Nuclear Applications (VIRENA) ASIC and the elaborate multi-level triggering scheme in the Electronics for VIRENA Interface Logic (EVIL) Field Programmable Gate Array (FPGA). They serve additional purposes (such as monitoring of the overall health of RAD) which are neglected in the following.

The VIRENA is fed with the signals from the sensor head and consists of a set of 36 parallel and identical signal processing and amplification chains which can be tuned in a lot of different parameters. The output of these 36 chains is then fed to a single, multiplexed 14 bit-ADC. It contains adjustable threshold comparators to produce digital signals for the trigger logic and contains an additional programmable gain amplifier. This programmable gain amplifier can be software-set to a gain of $1\times, 2\times, 4\times$ or $8\times$, independently for each channel.

As 36 channels are available on the front end of the VIRENA, each signal of the total of 17 sensor head channels is fed twice into the VIRENA to exploit this available redundancy, leaving 2 channels for test purposes. By selecting different VIRENA gains for the same sensor head channel, the dynamic range of the channel, as seen by the ADC, can be extended. For a given channel, the redundant channel is either named with **r** appended[5], or the following

---

[4] Note that somewhat confusingly, RAD describes just a single REB here.

[5] Some confusion exists about the F2 and F2r channel. Due to a naming error in some of the ground support software, the meaning of redundant and non-redundant channel is in some contexts switched for the

naming scheme is used:

- A high-gain channel splits into a ***H** and a ***U** channel, with the ***U** channel having the higher selected VIRENA gain.
- A medium-gain channel splits into a ***M** and a ***I** channel, with the ***I** part having the higher gain.
- and a low-gain channel splits into ***L** and ***N**, with ***N** having the higher gain.

Thus, for the D scintillator, the available channels are, in decreasing order of gain: DU, DH, DI, DM, DN, DL. Changing the VIRENA gain scale setting also changes offset positions and requires recalibration of the energy scale. Each channel for each gain setting has a DC offset which gives the ADC value for an energy deposit of zero. These offsets are mostly in the range of 1500 . . . 2200 ADC values. Let ADC henceforth denote the unit of a one least significant bit change of the ADC sampling value for a channel in a given context. The gains and offsets vary from channel-to-channel in each VIRENA and the VIRENAs in different REBs are not comparable. A calibration is thus needed for each individual channel and gain setting.

If the trigger logic decides to sample an event, the VIRENA will hold all signals until the ADC has read them. As a single multiplexed ADC is used for reading, the values are sampled sequentially. The digitization is where the largest amount of time is spent per event. To reduce digitization time, the trigger logic can select to only sample a subset of the available channels.

The signals from the trigger electronics in the VIRENA, which are further split into individually configurable fast and slow trigger paths per channel, are moved from this 1^{st}-level trigger logic to the 2^{nd}-level trigger logic (L2) inside the EVIL FPGA. The EVIL trigger logic is used to select (with software-configurable trigger tables) the events of interest from the set of triggered channels and also to determine the set of channels which should be read out for a particular trigger input. Further, it contains a First In First Out (FIFO) register to decouple event processing by the following onboard processor from event taking. A priority scheme in the trigger tables determines which event types are handled first in high rate conditions. For performance reasons, energy reconstruction from a set of multiple readouts per physical detector is also done in the EVIL FPGA. This reconstruction algorithm and its limits are discussed in more detail in Sec. 3.8.

Finally, the onboard processor receives events from the EVIL FIFO and processes them into histograms whilst also keeping a certain subset of PHA words for downlink. For the flight unit, it is loaded with a sophisticated data reduction software designed to handle the data according to the goals of RAD. The output and inner workings of this software are not covered in more detail here, because most of the data taken so far is raw and without further reduction. In principle and especially if unforeseen conditions appear, one is able to change the onboard processing arbitrarily in-flight. The processor is connected by two serial links to the outside of RAD. One link is the nominal channel to the rover bus, with a data rate of 56 kbps and one is the so called high-speed link with a data rate of 1 Mbps. To get a undistorted view of all sampled PHA data during calibration runs, the onboard software is configured to simply transmit the data from the EVIL FPGA on the high-speed link.

F2 channel. The corresponding VIRENA gain table should therefore be consulted when processing data from this channel. The F2 and F2r are to be considered readout channels for the same F2 PIN diodes henceforth.

2.8 The DIRENA

An additional readout system called DIRENA, designed by S. Böttcher, has been used for a lot of measurements involving the PF RSH. It is used in this work for some of the measurements presented in Sec. 3.5. A block diagram of the options of mating a sensor head to a readout electronics is given in Fig. 2.9. As laboratory electronics is free from the requirements of space electronics, notably the power constraints, the DIRENA uses a completely different signal processing scheme, derived from the scheme used in high-energy physics experiments. It contains a set of 18 parallel 12-bit ADCs, which is, in the case of using the DIRENA for RAD, connected to each output signal of the RSH (one spare channel remains). The ADCs are controlled by a single FPGA and are set to constantly sample their inputs at a rate of 3 Msps. Custom logic in the FPGA then digitally reconstructs the pulse heights of the input pulses and contains the configurable trigger logic to select the events. The trigger logic is currently kept simple as a large OR-gate with a configurable threshold for each channel.

The pulse height reconstruction method inside the DIRENA is the so-called optimal filtering process. For each time step of the digitization, the waveform sampled by each ADC (in a limited time frame) is constantly compared to a prototype waveform which is given by the theoretical shape of the shaper output. The comparison is done by interpreting the prototype and a measured signal as a vector of values and calculating the scalar products as the steps of a discrete convolution process[6]. This gives a time series of reconstructed pulse heights, for which the maximum (again in a given time frame) is then taken as the pulse height of the measurement. ADC resolution, phase mismatch between the prototype waveform and the measurement as well as the finite sampling rate limit the accuracy of this measurement. The output of the DIRENA is connected to a PC and allows to sustain a maximum output event rate (for full readout of all channels) of about $1000\,\mathrm{s}^{-1}$. The DC level of the prototype waveform is adjusted to be zero. This causes the reconstructed pulse height (and therefore energy) scale also to start at zero, which simplifies data analysis[7]. A schematic view of this process can be seen in Fig. 2.8.

Two different versions of the DIRENA exist, DIRENAv1 and DIRENAv2. The difference of the v2 to the v1 version is mainly an additional set of input amplifiers, to move the voltage swings of the RSH outputs into a range more suitable for processing by the ADCs. This reduces the amount of quantization noise and reduces the noise feedback from the digital parts on the v2 DIRENAs. The noise is, compared to REB figures, quite large for the DIRENAv1 ($\sim 1\,\mathrm{mV}$).

2.9 Ground level processing

The data that is received on earth is stored for long-term archival in the NASA Planetary Data System (PDS) as so-called level zero data. A set of software tools, still in the process of being written and with input of this work, will then be used to derive physically meaningful particle fluxes and energy distributions for general use.

The engineering models as well as testing of the flight models is handled using the Ground Support Equipment (GSE) with a software package aptly named Ground Support Equipment Operating System (GSEOS).

---

[6] In the real DIRENA, this is slightly different and gaps exist in the prototype waveform.

[7] Due to a second step in the default processing of DIRENA data, which takes the maximum of several pulse heights, a slight shift from zero exists. This minor effect has been ignored for all analysis of DIRENA data done here.

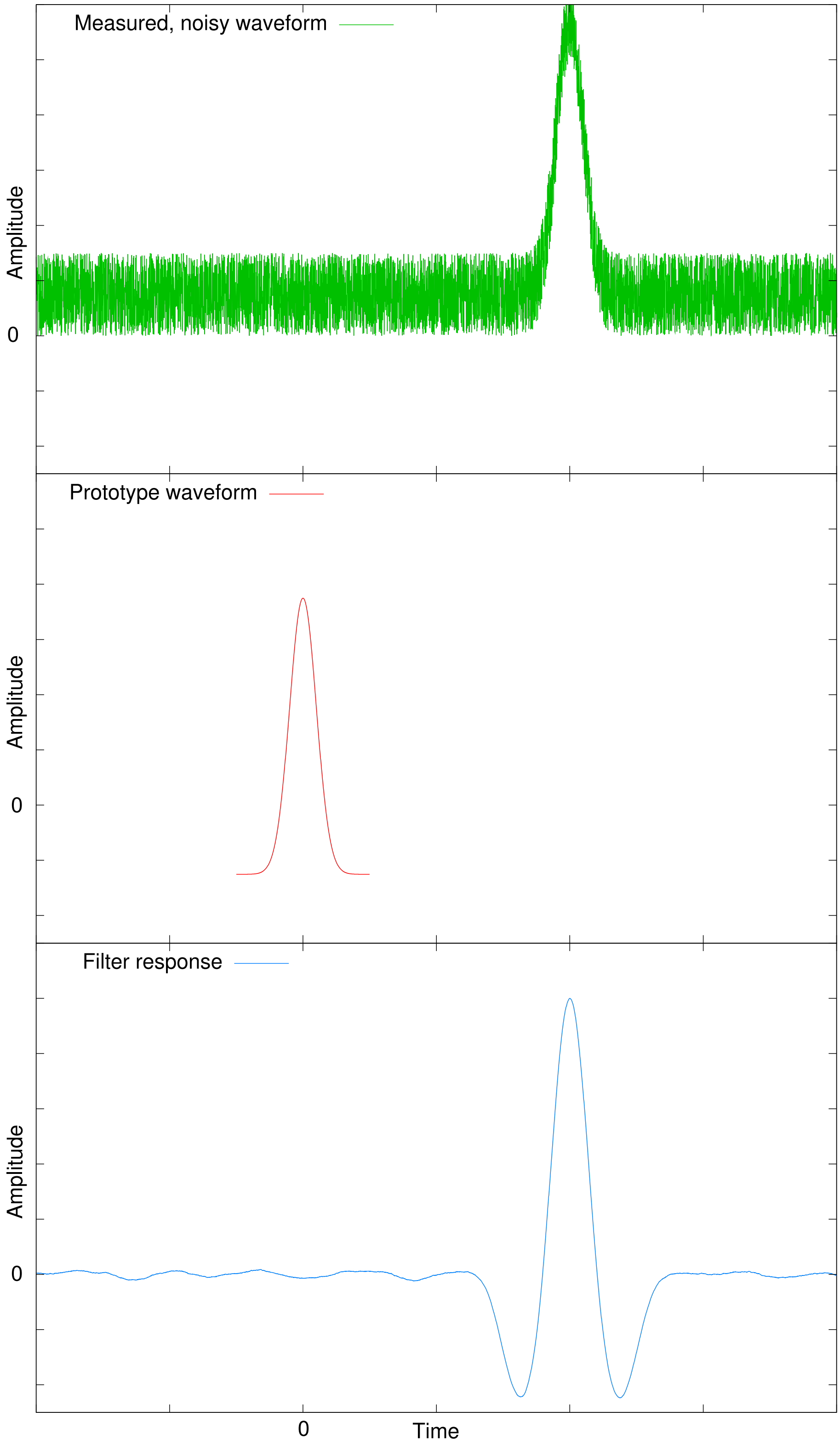

Figure 2.8: Optimal filtering schema as approximately implemented in the DIRENA. The top waveform shows a noisy input measurement with a DC offset $\neq 0$. The curve in the middle is the prototype waveform that is used for optimal filter. In the bottom panel, the reconstructed pulse heights for each processing step are displayed. As the mean of the prototype waveform has been selected to be zero, the mean value of the reconstructed waveform is zero, too. In the real DIRENA, the number of the prototype waveform samples is much lower than shown (16 selectable positions on a set of the last 32 sampled ADC values).

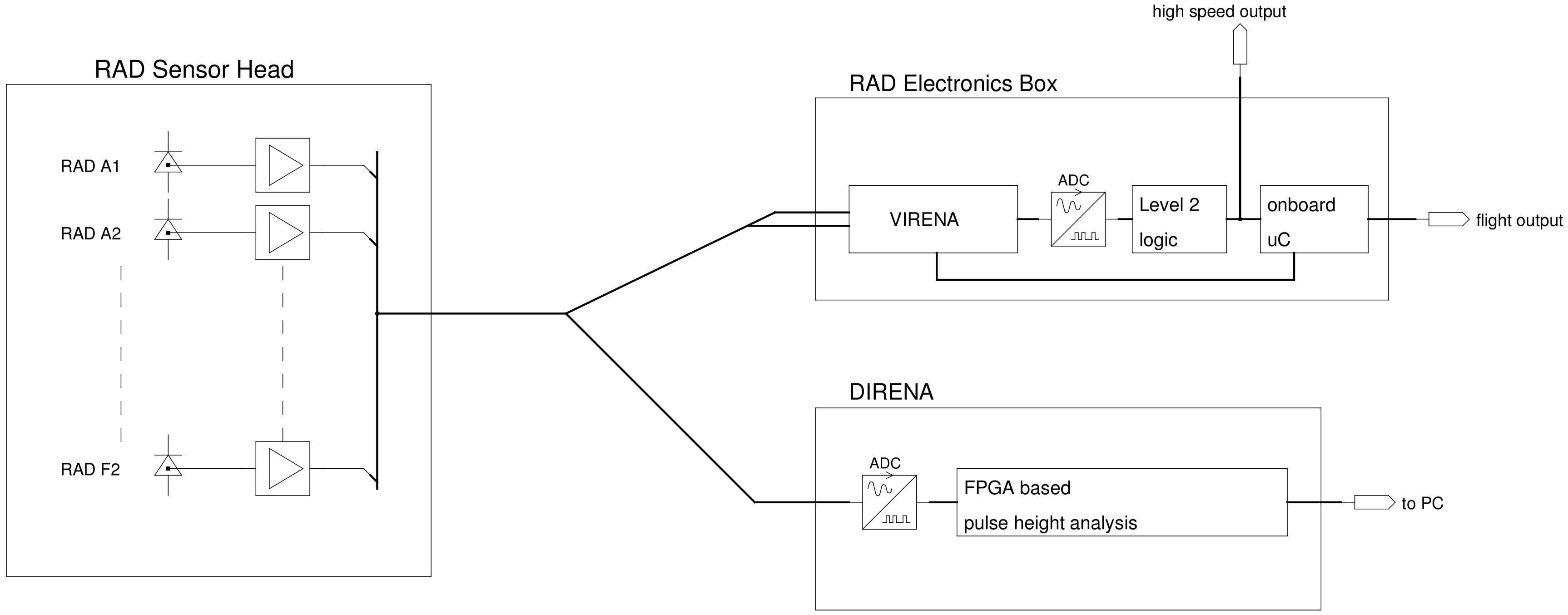

Figure 2.9: Rough overview of the logical data processing components in the RAD instrument and the two available alternatives DIRENA vs. VIRENA. It is not entirely correct that the high speed output gives the data before the onboard microcontroller (uC) handles it. For the high speed data output, the microcontroller just copies the data without any further processing.

2.10 Calibration runs

The RSHs and REBs have undergone a lot of testing in particle beams in parallel to the final development of the flight models. A lot of beam measurements have been done with the PF RSH and some early ones using the DIRENA electronics. The following list gives a broad, approximately chronological overview over the set of measurements done with any RAD-related equipment:

Detector performance tests The initial detector selection for FM1 and FM2 has been done using custom laboratory multi-channel analyzer hardware.

PF lab tests All early tests of the PF have been done using DIRENAv1.

BNL relativistic ion beam tests 2007/2008 All RAD sensor heads have been irradiated with relativistic ion beams at the NASA Space Radiation Laboratory (NSRL)/BNL. The PF has been tested using DIRENAv1 and early versions of the REB, with 1 GeV nuc^{-1} iron and proton beams. Quenching behaviour of the D scintillator has been derived mostly from these measurements. Additionally, and to test with better statistics for fragments with lower z, titanium and carbon beams have been used.

The two flight units have been cross-calibrated using iron and protons at BNL. This is the only high-energy cross-calibration which exists for FM1 and FM2. Other cross calibrations that have been done are radioactive source and muon runs.

To see stopping particles, additional runs have been performed during each beam time with a binary filter and collimator in front of the instrument, down-tuning the input energy to values expected to stop in the instrument.

CERF The PF with the DIRENA has been used to measure at the CERN/CERF calibration field [*Mitaroff and Silari*, 2002]. Using a manually operated external triggering telescope, limited AC positional response testing has been done. The high amount of noise of the DIRENAv1 limits the usefulness of this data for AC investigations and the HIMAC run (see below) has been used for this.

iThemba The PF has been tested with neutrons having an energy of 100 MeV and using an early prototype FlatRAD. Only a limited amount of statistics is available.

PTB RAD has been tested with neutrons in the 5 ... 19 MeV range at the Physikalisch-Technische Bundesanstalt (PTB). The details of this run are covered in Chapter 7.

IABG/KT assembly and tests During assembly and testing of the flight units, several calibration runs using either ^{207}Bi (for single silicon detectors) or a pure aliveness test using a ^{60}Co have been performed. The DIRENA has been used for this.

NIRS/HIMAC Most important for this work is the AC testing done at the HIMAC beam line in early 2010 (see Chapter 5). Additionally, tests using helium and proton beams with energies close to being stopped in RAD, have been done at HIMAC.

RTG testing The FM1+CalRAD setup has been tested with the MSL RTG in April 2010. The absorbing material in between RAD and the RTG as well as the distance from the RTG have been approximated to the values expected for the final flight configuration.

Final tests at SwRI Mainly using cosmic muons and radioactive sources, the FM2 with FlightREB and the FM1 with CalRAD have been used for test runs at SwRI. Several of these runs have been done to test the behaviour of the final flight software.

Chapter 3

Optical photon simulation

The optical model described here is a basic building block of the modeling and data analysis efforts described in the later chapters. In the first part of this chapter, the description of the pure optical model of the scintillators is given. In the second part, the optical model is applied to some measurements involving the D scintillator, replacing particle physics modeling with a few simple assumptions. The model is extended with the input from particle physics and readout effects to forecast Martian conditions in Chapter 6 and used to analyze neutron data in Chapter 7.

Various parts of the RAD instrument and instrument software design are affected by light collection issues of the scintillation detectors and the need to handle them properly:

1. Silicon hit rejection cuts have to be selected. Energy deposits in both the silicon and the bare scintillator volume need to be separated from each other. The amount of falsely flagged silicon hits (false positives as well as false negatives) and the influence on the angular acceptance function needs to be known. The best silicon cut given the onboard processing constraints needs to be selected.

2. The best (lowest noise) scintillator energy reconstruction has to be selected. Apart from dequenching, the correct linear combination (with the lowest noise) of photo diode signals for a given particle type and energy range should be found. This reconstruction is constrained by additional limits in the signal processing chain.

3. The AC efficiency needs to be known and it is helpful to have a spatial (and angular) mapping of its behaviour. To get good numbers for the charged particle contribution in the neutral channels, the response of the AC to a given charged particle field needs to be known; this field could be different from the test conditions that have been created on Earth.

4. The general broadening of the seen energy deposits due to optical effects in RAD's scintillators needs to be known. This is important both for the AC to calculate the rejection rate, and for D and E to know the energy resolution of these scintillators.

These peculiarities of the scintillation detectors warrants a closer look at the collection process of the scintillation light. To aid in this, an optical model of the scintillators has been developed. The model is a photon Monte-Carlo (MC) model similar to the ones implemented in `GEANT4` [*Agostinelli and others*, 2003] or `litrani` [*Gentit*, 2002]. In contrast to the models described therein, the approach described in the following allows direct use of the complex geometries of RAD's scintillators and (contrary to `GEANT4`) only covers the optical parts of the setup and not the full MC chain. Earlier studies of the RAD scintillators in `GEANT4` have been performed by *Kortmann* [2006]. The optical model covers

- The influence of the distribution of the primary particle tracks,
- reflectivity of the wrapping material and absorption in the scintillator bulk,
- and, most important for the setup in MSL/RAD, the exact geometry of the particular scintillator and the arrangement of the readout photo diodes on the signal seen for the scintillator.

Using the verified model, the issues described by the points above can be approached:

1. The influence of silicon hit rejection cuts on the angular acceptance can be modeled, as well any possible influence of such cuts on energy-dependent detection efficiency.
2. The influence of light distribution on energy reconstruction can be estimated and the gain scales as well as reconstruction algorithms can be tuned accordingly.
3. Angular acceptance effects in the AC can be extrapolated from a validated model and applied to any assumed directional distribution of MIPs (and later, any particle field that can be simulated in `GEANT4`, see Chapter 6).
4. The broadening due to positional variation of tracks in a scintillator is a direct output of the optical model for a given distribution of particles.

The simulation does not cover more complicated processes such as light polarization, more elaborate surface models, wavelength-dependent effects (such as wavelength-dependent refraction) or any effects due to wave-like behaviour of the scintillation light.

The following section describes only the physical part of the model; Some more details regarding the technical side of the model are given in App. F.

3.1 Optical photon model

The model should be able to give the light output distribution of the N photo-diodes attached to a given scintillator volume $V \subset \mathbb{R}^3$, for a given input particle distribution.

A nested integration across two distributions is done. One is the angular and positional distribution of primary particle tracks with a certain energy loss along their path through the scintillator. The second is the integration of light produced along each track reaching a given photo diode.

Assume each diode $i \in \{1, \dots, N\}$ gets a certain fraction of light ξ_i for a given primary particle energy loss, and define the total fraction of light reaching any diode as

$$d := \sum_i \xi_i. \tag{3.1}$$

Assume further that all particle tracks $T_{\mathbf{a},\mathbf{b}}$ with $\mathbf{a}, \mathbf{b} \in \mathbb{R}^3$ are straight lines crossing the scintillator (high-energy charged particles)

$$T_{\mathbf{a},\mathbf{b}}([0,1]) \cap V \neq \emptyset \tag{3.2}$$

where

$$T_{\mathbf{a},\mathbf{b}}(t) : t \mapsto (1-t)\mathbf{a} + t\mathbf{b} \tag{3.3}$$

for $t \in [0,1]$. Interactions with γ-photons would be modeled as point-like by converging $b \to a$ and thus having T as a δ-distribution. Complex tracks in the scintillator or step-wise interactions from a particle physics MC simulation such as `GEANT4` fit into this picture by applying the optical model along each individual step. The path for a particle losing energy in a step is modeled as a straight track and the output over a set of tracks is summed. This more complex case of a combined particle physics and optical model is described in Chapter 6.

Let $\frac{dL}{dx}(\mathbf{x})$ be the differential light production along the given track, at position $\mathbf{x}$. Usually, $\frac{dL}{dx}$ would depend on $\frac{dE}{dx}$ through the quenching relation (for quenching details, see Sec. 7.5.1). The model does not look at any quenching effects, as this happens before light production and can thus be done before processing any optical effects, and can therefore be completely integrated into the regular high-energy physics models.

Let

$$F(T) = \int\limits_{t \,\in\, [0,1]} \|\mathrm{b} - \mathrm{a}\| \frac{dL}{dx}(T(t))dt \tag{3.4}$$

be the total light production of T inside in the scintillator.

Let $P_i(\mathbf{x})$ be the light fraction reaching detector i for an isotropic point source at location $\mathbf{x}$. It is assumed that light production through scintillation in any scintillator is isotropic for each point along the Primary Particle Track (PPT).

It is then

$$\xi_i = \frac{1}{F(T)} \int\limits_{t \,\in\, [0,1]} P_i(T(t)) \|\mathrm{b} - \mathrm{a}\| \frac{dL}{dx}(T(t))dt \tag{3.5}$$

Here, the optical model of the scintillator only shows up in the mapping $P_i(\mathbf{x})$. Thus, if the value of $P_i(\mathbf{x})$ is known for all $i \in \{1, \ldots, N\}$ and $\mathbf{x} \in \mathbb{R}^3$, the response of the scintillator can be calculated for any incoming PPT (or, consequently, distribution of PPTs). This is used to speed up processing by dividing the processing into two separate steps (see below).

The value of $P_i(\mathbf{x})$ is calculated by integration over all possible photon directions of the position- and direction-dependent light response $W_i(\mathbf{x}, \varphi, \theta)$ (with azimuth angle $\varphi \in [0, 2\pi)$, and angle to zenith $\theta \in [0, \pi]$):

$$P_i(\mathbf{x}) = \int\limits_{\varphi} \int\limits_{\theta} \sin(\theta)\ W_i(\mathbf{x}, \varphi, \theta)\ d\theta\ d\varphi \tag{3.6}$$

The value of $W_i(\mathbf{x}, \varphi, \theta)$ is the relative response of PIN diode i to a narrow pencil-shaped beam of a unit of light energy going into direction (φ, θ) from location $\mathbf{x}$. Most of the model implementation covers the geometry of such *photon tracks.* As one can easily imagine, the function W_i is, in realistic geometries, a highly nonlinear function in each direction $\mathbf{x}, \varphi$ and θ and has a lot of discontinuities.

In the numerical calculations, the main two, global integrations (Eqs. 3.5, 3.6) are done through the MC method. To calculate W_i and in turn P_i, *optical photons* are created at discrete points on a regular grid through the scintillator volume, with random directions. These optical photons are then traced through the scintillator geometry.

A *bulk model* describes the propagation of photons in the bulk material and a *surface model* describes the interaction between two different bulks in the simulation.

Photons are traced until they would either hit one of the sensitive surfaces (photo diodes) attached to the scintillator or until a runaway stopping criterion is met. Currently, photons are considered as lost when the number of surface interactions exceeds 1000. Upon reaching

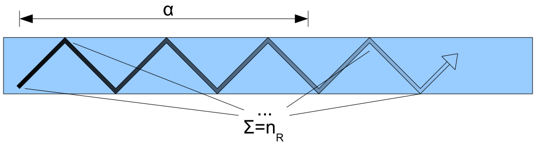

Figure 3.1: Illustration of the dependency between α, R, l and n_R of a photon track.

a detector, each photon is then weighted and counted. For a given track length l and number of reflections n_R, the weight (relative intensity I) has to be calculated as

$$I = e^{-\frac{l}{\alpha}} \cdot R^{n_r} \tag{3.7}$$

with α being the mean absorption length in the scintillator bulk[1] and R the coefficient of reflectivity for the scintillator-to-air (or vacuum) interface. The normed sum of all weighted photons gives the value of $P_i(\mathbf{x})$. It is important to note here that a simulated photon track will never be split up into two distinct parts upon being partially reflected on a scintillator surface. Instead, a BERNOULLI-trial is done with the appropriate probabilities for reflection and transmission. This allows to handle photon tracks as one-dimensional list structures in software. Further, if a linear relation between l and n_r is assumed, Eq. 3.7 reduces to just one single exponential law. Although no direct relation exists, a strong correlation between l and n_r is expected and can be exploited to give good average figures of the scintillator behaviour for a change in either of the parameters l and n_r. This is covered in detail at the end of this chapter in Sec. 3.9.

Applying the extinction due to self-absorption inside the scintillator or at its surface boundaries at the end of tracing a photon track has another numerical advantage. The computationally costly tracing through the scintillator geometry needs to be done only once for any set of α, R values deemed to be of interest later on. Changes of reflection or transmission probabilities would need a recalculation.

When working without more complex input from a particle physics model, the calculation of the $P_i(\mathbf{x})$ values on the grid through the scintillator is followed by a simple integration over a set of PPTs. The response to each PPT from a given PPT distribution is calculated by doing the integration in Eq. 3.5 on the linear interpolation of the grid. This gives simulation hits, akin to `GEANT4` energy deposits for each primary particle event. Then, in the very last step, additional broadening due to energy loss straggling and readout noise and the silicon-to-light ratio is applied to approximate the behaviour of the real scintillator. This process is described in more detail in Sec. 3.4, and even more detailed, incorporating the input of `GEANT4`, in Chapter 6.

Plots of values in the interpolation grid itself are of interest to get a qualitative understanding of the light collection issues in a particular scintillator. Although the focus in this work has been put on a full integration of the optical model, early investigations of the scintillators in questions have been done mostly using such readout maps. For the D and F scintillator, spatially resolved maps of the scintillator behaviours are given in Sec. 3.7.3 and App. D.4 respectively.

---

[1] Note that, for simpler handling throughout this work, α is the absorption length and *not* the absorption coefficient (in units of $[\mathrm{m}^{-1}]$), as it sometimes alternatively specified.

3.1.1 The bulk model

The scintillator bulk is modelled as a free-flight path for photons, with possible absorption by the simple exponential extinction law as stated above.

Absorption is assumed to be isotropic in direction and position inside the scintillator bulk, to allow for a faster calculation of a weighted photon contribution at the end of the track, as given in Eq. 3.7. This also reflects the fact that only homogeneous scintillator materials are used in RAD. Scattering is assumed to play only a minor role in the scintillators and consequently no additional scattering effects are assumed to occur inside the bulk material of the scintillator.

3.1.2 The surface models

A few different, simple surface models have been implemented to check the influence of the exact surface model on the light propagation in the scintillator and also to investigate the behaviour of the scintillators for the corner cases of light propagation.

For all models, the surface is assumed to be homogeneous, as, during assembly of the sensor head units, the highly reflective wrapping has been put onto the scintillators as evenly as possible and it has been applied everywhere except for those areas where a readout diode is attached. In principle, the current implementation of the model allows to apply different wrappings to different parts of a scintillator, but this has not been used or even further tested yet. Currently, every point on the surface of the scintillator which is not covered by a photo diode is assumed to be covered by the scintillator wrapping. As the surface models affect the path the simulated photons take in the scintillator, the whole photon tracing needs to be rerun for each surface model and the complete model can not be implemented as a weighting formula at the end of a run.

To describe the surface models in more detail, let D^3 be the set of direction vectors

$$D^3 := \left\{ \mathbf{x} | \mathbf{x} \in \mathbb{R}^3 : \|\mathbf{x}\| = 1 \right\}. \tag{3.8}$$

The surface is then modeled by a function

$$S(\mathbf{n}, \mathbf{d}, \mathbf{o}) : D^3 \times D^3 \times D^3 \to \mathbb{R}, \tag{3.9}$$

the conditional probability of emission for a photon into the outgoing direction $\mathbf{o}$, given an incoming direction $\mathbf{d}$ and a hit with a surface having an outer normal $\mathbf{n}$. The description of the surface models could be further simplified by rotating all vectors such that $\mathbf{n}$ corresponds to a selected default plane (say $\mathbf{n} = (1, 0, 0)$). To avoid this additional rotation step in the simulation code, the implementation of the surface models uses a description close to the one given given in Eq. 3.9. The major difference being that drawing from the $S(\mathbf{n}, \mathbf{d}, \mathbf{o})$ distribution is directly done as a MC step. For this reason, the description of the surface models will be done using the relation between the three vectors $\mathbf{n}, \mathbf{d}, \mathbf{o}$ instead.

Four models have been implemented. The two corner cases are `mirror` for mirror-like and `diffuse` for completely diffuse reflections. They are mainly used to see the maximum possible effect of the surface model on the light propagation in the scintillator. The diffuse case has been further split up into a 2π uniform emission extreme case and a LAMBERTian diffuse reflector. The model `total` covers the total reflectance case and `fresnel` also covers partial reflection and refraction to the reflector material (reflecting back into the scintillator again). An overview over the models as well as the values involved is displayed in Fig. 3.2.

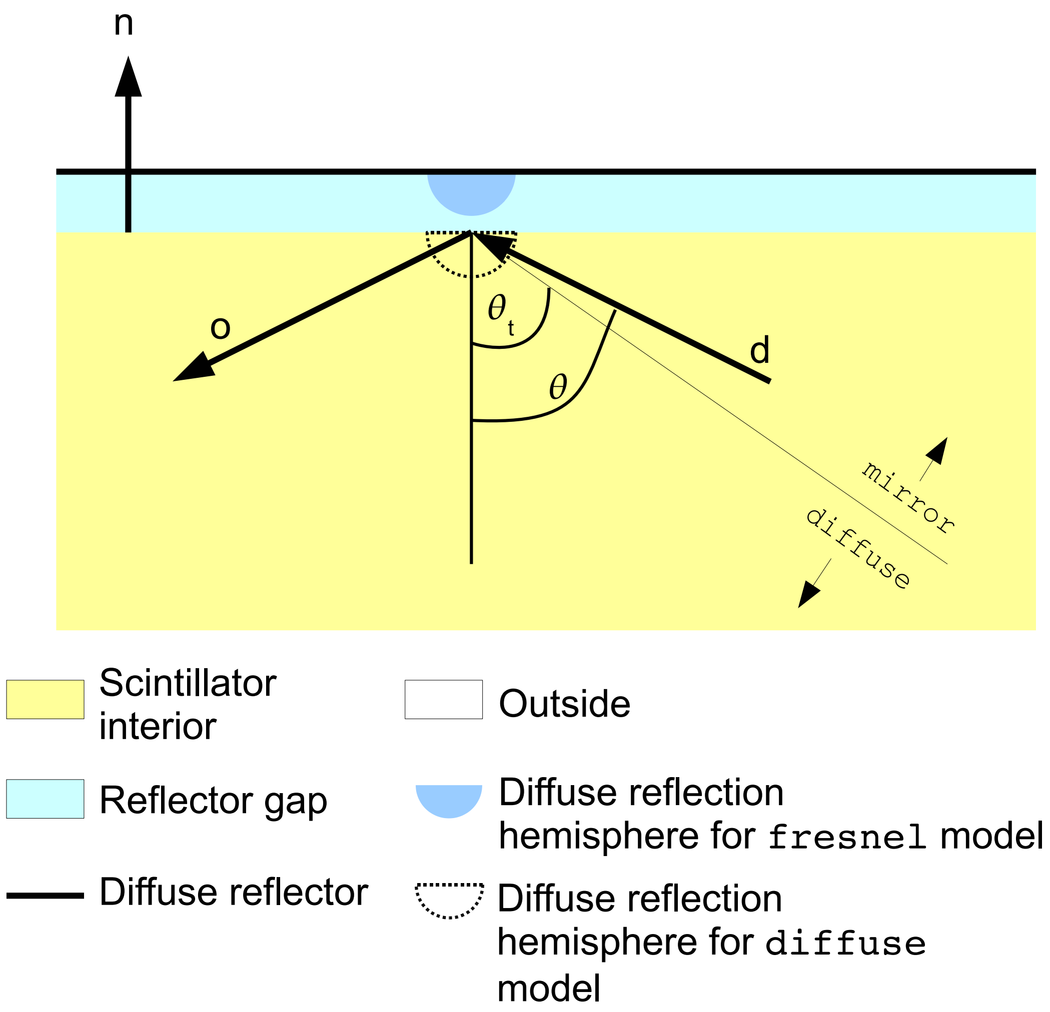

Figure 3.2: Overview of the surface models. The outer (top) diffuse hemisphere with the (Martian) air gap in between is used for the `fresnel` model, and for the purely diffuse model, it is assumed that the scintillator surface itself reflects diffusely (bottom dashed hemisphere). The LAMBERTian diffuse case, not separately shown here, weights with the cosine angle between $-\mathbf{n}$ and $\mathbf{o}$.

Diffuse reflection. In the `diffuse` case, the outgoing direction of the photon is assumed to be completely independent of the incoming direction. It will be reemitted either uniformly into the 2π solid angle facing inwards from the given surface point (the '2π' case):

$$S_d = (\mathbf{n}, \mathbf{d}, \mathbf{o}) = \begin{cases} \frac{1}{2\pi} & \text{if } \mathbf{n} \cdot \mathbf{d} < 0 \\ 0 & \text{else} \end{cases} \tag{3.10}$$

or is, for LAMBERTian diffuse reflection, given as

$$S_d = (\mathbf{n}, \mathbf{d}, \mathbf{o}) \sim \begin{cases} \cos\theta_o := -\mathbf{o} \cdot \mathbf{n} & \text{if } \mathbf{n} \cdot \mathbf{d} < 0 \\ 0 & \text{else.} \end{cases} \tag{3.11}$$

Mirror-like reflection. In the `mirror` case, the angle of emergence simply equals the angle of incidence and it is thus

$$S_m = S(\mathbf{n}, \mathbf{d}, \mathbf{o}) = \delta(\mathbf{o} - \mathbf{d} - 2 \cdot \mathbf{n} \cos\theta) \tag{3.12}$$

with

$$\cos\theta := \mathbf{d} \cdot \mathbf{n} \tag{3.13}$$

here.

Total reflectance. The simple model for total reflectance simply switches between the above `diffuse` and `mirror` model, depending on the critical angle θ_t for total internal reflection. The angle θ_t is given by SNELLs law for scintillator Index Of Refraction (IOR) n_i and outside (air/vacuum) IOR (n_o) as

$$\sin(\theta_t) = \frac{n_o}{n_i} \tag{3.14}$$

The surface model in this case becomes (for incidence angle θ)

$$S_t = \begin{cases} S_m & \text{if } \theta > \theta_t \\ S_d & \text{else} \end{cases} \tag{3.15}$$

The rationale for this mix of diffuse and specular reflection is that, in the case of the scintillator wrappings used for RSH, the reflector material is separated from the scintillator by a small air gap. This air gap changes the geometry of the scintillator only by an insignificant amount, but allows for total internal reflection to occur.

This model needs the scintillator IOR as an additional parameter. For the materials used in RAD, the values are known. For CsI [*Brose et al.*, 1998; *Valentine et al.*, 1991] it is assumed that

$$n_{\mathrm{CsI}} \approx 1.79 \tag{3.16}$$

and it is also assumed that BC430, BC430M and BC432M all share the same IOR of that of BC430, from *Saint-Gobain Crystals and Detectors* [2005-8]:

$$n_{\mathrm{BC43X(M)}} \approx 1.58. \tag{3.17}$$

The glue layer and its IOR is *not* taken into account in the simulations. For the RAD PF assembly, the glue layer out of the so-called 'RTV' material has been measured to have an IOR (measured on a equilateral prism cast out of RTV at a wavelength of approx. 635 nm of a red diode laser) of

$$n_{\mathrm{RTV}} \approx 1.43 \pm 0.05. \tag{3.18}$$

Partial (Fresnel) reflectance. This model (`fresnel`) is the most complex of the above and, from the set of implemented models, deemed to be most accurately describing the case of the RSH scintillators. The `total` reflectance model still misses the case of partial reflection as well as the reentrance of the ray from the diffuse reflector outside the scintillator back into the bulk volume.

Partial reflectance is incorporated by looking at the reflected I_r and refracted fraction $I_t = 1 - I_r$ according to the FRESNEL formulas [*Born and Wolf*, 1980].

The ray is then reflected with probability I_r. If it is not reflected, it reappears in the scintillator with a different angular distribution. This case models a ray exiting the scintillator bulk and bouncing back and forth in the air gap between scintillator and reflecting material. The new, incoming ray back into the scintillator is then calculated by taking multiple reflection in the air gap into account.

To calculate the direction of this new photon, a new ray towards the scintillator is generated, drawn from a distribution with probability density which is proportional to the transmitted intensity fraction (according to the now swapped FRESNEL coefficients) from the outside to the inside for the given incidence angle θ_i, let this be $I_t(\theta_i)$. This models diffuse reflection from the wrapping material, followed by either reflection back to the wrapping material (i.e. rejection by the MC sampling) or transmission into the scintillator bulk at the scintillator boundary layer.

The resulting incoming angle is then properly refracted according to SNELLs law, yielding the final direction given by the surface model.

No light is assumed to be lost when exiting the scintillator; the wrapping of the scintillator is assumed to have 100% reflectivity for the multiple reflection calculation. It is also assumed to be completely diffuse and therefore behave like the `diffuse` model for photons inside the gap. As a simplification, imperfect reflectivity is subsumed in the single R reflectivity constant for all light being reflected from such a surface (independent on whether specular or diffuse reflection happened and independent on how many reflections happened). Also, the possible partial polarization happening during reflection is completely neglected in this model.

3.2 Resulting parameter set for the optical model

Owing to the relative simplicity of the above optical model, the total number of free parameters for the optical model alone is quite small. The full set of parameters is:

α The (isotropic) absorption length in the bulk material.

R The reflection coefficients for the surface interaction. Each surface interaction is assumed to attenuate the reflected light by a factor R.

- and the exact surface model used (`diffuse`, `mirror`, `total` or `fresnel`), uniform 2π- or LAMBERT-diffusion

The effective differences between the surfaces models are discussed in Sec. 3.10.

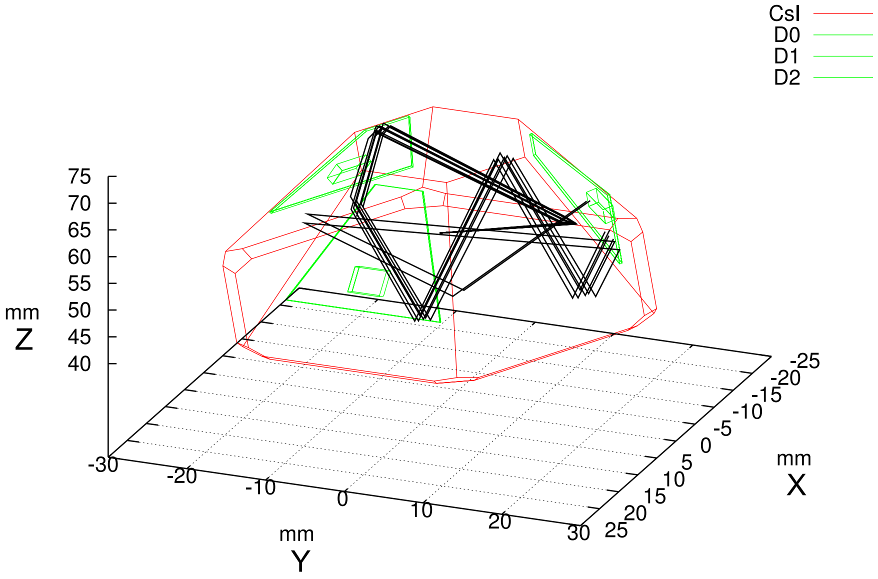

Figure 3.3: CAD model of the D-detector and attached photo diodes D0, D1, D2. The traces of a few simulated optical photons are shown in black. A bunch of photons are created on the z-axis, at $x, y, z = (0, 0, 55\,\mathrm{mm})$, with a slight random variation in direction, to show the effect of diverging photon tracks. The surface of the scintillator is simulated with the `mirror` model here.

3.3 Geometry

It should be noted here that a major part of the implementation of the model deals with importing the complex geometry from the reference CAD model of the RAD Sensor Head, to be as close as possible in the simulation to the real shape of the scintillator in question. The geometry is split by the export facility of the CAD system into a surface model made out of a closed set of triangle faces. Internally, intersection and inside/outside tests are handled using a Binary Space Partitioning (BSP)-tree data structure for holding the geometry. This structure from the computer graphics realm has been used to significantly speed up the geometry handling in the simulation and thus allows to import the complex scintillator shapes as they are used inside RAD. It is also successfully used in the context of `GEANT4` for RAD (See Chapter 6 and the following chapters).

Fig. 3.3 shows the general setup as it is used for the D detector, showing the outline of the detector and a few traced photon tracks according to the `mirror` model. For more technical details, see App. F.

3.3.1 Primary particle track distributions

The behaviour and especially the light distribution (see below) between the photo diodes attached to a scintillator largely depends on the 3D-position dependent ionization density of each incoming particle track. It is therefore important to look at the light distribution for different input particle spectra.

If not noted otherwise, the energy loss for penetrating particles is assumed to be constant along the track (ignoring the Bethe-Bloch formula (Eq. 2.1) due to the test particles being mostly penetrating MIPs) and thus also

$$\frac{dL}{dx} = \text{const.} \tag{3.19}$$

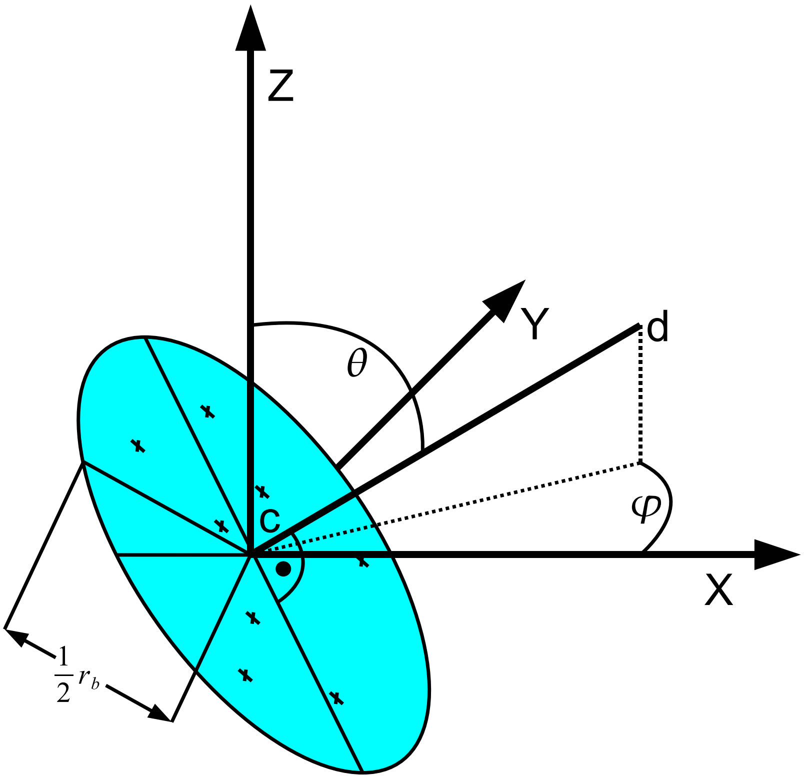

Figure 3.4: Position and direction sampling for a given PPT.

In this case, the calculation of the resulting scintillator energy loss spectra is reduced to a purely geometrical problem.

Instead of start- and endpoint $(\mathbf{a}, \mathbf{b})$, the PPTs are also fully characterized by the pair $(\mathbf{x}, \mathbf{d})$ of start position and direction in the scintillator. This notation is used in the code as it allows a better separation of the directional distribution of PPTs from their spatial spreading. Note that the sign of the direction is not of interest in the case of constant energy loss. The distributions and selection processes described here will be also used for generation of primary particle events for `GEANT4` when using the sequential model.

For all early scintillator light imbalance checks in this chapter, data from a broad, homogeneous beam is used, such that the position is simply drawn from a uniform random distribution. Except for a ratio of light between diodes, one single measurement with a pencil beam will not yield any additional information useable to verify the optical model. In Chapter 5, a *series* of such pencil beam measurements is done to estimate parameters for the AC.

Let r_b the length of the diagonal of the bounding box surrounding the simulated setup, and let $\mathbf{c}$ be the center of the bounding box. To generate $(\mathbf{x}, \mathbf{d})$, the direction $\mathbf{d}$ is first drawn from the corresponding directional distribution. To generate $\mathbf{x}$, a uniform random position $\mathbf{x_0}$ on a circular disc with radius $r_d = \frac{1}{2}r_b$ is selected, with the center of the disc at $\mathbf{c}$ and the normal of the disc being $\mathbf{d}$. Let $\mathbf{x} := \mathbf{x}_0 - r_d\mathbf{d}$ to shift it outside of the active volume towards the front of the instrument. The coordinate system used for this process is illustrated in Fig. 3.4. The main distributions which are used for validation of the simulation results are detailed in Tab. 3.1.

Distribution name	**φ distribution**	**θ distribution**
`straight-x`	0	$\frac{\pi}{2}$
`straight-y`	$\frac{\pi}{2}$	$\frac{\pi}{2}$
`straight-z`	-	π
`isotropic`	$p(\varphi) = \frac{1}{2\pi}$	$p(\theta) \sim \sin\theta$
`cossq-z` (cos^2 muons)	$p(\varphi) = \frac{1}{2\pi}$	$p(\theta) \sim \sin\theta \cdot \cos^2\theta$

Table 3.1: Directional distributions used for the photon MC simulations. $\varphi \in [0, 2\pi)$ is the azimuth angle and $\theta \in [0, \pi]$ the angle against zenith. More details on the $\cos^2$ distribution can be found in App. D, Fig. D.3.

3.4 Optical modeling of the D scintillator

The model is easiest to validate for the D scintillator, as the energy loss per path length for MIPs as well as 1 GeV protons is highest (see App. D, Fig. D.1 for a calculated energy loss spectrum). Also, the effective light yield (per MeV) of the CsI material is much higher (See also the results in Sec. 6.5) compared to the BC43X(M) material as it has been used for the AC and neutron channel. In all following discussions of the optical model, here and in later chapters, the `fresnel`, 2π detailed surface model will be used. For the minor differences to LAMBERTian reflection, see Sec.3.10.

The readout and processing of the data from the D scintillator is affected by any imbalance in the light L_i (resp. light fraction ξ_i) seen by the three attached pin diodes (DH, DM, DL, simply called H,M and L in this section), as the different gains of the diodes produce different noise figures in the different channels. Saturation of any channel allows to use only parts of the L_i values to reconstruct the total amount L of light seen (and thus the reconstruction of the energy deposit after the possible dequenching). To fully understand the sources of energy broadening during D scintillator reconstruction, it is necessary to also extend the described optical model to include electronics noise as well as broadening of the energy deposit due to straggling energy loss in the scintillator as well as the attached silicon diodes.

Validation goal. Validation of the results of the model for the D scintillator is done by comparing the data taken during runs with MIP-like particles with the output of the extended model. It will first be done qualitatively with a set of 2D histograms describing the overall behaviour of the D scintillator, followed by a short look at the numerical values of a parameter describing the amount of geometrical noise.

To have a better view on any differences between the optical model and the measured data, a parameter which is most sensitive to changes in light collection has to be found. Let H, M be the total scintillator energy, reconstructed from the corresponding single channel energy for the D_{Hi} resp. D_{Medium} PIN diode.

The value of the D_{Low} diode will be ignored as noise values as well as quantization levels are too large to give meaningful results (see also Sec. 7.2). Any imbalance in the light collection (for symmetric cases of the PPT distribution) can be seen by looking at the distribution of the value h, defined as

$$h := \frac{H}{E} \tag{3.20}$$

Source	**Particle**	**Energy**	**Direction**	**Unit**	**Reference**
Cosmics	μ	MIP (3.5 GeV in sim. in this chapter)	$\cos^2\theta$	FM2	[#6, μ-FM2-fREB]
BNL	p	1 GeV	0° (zenith)	PF	[#1, p-PF-1 GeV-0°]
BNL	p	1 GeV	$25^\circ \circlearrowleft_y$	PF	[#4, p-PF-1 GeV-$25^\circ \circlearrowleft_y$]
BNL	p	1 GeV	$90^\circ \circlearrowleft_y$	PF	[#5, p-PF-1 GeV-$90^\circ \circlearrowleft_y$]

Table 3.2: Overview of beam tests used for validation. All beams are assumed to immerse the whole instrument. The approximately square-shaped beam used at BNL has an edge length of approx. 20 cm.

Also define $m := \frac{M}{E}$ correspondingly.

Total deposited energy E in any of the following 2D-histogram plots will be reconstructed by the straight-forward way from two channels as

$$E := \frac{1}{2}(H + M) \tag{3.21}$$

Another way to define H, M and E would be $E = \frac{3}{2}(H + M)$ with H and M being the fractional energies in the respective channels. The selected reconstruction avoids needing to distinguish between units of 'total energy' and 'energy per channel' in this chapter. Ignoring the low gain channel in the energy sum here already introduces unavoidable intrinsic broadening in the energy axis direction.

Getting large variations in light collection requires broad particle beams. Unfortunately, γ-sources can not be used to study any optical effects, as in the energy range for γ-photons, the broadening due to electronics and detector noise is too high to get good results (see Sec. 7.2 and Sec. A.2.2).

Also, to exclude the effects of quenching for optical studies, it is important to have a $\frac{dE}{dx} = \text{const}$ beam, which demands penetrating particles with high energy so that the energy loss inside the scintillator is small compared to the total particle energy. A small energy loss leads to relatively larger energy loss straggling broadening of the test beam (see Sec. 2.1.1). This effect needs to be included in the model.

The only well-defined uniform particle beams where controlled tests have been done are different run positions with a broad 1 GeV proton beam at BNL(2007) and laboratory testing with $\cos^2$ angular distributed cosmic muons. Tab. 3.2 lists all runs used for checking of the D scintillator optical photon model.

3.4.1 Scintillator energy loss straggling

The mean energy loss for a minimum ionizing μ- or p-particle is in the range of about 20 MeV for a passage straight through the center of the crystal. The energy loss distribution for a passage of a pencil-shaped beam through the center of the D scintillator (with 28 mm thickness) has been simulated by C. Martin and can be seen in App. D, Fig. D.1.

As the model is initially only an optical one, the energy loss straggling is included after the fact. To be able to rely on proven energy loss models inside the well-tested particle MC software, the energy loss from the MC simulation by C. Martin using `FLUKA` [*Battistoni et al.*, 2007], as shown in Fig. D.1 is used. The energy loss is sampled randomly from the `FLUKA`-simulated 100 k events.

The energy loss in App. D is only given for the full scintillator path length of $q = 28\,\mathrm{mm}$. For different path lengths q through the scintillator, the distribution of energy loss is appropriately scaled and shifted. If $S_{\overline{E}}(E)$ is the probability density for *seen* energy loss E (including straggling) for mean energy loss $\overline{E}$ as given by the above simulation result, it is assumed that the distribution $S_{\overline{E'}}(E)$ for a different mean energy loss $\overline{E'}$ is given by

$$S_{\overline{E'}}(E) = \frac{1}{\sqrt{\frac{\overline{E'}}{\overline{E}}}} S_{\overline{E}} \left(\frac{E - \overline{E'} + \overline{E}}{\sqrt{\frac{\overline{E'}}{\overline{E}}}} \right). \tag{3.22}$$

It thus is assumed here that the shape of the energy loss distribution holds for any crossed thickness q' of scintillator material, assuming

$$\overline{E}' = \frac{q'}{28\,\mathrm{mm}} \overline{E} \tag{3.23}$$

with the mean being shifted to the correct mean energy loss and the width of the distribution scaled by the factor

$$\Sigma := \sqrt{\frac{\overline{E'}}{\overline{E}}} \tag{3.24}$$

Modeling the broadening like this is justified only by the broadening behaviour of a sum of N equal, independent GAUSSian pdfs (factor $\sqrt{N}$) and a behaviour like this in the $q \to \infty$ (thick) case due to the central limit theorem. A GAUSSian is already a reasonable approximation, see Fig. D.1.

3.4.2 Silicon and optical energy scales

Silicon hits and scintillator photons have two different energy scales in the same electrical detector. The ratio of these energy scales needs to be well-defined to be able to compare results and to put the values found in this work into context. The usual way to compare optical and silicon energy scales is to look at the position of a prominent peak due to interaction in the scintillator, with energy E_o and another feature happening solely due to interaction in the silicon (e.g. the MIPs signal in silicon without a scintillator attached or the 60 keV γ-line of ^{241}Am). Assuming that the pulse heights for both interactions with deposited energies of E_o resp. E_s are given as u_o and u_s, the straight-forward silicon-to-light energy scale w is then given as

$$w := \frac{u_s E_o}{u_o E_s}. \tag{3.25}$$

The calculation of this single value w becomes problematic in the following cases:

- When multiple readout detectors are attached to a single scintillator, the light distribution between the detectors needs to be accounted for and it has to be stated for which detector sum the ratio w is given.
- If the scintillator is imperfect and light losses occur ($d < 1$), the value will depend on the scintillator geometry. This obscures any common parameters when comparing different scintillator pieces.

It is also very important to state that any given, fixed ratio w as defined above implicitly assumes a certain integration resp. averaging with a certain set of incoming particle tracks and resulting light distribution inside the scintillator. For particle distributions with overall isotropic light distribution inside a scintillator (cosmic muons, broad homogeneous beam covering the whole scintillator), the values of w should be roughly comparable, though. More on the effects of averaging for the optical behaviour of RAD's scintillators can be found in Sec. 3.9. To avoid the above problems when using a single w value, a few of the more basic parameters describing the scintillator and silicon behaviour are now introduced.

Given a silicon energy deposit E_s, a number of charge carrier pairs u_s results as

$$u_s = \frac{E_s}{a}, \tag{3.26}$$

with $[a] = [\mathrm{eV}]$. It can be again assumed that $a = 3.6\,\mathrm{eV}$.

The number of charge carriers resulting from a scintillator energy deposit depends on more factors. Given an energy deposit E_o in the scintillator volume, a number of photons

$$N_p = b \cdot E_o \tag{3.27}$$

results, with proportionality b [photons/eV]. The photons go through the scintillator, and on *average*, a fraction f_i reaches a given photo diode with index i, giving $\hat{N}_p$ photon hits there:

$$\hat{N}_{p,i} = f_i \cdot N_p. \tag{3.28}$$

This averaging of f_i is done for a specified input particle field. It can be further factorized into the fraction d of light reaching any detector, such that $1 - d$ is the fraction of produced light absorbed anywhere on the way to a detector, and into the relative amount of light collected by the readout detector in question v_i:

$$f_i = d \cdot v_i \tag{3.29}$$

For the sum of all detectors, $\sum\limits_i v_i = 1$. To simplify notation, an arbitrary index i is now selected for a single detector. The resulting number of charge carriers is determined through the quantum efficiency η (also assumed to be equal across all photo diodes):

$$u_o = \eta \cdot \hat{N}_p. \tag{3.30}$$

Assuming homogeneous illumination of all readout detectors, the value v can be calculated as the ratio of the detectors surface area A to the total surface area A_{total} of all detectors attached to the scintillator:

$$v = \frac{A}{A_{\text{total}}}. \tag{3.31}$$

In summary, the energy deposit E_o translates into a number of charge carriers (pulse height) by

$$u_o = d \cdot v \cdot b \cdot \eta E_o \tag{3.32}$$

Without detailed optical studies, the product $b\eta$ can not be separated further. But as it is solely a material constant that relies on the optical properties of the scintillating material and the diode properties, it is the same for all plastic scintillators in RAD.

3.4.3 Silicon diode energy loss straggling

The energy loss in the diodes is assumed to be distributed according to the LANDAU probability distribution. In *Bichsel* [1988], Tab. IX, values for the most probable energy loss, denoted as Δ_p there, as well as the Full Width At Half Maximum (FWHM) and other parameters are given. The width parameter ξ of the LANDAU distributed can be calculated as

$$\xi = 0.017\,825\,\mathrm{keV}\,\mu\mathrm{m}^{-1}\frac{z^2 q}{\beta^2} \tag{3.33}$$

with detector thickness q, $\beta := \frac{v}{c}$ and particle charge number z. This gives ξ values for $q = 300\,\mu\mathrm{m}$ as $\xi_{\mathrm{proton}} = 7.1\,\mathrm{keV}$ and $\xi_{\mathrm{muon}} = 5.3\,\mathrm{keV}$, assuming $\beta^2_{\mathrm{proton}} = 0.75$ and $\beta^2_{\mathrm{muon}} = 1.0$. Assuming that the proportionalities $\xi \sim q$ and $\overline{E} \sim q$ hold, the given distribution for $q = 300\,\mu\mathrm{m}$ is then scaled by the ratio $\frac{q}{300\,\mu\mathrm{m}}$ before drawing appropriate silicon energy loss values E_s.

Finally, the silicon energy loss E_s is scaled into its CsI energy loss equivalent E_c with a scaling factor w

$$E = wE_s. \qquad [w] = \left[\frac{\mathrm{MeV}_{\mathrm{CsI}}}{\mathrm{MeV}_{\mathrm{Si}}}\right] \tag{3.34}$$

The meaning of this value is just as described in Sec. 3.4.2, Eq. 3.25. The value of w is calculated for an optical energy scale which assumes that the total energy calculates as the average

$$E = \frac{1}{3}(\mathrm{High} + \mathrm{Medium} + \mathrm{Low}) \tag{3.35}$$

instead of the simple sum. It thus gives the value of the silicon-to-light ratio in the usual way for the total sum of all three detectors.

3.4.4 Electronics noise

Electronics noise is simply assumed to be GAUSSian in shape and to be uncorrelated for each channel. Crosstalk effects are ignored, as are any higher order effects of the data acquisition system (such as the quantization effects of the DIRENAv1). The signal seen for each diode is broadened with the electronic noise widths as given in Tab. 3.3 below.

3.4.5 Other sources of noise

The detailed analysis of the behaviour of the MSL/RAD as well as the crystals for the planned Solar Orbiter mission in *Gooß* [2006], and also an additional check using the extended model (see Sec. 6.5.2) hint at a resolution function with a negligible term for the photon statistics $\sim \sqrt{E}$. Photon statistics are thus ignored in the model described here.

3.5 Validation results

The above extended model has only the additional parameter w which needs to be fitted to the data. The Si and CsI energy loss straggling is completely fixed by the values from the literature resp. the simulation results from `FLUKA`.

The list of all parameters deemed to be the optimal match, from a *visual 'by-eye' fit* of the surface model as well as the Silicon-to-Light-ratio w of the model to the data are listed in Tab. 3.3. The perfect case $\alpha = \infty, R = 1$ of the `fresnel`, 2π model, as stated, is selected.

The direct comparison of the MC simulation results and the measurements can be seen by comparing the (h, E) histogram plots for the measurements in Figs. 3.5, 3.6, 3.7 and 3.8 with those of the simulation results given in the same figures.

As the geometry of the D scintillator is designed to be identical for both the PF as well as the FM1/FM2 model of the instrument, it is assumed that the optical behaviour of both scintillators is comparable. The notable difference that is completely ignored in the simulation is the addition of intransparent glue material to the scintillator for holding the electronic boards in case of the flight models. It is also assumed (by using only a single value w) that the ratio of light to silicon for the two scintillators is virtually identical. Differences between the two scintillator pieces, which may exist e.g. due to a difference in the concentration of Tl-dopant between both, are assumed to be negligible.

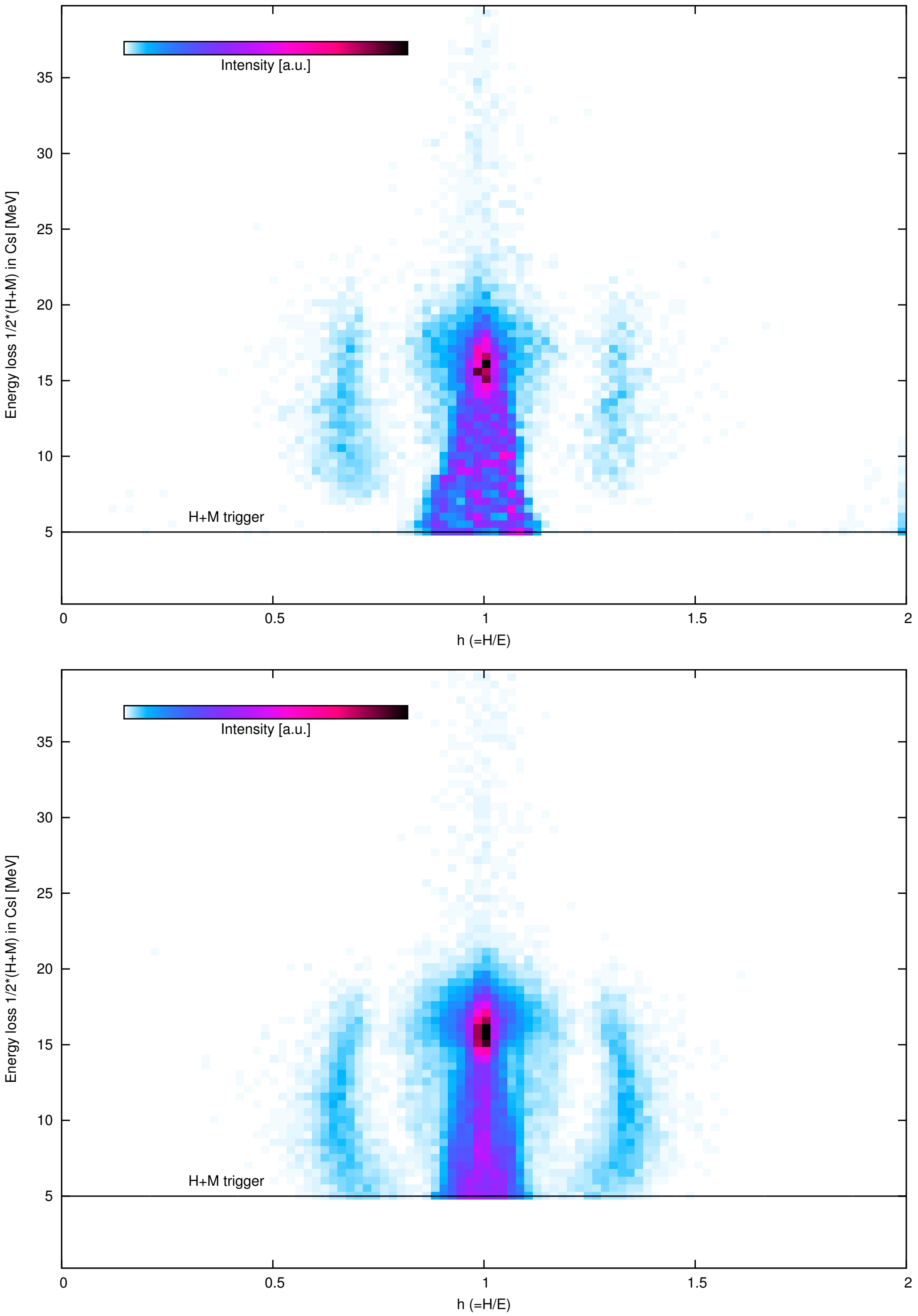

Figure 3.5: Influence of optical effects in a plot of h vs. total Energy, comparing measurement and simulation. Shown is the H light fraction h vs. the total energy E ($\sim$ PPT path length). The top plot shows the results from the measurement, whereas the bottom plot shows the simulation results using the optical model and the selected parameter set. The data set is selected from [#1, p-PF-1 GeV-0°]. The bottom line shows the software trigger condition applied to the sampled data (a hardware trigger with a lower value but additional jitter has been set). An explanation for the imbalance between the left and right arm structure that is visible in the measurement is a slightly inhomogeneous beam shape. The energy axis is only valid for particles without quenching effects.

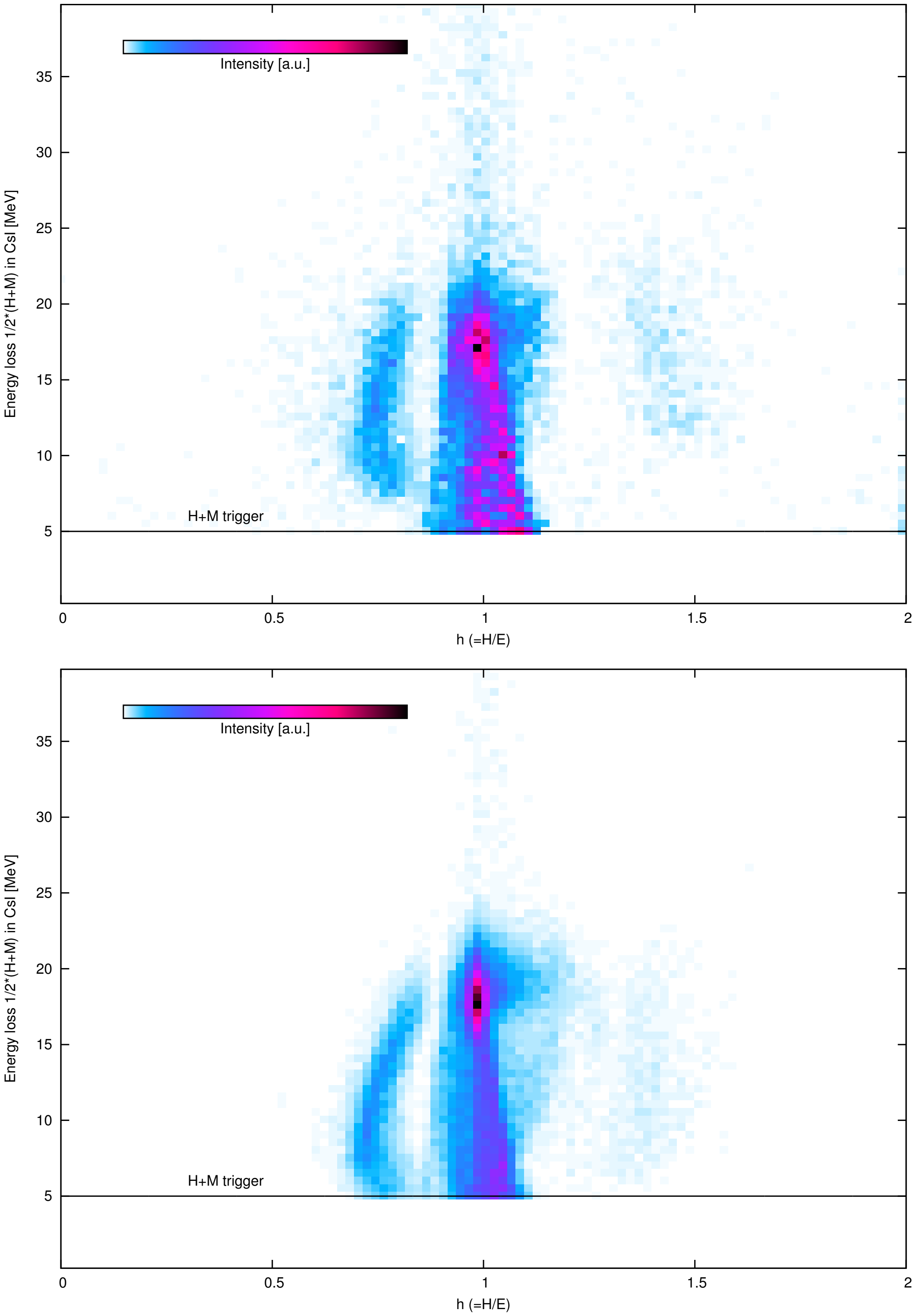

Figure 3.6: H light fraction h vs. total energy E, compare also Fig. 3.5. In this run, the instrument is rotated by 25° around the y-axis. The data underlying this measurement is selected from the file [#4, p-PF-1 GeV-25° $\circlearrowleft_y$]. The top view shows the measured data and the bottom view the simulation result.

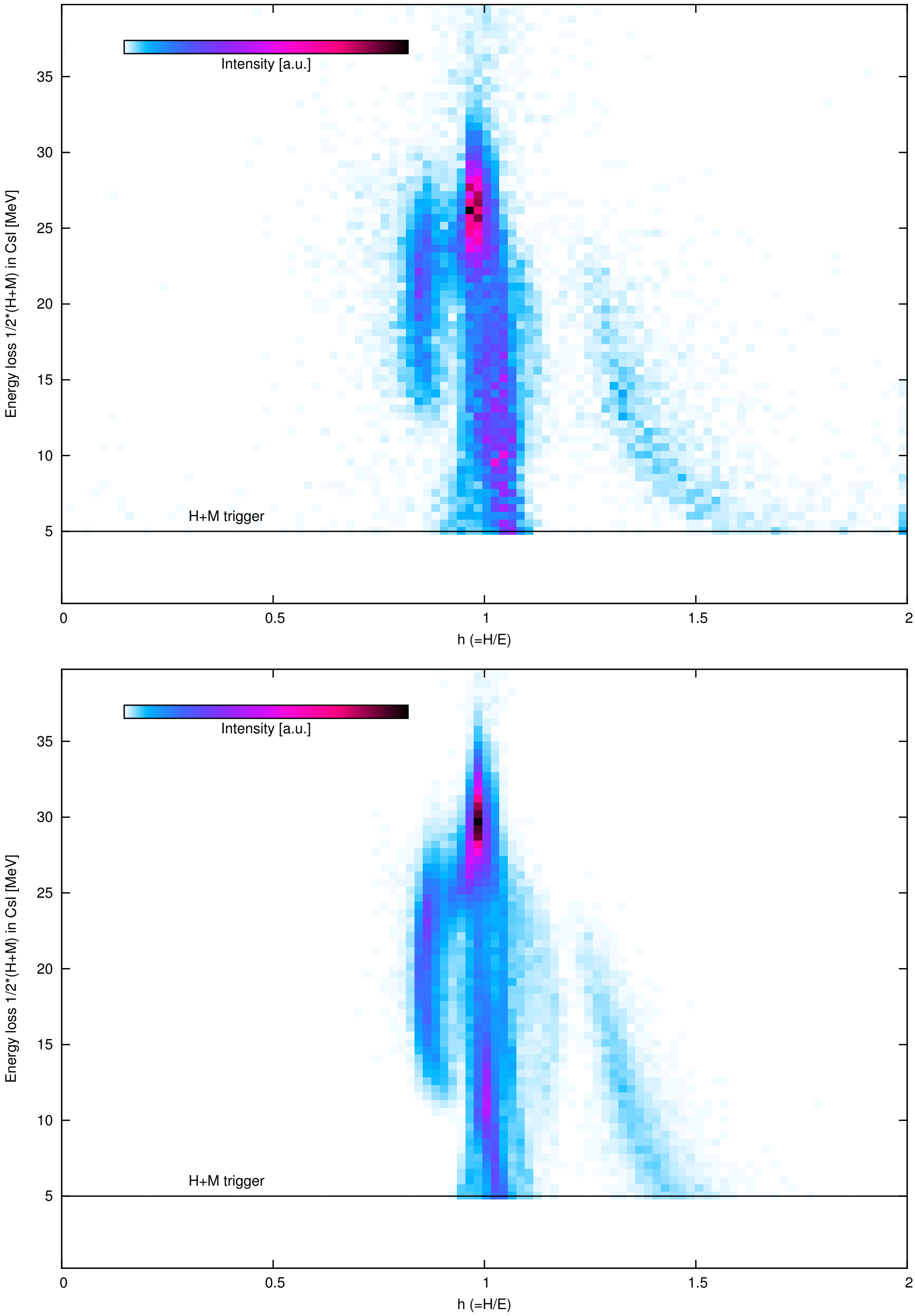

Figure 3.7: H light fraction h vs. total energy E. In this run, the instrument is rotated by 90° around the y-axis such that the instrument is immersed in the proton beam from the side. The top view shows the measurement, the bottom view the simulation result. See also Fig. 3.5. The data for the measurement is selected from [#5, p-PF-1 GeV-90° $\circlearrowleft_y$].

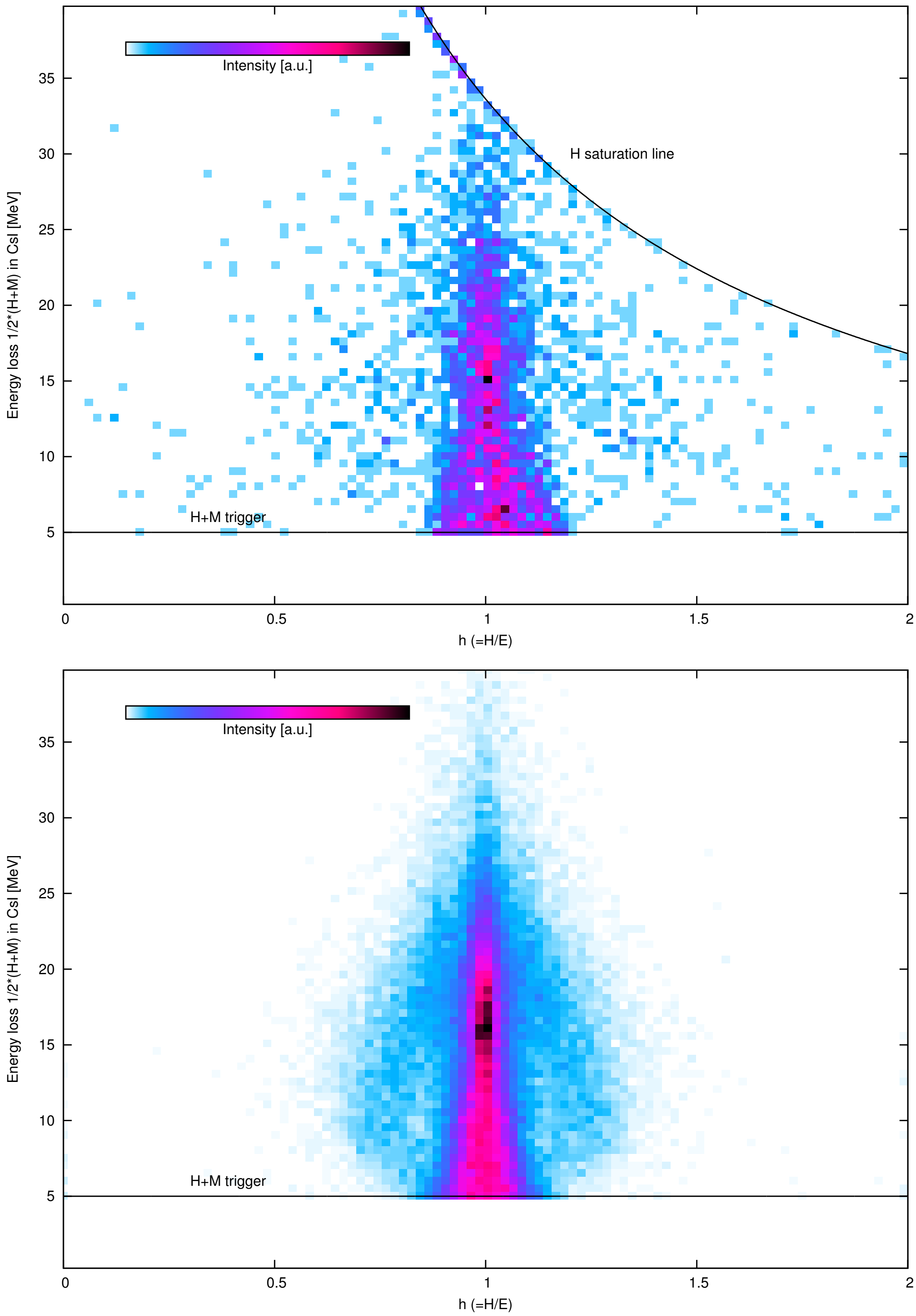

Figure 3.8: H light fraction h vs. total energy E. For cosmic muons with $\cos^2\theta$-angle distribution. The top view shows the measurement, and the bottom view again shows the simulation result. See also Fig. 3.5. The data for the measurement is selected from [#6, μ-FM2-fREB].

Parameter	**Value**	**Notes**
Absorption length α	∞	Lossless optics
Reflectivity R	1.00	
Surface model	`fresnel`, 2π diffusion	
Index of refraction n	1.787	
Electronics noise PF H	142 keV	
Electronics noise PF M	101 keV	
Electronics noise FM2 H	136 keV	Total electronic noise; compare also noise values in Tab. A.2 in App. A.2.2. Note that these noise values are not estimated in a final flight configuration.
Electronics noise FM2 M	222 keV	
Silicon to light ratio w	$15.9\,\frac{\mathrm{MeV_{CsI}}}{\mathrm{MeV_{Si}}}$	An error of about $1.5\,\frac{\mathrm{MeV_{CsI}}}{\mathrm{MeV_{Si}}}$ can be assumed here (visual estimate).

Table 3.3: Parameter set as used for the optical MC model (and the included simple straggling energy loss and noise model).

The general origin of the features visible in the plots can be explained exemplarily for the plots in Fig. 3.5. In the illustration in Fig. 3.9, the data for the 0° case is colored in different colours and numbered for the different parts. The two red areas (1, 2) to the left and right are due to silicon hits in the M- (left) and the H- (right) diode of the D scintillator, respectively. The light distribution inside the main CsI crystal part (3) of the scintillator can be seen in the green shaded center; the high energy tail of the protons (4), as it is also visible in the `FLUKA` simulation of C. Martin, is marked in light yellow.

As it is clearly visible from the preceding set of plots, the simulation reproduces the general shape of the optical distribution between the diodes quite well. A notable difference is the extension of the silicon hit arms into the low energy areas in the simulated case. This could be explained for example with a slightly inhomogeneous beam shape at BNL, with a higher intensity in the center of the instrument. Such a beam shape would leave out the outer parts of the crystal, where a silicon hit and a relatively small light signal is generated when the proton goes through a diode and a short length of scintillator. Another set of smaller deviations can be seen when looking closely at the shape of the main optical part of the energy loss between simulation and measurement (such as the slightly different curvature at the center bottom of Fig.3.7). In the following, the influence of the various parameters on the distribution as well as a quantitative comparison of the results will be discussed.

3.5.1 Effects of the parameter set on the simulation results

The results of the simulation for the 0° BNL run will now be used to demonstrate the effects of the parameters on the broadening in the various directions. This gives more insights into the results of the optical model as well as highlighting the areas where additional tests could be done with further experiments.

Obviously, the straggling energy loss in the crystal affects all diodes equally and is thus only visible in the direction of the E axis. Removing particle straggling in the scintillator from the model gives a much better picture of the purely optical effects in the scintillator.

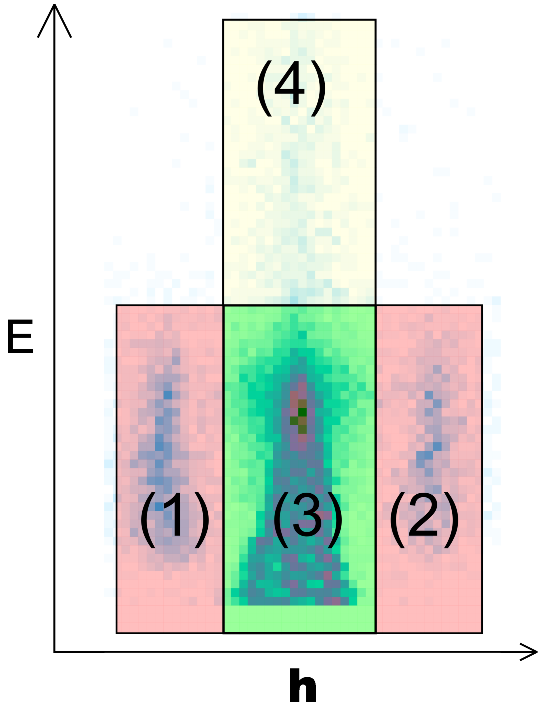

Figure 3.9: Shape of BNL measurement for 0°, with markers for the different distributions.

Also, the effect of electronics noise in the given energy range is on the order of

$$\sigma_{\mathrm{HM}} := \sigma_{\mathrm{H,elec.}} \approx \sigma_{\mathrm{M,elec.}} \approx 150\,\mathrm{keV}. \tag{3.36}$$

Assuming gaussian error propagation and independent electronic noise,

$$\begin{aligned}\sigma_h^2 &\approx \left(\frac{\partial}{\partial H}\left(\frac{H}{E}\right)\cdot\sigma_H\right)^2 + \left(\frac{\partial}{\partial M}\left(\frac{H}{E}\right)\cdot\sigma_M\right)^2 && (3.37)\\ &= \frac{\sigma_{HM}^2}{E^4}\left(\left(1\cdot E-\frac{H}{2}\right)^2+\left(0\cdot E-\frac{H}{2}\right)^2\right) && (3.38)\\ &\le \frac{\sigma_{HM}^2}{E^4}2E^2 = 2\frac{\sigma_{HM}^2}{E^2}. && (3.39)\end{aligned}$$

And thus at the point of mean energy loss as a typical energy to look at,

$$\sigma_h \lesssim \frac{\sqrt{2}\cdot 150\,\mathrm{keV}}{10\,\mathrm{MeV}} \approx 0.02. \tag{3.40}$$

This value is small, compared to the optical effects visible. It is therefore safe to assume that the electronics noise will only broaden the response in the H direction and will not change the overall shape of the distribution very much, even though the relation $h(H, M)$ is non-linear in H and M. This only holds for the higher energy parts of the plots, but even for the selected threshold energy of 5 MeV, the electronic noise is not dominant.

As the shape of the silicon distribution is a well-known LANDAU shape and not of interest in itself here, the silicon light scattering can also be removed (and replaced with a δ distribution shifted to the mean energy loss - proportional to the length travelled) to show the optical distribution for the combined silicon and light part of the scintillator response.

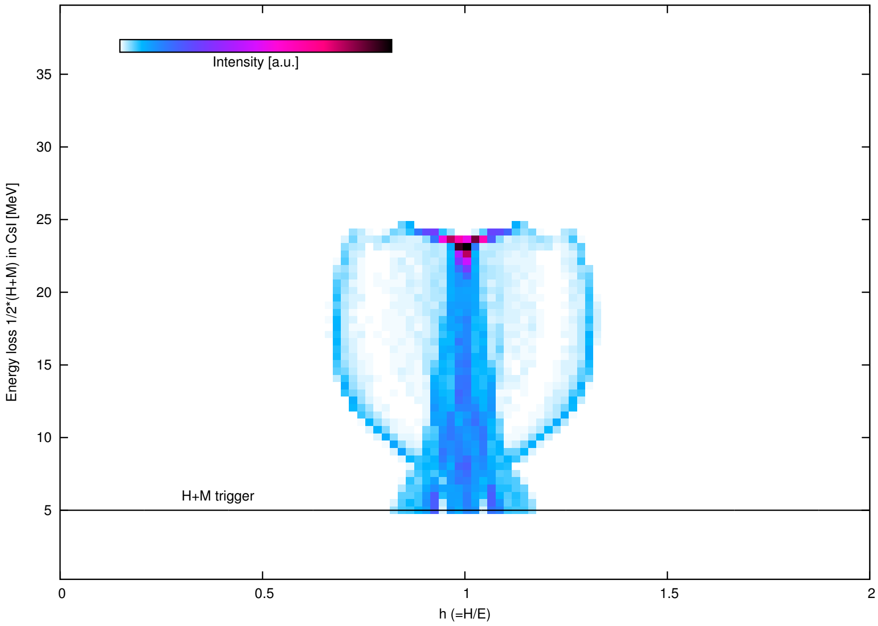

Figure 3.10: H light fraction h vs. total energy E/PPT path length, for straight 0° incidence. Purely optical *simulated* run with 1 GeV protons. No electronic noise or energy loss straggling (neither in the scintillator nor the silicon) is assumed. Fixed parameter w is still from Tab. 3.3. Note that as energy loss straggling is happening according to a non-symmetric distribution, which is *not* included here, the energy scale may seem to be slightly shifted when comparing to the previous figures. This effect causes the peak to appear at ≈ 22.5 MeV instead of ≈ 16 MeV as in Fig. 3.5.

Finally, in Fig. 3.10, the pure optical simulation result (with the above simplifications) is shown. Some details appear which are hidden in Figs. 3.5-3.8, due to the noise and straggling effects. The validity of the simulation in this interesting detailed range could unfortunately not be checked with the available test data.

For completeness it should be stated that the shape of the two silicon arms is affected strongly by additional light being produced close to the diodes. If $E_0 = H_0 = M_0$ is the energy in M and H, assuming no light distribution, and $H := H_0 + E_s$ is the signal in H due to the light contribution H_0 and an additional silicon signal part with energy equivalent E_s, the shape of h becomes

$$h_{(H+)} = \frac{H}{E} = \frac{E_s + H_0}{E} = \frac{E_s + E_0}{\frac{1}{2}\left(2E_0 + E_s\right)} = 1 + \frac{E_s}{E_s + 2E_0}. \tag{3.41}$$

A symmetrical calculation holds for the shape of h for $= M = M_0 + E_s$ with

$$h_{(M+)} = 1 - \frac{E_s}{E_s + 2E_0}. \tag{3.42}$$

The resulting shape of the very simple silicon hit model of just adding a constant amount of signal to the light in the scintillator can be seen in a (h, E)-plot in Fig. 3.11. Obvious from that picture, the shape of the silicon arms would not fit the results. In the simulation, the silicon hits can be clearly marked and separated from the rest of the data. To see how light affects the shape of the arms, it is most descriptive to vary the w parameter and look at the shape of the distribution. A scatter plot with varying values of w overlaid can be seen in Fig. 3.12. The main part of the plot (in red) shows the signal of the scintillator for

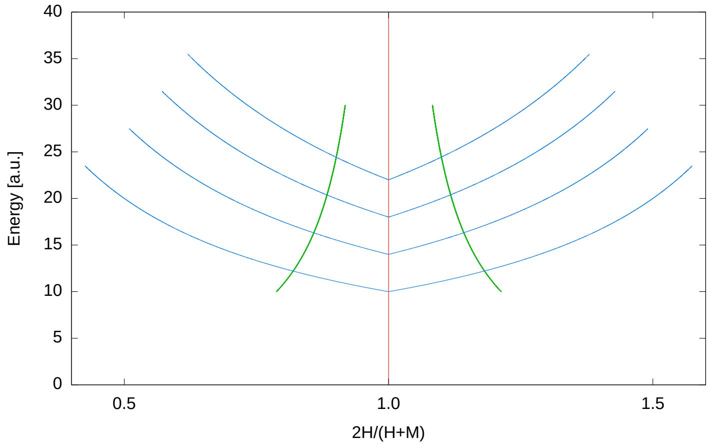

Figure 3.11: Expected shape of the (h, E) plot, assuming no energy loss straggling, no inequal light distribution, giving the red single line at $H = M = 1$ and the silicon hit curves in a shape like the marked green curves. The blue curves mark the ways the silicon hit for different total energies E move when varying the parameter w.

paths not hitting any diodes. Even for an insignificant contribution of silicon hits to the light signal, the PPTs running close to the diodes quite clearly change the shape of the resulting light distribution and even account for most of the variation seen in h for the finally selected value of w (violet scatter dots). The light blue marked part of the distribution shows the case of $\mathbf{w = 0.0}$, but with a geometrical path through the silicon and thus the variation for silicon-hit paths but purely due to optical effects in the scintillator. The center part of this distribution stems from hits close to the low gain diode. Similar changes can be observed for the other runs with different input angles. Regarding the silicon hits, it can be therefore concluded that

1. the two curve shaped features to the left and right of the main light distribution are indeed attributable to combined light and silicon interactions, with the light playing the main role in the D scintillator and
2. that they are, in the considered cases, clearly separated, as intended, from the rest of the distribution, even for the case of no silicon energy deposit.

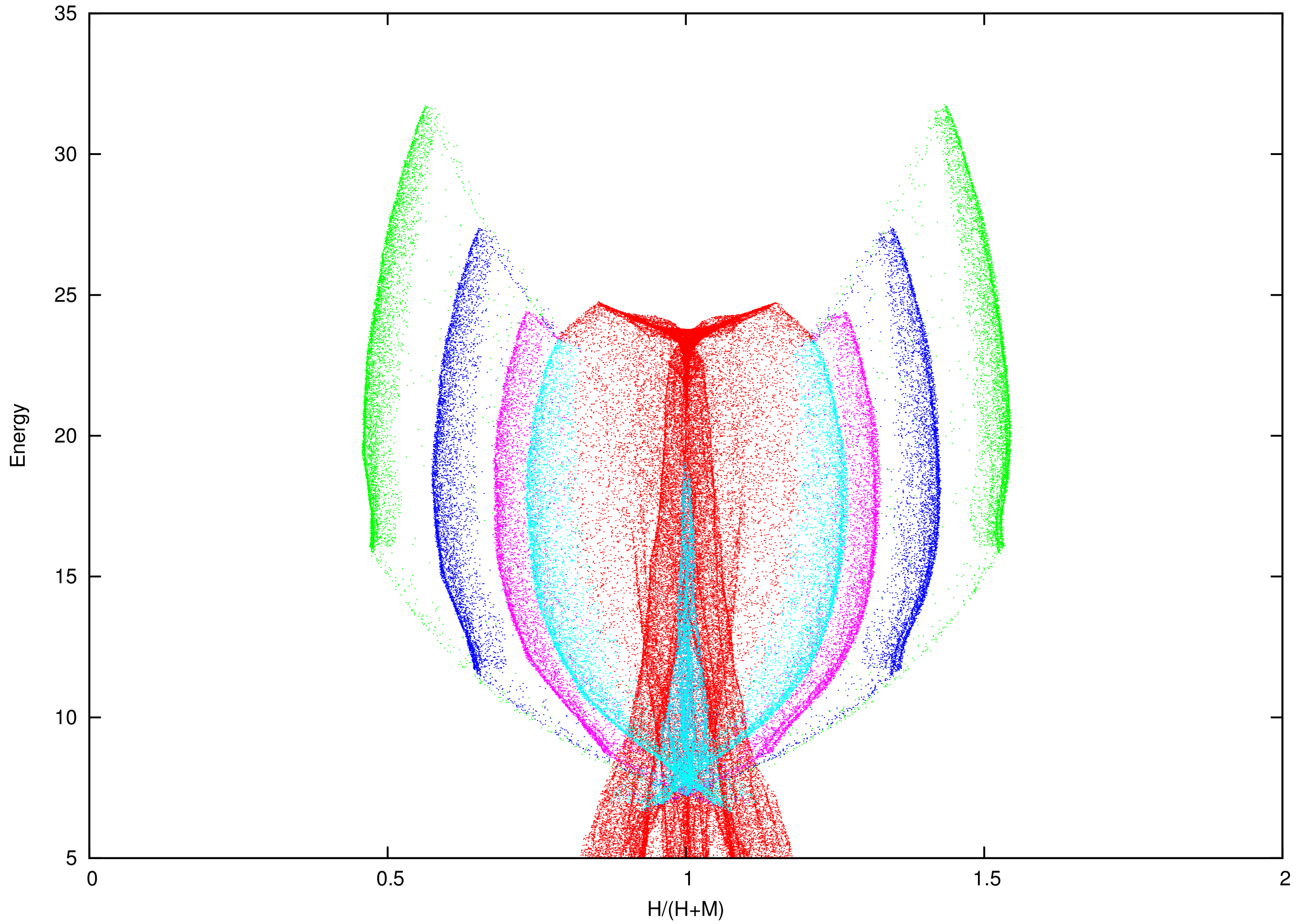

Figure 3.12: Scatter plots of combined Silicon and light hits in the (h, E) plane, same parameters as in Fig. 3.11, except that the value of w is varied. It is $w = \mathbf{0.0}, 15.9, 50.0, 100.0 \frac{\mathrm{MeV}_{\mathrm{CsI}}}{\mathrm{MeV}_{\mathrm{Si}}}$ in the order light-blue, violet, blue, green. The red dots represent the light-only hits, the light blue dots represent the light-only part of hits which geometrically also go through a silicon diode. The large optical contribution to the silicon arms can be clearly seen in this picture.

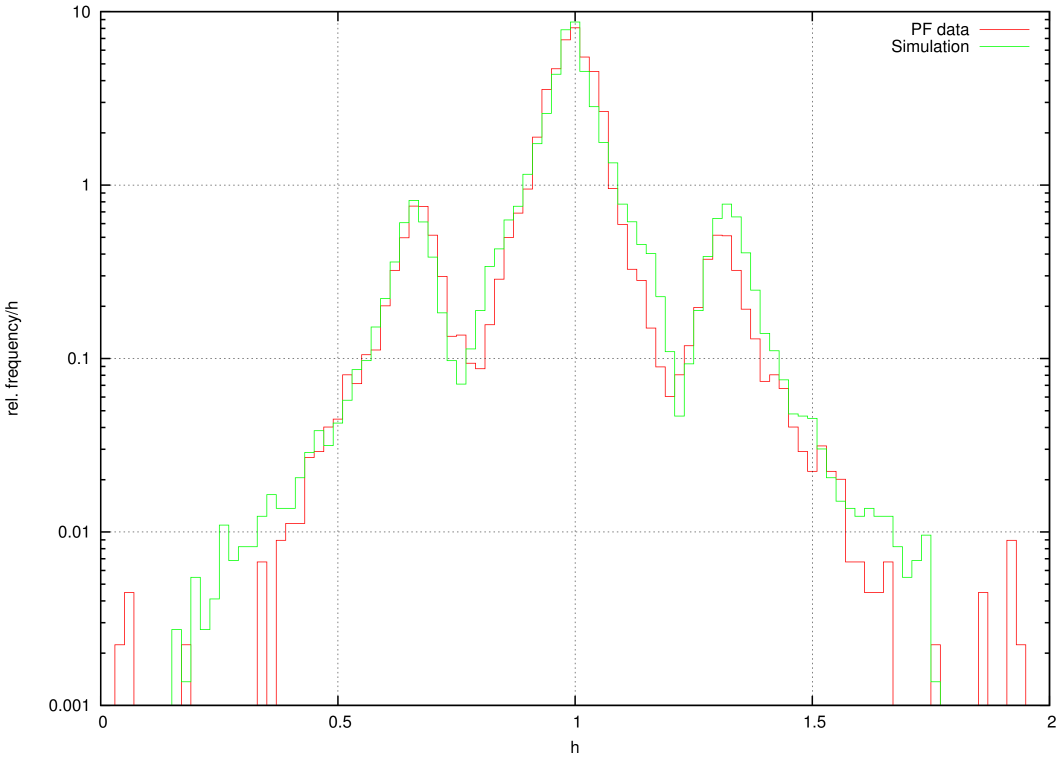

Figure 3.13: Histogram of h values for $0°, p\ 1GeV$, PF run, with an energy cut on the CsI energy value of $10MeV \le E \le 40MeV$. The large peak in the middle is the optical signal, the peaks to the left and right show the combined optical+silicon signal.

3.5.2 Projection onto h-axis

Projecting parts of the above runs onto the h axis helps to get a better view on the shape and width of the light/silicon part in the scintillator. It will also be used to further numerically compare the simulation results to the measurement in the next section.

Acknowledging the obvious departure of the shape of silicon arms from the expected behaviour for the case of $E \in [5\,\text{MeV}, 10\,\text{MeV}]$, a cut of $E \in [10\,\text{MeV}, 40\,\text{MeV}]$ is selected for the histogram of the 0° case shown in Fig. 3.13. It should be clearly noted here that far from all h-projections match as close as the one shown in Fig. 3.13. The silicon tails as well the main optical part show good agreement. An imbalance in the number of silicon hits of the H and the M channel is again observed. The slight shift in the peak position of the silicon+light peaks could be adjusted with a change in w. But the value of w had to be selected as a single compromise value to explain all four beam runs.

The silicon+light part for M has a larger discrepancy due to a different shape as well as a slight shift in the h-peak position of the combined light+silicon signal in M for the case of protons at 25° rotation. No satisfying explanation has been found so far for this deviation. To rule out a wrong assumption on the internal placement of the PIN diodes in the PF during the BNL run, the behaviour of the crystal has been checked also for rotation around the other axis and into the other direction. The result is best described by the set 25° rotation around the y-axis.

Data set	h_{min}	h_{max}	E_{min} $[M\mathrm{eV}]$	E_{max} $[M\mathrm{eV}]$
center	0.8	1.2	5	10
center	0.8	1.2	10	15
center	0.8	1.2	15	20
center	0.8	1.2	20	40
M+si	0.01	0.8	10	30
H+si	1.2	1.99	10	30

Table 3.4: Boxes used for comparison of $\sigma_{\mathrm{simulation}}$ vs. σ_{real}. In the case of muons in FM2, the boxes which would included saturated data in the comparison have been removed from the selection. The border cases $H = 0$ or $M = 0$ are excluded to exclude silicon-only hits and triggers on single detector noise.

3.5.3 Comparison of measured and simulated (optical) broadening

After a qualitative overview of the measurements and simulation results, a simple test of the quantitivate performance of the model is made. Relying on this and the previous comparisons, some further extrapolations of the model are then presented in the next section, with a focus on the energy reconstruction for various inputs to the D scintillator.

The final overall figure of major interest is the energy resolution of D. The behaviour of h gives the optical contribution to this, and a numerical comparison between the variations in h direction between measurement and simulation is helpful. This is calculated as the standard deviation of σ_h, giving the width of the different peak shapes exemplarily shown in Fig. 3.13. This test gives a rough overview of the accuracy of the model as well as the ranges for which it is checked.

In Fig. 3.14, the value of σ_h is compared to the simulated value of σ_h for different selection criteria from the distribution as shown in Figs. 3.5 . . . 3.8. The data sets are cut into selection boxes in the (h, E) plane, which can be seen in Tab. 3.4. They are selected such that the silicon+light arms and the main optical part in the (h, E) plane are separated from each, as well as dividing the energy axes into a few, broad bins. The large deviation of the silicon plus light signal in M is due to the aforementioned discrepancy in the shape of h for the $(PF, 1G\mathrm{eV}\ p, 25^\circ)$ case and can be seen as the top right outlier in the comparison. Note that these box cuts remove possible different outlier fractions from the data. As these are in a range where a silicon hit rejection cut will be applied anyway, they are not of further interest here.

It can be seen that the optical part matches reasonably well and, although more tests are needed (see also Chapter 6) will now be used in the following to give expected geometric broadening (‘geometric noise’ or ‘optical noise’ from now on) figures and qualitative behaviour for cases which are hard to assess using experimental data alone.

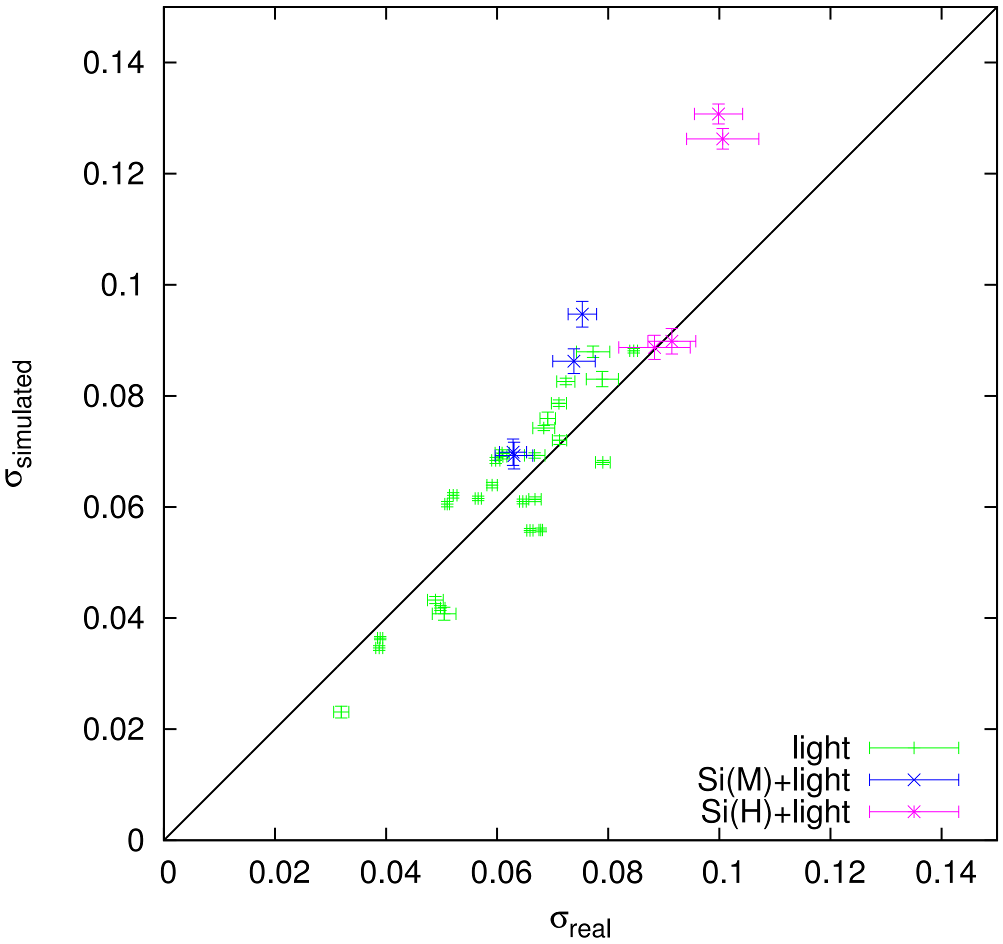

Figure 3.14: Values of $\sigma_{\text{simulated}}$ to the measured values σ_{real}, for different cuts in the (E, h) plane and the D test runs used (as given in Figs. 3.5…3.8). Note that the shown error bars are 1 standard error of the standard deviation from the statistics of the data [*Stuart and Ord*, 1987] and the MC simulation and do not reflect in any way the accuracy and systematic deviations of the model. The cases where the H-channel for the selected box in the (E, h) plane would be saturated in the measurement or when the number of hits is $N < 100$ have been excluded from this comparison. Calculating the straight-forward *unweighted* PEARSON correlation coefficient for this data gives $r_{\sigma,\sigma} \approx 0.93$.

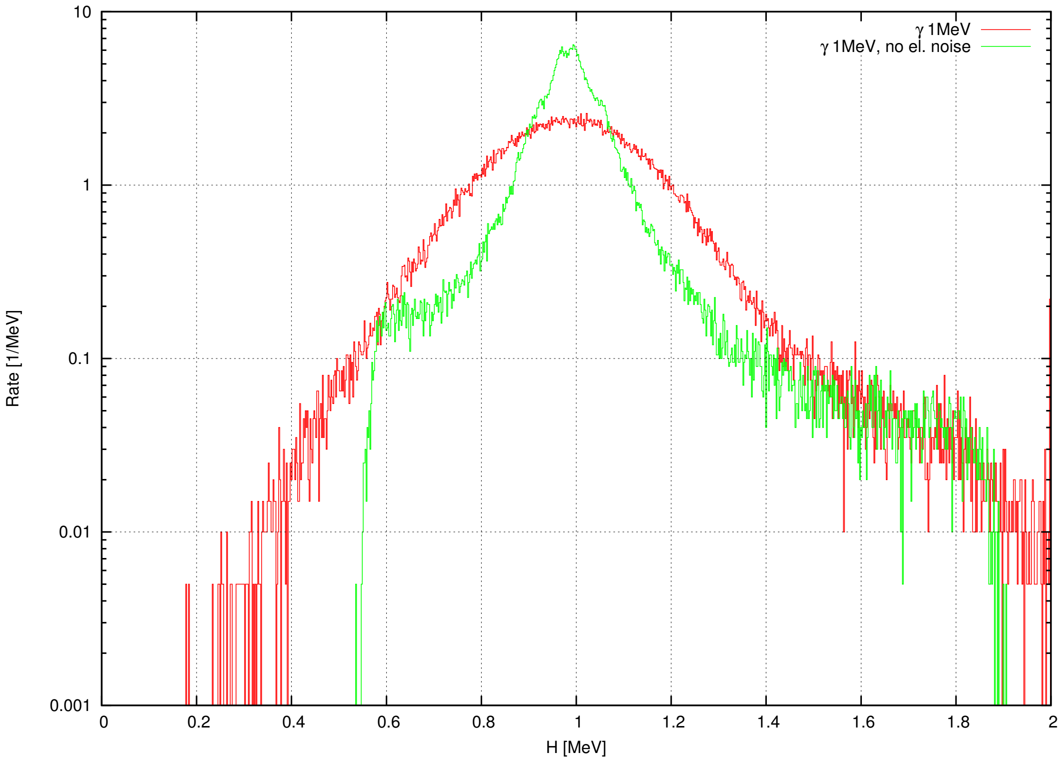

Figure 3.15: Simulation of the response of FM2 to a single γ-line with $E = 1\,\mathrm{MeV}$. The pure optical and the optical+electronic noise behaviour is shown.

3.6 CsI γ-ray resolution

The sum of the electronic as well as the optical noise for γ-photons is too high to reliably use the CsI crystal for real γ-spectroscopy. At most a few COMPTON edges should be visible in the data from the flight configuration. An example of a γ-measurement in a RSH/REB configuration is given later on in Sec. 7.2.

In Fig. 3.15, the simulated single-channel reconstructed energy of the D detector for a δ-shaped γ-field with an exemplary energy $E = 1\,\mathrm{MeV}$ is shown, in order to have a view on the different contributions to the energy resolution for γ-rays.

In this setup, interactions with γ-photons are assumed to be evenly distributed across the whole scintillating volume and are assumed to occur point-like. It also assumed that photo effect is the only means of absorption here, to avoid having to use a full model of γ-interactions in the material. No electrons are assumed to escape or hit any of the readout detectors (no silicon hit effects). Even for this relatively low energy range, photon shot noise is still assumed to be negligible.

The red curve shows the effect of optical noise for a single-channel reconstruction, convoluted with the measured electronic noise of DH, FM2. The green curve shows only the optical response of a single scintillator channel. Note that the resolution figure $\frac{\sigma E}{E}$ is dominated in this low-energy region by the electronic readout noise for a single-channel reconstruction. For the electronic noise contribution σ_e, the relative noise varies as

$$\frac{\sigma_e(E)}{E} \sim \frac{1}{E}, \tag{3.43}$$

and thus basically disappears for high energies, whereas for the optical noise part σ_o, it is

$$\frac{\sigma_o(E)}{E} = \text{const.} \tag{3.44}$$

The broadening for a single-channel energy reconstruction in the D channel thus tends to the shape of green curve for large E as the limit case for energy resolution for point-like interactions.

As a further, minor note, the two edges visible in the green curves in Fig. 3.15, the sharp edges of minimum and maximum seen energy in a diode for a given energy loss, can be related to each other. Assume that L_{min} is the minimum amount of light a single diode of D sees for a given fixed amount of total light L. For a maximum in one diode, the two other diodes still at least get their respective minimum amount of light L_{min}. Thus, for the maximum amount of light L_{max} that can be seen in D, due to symmetry of the three readout diodes, the relation

$$L_{\text{max}} \leq L - 2 \cdot L_{\text{min}} \tag{3.45}$$

holds. In the case of no optical losses, as discussed here, the inequality $\leq$ can be replaced with equality in Eq.3.45. With H scaled as $H = 3L_H$ to the full energy scale

$$\begin{aligned} H_{\text{max}} &= 3L_{\text{max}} && (3.46) \\ &= 3\,(L - 2 \cdot L_{\text{min}}) && (3.47) \\ &= 3L - 2H_{\text{min}}. && (3.48) \end{aligned}$$

Identifying $L = E$ and thus $L = 1\,\text{MeV}$ equivalent, the left border visible at about a value of $H_{\text{min}} = 0.55\,\text{MeV}$ relates to the right at about $H_{\text{max}} = 1.9\,\text{MeV}$ as described.

More generally, for three identical detectors symmetrically attached to a scintillator in a symmetric particle field and without light losses, the optical noise contribution halves when reconstructing from two instead of one diode (and obviously disappears when all light is collected by reconstructing from three diodes). For this, see also the following Eq. 3.53.

Finally, it should be emphasized that this energy reconstruction only behaves like this for isotropically distributed γ-like interactions. Resultion gets better when selecting, with the help of the particle telescope, a narrow path for charged particles into/through D.

3.7 Angular and positional effects in D

Owing to the segmented telescope of RAD, different view cones can be selected, depending on conditions such as expected flux or allowed data rate.

The expected minimum resolution loss due to optical readout for a subset of one or two detectors can be investigated using the photon model. A more general approach is to look at the dependency of the energy resolution for a single- or dual-channel reconstruction depending on the opening angle of the view cone of the instrument. Energy resolution as well as imbalance in reconstructed energy for varying φ angles can be studied in a similar way.

The (φ, θ) angles mentioned in the following are same as they are shown in Fig. 3.4. Here, the pair (φ, θ) is describing the direction the particle is going to, not the direction the instrument is looking at.

3.7.1 Dependency on opening angle

The results from the simulation are visible in Fig. 3.16. Several simplifications are made. The particles are assumed to stop on their full length through the scintillator, but still with

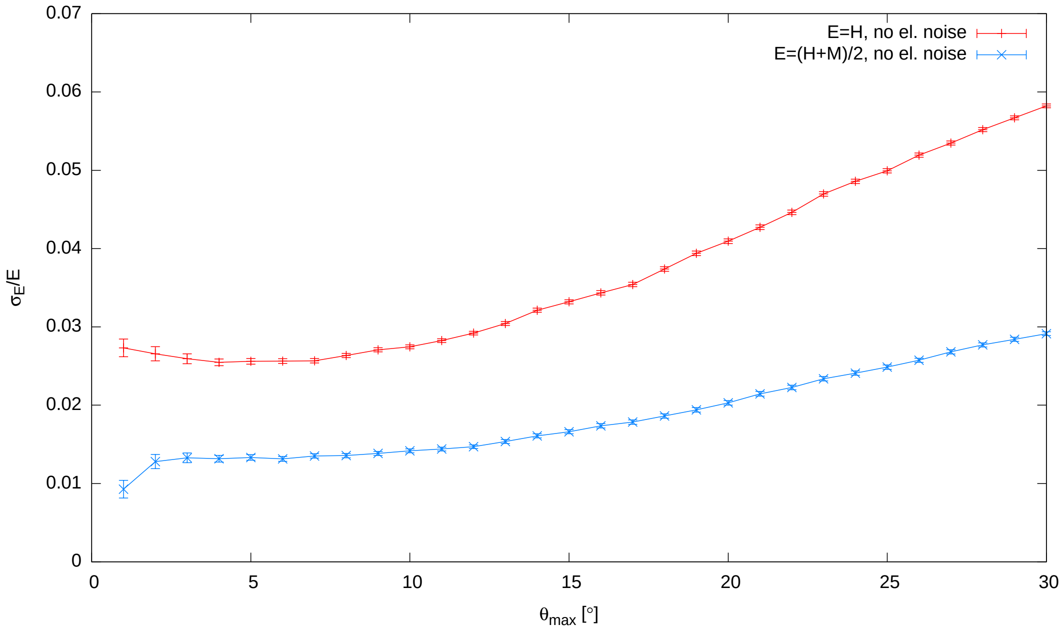

Figure 3.16: Plot of the simulated energy resolution $\frac{\sigma_E}{E}$ for MIPs and different acceptance cones θ_{max}. The cone's half opening angle is given on the x-axis. The error bars are just from the statistics of the photon MC run and do not include any further errors arising from comparison with real data. No signal due to silicon hits is assumed, as well as no energy loss straggling or electronic noise. Also, the effect of varying path lengths is not visible due to the described method by which the energy resolution is calculated here.

$\frac{dE}{dx} = \mathrm{const}$. The effects of different geometrical path lengths through the scintillator are not considered here, as each seen energy loss is divided by the total energy loss along the track to calculate $\frac{\sigma_E}{E}$.

The setup for the simulation is an isotropic field of MIPs particles. An additional trigger on the inner C detector is selected to form an appropriate view cone in the simulated instrument. Integrated behaviour for any angle up to θ_{max} is shown in the figure, but it is possible to select a hollow view cone in RAD by means of a trigger on A_{outer} without A_{inner}. The calculated broadening for this case as well as all other cases which are of interest is printed in Tab. 3.5. The actually hexagonal opening cones are approximated using mathematical cones here (in the full model in Chapter 6, they are replaced with the proper shapes from the vendor chip mask).

The normal-incidence case gives a minimum of $\frac{\sigma_E}{E} \approx 3\%$ for charged particles and single channel reconstruction. Incidentally, this matches the resolution loss happening due to `int` → `float8` data conversion and reduction[2]. The used 8 bit floats have a 3 bit exponent and a mantissa of $m = 5$ bit, which gives a maximum resolvable change between two different energy levels of

$$\frac{1}{2^m} = \frac{1}{32} \approx 3\%. \tag{3.49}$$

As no light loss is assumed to occur in the scintillator, the curve for the $E_{H+M} = \frac{H+M}{2}$ case is half of the curve for the $E_H = H$ case (assuming no electronic noise), as it is for

---

[2] The details of the conversion process are visible in the L2 FPGA code, file `l2trig.v` by S. Böttcher.

θ_{min} [°]	θ_{max} [°]	$\frac{\sigma_E}{E}$ [%]
0	15	1.7
15	30	3.2
0	30	2.9

Table 3.5: Simulated, purely optical energy resolutions for different view cones resp. trigger masks. Relative statistical errors of σ_E/E from the simulation are $< 2\%$.

total energy $E_t = \frac{1}{3}(H + M + L)$ due to symmetric geometrical noise of each channel in the scintillator:

$$\begin{aligned}
\sigma(E_H) &= \sigma(3E_t - M - L) && (3.50)\\
&= \sigma(M + L) = \sigma(H + M) && (3.51)\\
&= \sigma(2E_{H+M}) && (3.52)\\
&= 2\sigma(E_{H+M}). && (3.53)
\end{aligned}$$

The first equality holds due to no assumed light loss in the scintillator, the second due to the assumed symmetry of the geometrical structure as well as the test beam.

3.7.2 Dependency on azimuth

For isotropic incidence, a trigger on C and an additional cut of $\theta \in [0°, 30°]$ the response to varying values of φ can be seen in Fig. 3.17. The simulated events are collected into 30 bins in φ to produce this plot. This plot shows the change in reconstructed energy (deviation from the mean) and not the broadening for a given φ. Changes in $\frac{\sigma_E}{E}$ are small compared to the changes in total light seen. The variations visible in this plot (up to $\frac{\sigma_E}{E} \approx 8\%$) account for some of the broadening in single-channel reconstructed energy, as most expected particle distributions on Mars are assumed to be isotropic in φ direction as long as the rover is not standing on a hill. This also means that any expected or seen anisotropy in φ must be carefully analyzed, as it can lead to changes in the D scintillator energy scale.

The shape of the plot is as one would expect with the most naïve assumptions. Over-estimation of energy occurs for PPTs facing the high-gain diode and under-estimation happens for tracks close to the other two diodes, as they will draw some of the light away (compare also Eq. 3.48).

3.7.3 Positional dependency

Although any particle field to be encountered on Mars will surely be isotropic in the position of PPTs and no trigger condition can be selected for RAD which would select meaningful, asymmetric track positions through the D scintillator, it is helpful to have a look at the expected positional anisotropies in D to put the effects of varying φ and θ into context. The simplest case, which is selected here, is the dependency of seen energy on position for particles coming straight from zenith.

In Fig. 3.18, the result of the corresponding simulation can be seen. The most visible features are, as expected, showing that the position closest to the high-gain diode sees the most light and least light is seen for light being produced close to the entrance diode of

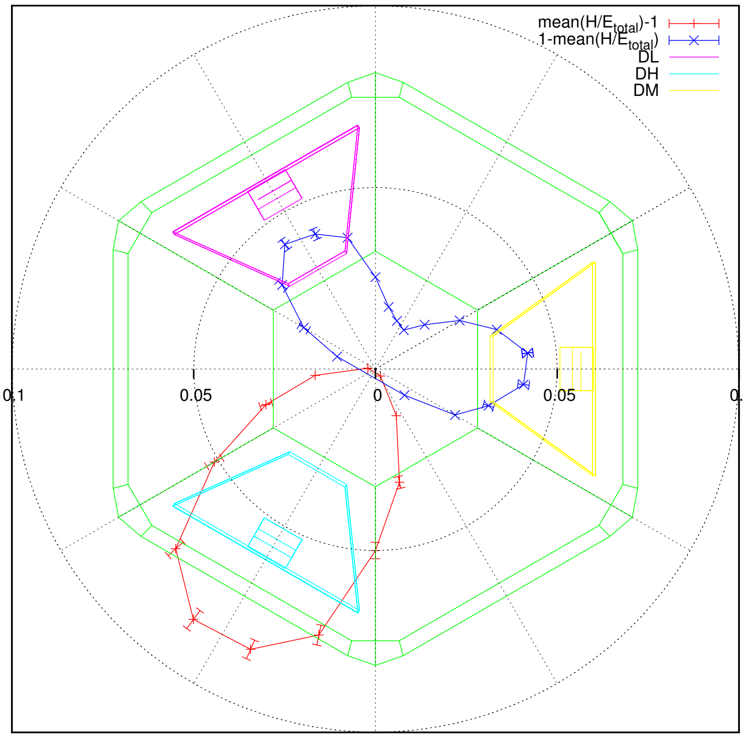

Figure 3.17: Simulated deviation of the single channel reconstructed energy from the mean energy deposit in the scintillator, for single-channel reconstruction through the high-gain channel. The deviation of $\frac{H}{E}$ from 1 is shown as a variation in the radius from the center and the polar angle is φ. The red curve denotes φ-ranges with a higher signal than the mean, the blue curve a lower signal. The positions of the detectors as well as the orientation is superimposed on the plot. The error bars are just 1 standard error of the standard deviation from the statistics of the photon MC run and do not include any further errors arising from comparison with real data.

another diode. The variance is in the same range as the change due to different φ incidence angles.

3.8 Effects of in-flight high-rate data processing

Due to energy consumption and space constraints, the processing power for pulse height data in the REB's firmware is quite limited. On the other hand, a goal of RAD is to achieve a good trade-off between energy resolution, dynamic range and data reduction.

As described in Chapter 2, to take processing load from the onboard microcontroller, a major part of the energy reconstruction algorithms is offloaded into the Level two (L2) module inside the EVIL FPGA in the REB.

This energy reconstruction algorithm produces the final seen energy of a single physical detector A. . . F from the multitude of available channels per detector. Again for constraints in the power and size of the processing pipeline, the algorithm to perform this reconstruction is a simplified linear combination, subject to some constraints. Another part of the L2 module covers the silicon hit rejection, which is also done according to a single hard-wired formula with additional constraints.

The constrained algorithms have a set of tunable parameters, for which the optimum

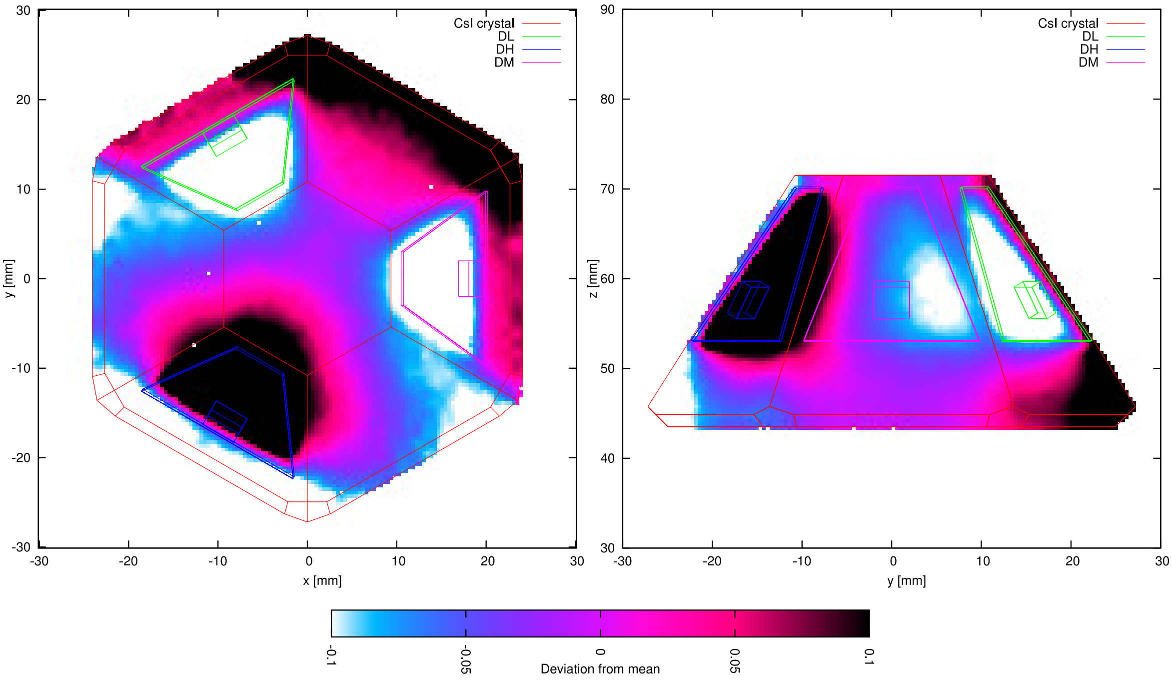

Figure 3.18: Simulated relative deviation of mean reconstructed energy loss seen in H, $\overline{\left(\frac{dL}{dx}\right)}$ for charged MIPs, depending on position to $\overline{\frac{dL}{dx}}$, from symmetric, central incidence. Calculation of the mean is done along the whole length of the track in the crystal. Incidence from zenith in left plot and incidence from the side, 90° in right plot. The visible range is clipped to $\left|\Delta\frac{dL}{dx}\right| < 0.1$ to bring out the effects in the central part of the crystal which is of most interest. Default set of model parameters from Tab. 3.3.

values, given the energy-resolution trade-off, should be found. In the following, the reconstruction method and silicon hit rejection method is described as well as a way to find good parameters. It is done exemplarily here and a more detailed analysis including an error estimation and temperature effects should be set up to cover the whole picture. For more details on the algorithms and their implementation in the FPGA, see *Böttcher* [2007] and *Böttcher* [2008].

Gain scales. To have a larger dynamic range, the REB has a two-channel redundant readout for each shaper from the RSH. A separate, additional gain of $1, 2, 4$ or 8 can be set individually for each channel. For the scintillation detectors D and E, this gives a total of six values to be processed to get the seen energy in the particular detector. For the silicon channels A, B and C, two redundant shapers are attached to each CSA, each again with different gains, giving four channels to be processed.

For energy reconstruction of any detector in the L2 module, the individually offset corrected and gain scaled channels are processed in the order low- to high-gain channel. An accumulator value is filled with a linear combination of the current and the last reconstructed energy value, depending on a set of conditions. For the scintillating detectors, this is a set of channels denoted as C here, with

$$C \subseteq C_0 := \{\mathrm{L}, \mathrm{N}, \mathrm{M}, \mathrm{I}, \mathrm{H}, \mathrm{U}\} \tag{3.54}$$

with L . . . U being the different gains of the detector. The channels are listed here in order of increasing gain. For the origins of this naming scheme, see Sec. 2.7 and for more details, see *Böttcher* [2008]. In the case of silicon channels, which are not further investigated here, the channels with names N and I are missing. The channels N and I can also be excluded in the case of the broken FM1 DM detector.

More specifically, let E_i be the current reconstructed energy value in the accumulator for step $i \in \{1, \ldots, n\}$ with $n := |C| - 1$. Let $E_0 := E_L$ be the sampled energy for the lowest gain channel. Let $\hat{E}_i$ be the energy value of the channel i currently being processed, with channel gains increasing with i, and starting with the second-lowest gain channel at $i = 1$. The physical connector layout of the channels into the VIRENA chip is such that the channels are read out in this increasing order.

The value of the next reconstruction step E_i is calculated as follows

$$E_i = a_i E_{i-1} + (1 - a_i)\hat{E}_i \tag{3.55}$$

but only if the following two conditions

$$\hat{E}_i > E_{\min,i} \tag{3.56}$$

and

$$\hat{E}_i < E_{\max,i} \tag{3.57}$$

are met. The values $E_{\min,i}$ and $E_{\max,i}$ are freely selectable for each reconstruction step i and detector set, whereas the fixed parameter a_i has to be selected from the constrained set of

$$a_i \; \in \; A := \left\{0, \frac{1}{8}, \frac{1}{4}, \frac{1}{2}\right\}. \tag{3.58}$$

It can also be selected independently for each step i though. The scheme in Eq. 3.55, together with the set possible values for a_i in Eq. 3.58 ensures that the higher gains get equal or higher weights $1 - a_i$ compared to a_i as the accumulator weight. If any of the above two conditions are not fulfilled, the reconstruction process is aborted and the value of E_{c_i} is taken as the result of the energy reconstruction.

The condition in Eq. 3.56 is applied to detect energy overflows in the next detector by extrapolation from the value in the current detector, the one in Eq. 3.57 to detect ‘underflows’, cases for which the noise in the current channel is considered to be too high for the channel to be of interest. The assessment of the validity of the data in the next channel to be read out is done in the current step to speed up data acquisition by digitizing only those channels for which good pulse height values are to be expected. Both the occurrence of the under- and the overflow conditions are stored in separate flags for further processing by the software in the onboard microcontroller.

Silicon hits. Additionally, silicon hit rejection will be done for each step and for those detectors for which it makes sense (D, E), by checking for the conditions (after checking the other two inequalities)

$$R_{\min,i} \leq 64 \frac{E_i - \hat{E}_i}{E_i + \hat{E}_i} \leq R_{\max,i} \tag{3.59}$$

and, when any of these is violated, selecting the value

$$E := \min(\hat{E}_i, E_i). \tag{3.60}$$

Again, the values of $R_{\min,i}$ and $R_{\max,i}$ are selectable for each detector and reconstruction step. In this case, they are constrained to be integer numbers, which reduces the resolution of the above silicon hit rejection criteria. To increase the resolution and to allow fractional silicon-to-light hit rejection ratios, the factor of 64 has been inserted into the formula above. The silicon hit detection will set a flag for further processing as well.

3.8.1 Parameter estimates

The above process needs tuning of the parameters $R_{\text{min}}, R_{\text{max}} \in \mathbb{N}^n$, $a \in A^n$ and $E_{\text{min}}, E_{\text{max}} \in \mathbb{N}^n$. An exemplary search for good parameters for the D scintillator is done.

This search is accomplished by using the above *simulated* optical data for D. Much like for the estimation of the energy resolution broadening in the preceding sections, appropriate GAUSSian noise is added to the pure optical data. In contrast to the electronics noise contribution to each scintillator channel, the amount of correlated noise between redundant readout channels is important and needs to be taken into account.

As the input to the VIRENA (for the D channel) is a total of six signals from three independent detectors, with a redundant pair for each[3], a significant part of the noise will be coherent between the redundant channels. The noise model from Sec. A.2 is used to give the noise contribution and correct amount of correlation for all six channels. In the following examination, the photon output of the scintillator is assumed to be affected by additive noise by the estimates given for the FlightREB+FM2 combination.

It is also additionally possible to vary the values of the gain scales s and t, as defined in Sec. A.2.1, in the VIRENA. A full study could check the influence of these settings on the achieved noise, but would extend the parameter space by a large margin. It would also need a full set of all measured VIRENA gain scale values s, t. To keep the parameters in the range where the noise model has been evaluated, the parameter for set of s and t is held constant. It is assumed that

$$s_u = 8, s_i = 2, s_n = 2 \tag{3.61}$$

and that

$$t_h = 1, t_m = 1, t_l = 1. \tag{3.62}$$

For each given event with seen energy deposits (from the optical model), a set of noise values is produced by using the random variable description of the noise in each channel from Eqs. A.1 and A.2 in App. A.2.1, with the values for the σs and φ from the noise model fit. This is then added to the pure values from the optical model to arrive at the expected behaviour of the scintillator and the electronics distribution.

A certain energy loss path distribution inside the scintillator has to be selected to be able to get the light distribution behaviour between the scintillator's diodes. In this case, the light distribution for tracks of charged particles with even energy loss, going straight (0°) through the D crystal is assumed, with uniform probability to hit anywhere on the C detector.

It is assumed that good values for values E_{min} are selected by separating a small number of noise width standard deviations of each electronic noise peak. In the following, set $E_{\text{min}i} = 3\sigma_{A_i/B_i}$ with σ_{A_i/B_i} being the electronic noise width for the particular channel i. Sensible values for E_{max} can also be easily determined. As the response of the REB ADC seems to be mostly linear for the full ADC range $0 \dots 16383$, they have been set to the energy corresponding to the somewhat arbitrary ADC value 16300 for each channel. This leaves R and a as unknown values. As a is discretized, only

$$N := |A^n| = \left|A^5\right| = 4^5 = 1024 \tag{3.63}$$

different combinations can be selected. The best values for a (for varying definitions of 'best', see below) can thus be found with a brute-force search. For the determination of the values a_i, no silicon hits are assumed and thus not silicon hit rejection is applied (and thus $R_{\text{min}} = -\infty$, $R_{\text{max}} = +\infty$ are selected correspondingly).

---

[3] A possible partial channel selection mask is not covered here.

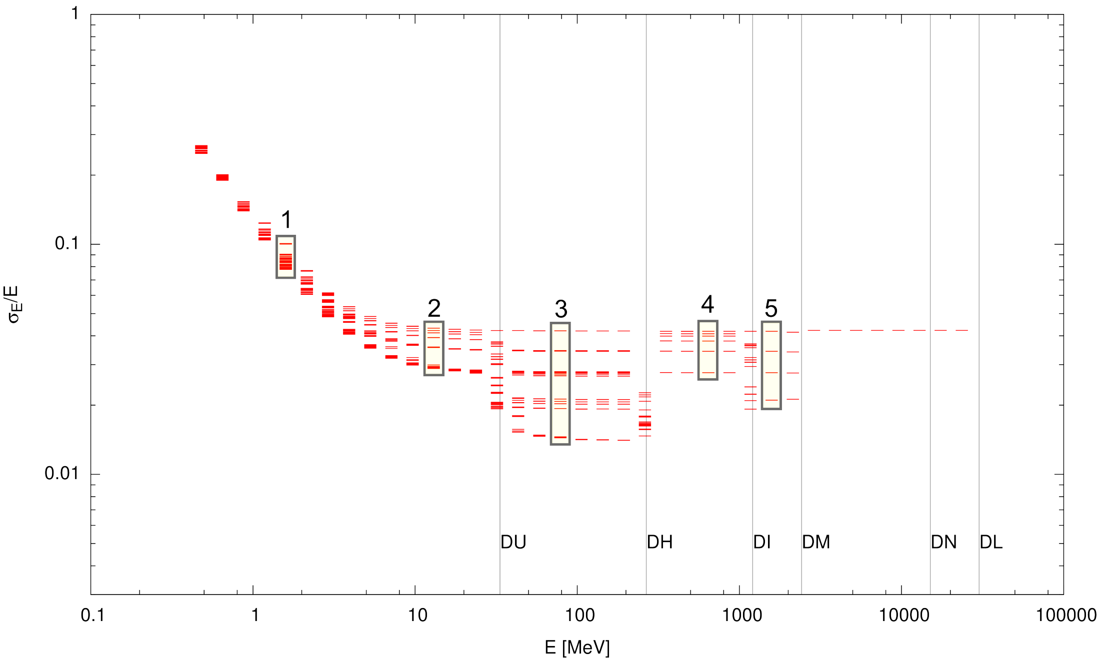

Figure 3.19: Reconstructed energy widths of delta peak shaped energy inputs into the scintillator. Shown is the reconstructed width for all possible values of a vs. the set position of the peak energy. Note the logarithmic y scale. The vertical lines denote the $E_{\max}$ threshold values for the channel in the label attached to the bar. The energy axis assumes no quenching. For the meaning of the boxes, see text.

A set of energies covering the whole range of the D scintillator have been processed according to the scheme described above. The set of energies used for processing is

$$E_k = e^{0.3k-0.1}\text{MeV}, \tag{3.64}$$

with $k \in \mathbb{Z}$ appropriately.

In Fig. 3.19, the resolution for the different energy steps and all possible values $a \in A$ is shown. The change achievable with a 'good' selection for a can be seen to be negligible for the very-low ($E \leq 1\text{MeV}$) and the very high-energy range ($E \geq 2\text{GeV}$). For the low energy range, this can be explained by the $E_{\min}$ noise cut-off ignoring the lower gain channels and conversely by the $E_{\max}$ thresholds ignoring the higher gain channels for the very high energy range. Note that the decision whether to include DN or not in the selection for averaging does not change the energy resolution considerably.

The behaviour is, as expected, continuous between the different selection steps at the $E_{\min}/E_{\max}$ borders. The values close to the borders show more complex behaviour (e.g. at the DH-$E_{\max}$ border in Fig. 3.19) and will be ignored from now on. A more detailed analysis may be needed to apply correct weighting of counts close to these borders where gains are switched.

Only the set of a values yielding the lowest $\sigma E/E$-value for any of the tested energies (as seen in Fig. 3.19) are further considered. The set is further reduced by removing the a values which have essentially the same resolution figures ($\Delta(\sigma E/E) < 1‰$) or where the granularity of the MC simulation would need to be enhanced. Entries which give the same or worse results for all of the representative energies $E_1, \ldots, E_5$ are ignored, too. The ad-hoc reductions are done to reduce the number of a values to investigate here.

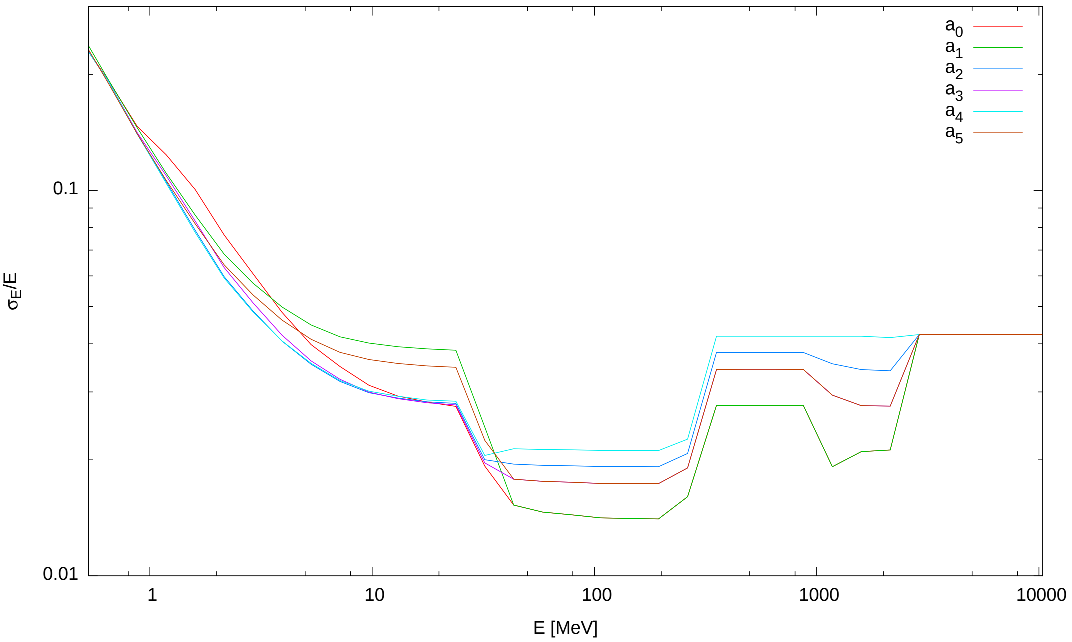

Figure 3.20: Resolution figures for a values from Tab. 3.6. Line plot to be able to distinguish the different a values; the slopes at each of the $E_{\max}$ borders are artifacts.

In Fig. 3.19, five representative energy positions $E_1, \ldots, E_5$ for the following energy resolution study have been selected, at (see boxes labelled $1 \ldots 5$)

$$(E_1, \ldots, E_5) = (1.6, 13, 79, 645, 1590)\text{MeV}, \tag{3.65}$$

ignoring the ranges where there is no change in energy resolution. In Tab. 3.6, the set of the selected a values is given, together with the resolution figures at the above five energy values. The corresponding slopes of expected energy resolution can be seen in Fig. 3.20. Immediately noticeable is the (expected) trade-off between the resolution in the high- and the low energy range, with weighting values for the low or high-gain channels varying correspondingly.

A good compromise resolution can for example be found with $a_3 = (\frac{1}{8}, \frac{1}{4}, \frac{1}{2}, \frac{1}{2}, \frac{1}{2})$. At Energy E_3, the resolution can be compared to the $\theta = 0$ extrapolation in Fig. 3.16. The on-

Index	a **(low ... high)**	$\frac{\sigma(E_1)}{E_1}$	$\frac{\sigma(E_2)}{E_2}$	$\frac{\sigma(E_3)}{E_3}$	$\frac{\sigma(E_4)}{E_4}$	$\frac{\sigma(E_5)}{E_5}$
0	$(\frac{1}{8}, 0, \frac{1}{2}, \frac{1}{2}, \frac{1}{2})$	0.078	0.029	0.021	0.042	0.042
1	$(\frac{1}{8}, \frac{1}{8}, \frac{1}{2}, \frac{1}{2}, \frac{1}{2})$	0.079	0.029	0.019	0.038	0.034
2	$(\frac{1}{8}, \frac{1}{4}, \frac{1}{2}, \frac{1}{2}, \frac{1}{4})$	0.082	0.036	0.017	0.034	0.028
3	$(\frac{1}{8}, \frac{1}{4}, \frac{1}{2}, \frac{1}{2}, \frac{1}{2})$	0.083	0.029	0.017	0.034	0.028
4	$(\frac{1}{4}, \frac{1}{2}, \frac{1}{2}, \frac{1}{2}, \frac{1}{8})$	0.086	0.039	0.014	0.028	0.021
5	$(\frac{1}{4}, \frac{1}{2}, \frac{1}{2}, \frac{1}{2}, \frac{1}{2})$	0.100	0.029	0.014	0.028	0.021

Table 3.6: Final selection of a values and the expected energy resolution at five reference energies.

board accumulator based processing with expected resolution of $\sigma(E_3)/E_3 = 1.7\%$ compares to about the expected resolution for a sum of two channels in Fig. 3.16.

3.9 Average responses from photon Monte-Carlo code

All of the preceding considerations in this chapter focused on the behaviour of the scintillator for different particle fields and especially the single-channel energy reconstruction behaviour. It also focused on the perfect reflection case as it was a sufficient description of the D scintillator.

Here, the average behaviour of the scintillator for point-like energy losses (without PPT integration) and just single photon tracks over the full scintillator volume is further investigated. When looking at the average behaviour of the scintillator with a change in absorption length α and/or reflectivity R, some very general findings can be extracted out of the model that broadly describe the overall scintillator behaviour for variations of these parameters. Specifically, due to a strong correlation between the track length of photons and their number of reflections, both parameters, α and R, can be exchanged in this average case. In this work, their influence can not be further separated.

Scintillator	$\overline{n}$	$\bar{l}$ [mm]	b [mm]	Corr. coeff.	κ_α	ω_α	$\kappa_{\overline{R}}$	$\kappa_{\overline{R}}$
D	7.4	160	20.6	0.99	11.0	-0.94	0.65	0.92
E	10.3	209	18.9	1.00	8.45	-0.88	0.55	0.85
F	19.9	493	23.6	0.95	17.0	-0.83	1.19	0.83

Table 3.7: Simulated average behaviour of the scintillators for random photon tracks inside its volume. Surface model is `fresnel`, 2π. The values of b are accurate to within 2% *to the model.* For the meaning of κ_x, ω_x, see Sec. 3.9.2.

3.9.1 Correlation between optical parameters

For a given single photon track through a scintillator, with number of reflections $n(\mathbf{d}, \mathbf{x})$ and track length $l(\mathbf{d}, \mathbf{x})$, with direction $\mathbf{d}$ and spatial position $\mathbf{x}$, the intensity of that track in the described model (Sec. 3) is

$$
\begin{aligned}
I(n, l) &= I_0 R^n \cdot e^{-\frac{l}{\alpha}} && (3.66)\\
&= I_0 e^{n \log R - \frac{l}{\alpha}}. && (3.67)\\
&\Rightarrow \log I = n \log R - \frac{l}{\alpha}, && (3.68)
\end{aligned}
$$

which would allow, in the case of $n \sim l$, to replace either R or α with the respective other value. One can relate the light loss due to imperfect R to the same light loss due to a change in α, by requiring

$$
I(0, l(n)) \stackrel{!}{=} I(n(l), 0) \tag{3.69}
$$

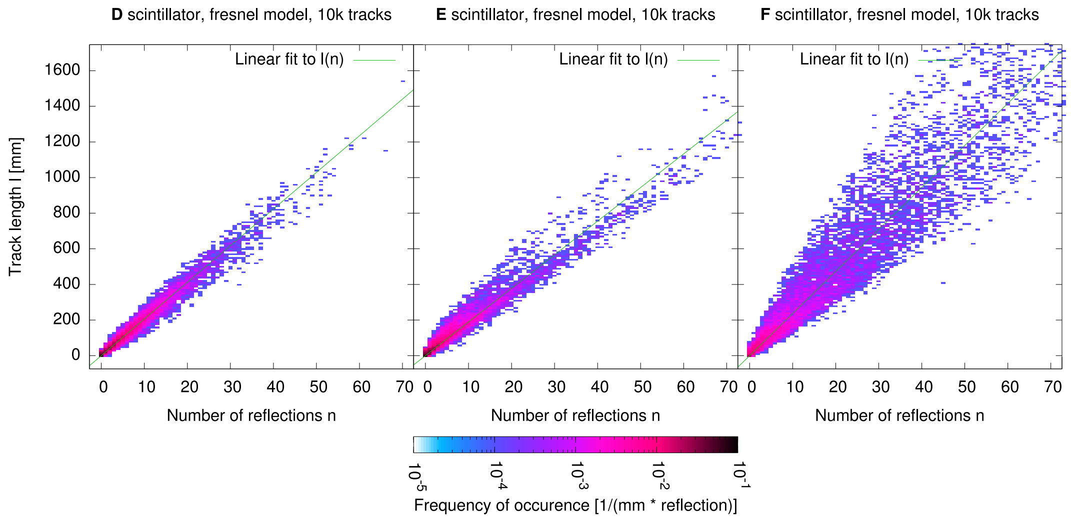

Figure 3.21: Number of reflections for a random ray inside the scintillator volume and the corresponding track length, for the assumption of perfect optical behaviour $\alpha = \infty$, $R = 1.0$. This is a result from simulation with the `fresnel`, 2π model.

which then leads to

$$
\begin{aligned}
& n \log R = -\frac{l}{\alpha} && (3.70)\\
\Rightarrow\quad & \alpha \log R = -\frac{l}{n} && (3.71)\\
\Rightarrow\quad & \alpha(R-1) \approx -\frac{l}{n} && (3.72)\\
\Rightarrow\quad & \alpha(1-R) = \alpha\overline{R} \approx \frac{l}{n} =: b, && (3.73)
\end{aligned}
$$

with $\overline{R} := 1 - R$. This gives a mean free path length b (in the sense of the mean free path between reflections) which can be used instead of α and R when looking at the overall scintillator behaviour and if n and l are sufficiently correlated. This correlation between α and R can be found in the simulations shown in Fig. 3.21. The correlation coefficients between n and l as well as the calculated mean free path lengths can be found in Tab. 3.7. For each scintillator, the value of b is in the range of its respective thickness.

3.9.2 Imperfect scintillators

By varying α resp. R without the PPT integration, the change of the total amount of collected light and energy resolution when doing a *sum reconstruction* from all scintillators can be calculated. In Fig. 3.22 and 3.23, the simulated change of the spread of the I values, $\frac{\text{std}\ I}{<I>}$, on the left y-axis and the light loss fraction on the right y-axis is displayed for a variation of α resp. $\overline{R}$. The respective other value is left at the perfect-case value. The characteristics of all three scintillators are shown. The light loss vs. reflectivity curves give a similar behaviour to the results given in *Pauls* [1998]. The value of std I is similar to but not the same as σ_E, which is given below. The standard deviation of I is calculated without doing the 4π solid angle averaging for each scintillation point in a volume. It is given as a value describing the amount of variation that is possible with single photon tracks in a scintillator. It is

$$\frac{\mathrm{std}\ I(\alpha,\overline{R})}{< I(\alpha,\overline{R}) >} \quad \geq \quad \frac{\sigma_E(\alpha,\overline{R})}{E(\alpha,\overline{R})}. \tag{3.74}$$

For point-like PPTs with the integration/averaging over all directions, the resulting variation of $\frac{\sigma_E}{E}$ can be seen in in Figs. 3.24, 3.25. This plot thus gives the simulated limit to the γ-resolution obtainable for each given scintillator and sum reconstruction of the energy. In the shown range, the simulation curve fits well to a monomial of the form

$$f(x) = \kappa x^{\omega} \tag{3.75}$$

to the simulation in range of $\alpha \in \{1\,\mathrm{mm} \ldots 1\,\mathrm{m}\}$. (with fit weights inverse to the value of σ_E/E). These fit parameters are also given in Tab. 3.7, as $\kappa_{\overline{R}}$ and $\omega_{\overline{R}}$ when identifying $x \hat{=} \overline{R}$ and correspondingly as κ_α, ω_α for $x \hat{=} \frac{\alpha}{\mathrm{mm}}$. The simulation results of the calculated scintillator grids for D, E and F have been used for Figs. 3.24, 3.25 and therefore show the arbitrarily selected spacing of α and R values for which corresponding scintillator grids have been calculated. For example, a value of $\alpha = 200\,\mathrm{mm}$ (see Sec. 5) in the E scintillator gives a resolution due to optical absorption for point-like energy deposits of

$$\kappa_{\alpha,E} \cdot \left(\frac{200\,\mathrm{mm}}{\mathrm{mm}}\right)^{\omega_{\alpha,E}} \approx 8\%. \tag{3.76}$$

A range of $\alpha \in \{100\,\mathrm{mm}, \ldots, 300\,\mathrm{mm}\}$ gives a corresponding range for the energy resolution for point-like interactions of $5.7\% \ldots 14.9\%$. This can also be taken as a limit on the neutron resolution, when imprecisely assuming that neutrons interact point-like.

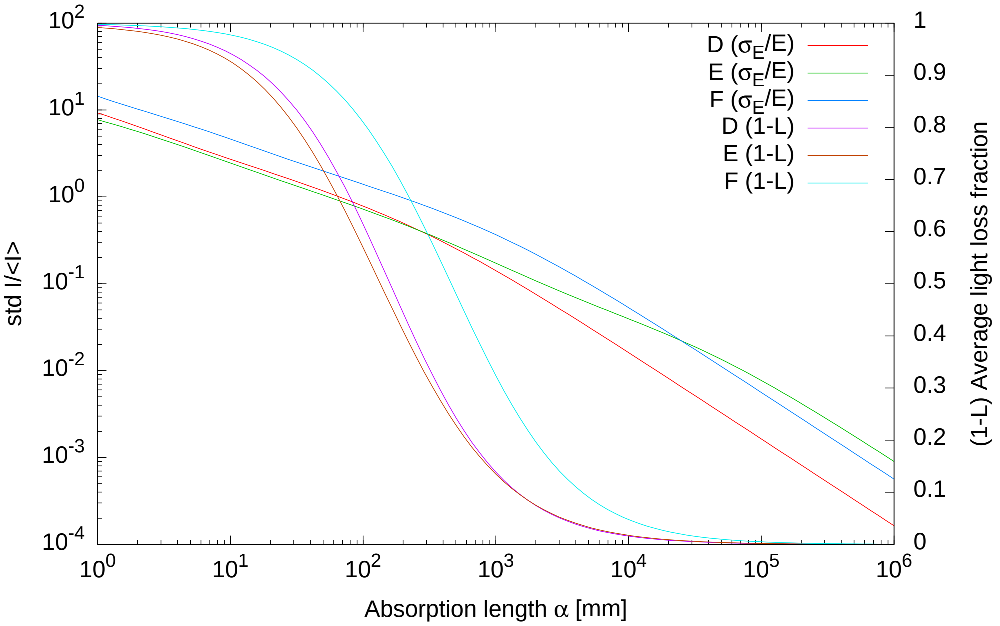

Figure 3.22: Simulated dependency of the behaviour of the D, E and F scintillator on the absorption length α. For each $10k$ isotropically distributed single photon tracks hitting the respective scintillator, the average light loss fraction $1-d=\frac{1-L_{\text{seen}}}{L_{\text{total}}}$ is show on the right y-axis. On the left y axis, the spread of the received photon intensities is given. Reflectivity is assumed to be $R=1.0$ here. The `fresnel`, 2π surface model is used.

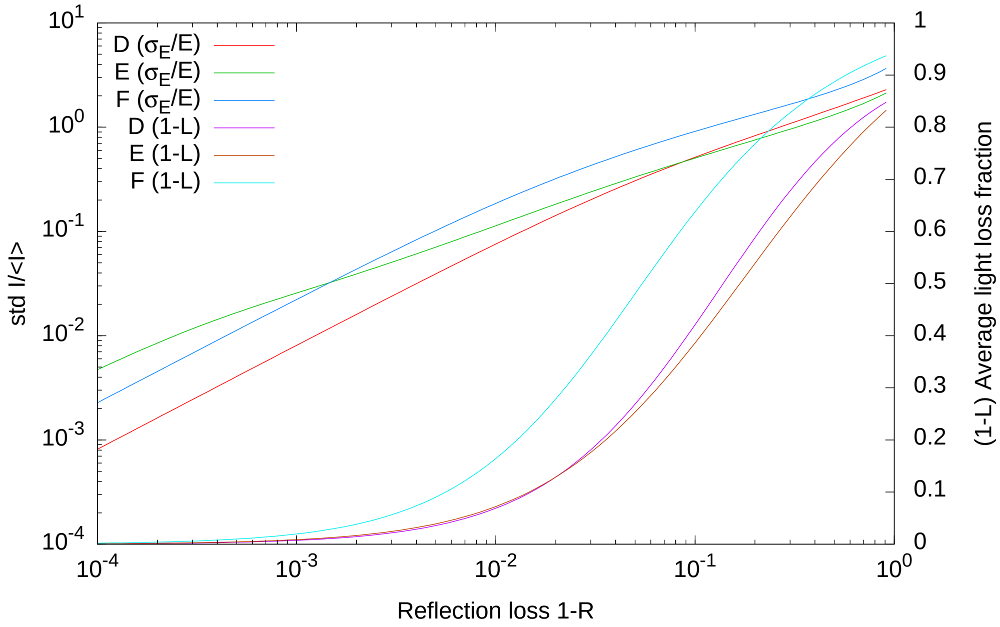

Figure 3.23: Simulated dependency of the behaviour of the D, E and F scintillator on the reflectivity R. For each $10k$ isotropically distributed single photon tracks hitting the respective scintillator, the average light loss fraction $1-d=\frac{1-L_{\text{seen}}}{L_{\text{total}}}$ is show on the right y-axis. On the left y axis, the spread of the received photon intensities is given. Absorption length is assumed to be $\alpha=\infty$ here. The `fresnel`, 2π surface model is used. It should also be noted that instead of R, $1-R$ is put onto the x-axis, to clarify the view on the interesting parts of the data.

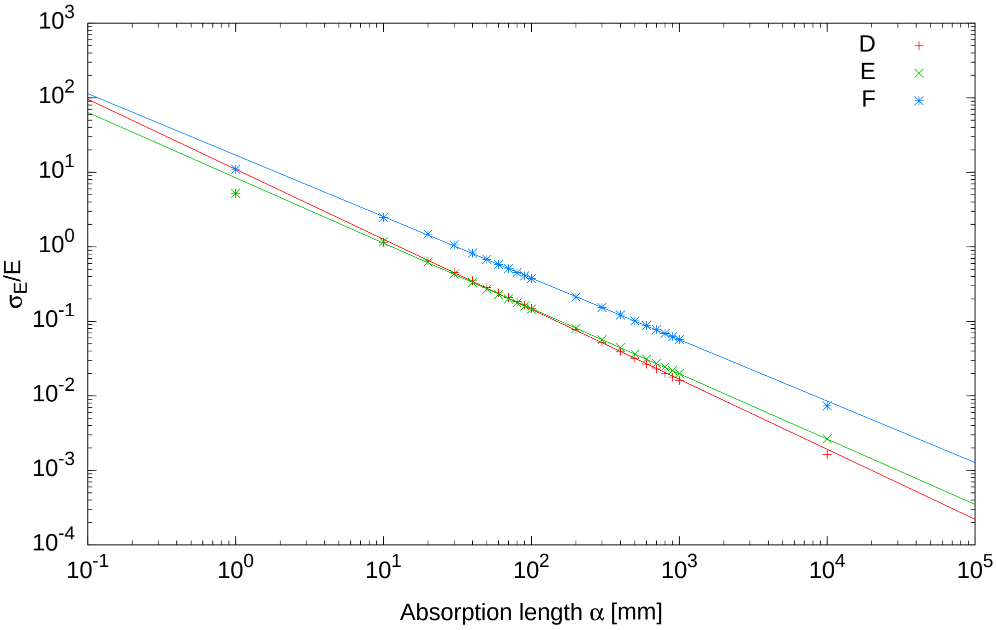

Figure 3.24: Simulated energy resolution vs. absorption length for the total light output (sum signal of all attached diodes) out of each scintillator D, E and F. Again, reflectivity is assumed to be $R = 1.0$ here. The `fresnel`, 2π surface model is used.

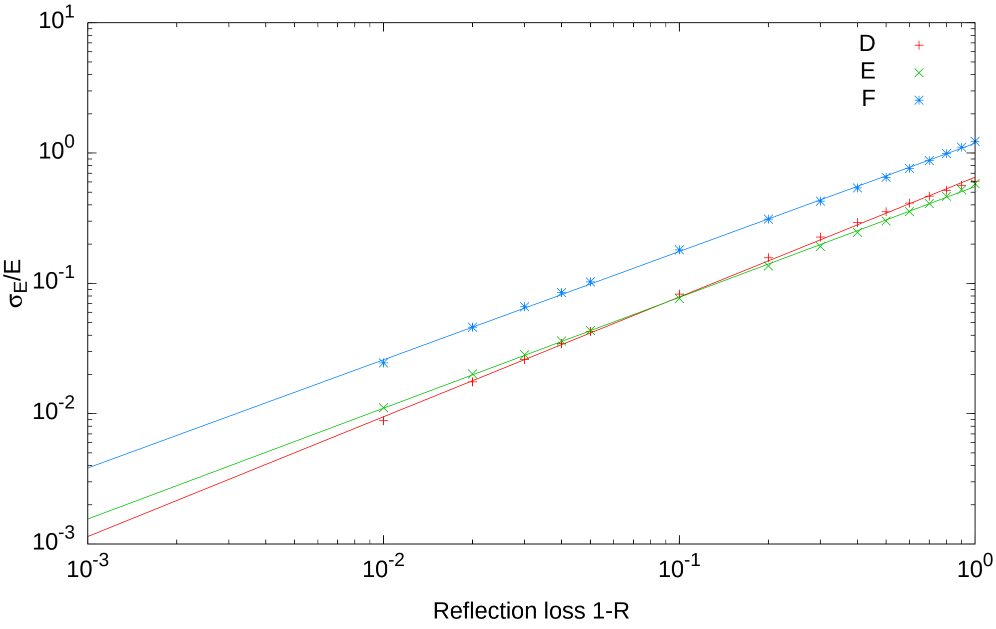

Figure 3.25: Simulated energy resolution vs. reflection loss for the total light output (sum signal of all attached diodes) out of each scintillator D, E and F. It is as assumed that $\alpha = \infty$ and the `fresnel`, 2π surface model.

Surface Model	α	**Detector**	**Mean rel. light output** [%]
`mirror`	∞	B	17.4
`mirror`	∞	T	47.9
`mirror`	200 mm	B	4.6
`mirror`	200 mm	T	4.5
`diffuse`, 2π	∞	B	16.1
`diffuse`, 2π	∞	T	51.8
`diffuse`, 2π	200 mm	B	5.4
`diffuse`, 2π	200 mm	T	5.1
`diffuse`, L	∞	B	15.1
`diffuse`, L	∞	T	54.6
`diffuse`, L	200 mm	B	4.5
`diffuse`, L	200 mm	T	4.3
`fresnel`, 2π	∞	B	16.2
`fresnel`, 2π	∞	T	51.4
`fresnel`, 2π	200 mm	B	4.6
`fresnel`, 2π	200 mm	T	4.4
`fresnel`, L	∞	B	16.3
`fresnel`, L	∞	T	51.1
`fresnel`, L	200 mm	B	4.5
`fresnel`, L	200 mm	T	4.4

Table 3.8: Means for different surface simulation models, for the top T and the first bottom B readout. The fraction of light reaching the noted detector is given. The statistical errors are < 3‰. 2π denotes diffusion uniformly into 2π from a surface and L denotes the LAMBERTian cosine law. Except for just taking a single channel value, this calculation is comparable to what is done in Sec. 3.9.

3.10 Surface model comparison

The different surface models are compared to test the range of responses given by these models and thus give a rough estimate of the errors introduced by the simplifications made in the models. The following sets of tests are done exemplarily between simulated sets of data for the F channel, as the surface model is deemed to be most important in this case.

A set of $N = 1000$ random points has been selected inside the F volume. For each of those 1000 points, the scintillator response for each surface model is calculated, with 10 k photons for each point. Let the responses of each model m be T_m for the top readout diode of the F channel (F1) and B_m for the (first) one of the bottom (F2) diodes. For a selection of $\alpha = 200\,\mathrm{mm}, R = 1.0$ (which relates to the findings in Chapter 5), for each two models l and m, the standard deviation of $T_l - T_m$ resp. $B_l - B_m$ is calculated and subsequently divided by the overall means $(\overline{T_l}, \overline{T_m})$ resp $(\overline{B_l}, \overline{T_l})$ to get a relative change. The mean for each model gives the possible shift in total readout between the two surface models and the sample standard deviation of $T_l - T_m$ gives a value describing the amount spatial differences resulting from the simulation when changing between the two surface models.

The resulting means are given in Tab. 3.8. For pairs of models l, m, the described standard deviations are given in Tabs. 3.9, 3.10, 3.11 and 3.12. For brevity, only the extreme cases and the selected (see below) model is included in these tables.

The largest difference can be seen between the `mirror` model and the `diffuse` model

	`mirror`	`diffuse`, 2π	`diffuse`, L	`fresnel`, 2π	`fresnel`, L
`mirror`	-	22.3	22.5	7.8	8.5
`diffuse`, 2π	22.3	-	4.4	19.6	19.6
`diffuse`, L	22.5	4.4	-	20.0	20.3
`fresnel`, 2π	7.8	19.6	20.0	-	4.2
`fresnel`, L	8.5	19.6	20.3	4.2	-

Table 3.9: Standard deviations divided by the sum of means, times hundred. For the bottom readout diode and the $\alpha = \infty$ case. The expected deviation due to statistics is ±3.2% in absolute change of the values given here, derived from running the `fresnel`, 2π model twice.

	`mirror`	`diffuse`, 2π	`diffuse`, L	`fresnel`, 2π	`fresnel`, L
`mirror`	-	11.6	10.4	6.2	7.0
`diffuse`, 2π	11.6	-	2.6	7.5	8.1
`diffuse`, L	10.4	2.6	-	6.8	8.0
`fresnel`, 2π	6.2	7.5	6.8	-	2.9
`fresnel`, L	7.0	8.1	8.0	2.9	-

Table 3.10: Standard deviations divided by the sum of means, times hundred. For the top readout diode and the $\alpha = \infty$ case. The expected deviation due to statistics is ±1.4% (absolute change), derived from running the `fresnel`, 2π model twice.

	`mirror`	`diffuse`, 2π	`diffuse`, L	`fresnel`, 2π	`fresnel`, L
`mirror`	-	43.1	43.1	10.9	12.4
`diffuse`, 2π	43.1	-	12.1	38.7	38.7
`diffuse`, L	43.1	12.1	-	38.8	39.5
`fresnel`, 2π	10.9	38.7	38.8	-	5.8
`fresnel`, L	12.4	38.7	39.5	5.8	-

Table 3.11: Standard deviations divided by the sum of means, times hundred. For the bottom readout diode and the $\alpha = 200\,\mathrm{mm}$ case. The expected deviation due to statistics is ±4.6% (absolute change), derived from running the `fresnel`, 2π model twice.

	`mirror`	`diffuse`, 2π	`diffuse`, L	`fresnel`, 2π	`fresnel`, L
`mirror`	-	27.2	26.2	13.3	14.3
`diffuse`, 2π	27.2	-	4.2	17.2	16.8
`diffuse`, L	26.2	4.2	-	16.0	15.5
`fresnel`, 2π	13.3	17.2	16.0	-	2.7
`fresnel`, L	14.3	16.8	15.5	2.7	-

Table 3.12: Standard deviations divided by the sum of means, times hundred. For the top readout diode and the $\alpha = 200\,\mathrm{mm}$ case. The expected deviation due to statistics is ±2.1% (absolute change), derived from running the `fresnel`, 2π model twice.

with 2π uniform angular distribution of about 40%. This is expected as these two models are devised to cover two extreme cases. This number gives also, approximately, the maximum influence of the surface model on the results of the modeling.

As also visible, there is effectively only a slight difference of at most $< 6\%$ ($< 2\%$ when taking into account the statistical error from the MC) between all `fresnel` cases with 2π or LAMBERTian selection of the diffuse case. In the following, the `fresnel` case with uniform 2π diffusion has been selected.

3.11 Conclusions

The implementation of the optical model is described. It is subsequently applied to measurements involving optical variation in the D scintillator and it is shown that the optical model describes the behaviour of the D scintillator successfully. In a set of further tests and forecasts, the possibilities of the optical model for further exploration as well as its value in aiding for energy resolution studies is shown. Finally, a top-level review of its behaviour in the mean case is given and the effects of varying the different parameters and selecting the corner cases of the model are discussed.

Chapter 4

Anti-coincidence

One of the design goals for RAD is the measurement of neutral particles (n, γ) to be able to estimate variables such as the neutron dose rate on the surface of Mars.

Apart from being the end-part of the charged particle telescope in RAD, the D detector is intended to be the primary detector to detect γ-photons (and to do limited spectroscopy on them, for details see Sec. 3.6) and is thus sometimes referred to as the γ-channel in RAD. Complementing the D scintillator, the E scintillator, being rich in hydrogen, is suited to detect fast neutrons on Mars. No special detector exists to measure the rate of thermal neutrons and the response of the instrument has not been explicitly tested for those. In the context of RAD, the E scintillator is also called the neutron channel.

Energy deposits by charged particles in D or E need to be distinguished from those by neutrons (or γ-photons) to be able to sort them into the appropriate histogram bins. Charged particles will lose energy constantly along their tracks according to Bethe-Bloch, whereas neutral particles will mostly generate single detector hits.

This is exploited by using the detectors surrounding each neutral channel as an AC shield to sort out those particles hitting both the enclosed and any of the outer detectors.

4.1 The F scintillator

To prevent leakage of charged particles from any direction into a particular neutral channel, an additional, separate outer detector F encloses both D and E. It is sometimes called *the* AC detector, but one has to keep in mind that for D as well as E, the F detector will only form part of the whole AC channel selection.

Trade-offs done during design of the AC do not allow for an F scintillator which is able to clearly decide between passing charged and uncharged particles for all particle fields. In contrast, the silicon detectors as well as the D scintillator can be assumed to have this property to a very high degree (see App. G, Fig. G.1 for an example of the performance of the C2 channel).

The major trade-offs during design for the AC are

- Limited mass and (thus also thickness) of the AC. The AC is the largest and most massive part of the RSH
- Scintillator material choice (light output in the range of the sensitivity of the photo diodes)
- Photo diodes instead of photo multiplier tubes to avoid the complexities of high voltage in the instrument.

This causes the expected signal in the AC for minimum ionizing particles to be hard to detect and further causes the detection probability for charged particles to be dependent on their $\frac{dE}{dx}$, incoming position and angle. Instrument temperature and long-term degradation of the noise figures is expected to play a major role as well, but this is not further covered in this work. Also, leakage of secondaries from neutrons into the AC as well as electronic crosstalk will change the detection efficiency for neutral particles in the E channel. This wide field of parameters makes it worthwhile to model the AC to be able to forecast its behaviour for any expected charged particle flux. Details on this effort are covered in Chapter 6. In the following, the basic parameters of the AC and its effects on the instrument parameters are discussed. A simple fit of an empirical energy loss distribution shape is done, in order to have a first rough view on the efficiency figures.

Due to the complexity of the AC and the limited amount of beam time available for testing the AC in flight configuration for a comprehensive set of directions and positions, no satisfactory direct measurement of the AC response and thus realistic, measured efficiency figures do yet exist. Plans exist to have a thorough investigation of the AC in the CERF field.

4.2 Desired anti-coincidence performance

Determination of the AC trigger threshold has to weight the influence of AC *false negatives* (which, in this context, are unwanted charged particles in the neutral channel) to the suppression of genuine neutral hits in the neutral channel (*false positives* here) by noise signals in the AC detectors.

The silicon detector based AC that has been built into the NEUtron DOSimetrie (NEUDOS) detector [*Burmeister*, 2006] has been used as a guide for the design of the RAD AC. The scintillating material is slightly different (BC430 instead of BC432M, and BC432M has approx. 10% lower light yield[1] than BC430) and a different wrapping material has been chosen.

In *Burmeister* [2006], the NEUDOS detector achieves a rejection probabilities for MIPs of 96% for a single scintillator plate and, as the instrument is completely surrounded by AC scintillator plates, a final AC rejection probability of 99.6% is achieved. RAD's AC aims to achieve similar rejection rates.

4.3 Anti-coincidence geometry and detector sets

To have a neutral channel combination D/E, it is necessary to select the C2 channel and the C channel as an additional AC signal. Owing to the telescope geometry resp. the wiring of the segments of the C detector, a gap exists between the F1 and the C detector [*Böttcher*, 2008], which has to be closed by including the C2 detector in the AC (again see Fig. 4.1). The C2 selection also guards against particles crossing through the guard ring between the innermost and next-inner segment by including the appropriate parts on the B detector. Particles through the outer guard rings can be expected to also cross the F scintillator and thus be still detectable. Together with the F channel, an AC completely surrounding the D/E detector stack (see Fig. 4.1) is formed.

In addition, if exact single channel hits in D or E are requested, the respective other channel can also be included in the AC mask. This topic is not further discussed here and

---

[1] From eMail communication with the material manufacturer Saint-Gobain.

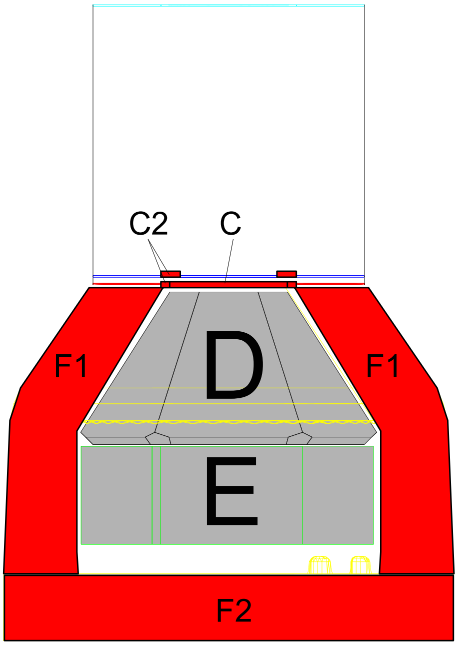

Figure 4.1: Schematic side view of the geometry of the AC selections, marked in red, for the D and E channel. For details on the selected segments of the silicon channels, refer to *Böttcher* [2008].

depends on the detailed results from applying the inversion method [*Böhm and Kharytonov*, 2008], which is still a work-in-progress.

4.4 Definitions

To be able to discuss and cleanly separate the different influences on the AC performance, and as the AC performance can not be easily described as a single rejection rate (see below), a set of definitions that helps in the discussion of AC parameters is given now.

Particle field response. Here, a particle field response is a function

$$F : \mathbb{R}^n \to \mathbb{R}, x \mapsto F(x) \tag{4.1}$$

giving the differential rate in units of $[\mathrm{ADC}^{-n}\mathrm{s}^{-1}]$ for a given vector of n *seen* energy deposits (in different channels) x in the various detectors of RAD. Although particle field responses are in units of discrete ADC units, it is simpler to view certain theoretical AC rates as an integration along axes in units of offset-corrected ADC values instead of a discrete summation (see below). Assume from now on that ADC units are real-valued and offset-corrected here ($\Delta E = 0$ corresponds to $0\,\mathrm{ADC}$). Exact primary particle *energy deposits* due to particle physics alone are not of interest in the context of AC performance estimation but the mangled energy deposit figures due to the discussed imperfections are. Denote the field response, with a given (anti-)coincidence condition A applied, as

$$A(F) : \mathbb{R}^n \to \mathbb{R}, \mathbf{x} \mapsto \begin{cases} F(\mathbf{x}) & A \\ 0 & \neg A \end{cases} \tag{4.2}$$

Fields. Let N be a given input field of neutrals and C be an input field of charged particles. The full field V in the context of AC efficiency figures is assumed to be simply $V = N + C$.

AC rates. Let the response of the AC channel a (defined in the particular context), for a given field response X and ADC value v be $\mathrm{ac}_X(v)$ [$\mathrm{ADC}^{-1}\,\mathrm{s}^{-1}$]:

$$\mathrm{ac}_X(v) := \int\limits_{\{y\,\in\,\mathbb{R}^n | y_a = v\}} X(y)dy \tag{4.3}$$

Total rates. Let $\|X\|$ be the total rate of particles in the response X, thus defined as

$$\|X\| := \int\limits_{\mathbb{R}^n} X(v)dv. \quad [\mathrm{s}^{-1}] \tag{4.4}$$

Efficiencies. Here $\eta(\mathbf{A})$ for an AC selection $\mathbf{A}$, describes what is called *AC efficiency* here, which is solely depending on the charged particle properties of the AC, and is defined as the ratio of rejected charged particles to the total number of charged particles:

$$\eta(\mathbf{A}) := \frac{\|\mathbf{A}(C)\|}{\|C\|}. \tag{4.5}$$

For any rejection efficiency η, define $\overline{\eta}$ as the leakage rate, that is $\overline{\eta} := 1 - \eta$. Analogous to $\eta(\mathbf{A})$, define λ as

$$\lambda(\mathbf{A}) := \frac{\|\mathbf{A}(N)\|}{\|N\|}, \tag{4.6}$$

the fraction of neutral particles being rejected for a given cut $\mathbf{A}$. Let $\overline{\lambda} := 1 - \lambda$ as well. Define the neutron-to-proton (more exactly, neutral-to-charged) signal-to-noise ratio ρ as

$$\rho(\mathbf{A}) := \frac{\|\neg\mathbf{A}(N)\|}{\|\mathbf{A}(C)\|}. \tag{4.7}$$

a second figure $\hat{\rho}$ that describes the signal-to-noise under the assumption of an equal number of neutron and protons in the incoming field can be calculated as

$$\hat{\rho}(\mathbf{A}) := \frac{\overline{\lambda}}{\eta}(\mathbf{A}). \tag{4.8}$$

From these definitions, it can already be seen that the AC efficiency figure alone is not a good measure of the AC performance. Rather, a maximization of ρ is desired for RAD. Additional constraints apply, as the error $\Delta\rho$ should be minimized as well. This error directly affects the accuracy of any neutral particle measurements, such as the neutral particle dose rate!

4.5 Detection principle

For each event, the response of the AC channels around a selected neutral channel need to be used to decide whether the hit is due to a γ/n or a charged particle. In the case of RAD, a simple threshold v_a for the AC channel is used to make this decision. Thus the F-AC selection $\mathbf{A}$ in this context is

$$\mathbf{A} := x_a > v_a \tag{4.9}$$

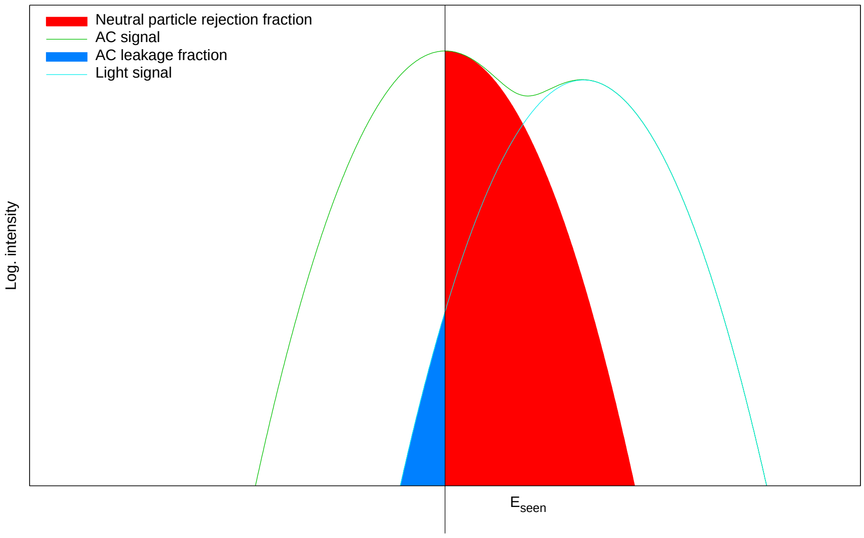

Figure 4.2: Schematic view of the expected energy loss (or ADC) histogram of the events seen in any single AC channel, given a mixed (charged/neutral) input field for RAD. The x-axis is the AC signal in units of energy resp. ADC values, the y-axis shows the differential intensity. The vertical bar in the middle of the graph gives an example cut that can be done on the AC, yielding the given rates marked as the coloured areas.

with x_a being the F-AC signal. The AC signal that is mostly discussed in this context is the simple sum $x_a = \mathrm{F1} + \mathrm{F2}$, or a single channel cut $x_a = \mathrm{F1}$ or $x_a = \mathrm{F2}$. If any of the AC thresholds is exceeded by the ADC value for any AC channel, the particle is assumed to be charged and excluded from further neutral particle hit handling.

For the silicon channels b_i, another selection

$$\mathbf{B} := \bigvee_i x_{b_i} > v_{b_i} \tag{4.10}$$

is done, with x_b being the signals in the silicon detectors with thresholds v_b. The total AC selection is then $\mathbf{A} \vee \mathbf{B}$. For the silicon channels where the energy loss distribution function of charged particles can be clearly separated from an electronic noise signal, the choice of this threshold is rather easy. Setting the threshold in between the noise peak and the, in the case of a silicon channel distinctly remote, approximately LANDAU-distributed charged particle distribution will give the desired AC behaviour $\lambda(B) = 0$ and $\eta(B) = 1$. Deviations from this perfect case in silicon are not further investigated here. Due to significant broadening of the energy loss distribution, this simple threshold selection is not possible in the F (and E in the case of a D-only neutral selection) channels. A trade-off between the reduction of the neutral particle rate and the contamination of the neutral channel with charged particles is necessary ($\max \rho$ and $\min \Delta\rho$)in the estimate of ρ.

For a mixed input particle field, the energy deposits in the AC will give a bimodal distribution, consisting of the neutral particle hits with zero energy loss and charged particles with their straggling energy loss distribution. This signal is then convoluted with a the unavoidable electronic noise signal, giving approximately the shape as illustrated in Fig. 4.2, with a GAUSSian noise peak (width σ_n) around zero energy loss and the overlapping charged particle energy loss distribution. Thus, using the above definitions (and the function ac describing solely the F signal from now on), it can be assumed that

$$\mathrm{ac}_N(v) \sim e^{-\frac{v^2}{2\sigma_n^2}} =: n(v, \sigma_n) \tag{4.11}$$

and thus

$$\lambda(A) = \frac{1 - \operatorname{erf}\left(\frac{v_a}{\sigma_n}\right)}{2}. \tag{4.12}$$

It is important to state here that this is only true in a perfect world where neutral particles produce perfect single detector hits. For high-energy neutrons, this assumption breaks down. See Sec. 6.8.1 for a detailed discussion of this effect.

Selecting a rejection threshold (in Fig. 4.2, the AC threshold, denoted by the vertical black line, has been set to the ADC value corresponding to $E = 0$) will then reject a number of genuine neutrals, as electronic noise will move them above the given rejection threshold (red area). On the other hand, some of the charged particles will have measured energy deposits below the detection threshold and will thus be falsely counted in the neutral particle channel (blue area).

Setting the threshold to exactly $v_a = 0$ at the center of the electronic noise peak [priv. comm. S. Böttcher] has the advantage that, independent of the actual width of the electronic noise peak, half of the neutral particles will be thrown away under the above assumptions, as $\operatorname{erf}(0) = 0$ and thus

$$v_a = 0 \Rightarrow \lambda(A) = \frac{1}{2}. \tag{4.13}$$

Although also displayed as a normal distribution here, the exact shape of the charged particle energy loss distribution is quite complicated due to the aforementioned dependence on a large set of parameters and its exact shape can only be found either experimentally through long-term measurements in the expected charged particle field or by a comprehensive and well-validated model of the energy-loss and optical effects in the AC. This is *the* main problem complicating the calculation of reliable AC figures.

As the amount of electronic noise is expected to change over time (degradation of the detectors and temperature variations), the above threshold of $v_a = 0$ makes data analysis, especially onboard analysis, simpler. Doing the AC-cut this way avoids having to deal with the actual width of the noise distribution. As the VIRENA/ADC DC-offsets are expected to shift with temperature, too, a map describing the change of the thresholds with temperature still needs to be supplied to the onboard data handling software. Setting the threshold on the noise peak adds the requirement that the measured noise peak shape is not or only slightly changed by overlapping charged particle signals. For (in-flight) calibration of the AC noise peak positions, data with mostly zero hits should be used, such as those produced by setting a low threshold on the A1 or A2 channel. A response curve of the AC for different thresholds will be given later on at the end of Chapter 6.

4.6 Extrapolated false negative rates

For rough figures on the F detector AC detection efficiency while avoiding having to deal with a sufficiently validated full model of the AC, a simple empirical model is fitted to the AC signals.

The model assumes the GAUSSian shape for the noise peak $n(\ldots)$ and an exponential behaviour for the left flank of the muon peak $c(\ldots)$, with constants a, b, y and σ_n. Note that the assumption about the exponential left flank of the muon peak implicitely makes the further assumption that there is always a slight non-zero tail below $E = 0$, even without the influence of noise, which will tend to overestimate the leakage fraction.

$$\mathrm{ac}(v) = y \cdot n(v, \sigma_n) + c(v, a, b) \tag{4.14}$$

with

$$c = \exp(ax + b). \tag{4.15}$$

This is only an empirical description of the low-energy AC behaviour. It is fitted to model the data only from the noise peak up to the peak of the muon signal. Taking a cut on the AC signal with $v_a = 0$ (and thus assuming a false positive rate of $\lambda = 50\%$), the number of missed charged particles n_c is then extrapolated as

$$\begin{aligned} \|\mathbf{A}(C)\| &= \int\limits_{-\infty}^{0} c(v, a, b) dv \qquad (4.16) \\ &= \exp(b) \left[\frac{1}{a} \exp(ax) \right]_{-\infty}^{0} \qquad (4.17) \\ &= \frac{1}{a} \exp(b) \qquad (4.18) \end{aligned}$$

and is compared to the total number of charged particles $\|C\|$ seen in the E channel (calculated here by excluding those explained by $n(v)$ from the total number of particles $\|V\|$)

$$\|C\| \approx \|V\| - \int\limits_{-\infty}^{+\infty} n(v) dv = \|V\| - \sqrt{2\pi} y. \tag{4.19}$$

which finally allows the calculation of the AC false negative rate $\overline{\eta}$ according to Eq. 4.5.

As the exact ratios are not of interest when calculating η or λ, the count values given in the form $\|\ldots\|$ are count values, not rates in the following section.

4.7 Measurements and results

As already stated, MIPs are the hardest test case for the AC and a cosmic muon run has therefore been used to collect data on its performance. The results are strongly dependent on the electronic noise performance of the instrument and good statistics paired with low cosmic muon rates require a long integration time.

Therefore a comparatively long run with the final flight REB electronics and the FM01 sensor head on top in flight configuration has been chosen, done at room temperature. The used file is [#8, μ-FM1-fREB]. For this run, the REB has been configured in a catch-all trigger with separate high-speed PHA output and no further onboard processing. If not noted otherwise, energy is given as raw ADC values. The instrument has been placed upright with the main axis pointing to zenith.

4.7.1 E neutron channel

Before any further processing, hits in E are selected with an appropriate AC-mask on the DU and the F channel and a cut on the C and C2 channel is made.

In this context, the set of events V_1 is the set of all events *with the C and C2 cut applied* and thus gives the performance of the AC when requiring a path through the scintillator.

The final efficiency figure has to be calculated by taking all events V into account (without a cut of C2), which will reduce the leakage ratio.

The DU channel is included in the AC to better work out differences between muons hitting the D and the E detector. For the same reason, the F1 and the F2 signal is analyzed separately. The energy selection in the E channel is done by summing the appropriately scaled signal of EU, EI and EL, whereas for the D channel, only the value of DU is used[2]. Rejection for energy deposit in D by considering only the DU channel is deemed to be sufficient as the muon light signal is cleanly separated from the electronic noise peak. For details regarding the AC behaviour of the D (and C2) channel, see App. G.

In Fig. 4.3, the response of the F1 AC detector and in Fig. 4.4 the response of the F2 AC detector can be seen for the selected particle set. The curves shown are the result from fitting the model described in Sec. 4.6, with an additional offset parameter included to cover offset alignment in the same data analysis step.

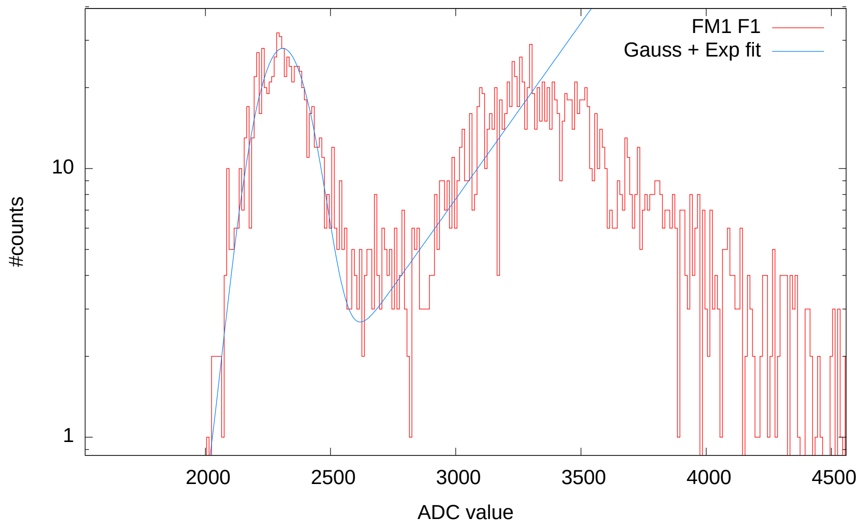

Figure 4.3: Response of the F1 channel for particles in E in a mostly cosmic muon field. To increase statistics per bin, the data has been collected into bins of 10 ADC values each.

Additionally, the results of the two fits can be seen in Tab. 4.1. The value $\overline{\eta}_F$ is the probability of a MIP to enter the E detector despite an active AC. It has been calculated separately for F1 and F2.

As stated, the leakage rate is expected to be overestimated and, as both F1 and F2 will be used as AC detectors, the resulting total leakage rate is the minimum of both leakage ratios.

4.7.2 D channel

A rather high energy cut on the D channel needs to be selected, as there is a low energy region in the D scintillator (γ-rays) where the F-AC signal only sees noise. For hits in the D scintillator, the F2(r) detector is unusable for application of this empirical method, as it can be seen in App. G. It should also be noted that the rejection for the D channel is believed to perform worse, as a higher cut on the D channel selects mostly long tracks in D, which on the other hand give short tracks in the AC.

---

[2] Due to the broken DM channel in FM1.

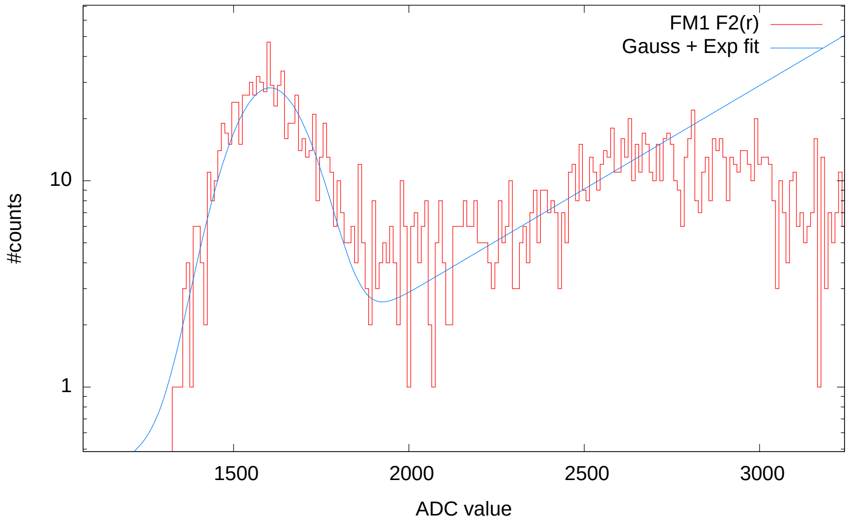

Figure 4.4: Response of the F2(redundant) channel for particles in E in a mostly cosmic muon field. Again, to increase statistics per bin, the data has been collected into bins of 10 ADC values each.)

N chan.	**AC chan.**	$\lVert V_F \rVert$	$\lVert C_F \rVert$	$\lVert N_F \rVert$	**Fit range (ADC)**	$\overline{\eta}_F$ [%]	χ^2
E	F1	2452	1766	32	1980 . . . 3130	1.8 ± 0.7	1.0
E	F2(r)	2452	1766	50	1330 . . . 2610	2.8 ± 1.4	1.3
D	F1	1018	854	48	1800 . . . 3500	5.6 ± 1.8	1.5

Table 4.1: Fitted parameter sets and resulting F-AC leakage rates $\overline{\eta}_F$ for the upright FM1 muon run. The histogram bins used for fitting are weighted according to POISSONian statistics. Error bars for $\overline{\eta}_F$ have approximated by bootstrap MC [*Press et al.*, 1988, 1992] and are 1σ statistical errors.

4.7.3 Sum of F channels

If both F channels are enabled and evaluated independently, the neutral particle rate will be reduced by neutral particles falsely detected as charged particles to $\frac{1}{4}$, as application of each of the terms

$$(F1 < 0) \wedge (F2 < 0) \tag{4.20}$$

will cut the neutral particle rate in half (still under the assumption that C and D are perfect ACs). The rejection can also be done on a (possibly weighted) sum of F1 and F2 instead

$$(a \cdot F1 + (1 - a) \cdot F2) < 0, \tag{4.21}$$

and only half of the neutral particles will be lost. This may also introduce additional charged particle leakage. Due to the different gains on the F channel fitting a model like above on the sum signal is more difficult. A safe overestimation of the resulting leakage rate $\overline{\eta}_F$ can be made by simply calculating the sum of the given values of $\overline{\eta}_F$ for F1 and F2, though. Fig. 4.6 illustrates the concept. F1 and F2 are designed to have the same gain scaling. This is used to justify setting $a = 0.5$ for the time being when using the $F1 + F2$ signal for AC rejection. A more thorough investigation may give a better value for a.

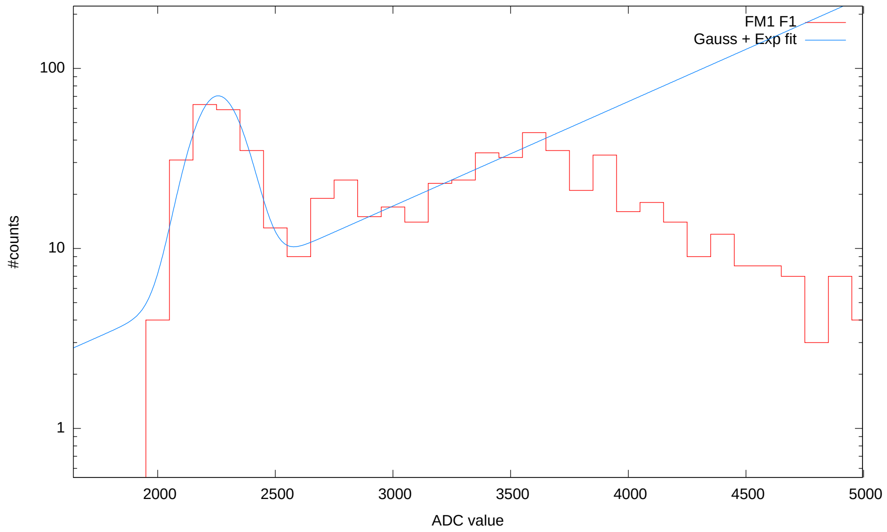

Figure 4.5: Response of the F1 channel for particles in D in a mostly cosmic muon field. Statistics in each bin is increased by rebinning into bins of 100 ADC values each.

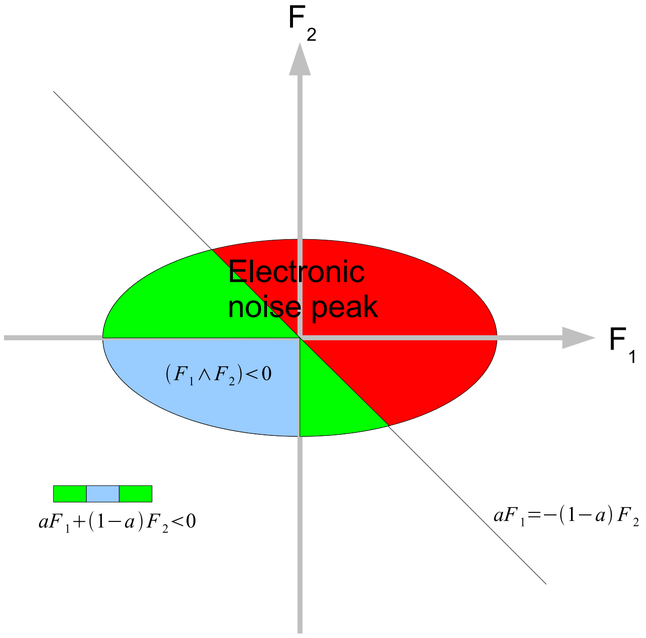

Figure 4.6: F channel AC selection scheme for $aF_1 + (1-a)F_2 < 0$ resp. $F_1 < 0 \wedge F_2 < 0$. The false negative rate for $aF_1 + (1-a)F_2 < 0$ can be safely overestimated with $\overline{\eta}_F \leq \overline{\eta}_{F_1} + \overline{\eta}_{F_2}$, as all false negatives still have to fulfill $(F_1 < 0) \vee (F_2 < 0)$.

Neutral channel	**AC channel**	$\|C\|$	$\overline{\eta}$ [%]
E	F1	7971	0.4 ± 0.2
E	F2(r)	7971	0.6 ± 0.3
D	F1	3567	1.3 ± 0.4

Table 4.2: Final AC false negative rates from exp-fits. Here, $\|C\|$ gives, as defined, the total number of charged particles in the respective channel for charged particles without any additional AC. Statistical error bars are approx. $1\sigma, \lambda = 0.5$.

4.7.4 Final anti-coincidence false negative rates

It should be noted that these final figures have been arrived at by dividing by the number of AC rejected counts, including the events hitting C and C2. Assuming the efficiency of the AC is only affected by $\overline{\eta}_F$, a much better total AC rejection figure can be stated. Tab. 4.2 lists the false positive rates for the AC from the exponential extrapolation. The given error bars are simply scaled variants of the statistical error bars from Tab. 4.1, and the slight additional error due to statistics in the total count is neglected. The values are in a range comparable to those given in *Burmeister* [2006].

Chapter 5

Anti-coincidence optical parameter estimation

The opportunity of a collimated high-energy beam run at the NIRS/HIMAC facility (see *Takada et al.* [2000]) is used to check the behaviour of the AC for energy losses constrained to different paths through its volume. From the gathered data, the ratio of light in the F1- to that in the F2-channel can be measured. The results can be compared to simulations with different parameter sets and acceptable parameter sets are found for the optical simulation of the AC.

5.1 Setup

The FM1 instrument with the CalRAD REB is used for all measurements. A square-shaped collimator with an edge length of 5 mm (length approx 20 cm, half brass, half High Density Polyethylene (HDPE)) is inserted upstream to constrain the energy loss volume to a comparatively small part in the AC. Two sets of measurements are done, one shooting at different positions into the entrance window (`top` run) of the RSH and one shooting at an angle of 90° to the instrument's normal (`side` run). The `top` run is done using a 160 MeV proton beam whereas the `side` run is made using $180\,\mathrm{MeV\,nuc}^{-1}$ helium nuclei. Some top runs with helium exist, but they are not further analyzed in this context. The helium is used to get a large signal in the AC which is well above noise and still well below saturation and thus further analysis of the shape of the energy loss distribution is possible (though details of this have not been further investigated yet). The proton run is selected as the available helium beam is of too low energy to fully penetrate the instrument, and, more importantly, reach the bottom F-AC scintillator. The set of directions and positions for which the AC is tested can be seen in App. B. The position numbers are given in the order they have been measured.

5.2 Ratio measurement

Each position irradiated with the collimated beam is expected to give light output with only a small variation in the ratio F1/F2 of light seen in both AC detectors, as energy loss straggling will only affect the total amount of light being generated (the sum F1+F2(r)). As the change of this ratio with position depends on the optical parameters of the scintillator (see below), it allows to set constraints on the optical parameter set for the plastic scintillators.

As expected, for each run position, the variation in the energy loss between F1 and F2 is given by a line-shaped structure. Plots of the AC data for all run positions and the determined ratios are also given in detail in App. B, Figs. B.2 and B.3.

Positional inaccuracy is assumed to be quite large with a possible shift of about 5 mm in each direction. Angular inaccuracy is deemed to be insignificant in comparison and has been subsumed in the positional error. As it will turn out, positioning is an important factor in the accuracy of the measurement. The MC model needs to include energy loss along the path as the helium nuclei may stop in the instrument for some of the run positions.

5.3 Optical model of F

Very similar to the setup discussed in Sec. 3.4, the F scintillator is set up using its CAD geometry and the `fresnel` (2π) optical model. This includes all chamfered edges and the three cable ducts at the bottom of the top part of the F scintillator, which are used to route the signals from the D/E stack. The glued gap between the top and bottom part of the F scintillator gets no special treatment in the simulation and the effects of the partly separated glue in FM1 are not further considered in the simulation setup. Optical photons are assumed to freely cross the gap from the top to the bottom part and vice versa.

5.4 Model parameter estimation

To get insights on the optical parameter sets, a set of simulations with variation in the α parameter is done, while keeping $R = 1.0$. As the test of the D scintillator (see Sec. 3.4) is compatible with $R = 1.0$ and as the surface parameters between the plastic and the crystal scintillator are the same (same amount and type of wrapping material), variation in the parameter of α is considered to be the cause of any variation of the AC response here. It has to be noted, though, that at this stage of verification and due to the strong correlation between α and $\log R$ (see Sec. 3.9.1), these parameters still cannot be distinctly determined.

In the `GEANT4` simulation, unidirectional protons resp. helium nuclei are shot uniformly onto the collimator area, thus assuming a homogeneous input beam. The energy of the primary particles is adjusted to approximately account for energy losses in the upstream beam path at HIMAC and to account for the losses in the housing (details of it are not simulated as it is deemed to be insignificant) when the beam comes from the side. In the given simulation data, protons with 159.3 MeV to account for foil losses and helium with 179.3 MeV nuc^{-1} is used to account for the loss in about 1 mm of housing.

Except for the additional electronics noise model, the same chain of `GEANT4` and optical model as it has been used for the following, detailed discussion in Sec. 6 is used.

5.5 Results and conclusions

In Fig. 5.1, the main result from the HIMAC AC run is shown. The continuous line shows the natural logarithm of the measured HIMAC ratios for the different run positions, sorted by decreasing F1/F2 ratio. For the `side` run, this order coincides roughly with the positions going from top to the bottom of the AC.

The measured ratio may be affected by a difference in gain scales between the F1 and the F2 channel. No correction has been applied for such an effect and only ADC offsets are subtracted before calculating the ratio. As the natural logarithm of the F1/F2 ratio is plotted, any factor on the ratio in the plot is only a shift in vertical direction.

Additionally, a set of simulated F1/F2 ratios, each for an optical simulation with a variation in α is displayed. Shown are the results from an optical simulation with selected

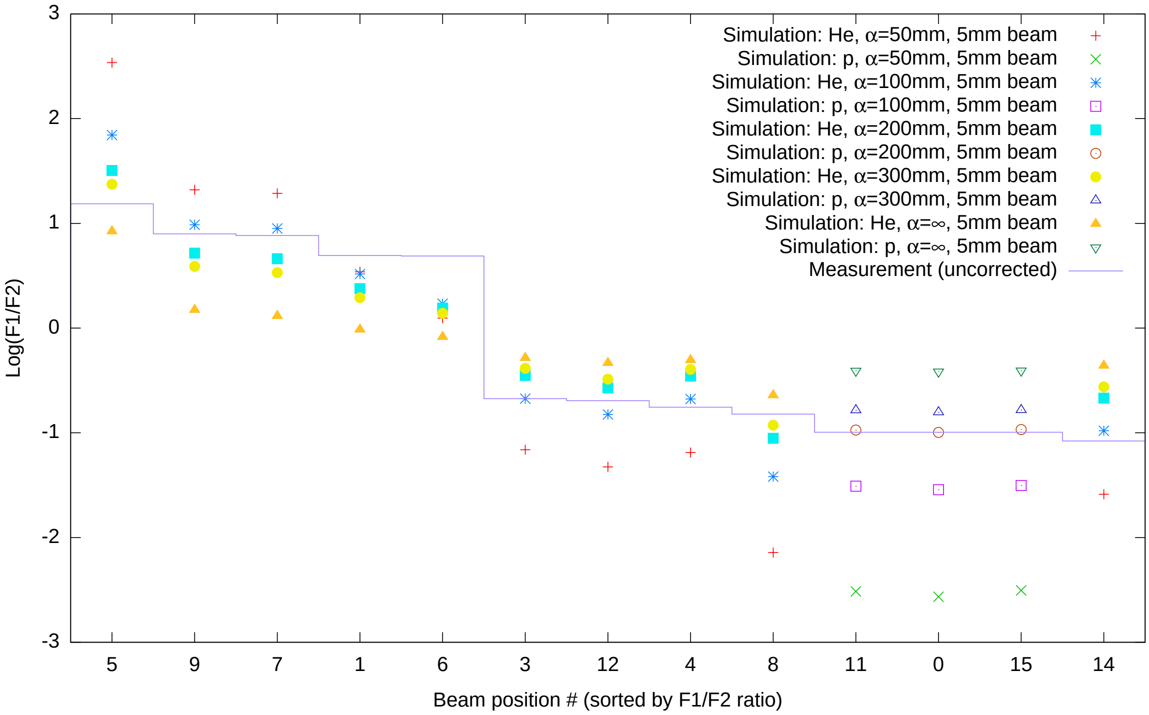

Figure 5.1: Measured F1/F2 ratios for the set of HIMAC runs and simulated F1/F2 ratios for the range of α parameters with comparable outcomes to the measurement. Simulation of energy loss distribution in the instrument has been done using the CAD-based `GEANT4` model. Possible quenching effects are not included and are not believed to cause larger changes in the results. The data is sorted by decreasing measured F1/F2 ratio. The x-axis denotes the run number/identifier.

$\alpha \in \{50\,\text{mm} \ldots 300\,\text{mm}\}$ and $\alpha = \infty$. As there are some outliers occurring in the simulation, the median value of the distribution of $\log(F1/F2)$ is taken in Fig. 5.1 (and Fig. 5.2) to represent the simulation results.

The model with $\alpha = 50\,\text{mm}$ can be discarded due to too high variation in F1/F2 ratio, and on the other side the model with $\alpha = \infty$ for too little variation in the ratio. The remaining three models with $\alpha \in \{100\,\text{mm} \ldots 300\,\text{mm}\}$ cover the variation of the measurement, without explaining it to full satisfaction. Without being able to derive a more definitive value for α from this measurements, $\alpha = 200\,\text{mm}$ can thus be selected.

One important contribution to measurement error in the setup is deemed to be positional accuracy. From the simulated data, the 3σ-width of the distribution of $\log(\text{F1/F2})$ has been calculated as an approximation of the expected error bars due to positional inaccuracies. The simulated beam size diameter has been varied[1] ($5\,\text{mm}, 7.5\,\text{mm}$ and $10\,\text{mm}$ edge length) to analyze the effects of having inaccurate positioning of the beam. The results of this can be seen in Fig. 5.2. For the position 6 with a larger variation in error bar size, the simulated distributions of $\log(F1/F2)$ are exemplary shown for the different beam size diameters in Fig. 5.3.

There is not much change in position sensitivity between a 5 mm and a 10 mm collimator, but for some of the interesting positions which are deemed most easy to measure (6, 7) the error bar for the 5 mm setting consists mostly of the uncertainty in the particle's position

---

[1] A more detailed process which could have been used instead would be a random variation of the used $5\,\text{mm} \times 5\,\text{mm}$ beam in the simulation setup.

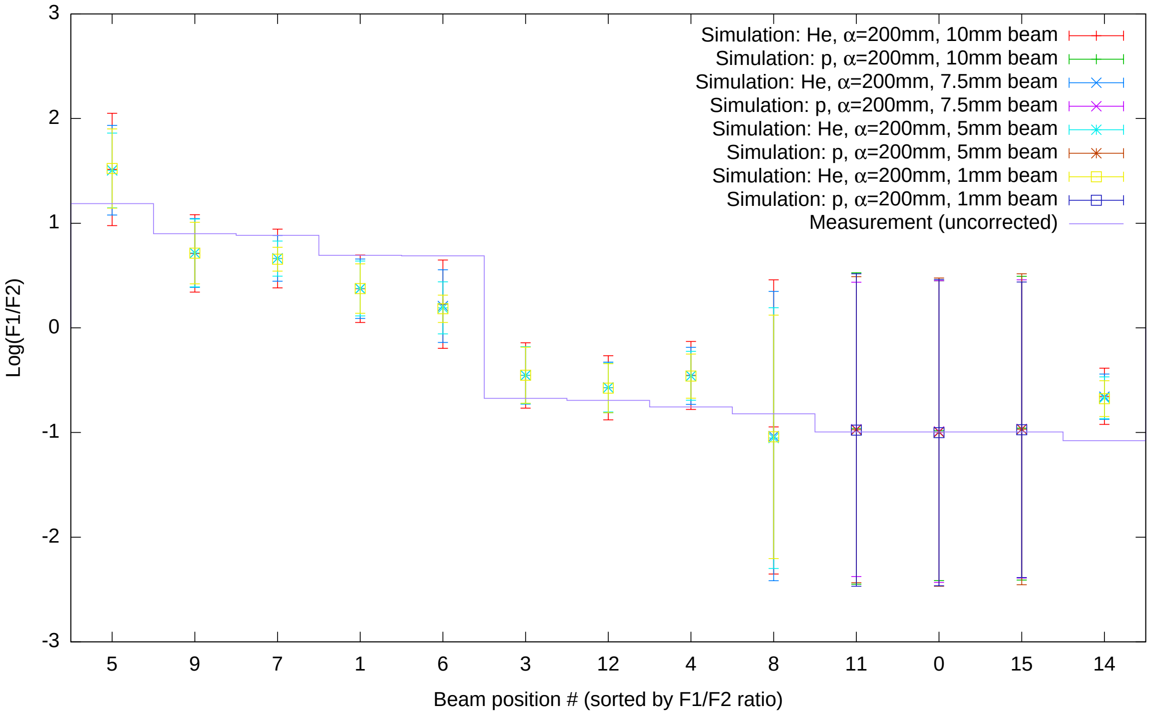

Figure 5.2: Measured F1/F2 ratios for the set of HIMAC runs and simulated F1/F2 ratios. Values of $\alpha = 200\,\text{mm}$ and $R = 1.0$ have been selected for the optical model. The error bars of the simulations are approximated by calculating the 3σ-width of the distribution of log(F1/F2) for varying beam size diameters, to simulate the effect of positional inaccuracy.

entering the instrument. No variation of the beam size diameter (collimator size) has been made in the experiment.

Thus the main result is that the model of a perfect scintillator without losses does not apply any longer to the comparatively large AC scintillator with its complex geometry. No single good point in the (α, R) parameter space could yet be found. Also the question whether the optical model is even good enough to support such an accurate measurement of α and R independently could not be settled yet and the error bars for the available (α, R) combinations still give a systematic difference between simulation and measurement. Nonetheless, with the available data, the above selected model with $\alpha = 200\,\text{mm}$, $R = 1.0$ supports the measurement best and is used for all further models of AC behaviour.

To be able to do more sophisticated checks on the AC model and the optical scintillator models in general, it would be necessary to do repeated measurements, similar to the above, with a sturdy mechanical setup. Such a setup exists and is awaiting a measurement using minimum ionizing halo muons at the CERN/CERF [*Mitaroff and Silari*, 2002] field. Additionally, the length scale of the changes seen in the model suggests that for the smaller scintillators, a better view on the scintillator readout could be achieved with a beam diameter in the range of mm than a range of cm. A bottom-up, direct measurement of all optical parameters and such a detailed comparison of measurement and model would allow a straight forward application of the results of the optical model.

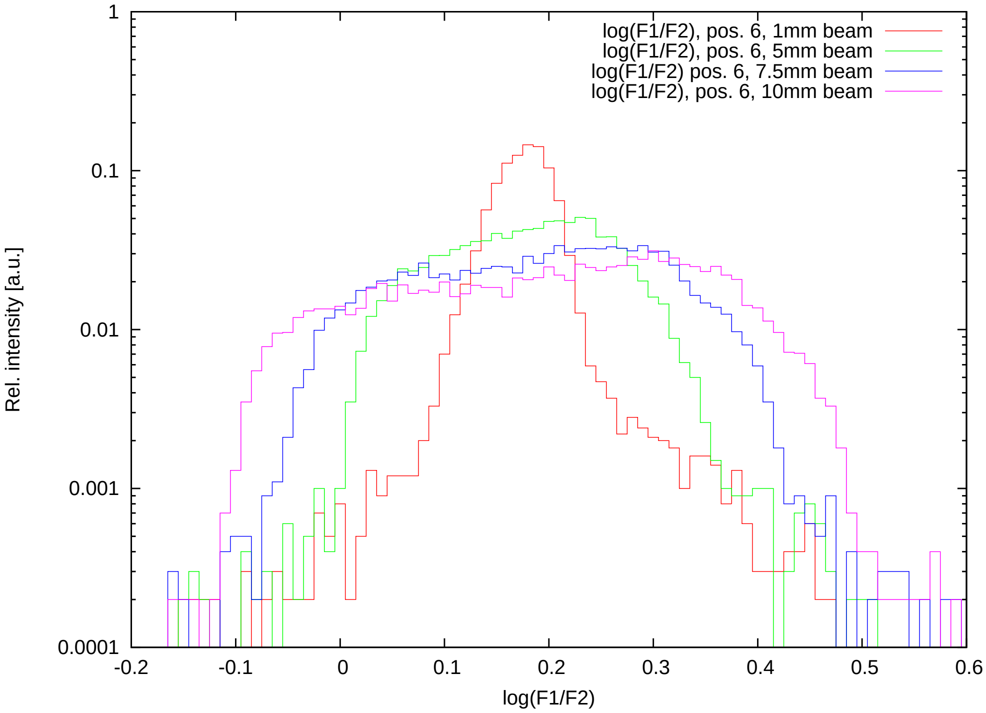

Figure 5.3: Simulated distribution of $\log(F1/F2)$, exemplarily for the run at position 6 which shows a large effect with changing beam diameter. Histograms for beam size diameters 1 mm . . . 10 mm are shown.

Chapter 6

Sequential model

Mainly to gather a set of further results on the AC behaviour and efficiency, the various models of parts of the MSL/RAD instrument behaviour are combined into a full sequence, covering both high-energy physics as well as the optical readout and energy resolution reduction due to electronics broadening. This combination will be referred to as the 'full model' throughout this section. Note that even though it is named 'full' here, some important effects, such as scintillator quenching as well as data reduction etc. are excluded from this model, to reduce complexity and as quenching effects are not of interest in the context of AC efficiency. Quenching is added to this model (except for a D parameter set) in the neutral particle discussion in Chapter 7. It is complete only in the sense that it covers the main aspect of the readout of the scintillators in RAD.

A preliminary study on geometrical effects of light generation and readout in the AC channels is performed and compared to this full model. Also, the model parameters are estimated based on single-channel histogram fits for selected muon data.

Finally, these parameters, together with Mars proton and neutron fluxes from an existing `PLANETOCOSMICS` simulation by B. Ehresmann (see App. D.1) are then used to derive a best guess estimate of the behaviour of RAD in the Martian environment. This extrapolation gives a second, more detailed estimate of the AC efficiency.

Model sequence. The full model consists of a chain of models, which roughly divides into the following three parts:

- The particle physics model
- For scintillators: The optical light propagation model (as described)
- The readout model, including electronics noise

6.1 Modified `GEANT4` model

The particle physics model is based on the `GEANT4` model that has been set up by E. Böhm and S. Böttcher [*Böhm*, 2006-2008; *Böhm and Kharytonov*, 2008] and is only a straight-forward extension/modification of it. This older model is implemented with a manual geometry description that differs from the detailed CAD model of RAD. Besides an overall transform of the frame of reference (which would be easy to account for), the shapes and sizes of the solids are slightly different and are missing some details. To account for this, the geometry in the old model has been replaced with the same solids (from CAD geometry) as they have been used for the optical scintillator models. The physics list is exactly the same as in *Böhm*

[2006-2008] and a few tests have been done to check for possible inconsistencies between the output for the new geometry and the old results.

In the MC, the silicon detectors are modeled as large hexagons encompassing the whole detector surface. The effects of segmentation and logical connection of the various detector segments is done in another post-processing step, which assigns energy losses to logical detectors, while taking the final mask of the chip vendor into account. A list of the differences to the old model is noted in App. D.3.

The output of this model are step-wise energy losses, annotated with a detector identifier and positional information. The position of the energy loss is stored in the output of the `GEANT4` stepping, in order to be able to have this as input for the following optical model.

6.2 Optical post-processing

In the case of a scintillation detector, the step-wise energy loss output from the `GEANT4` model is used to determine the amount of light on the readout diodes using the interpolated light distribution grid (as described in Section. 3.1). For each given point $\mathbf{x}$ inside a selected scintillator, the gridded and interpolated readout response $P_i(\mathbf{x})$ gives the fractional amount of light reaching a detector i (compare also Sec. 3.1). In this context, the light response of a readout diode ΔL_i for each stepwise energy loss ΔE is assumed to be

$$\Delta L_i = P_i(\mathbf{x}) \cdot \Delta E. \tag{6.1}$$

Energy loss is currently assumed to be occur point-wise *per step* (and light emission is isotropic, as usual) and no further integration or averaging along a single step is done. The output of the optical post processing are *per event* energy losses, broken down into losses per each detector as well as each readout diode, both the optical as well as the direct silicon hit contribution.

Descriptive plots of cuts of the expected performance, depending on position for light generation of the AC scintillator are presented in App. D.4.

6.3 Readout model

The combined output of the above two steps, the seen amount of light for each photo diode and the energy losses from the `GEANT4` MC have to be reduced to a single value in ADC units per electrical detector and event, to be compared to measurements. For example, for the E scintillator, the following set of values per event are given from the processing step before:

E The total energy loss in the E scintillator

E1...E3 The direct energy loss in the silicon of the readout diodes (silicon hits). As the model is not constrained by any gain scales, the naming H, M, L as used for the D scintillator in Sec. 3.4 is not used in the simulation setup.

oE1...oE3 The fractional amount of light times ηb (see Sec. 3.4.2), reaching each readout diode for the given interaction in the E scintillators.

The full set of output values from the combined `GEANT4` and optical model is described in App. C.1. In the case of the bottom AC where several readout segments are connected to individual scintillators, the simple, unweighted sum of all three segments is calculated before applying any other part of the readout models. Even though each individual CSA for each individual bottom F segment has a separate noise figure, this description should still be compatible to the noise part in the bottom F detector, as the same amount of electronic noise is seen, independent of the location of the particle hit or light collection.

A list of parameters $\mathbf{x} = (\hat{y}, c, \sigma_n, z, s, o(, m(, p)))$ deemed to describe the most important missing processes is selected. This set of parameters will scale the simulation into the proper ADC units and measurement counts so that it can be directly compared (and fitted) to measured data. So far, only comparisons on single channel spectra are done between model and measurement and therefore the set of parameters is applied in the context of calculating a histogram of a selected single channel of the simulation. The meaning of the particular parameters is:

$\hat{y}$ The y (rate)-scale of the model. One event in the simulation is equivalent to $\hat{y}$ measured counts after the data has been binned into ADC units.

c The silicon to light ratio. This value is used to weight the silicon part of the sum (e.g. E1) before adding it to the light signal (e.g. oE1) by calculating the total energy equivalent E seen in a single detector (such as EH, EM, EL), with a silicon energy X (such as E1) and an optical energy equivalent oX (such as oE1) as

$$E = \mathrm{oX} + c \cdot \mathrm{X} \tag{6.2}$$

to combine the output of the first two steps (`GEANT4` simulation and optical readout). This ratio is thus applied after light reduction due to $\alpha < \infty$ or $R < 1.0$ and thus gives the ratio between signal due to generated light per MeV and signal in silicon, *not* the ratio between the received light and the silicon signal. Using the definitions for the light loss parts from Sec. 3.4.2, the relationship between the w parameter for a full detector and c can be worked out.

The signal heights are

$$u_s = sc\mathrm{X} \quad \text{and} \quad u_o = s \cdot \mathrm{oX} \tag{6.3}$$

with corresponding energies

$$f\eta b \cdot E_o = \eta b \cdot \mathrm{oX} \quad \text{and} \quad E_s = X \tag{6.4}$$

and thus

$$w = \frac{u_s E_o}{u_o E_s} = \frac{sc \cdot \mathrm{X}\frac{\mathrm{oX}}{f}}{s \cdot \mathrm{oX} \cdot X} = \frac{c}{f}. \tag{6.5}$$

σ_n Electronic noise is modeled by convolving the resulting histogram with a Gaussian. As VIRENA reconstruction is not of interest here, the more detailed noise model (see Sec. A.2.1) does not need to be applied.

z Additional neutral particle hits in the trigger channel. Neither does the `GEANT4` MC model cover any random noise triggers nor is the always existing γ-background modeled. As γ-hits as well as random triggers in the selected trigger detector (selected cut) are expected to have no coincident signal in the channel being looked at, they can be modeled with additional hits having energy $E = 0$. The value z specifies the number of hits in the histogram bin covering $E = 0$, before scaling with $\hat{y}$ or any noise convolution is done.

s Energy scale in optical MeV per ADC. This value is used to finally scale the MC model from units of energy into the ADC values that are the result from the digitization. The electronics chain is assumed to be completely linear and no ADC nonlinearities or saturation are taken into account.

o Noise peak offset. This is the ADC value the energy for $E = 0$ is shifted to.

m Optional mixing parameter for a linear interpolation of two optical models.

As the parameters for the optical models have been selected *before* doing the computationally costly photon simulation of the scintillators, only discrete values for α and R and only values along the $R = 1.0$ and $\alpha = \infty$ line in (α, R)-space have been simulated so far. The data from the HIMAC run suggested a set of $\alpha \approx 200\,\mathrm{mm}, R = 1.0$. Values with $\alpha < 200\,\mathrm{mm}$ are taken to check whether additional noise can be explained through light losses. To have a more complete check of parameters, it is further tested whether an interpolation between different optical models can be done. For those interpolated models, the light response $L_i(1)$ for a parameter set (α_1, R_1) and the light response $L_i(2)$ for a second parameter set (α_2, R_2) is combined in the following way to form the total light response L_i:

$$L_i := mL_i(1) + (1 - m) \cdot L_i(2) \tag{6.6}$$

with $m \in [0, 1]$ selecting between the influence of the two models (1) and (2).

p Optional shot noise parameter, given in units of $\sqrt{\mathrm{MeV}}$. To check whether shot noise of the produced charge carriers can explain parts of the broadening seen in the measured data, the broadening $\sim \sqrt{E}$ is introduced by distributing a bin for a given energy E into the set of bins covering a Gaussian with width $\sigma = p\sqrt{E}$. It is important to note that this assumes that the shape of the Poisson distribution of charge carriers can be approximated as Gaussian for each given energy. Assuming that $N(E)$ charge carriers are received for a given energy E,

$$\frac{1}{p^2} = \frac{N(E)}{E}. \tag{6.7}$$

Thus, to summarize the above parameter descriptions, for a given event with seen light fraction E_o in the attached PIN diode and E_s in the diode's silicon, the resulting ADC value A is finally calculated as

$$A = s \cdot (\mathrm{oX} + cX) + o. \tag{6.8}$$

The broadening due to non-zero values of p and σ is assumed to be a single Gaussian with total width σ_t of

$$\sigma_t = \sqrt{\left(p\sqrt{E}\right)^2 + \sigma_n^2}. \tag{6.9}$$

When deriving single channel spectra, the broadening is not done through MC but rather through spreading with a discrete Gaussian of appropriate shape for each energy bin, in the very last step of the model, with both the unbroadened energy deposit and the noise scaled into ADC units. The values in Eq. 6.8 are binned into ADC values in a histogram. This histogram, scaled by $\hat{y}$, is used to calculate a sum of normalized, discretized Gaussians with width as given in Eq. 6.9 in the final output histogram $S(\mathbf{x})$. In the case of no photon shot noise, this process boils down to a convolution of the histogram with a Gaussian of fixed width $s\sigma_t = s\sigma_n$ in ADC units.

Broadening using an additional MC step is easier to implement, but is dismissed as it affects the stability of the minimization method.

6.4 Model fit

In this context, the full model is implemented with the goal to derive a second and more detailed forecast on the AC behaviour for Martian conditions. To get parameters on the AC, the above readout model parameters are derived from the same FM1 upright muon run [#8, μ-FM1-fREB] as for the application of the simple AC model in Sec 4.6, which has been taken with flight-like electronics attached in final, flight-like conditions. Additionally, a quick look is taken at the behaviour of the other channels for the same measurement, as it is a natural byproduct of the measurement as well as having all parts of the instrument implemented in the `GEANT4` MC.

6.4.1 Data set

For simplicity, the above readout model parameters are derived from a best fit of the modeled single channel spectrum fitted to the FM1 muon data. The corresponding input to the `GEANT4` model are $\cos^2$ angular distributed, monoenergetic ($E = 4.5\,\mathrm{GeV}$) approx. minimum ionizing muons with isotropic position distribution.

To prepare the fit, an appropriate cut is selected for a given channel, to exclude neutral particles from the muon signal. It is assumed that no additional errors in the fitted parameters result from misalignments between the measurement and model cut. For this reason, visible edges (E channel) or a cut in the low count-rate region between noise peak and muon peak (in the case of the silicon channel) are selected. Still, there will be some random triggers as well as triggers due to neutral particles not modeled which will then be represented with the z parameter as described above.

6.4.2 Minimization function

A straight-forward χ^2-minimizing fit is used, with the assumption that the statistical errors in the MC model can be neglected and the only error in the measured data stems from the counting statistics with usual square-root error bars. The weighted difference between single channel projections of the data is minimized. The additional statistical errors are the POISSONian count distribution of the simulation and further the minor influence of POISSONian statistics onto the precalculated photon MC map of each scintillator. It is assumed that the counting statistics of the simulated data is sufficiently high so that its effects can be ignored.

For a model parameter set x, let M_i be the histogram of the measured data and $S_i(\mathbf{x})$ the simulated one, with bin size b and index $i \in \{0, \ldots \frac{16384}{b} - 1\}$.

The function

$$f(\mathbf{x}) := \sum_i \left(\frac{M_i - S_i}{E_i} \right)^2 \tag{6.10}$$

is then minimized, with weights E_i defined as

$$E_i := \max\left(1, \sqrt{M_i}\right). \tag{6.11}$$

To avoid bins with very low counts which would invalidate the assumption that a χ^2-minimization is approximately right, both model and data will always be rebinned before the model is fitted. The bin size varies and will be specified for each particular fit. The binning that is used for the various fits is given in App. C, Tab. C.1, and the full model is consequently binned with the same bin size for the fit.

6.4.3 Fit error estimates

Fit error estimation is done with a simple MC method. The input spectrum is resampled (bootstrap method as described in *Press et al.* [1988, 1992]) and the start parameter values are selected from continuous uniform distributions centered around the respective best fit values which are based on assumptions for valid ranges of the parameters. This additional second step is done to guard against the possibility of always staying in a local minimum. The full width of this uniform distribution, depending on the parameter, can be seen in App. C, Tab. C.3. A set of ten MC estimates is done for each of the fits in Tab. 6.1 to get a first and broad view on the size of the error bars. In this table, fits that fail the criterion $\chi^2 < 3\chi^2_{\text{best}}$ have been removed before calculating the error bars, as instability is seen with the applied fit method. Random checks on the fits outside that range have been made. For those, it is concluded that (except for the c parameter, where data is missing in the E and F2 case) the misfits can not be another plausible explanation of the data.

For the selected best fits (marked in bold), a more detailed analysis is done, with 1 k MC runs. Histograms of the χ^2-value for each channel are shown in App. C, Fig. C.1. It can be clearly seen that there a several outliers/failed minimizations existing for each channel. For the calculation of the stated final error bars, these outliers are removed by applying a different manually selected cut on the χ^2 at the positions marked by the black vertical bars and measuring the standard deviation of each fit parameter. In consequence of the estimation method for the error bars, they do not include systematic devations between model and data.

6.5 Results

In Tab. 6.1, the results of doing the numeric fits for the C, D, E, F1, F2 channels, with varying sets of parameters as well as different selected trigger channels and for different values of α are shown. Additionally, the mixed model for two adjacent values of α (resp. a mix of the $\alpha = 200\,\text{mm}$ and $\alpha = \infty$) is fitted and is also shown in the table.

As VIRENA noise figures are not further analyzed here, only a single part of each redundant channel pair is selected and further analyzed. Also, due to symmetry of the input particle field and the instrument, for the D and E scintillator, only a single representative channel (DN resp. EU) is looked at.

The different background colours denote the scintillator or detector for which the fits are done, from top-to-bottom: CU, DN, EU, F1, F2(r).

The leftmost column shows the number of particles N simulated in the MC that is being fitted to the data. As a compromise between remaining statistical errors and computation time, the `GEANT4` runs are done using $N = 10^7$. For all scintillators, a smaller selection of $N = 10^6$ is used, to reduce the computational cost of the additional step of collecting the optical response data. For the silicon channel C, no such calculation is necessary and therefore the full $N = 10^7$ set is used. The next column `rdchisq` shows the reduced χ^2-value for the corresponding model. The next eight columns describe the best fit parameter set, with the meaning of the parameters as given above. Right of the thin vertical bar, the described, very rough MC error estimates are given in the same order. As only ten MC runs are used and as the $3\chi^2$-criterion does not exclude all misfits, these error bars should not be trusted too much and they will at most give a hint at the order of magnitude of the error. Values are marked in red if their value is deemed to be either out of range or the fit is not well supported by the data set that is used. The rightmost column shows the identifier that is used for the particular fit run. If (and only if) the identifier contains `_no_p`, the fit is done without the p parameter for photon shot noise.

N	rdchisq	$\hat{y}$	c	σ	z	s	o	m	p	$E_{\hat{y}}$	E_c	E_σ	E_z	E_s	E_o	E_m	E_p	Coincidence and model setting
		Meas/Sim Evs.	Opt/Si MeV	MeV	Sim Evs.	ADC/MeV	ADC		$\sqrt{MeV}$	Meas/Sim Evs.	Opt/Si MeV	MeV	Sim Evs.	ADC/MeV	ADC		$\sqrt{MeV}$	
10^7	1.21	0.013		0.0017	30878	4522.8	1749		0.03	0.004	0.001	0.00044	11478	3955.25	56.14		0.064	cosmic-muons-CU-coinc-BU
10^7	**1.28**	**0.012**		**0.0021**	**31612**	**4502.3**	**1748**			**0.001**	**0.000**	**0.00300**	**13834**	**344.86**	**32.01**			**cosmic-muons-CU-coinc-BU_no_p**
10^6	1.5	0.108	0.33	0.07	2259	62.0	1521		0.09	0.005	1.210	0.03	229	39.02	57.88		0.06	cosmic-muons-DN-coinc-CUBU_alpha50
10^6	1.14	0.108	0.22	0.12	2246	35.0	1521		0.07	0.008	0.535	0.04	98	6.14	28.6		0	cosmic-muons-DN-coinc-CUBU_alpha100
10^6	1.06	0.108	0.21	0.17	2229	23.6	1521		0.13	0.053	0.749	0.12	839	52.52	238.49		0.39	cosmic-muons-DN-coinc-CUBU_alpha200
10^6	1.07	0.108	0.37	0.30	2194	13.1	1520		0.25	0.015	1.384	0.19	451	4.62	28.64		0.09	cosmic-muons-DN-coinc-CUBU_alpha_1e+30
10^6	1.45	0.108	0.25	0.07	2167	57.0	1519	0.93	0.07									cosmic-muons-DN-coinc-CUBU_alpha_50_200
10^6	1.15	0.108	0.23	0.12	2235	35.0	1521	1.00	0.07									cosmic-muons-DN-coinc-CUBU_alpha_100_200
10^6	1.08	0.108	0.21	0.17	2256	23.6	1521	1.00	0.12									cosmic-muons-DN-coinc-CUBU_alpha_200_1e+30
10^6	1.44	0.108	0.21	0.07	2241	62.1	1521			0.006	0.732	0.03	308	3.78	25.66			cosmic-muons-DN-coinc-CUBU_no_p_alpha50
10^6	1.13	0.108	0.23	0.12	2234	35.0	1521			0.009	0.852	0.02	145	0.83	53.06			cosmic-muons-DN-coinc-CUBU_no_p_alpha100
10^6	**1.09**	**0.107**	**0.21**	**0.18**	**2264**	**23.5**	**1521**			**0.019**	**0.475**	**0.04**	**458**	**5.15**	**55.56**			**cosmic-muons-DN-coinc-CUBU_no_p_alpha200**
10^6	**1.18**	**0.106**	**0.22**	**0.33**	**2268**	**13.2**	**1519**			**0.034**	**0.268**	**0.62**	**4071**	**4.47**	**58.91**			**cosmic-muons-DN-coinc-CUBU_no_p_alpha_1e+30**
10^6	1.45	0.108	0.23	0.07	2252	61.1	1520	0.98										cosmic-muons-DN-coinc-CUBU_no_p_alpha_50_200
10^6	1.14	0.108	0.23	0.12	2234	35.0	1521	1.00										cosmic-muons-DN-coinc-CUBU_no_p_alpha_100_200
10^6	1.1	0.107	0.21	0.18	2265	23.5	1521	1.00										cosmic-muons-DN-coinc-CUBU_no_p_alpha_200_1e+30
10^6	4.3	0.110	9.64	0.03	31731	2843.1	1968		0.02	0.002	31.509	0.002	1172	28.38	11.22		0.009	cosmic-muons-EU-coinc-DU_alpha50
10^6	2.85	0.105	11.57	0.05	34233	1557.6	1968		0.05	0.004	3.489	0.007	4327	37.85	23.92		0.026	cosmic-muons-EU-coinc-DU_alpha100
10^6	2.6	0.104	8.94	0.07	34608	1066.0	1960		0.10	0.005	11.638	0.013	2562	60.59	24.17		0.089	cosmic-muons-EU-coinc-DU_alpha200
10^6	2.62	0.102	8.08	0.13	35032	600.7	1947		0.18	0.002	4.051	0.008	2727	10.93	13.19		0.041	cosmic-muons-EU-coinc-DU_alpha_1e+30
10^6	2.83	0.104	8.36	0.06	33939	1291.8	1947	0.27	0.02	0.005	9.471	0.010	6722	294.47	12.74	0.25	0.017	cosmic-muons-EU-coinc-DU_alpha_50_200
10^6	2.88	0.105	12.08	0.05	34401	1532.8	1968	0.97	0.05	0.018	45.228	0.018	6165	2047.06	23.87	5.66	0.034	cosmic-muons-EU-coinc-DU_alpha_100_200
10^6	2.63	0.104	9.40	0.07	34575	1066.2	1959	1.00	0.10	0.037	18.810	0.042	82761	1625.28	18.71	15.24	0.092	cosmic-muons-EU-coinc-DU_alpha_200_1e+30
10^6	4.2	0.109	10.16	0.03	32432	2861.3	1968			0.002	15.923	0.001	1990	23.86	7.44			cosmic-muons-EU-coinc-DU_no_p_alpha50
10^6	2.9	0.105	7.44	0.05	34597	1557.6	1968			0.004	10.082	0.005	2968	31.01	16.74			cosmic-muons-EU-coinc-DU_no_p_alpha100
10^6	**2.75**	**0.104**	**7.81**	**0.07**	**34330**	**1089.5**	**1937**			**0.005**	**23.616**	**0.002**	**4168**	**23.17**	**12.24**			**cosmic-muons-EU-coinc-DU_no_p_alpha200**
10^6	3.31	0.101	7.60	0.13	35523	611.7	1936			0.002	14.889	0.008	2974	7.39	10.39			cosmic-muons-EU-coinc-DU_no_p_alpha_1e+30
10^6	3.08	0.107	5.59	0.05	33054	1673.7	1964	0.59		0.005	26.519	0.024	11507	515.18	197.03	0.49		cosmic-muons-EU-coinc-DU_no_p_alpha_50_200
10^6	2.94	0.105	7.70	0.05	34101	1548.5	1966	0.99		0.011	7.440	0.022	8024	2850.63	15.39	2.64		cosmic-muons-EU-coinc-DU_no_p_alpha_100_200
10^6	2.79	0.104	7.81	0.07	34430	1089.5	1937	1.00		0.016	20.329	0.032	21326	1843.74	281.53	33.47		cosmic-muons-EU-coinc-DU_no_p_alpha_200_1e+30
10^6	1.45	0.115	9.78	0.04	18386	2667.0	2296		0.08	0.009	13.209	0.004	1642	53.94	8.15		0.031	cosmic-muons-F1-coinc-DU_alpha50
10^6	1.11	0.114	17.57	0.07	20295	1582.8	2293		0.15	0.011	7.809	0.003	3196	31.75	16.97		0.037	cosmic-muons-F1-coinc-DU_alpha100
10^6	1.22	0.113	28.36	0.09	20343	1015.2	2264		0.23	0.004	33.745	0.007	1590	29.70	6.93		0.081	cosmic-muons-F1-coinc-DU_alpha200
10^6	1.27	0.110	81.47	0.29	23816	363.2	2296		0.44	0.011	22.849	0.029	4408	23.54	7.54		0.074	cosmic-muons-F1-coinc-DU_alpha_1e+30
10^6	1.2	0.115	13.38	0.05	19511	1991.9	2296	0.79	0.09	0.107	4.578	0.011	8478	150.36	7.38	0.98	0.020	cosmic-muons-F1-coinc-DU_alpha_50_200
10^6	1.14	0.114	15.57	0.06	20183	1752.6	2296	1.17	0.12									cosmic-muons-F1-coinc-DU_alpha_100_200
10^6	1.13	0.113	27.64	0.10	21381	1033.2	2280	1.01	0.22									cosmic-muons-F1-coinc-DU_alpha_200_1e+30
10^6	1.48	0.115	9.66	0.04	18628	2675.0	2296			0.004	4.190	0.001	1076	36.86	0.87			cosmic-muons-F1-coinc-DU_no_p_alpha50
10^6	1.38	0.114	16.90	0.06	19483	1630.3	2264			0.013	21.138	0.005	3695	77.98	11.61			cosmic-muons-F1-coinc-DU_no_p_alpha100
10^6	**1.87**	**0.111**	**27.71**	**0.10**	**21270**	**1027.3**	**2264**			**0.009**	**31.259**	**0.008**	**2006**	**33.04**	**17.34**			**cosmic-muons-F1-coinc-DU_no_p_alpha200**
10^6	2.46	0.101	78.98	0.33	27053	363.7	2296			0.009	196.595	0.010	3237	3.78	6			cosmic-muons-F1-coinc-DU_no_p_alpha_1e+30
10^6	1.3	0.114	12.89	0.05	19947	2062.6	2284	0.81		0.013	0.655	0.002	2822	866.33	873.87	0.05		cosmic-muons-F1-coinc-DU_no_p_alpha_50_200
10^6	1.31	0.114	15.74	0.06	19953	1735.5	2280	1.12		0.014	36.339	0.010	3286	359.97	19.32	0.22		cosmic-muons-F1-coinc-DU_no_p_alpha_100_200
10^6	1.24	0.114	16.17	0.06	19644	1688.9	2291	1.23										cosmic-muons-F1-coinc-DU_no_p_alpha_200_1e+30
10^6	2.83	0.105	7.24	0.04	10288	3250.9	2312		0.01	0.010	18.904	0.006	2916	97.23	22.03		0.008	cosmic-muons-F1-coinc-EU_alpha50
10^6	1.38	0.111	14.83	0.06	10210	1781.1	2296		0.06	0.006	6.042	0.002	79	61.76	0.01		0.034	cosmic-muons-F1-coinc-EU_alpha100
10^6	1.24	0.112	26.09	0.09	10958	1081.9	2280		0.17									cosmic-muons-F1-coinc-EU_alpha200
10^6	1.37	0.109	82.77	0.30	12647	362.3	2296		0.31	0.006	30.109	0.019	71	9.98	7.1		0.037	cosmic-muons-F1-coinc-EU_alpha_1e+30
10^6	1.43	0.111	14.12	0.06	10762	1841.1	2295	0.63	0.03									cosmic-muons-F1-coinc-EU_alpha_50_200
10^6	1.28	0.112	17.55	0.07	10623	1542.2	2293	0.77	0.10									cosmic-muons-F1-coinc-EU_alpha_100_200
10^6	1.24	0.112	26.93	0.10	11057	1051.6	2280	0.99	0.17									cosmic-muons-F1-coinc-EU_alpha_200_1e+30
10^6	2.82	0.105	7.16	0.04	10306	3253.0	2312			0.008	11.138	0.005	1316	144.32	6.37			cosmic-muons-F1-coinc-EU_no_p_alpha50
10^6	1.44	0.111	14.72	0.06	10458	1791.4	2290			0.009	54.860	0.013	1608	47.16	22.31			cosmic-muons-F1-coinc-EU_no_p_alpha100
10^6	**1.73**	**0.108**	**26.02**	**0.11**	**11561**	**1077.7**	**2280**			**0.003**	**58.271**	**0.011**	**1689**	**25.48**	**23.98**			**cosmic-muons-F1-coinc-EU_no_p_alpha200**
10^6	2.12	0.104	83.56	0.37	13446	357.7	2296			0.005	262.252	0.023	831	8.22	9.72			cosmic-muons-F1-coinc-EU_no_p_alpha_1e+30
10^6	1.46	0.111	14.51	0.06	9800	1817.4	2264	0.59		0.101	112.565	0.026	3545	857.03	23.92	1.75		cosmic-muons-F1-coinc-EU_no_p_alpha_50_200
10^6	1.49	0.111	15.01	0.07	10880	1761.1	2308	1.00		0.010	6.613	0.002	1988	141.81	0.04	0.12		cosmic-muons-F1-coinc-EU_no_p_alpha_100_200
10^6	1.54	0.114	19.80	0.08	10473	1375.2	2277	1.11										cosmic-muons-F1-coinc-EU_no_p_alpha_200_1e+30
10^6	1.33	0.107	6.70	0.02	32862	4847.2	1587		0.01	0.003	22.853	0.002	2875	100.95	23.39		0.012	cosmic-muons-F2r-coinc-DU_alpha50
10^6	1.49	0.107	11.83	0.04	31706	2386.6	1585		0.17	0.004	14.382	0.007	3901	68.94	21.45		0.070	cosmic-muons-F2r-coinc-DU_alpha100
10^6	1.6	0.108	19.56	0.07	30517	1330.4	1594		0.29	0.005	68.479	0.014	3975	39.71	19.7		0.058	cosmic-muons-F2r-coinc-DU_alpha200
10^6	1.56	0.106	35.58	0.31	31271	353.0	1616		0.58	0.006	27.676	0.099	6292	23.94	34.72		0.141	cosmic-muons-F2r-coinc-DU_alpha_1e+30
10^6	1.35	0.107	7.35	0.02	32640	4622.2	1612	0.99	0.07	0.051	0.298	0.004	1774	936.17	64.23	0.87	0.009	cosmic-muons-F2r-coinc-DU_alpha_50_200
10^6	1.35	0.108	9.77	0.03	31337	3140.9	1584	1.32	0.10	0.008	19.259	0.026	7859	868.21	13.84	0.85	0.213	cosmic-muons-F2r-coinc-DU_alpha_100_200
10^6	1.61	0.108	19.53	0.07	30409	1329.3	1595	1.00	0.29	0.130	3.828	0.005	6798	1371.93	122.91	0.98	1.039	cosmic-muons-F2r-coinc-DU_alpha_200_1e+30
10^6	1.32	0.107	6.69	0.02	32848	4843.7	1589			0.003	13.841	0.003	2530	150.82	37.36			cosmic-muons-F2r-coinc-DU_no_p_alpha50
10^6	2.47	0.099	10.39	0.05	39449	2428.5	1616			0.003	13.054	0.009	3268	97.33	39.71			cosmic-muons-F2r-coinc-DU_no_p_alpha100
10^6	**4.13**	**0.098**	**17.25**	**0.08**	**38834**	**1431.8**	**1584**			**0.002**	**24.916**	**0.008**	**2282**	**28.28**	**17.25**			**cosmic-muons-F2r-coinc-DU_no_p_alpha200**
10^6	4.34	0.095	26.25	0.30	40203	395.2	1584			0.002	52.936	0.041	2714	9.97	29.34			cosmic-muons-F2r-coinc-DU_no_p_alpha_1e+30
10^6	1.31	0.107	6.25	0.02	32474	5117.9	1591	1.02		0.078	8.133	0.129	157321	1789.17	290.99	17.73		cosmic-muons-F2r-coinc-DU_no_p_alpha_50_200
10^6	1.31	0.108	12.16	0.03	32092	3898.4	1584	1.51		0.017	31.104	0.018	4483	933.51	37.7	1.86		cosmic-muons-F2r-coinc-DU_no_p_alpha_100_200
10^6	1.28	0.106	11.23	0.04	33220	2548.2	1597	1.18										cosmic-muons-F2r-coinc-DU_no_p_alpha_200_1e+30
10^6	1.44	0.120	8.17	0.02	10152	4733.6	1573		0.01	0.002	24.420	0.005	396	143.00	33.62		0.006	cosmic-muons-F2r-coinc-EU_alpha50
10^6	1.43	0.117	8.87	0.04	10765	2465.5	1552		0.03	0.002	18.517	0.006	933	34.14	13.29		0.025	cosmic-muons-F2r-coinc-EU_alpha100
10^6	1.24	0.115	11.86	0.07	11583	1403.3	1584		0.13	0.002	10.763	0.010	579	43.51	28.83		0.031	cosmic-muons-F2r-coinc-EU_alpha200
10^6	1.4	0.114	37.49	0.26	12201	413.3	1589		0.19	0.002	38.745	0.016	545	7.13	14.37		0.047	cosmic-muons-F2r-coinc-EU_alpha_1e+30
10^6	1.41	0.119	8.80	0.03	10324	3855.6	1552	0.89	0.02	0.094	4.837	0.014	2753	2786.85	38	2.21	0.083	cosmic-muons-F2r-coinc-EU_alpha_50_200
10^6	1.13	0.116	6.68	0.04	10741	2131.4	1582	0.84	0.11	0.078	3.369	0.013	2308	1306.56	50.36	27.65	0.124	cosmic-muons-F2r-coinc-EU_alpha_100_200
10^6	1.26	0.114	11.59	0.08	11647	1293.2	1584	0.96	0.12	0.051	47.322	0.458	321702	630.81	426.88	32.07	2.158	cosmic-muons-F2r-coinc-EU_alpha_200_1e+30
10^6	1.43	0.120	7.95	0.02	10012	4785.5	1561			0.004	25.074	0.000	1080	68.47	9.64			cosmic-muons-F2r-coinc-EU_no_p_alpha50
10^6	1.52	0.116	8.28	0.04	10830	2453.6	1552			0.002	12.848	0.006	596	71.75	25.74			cosmic-muons-F2r-coinc-EU_no_p_alpha100
10^6	**1.61**	**0.114**	**11.88**	**0.08**	**12104**	**1402.7**	**1584**			**0.002**	**22.532**	**0.009**	**874**	**25.87**	**15.64**			**cosmic-muons-F2r-coinc-EU_no_p_alpha200**
10^6	1.57	0.113	37.81	0.28	12407	414.1	1584			0.001	115.897	0.018	696	5.16	15.44			cosmic-muons-F2r-coinc-EU_no_p_alpha_1e+30
10^6	1.44	0.120	8.75	0.02	9999	4639.2	1554	0.98		0.003	9.419	0.007	1766	1164.64	6.96	0.32		cosmic-muons-F2r-coinc-EU_no_p_alpha_50_200
10^6	1.62	0.115	8.79	0.05	11475	2411.2	1584	1.01		0.054	19.198	0.011	2251	545.47	60.4	2.43		cosmic-muons-F2r-coinc-EU_no_p_alpha_100_200
10^6	1.59	0.113	12.78	0.09	12254	1216.0	1584	0.94		0.064	51.247	0.045	3092	784.34	57.04	1.58		cosmic-muons-F2r-coinc-EU_no_p_alpha_200_1e+30

Table 6.1: Comprehensive table of the single channel fits. The models tried are varied in α, are fitted with and without photon shot noise and mixed models for two adjacent α simulations are tried. The error bars in this full view should not be relied upon, they are just given for order of magnitude.

Fields are left blank where a parameter value does not apply. Additionally, the error estimation for some runs is unstable and in consequence, no error values are given in those two columns. In this context, unstable means that none of the ten error MC fits fell into the $3\chi^2$-criterion.

6.5.1 Muon rate consistency check

The very first check can be made by comparing the rate estimate from the $\hat{y}$ values to the expected value for directed cosmic muons at sea level [*Grieder*, 2001], of about

$$R = 1.68 \times 10^{-2}\,\mathrm{s}^{-1}\,\mathrm{cm}^{-2} \approx 1\,\mathrm{min}^{-1}\,\mathrm{cm}^{2} \tag{6.12}$$

for muons with energies above 350 MeV.

In the MC, the disc the muons are positioned on (for details see Sec. 3.3.1) has a radius of $r = 83\,\mathrm{mm}$ (which is derived from the CAD model's bounding box). Given a value for for $\hat{y}$ and number of MC particles N, the rate can then be very roughly estimated from the fit values as

$$R_M \approx \frac{\hat{y}N}{T\pi r^2} \tag{6.13}$$

This ignores any effects of angular distribution and assumes that the $\cos^2$ angular distribution of muons is unidirectional, straight from zenith.

Further neglecting any dead time effects, the duration of the selected measurement is

$$T = 29\,900\,\mathrm{s} \tag{6.14}$$

For example, by taking the fitted value of $\hat{y}$ for the D channel, which is $\hat{y} = 0.107$, this gives

$$R_M \approx 1.7 \times 10^{-5}\,\mathrm{s}^{-1}\,\mathrm{mm}^{2} \approx 1.04\,\mathrm{min}^{-1}\,\mathrm{cm}^{2}. \tag{6.15}$$

Which agrees quite well with the literature value. Note that there is another determination of the GCR muon flux available in *Martin* [2008b].

6.5.2 Parameters m and p

The next result that can be generally deduced (including the CU channel) is that there is no value in doing an interpolated fit for a pair of two optical models with differing α-values. The reduced χ^2-values do not differ significantly from those of the fits using only a single channel optical model. The same can be said of the p photon shot noise parameter. Both the introduced p and the m parameter is thus dismissed and not discussed any further here.

6.5.3 Further consistency checks

A few of the model parameters, although fitted separately for independent channels, are expected to be identical. The selected optical model should be the same for all BC432M-based scintillators (but it may indeed be different for the D scintillator!). Given comparable trigger cuts for both model and data, the value $\hat{y}$ should be identical. In Tab. 6.1, it can be seen that the variation in $\hat{y}$ is $< 15\%$. The parameters o, s and σ are expected to have individual values per RSH and VIRENA channel but be common across different cuts for the same channel (F1/F2, DU/EU cut). In Tab. 6.1, the changes are $< 5\%$.

6.5.4 Check of α and gain scale s

The discussed HIMAC run suggests a value of $\alpha = 200\,\mathrm{mm}$ ($R = 1.0$). A further check on the validity of this value is done by doing fits for different values of α to the FREBFM1 muon run. A single value of α spanning the E as well as both F readouts has to be found.

From the fit parameters for the plastic scintillators, it can be seen that again the parameter set for $\alpha = 50\,\mathrm{mm}$ is clearly too small and that with one exception, a value of $\alpha = 200\,\mathrm{mm}$ matches well for the BC432M material.

The one exception can be seen in Tab. 6.1 for the fit of the data to the F2 run and a DU coincidence. No satisfactory explanation for this artifact has been found so far. It can be speculated that this is related to the separated glue in the F1 model, or an additional contribution of charged particles from the side. Further tests on Pathfinder and FM2 and investigation of a sideways muon run could shed further light on this issue.

One notable discrepancy in that case is the gain scale s between the F1 and F2 channel. Expected to be about the same for both (see App. B.2), the F1 scale is about 30% . . . 40% smaller than the F2 scale for the $\alpha = 200\,\mathrm{mm}$ model. This value gets larger for smaller values of α but goes down to about 10% for the $\alpha = \infty$ case. When keeping the assumption that the F1/F2 gains are the same, it suggests values of α that are larger than 200 mm. No further tests on this have been done as a good and reliable F1/F2 gain scale is needed to do this.

Interestingly, the same model with value of $\alpha = 200\,\mathrm{mm}, R = 1.0$ also matches the D scintillator response well. This has to be compared to the assumption in Sec. 3.4 of $\alpha = \infty, R = 1.0$ for the validation of the optical model and the light distribution between diodes for the D scintillator. When changing from a value of $\alpha = \infty$ to $\alpha = 200\,\mathrm{mm}$, the corresponding geometrical noise σs undergo a relative change of $< 20\%$ (see Sec. 3.9).

Finally, the optical model with values of $\alpha = 200$, $R = 1.0$ is selected to model all plastic scintillators (E, F). This selection is given by the rows marked in bold in Tab. 6.1.

6.6 Model selection

Exemplary plots of the selected best fits for the C, E and F channel can be seen in Figs. 6.1, 6.2 and 6.3, respectively. This set of fits is completed with the figures in Appendix C. The corresponding final parameter sets for the C silicon detector can simply be taken out of Tab.6.1, whereas for the plastic scintillators, a common parameter set is found (see below).

The gray band shown in each plot gives the 3σ error range for the fit under the assumption that it describes the data correctly. The fit parameter error bars are calculated as described in Sec. 6.4.3 and correspond to the model errors shown here.

6.7 Final parameter set

The parameter set of the selected models has to be further reduced by deriving a single value for those parameters which are expected to be physically identical. The C and D channel, included in the fit to check the overall correctness of the method, are therefore not further discussed here. For the D scintillator, the silicon-to-light ratio can be derived from the values shown in Sec. 3.4. The silicon-to-light ratio c is a constant that is only dependent on scintillator and photo diode type and should also be the same for all BC432M scintillators.

When looking at the response of the F2 and E scintillator (Figs. 6.2, C.3, C.4), no distinct silicon hit structure can be seen in the histogram. This fact reflects in the large error bars for the F2 values of c. A distinct peak arises for the silicon hits in the F1 channel and the two values of c are therefore averaged to give the final value of c, ignoring the c values of

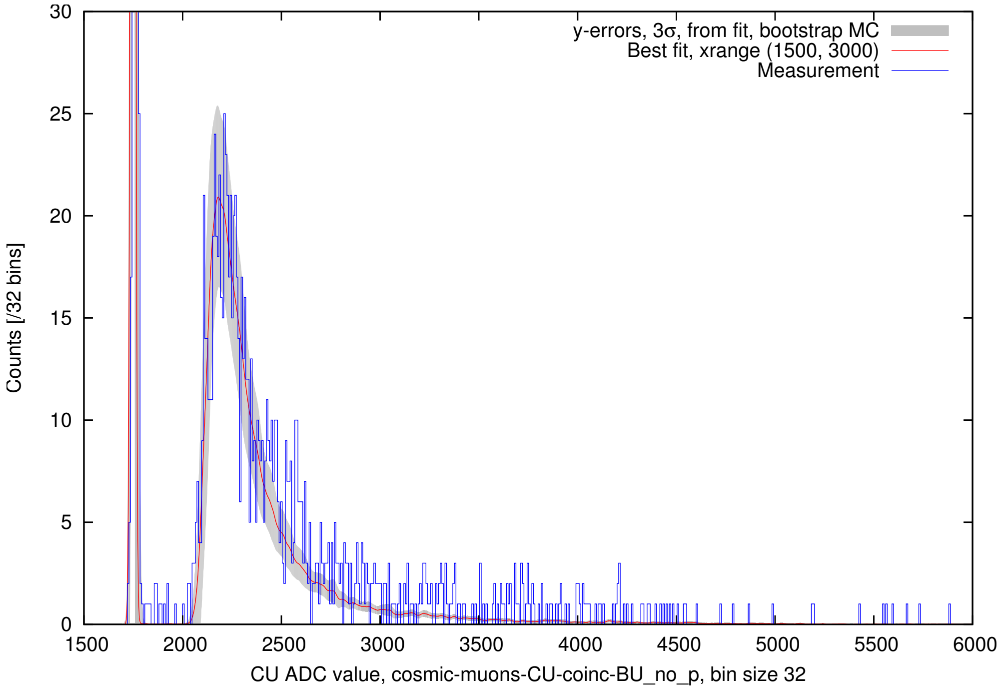

Figure 6.1: Selected best single-channel fit for **CU** channel to cosmic muon input data. Coincidence selected with BU channel. The noise peak can be seen at the left part of the spectrum, followed by the broad muon peak around ADC value 2200.

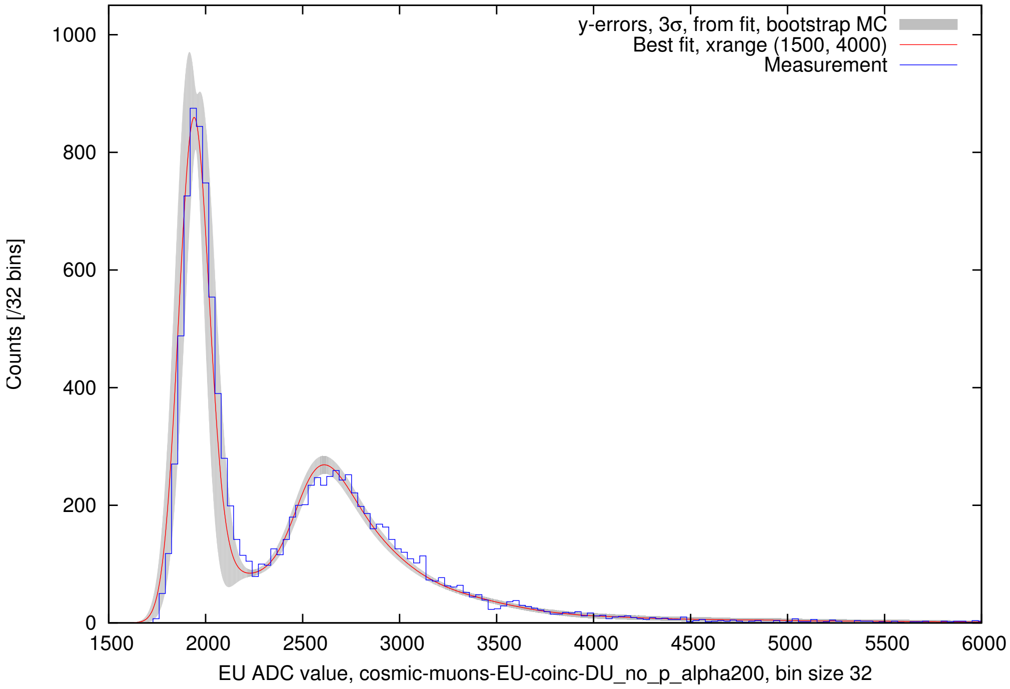

Figure 6.2: Selected best single-channel fit for **EU** channel to cosmic muon input data. Coincidence selected with DU channel. The noise peak and the muon peak in the scintillator (at ADC pos. approx. 2700) can be seen.

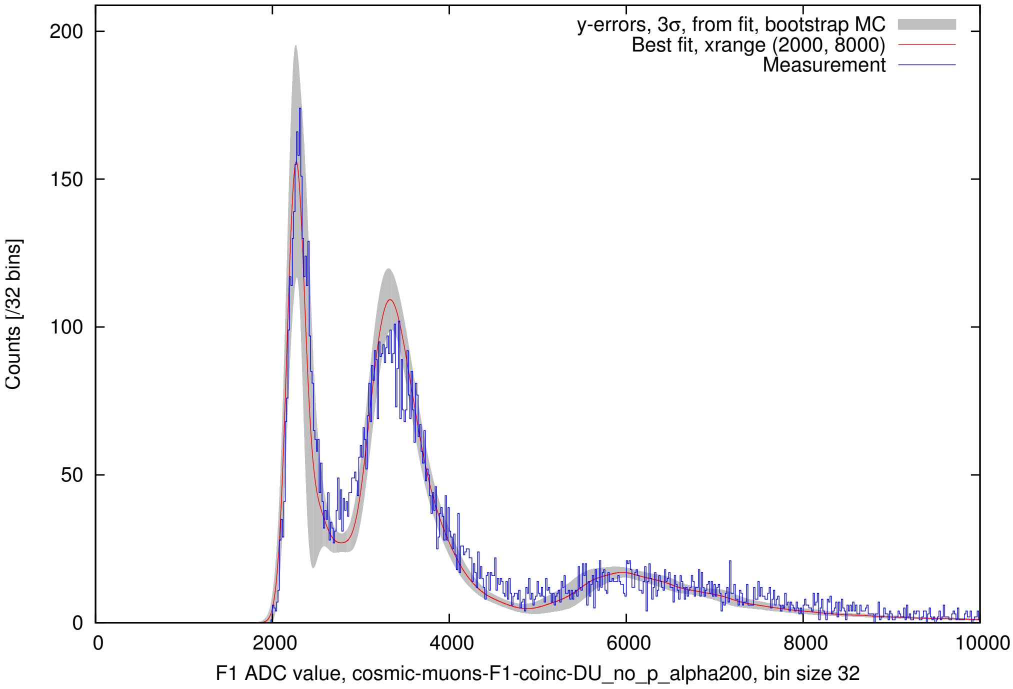

Figure 6.3: Selected best single-channel fit for **F1** channel to cosmic muon input data. Coincidence selected with DU channel. In addition to the noise peak and the muon peak in the scintillator, the silicon hits form a distinct peak around ADC position 6000.

$F2$ and E. For the remaining set of common fitted parameters, the simple average is also used to arrive at the final values. This set of final parameters used for further modeling and extrapolation of the FM1 plastic scintillator behaviour is given in Tab. 6.2.

6.7.1 Covariance matrix for error estimates

Non-zero correlation exists between the different parameter values that are given in Tab. 6.2. This correlation is contained in the 1 k MC fits done to estimate the statistical error bars of the fit function and thus the plots in Figs. 6.2, C.3, and C.4 properly account for this correlation. As the value of c has been selected from the F1 fit, no data exists that describes the covariance matrix entries depending on c for the EU and F2 channel. As the errors for the set of other important parameters σ_n, s, o are similar for all of EU, F1, F2, it is assumed that covariances regarding the c parameter can be taken simply from the F1 fit results. The parameters σ_n, s and o are otherwise assumed to be uncorrelated across different channels. The MC-estimated parameter variation can thus no longer be used for error estimates of further calculations and analyses of the simulation. Instead, the parameter values are varied (again via MC) with a multivariate GAUSSian to estimate further errors. The Σ-matrix of the multivariate GAUSSian is selected to be the covariance matrix combined in the described way. Again, it should be noted that this error propagation alone does not cover the existing systematic deviations. The numerical values of the matrix are given in App. C, Tab. C.2. As this is solely a forward calculation, all noise influences are calculated by applying MC noise to the modeled `GEANT4` data.

Channel	**Parameter**	**Value**	**Error**	**Notes**
-	$c(D)$	15.9 Opt/Si MeV	1.5 Opt/Si MeV	see Sec. 3.5
DN	σ_n	329 keV	97 keV	
DN	s	13.2 ADC MeV^{-1}	0.4 ADC MeV^{-1}	
DN	o	1519 ADC	1.3 ADC	
DU	σ_n	40 keV	–	by scaling DU/DN muons, PTB
DU	s	13.2 ADC MeV^{-1}	–	— ¨ —
DU	o	1759 ADC	–	simple noise peak fit
-	$c(E/F)$	26.9 Opt/Si MeV	1.3 Opt/Si MeV	from F1 fit
EU	σ_n	72 keV	4 keV	
EU	s	1089 ADC MeV^{-1}	23 ADC MeV^{-1}	
EU	o	1937 ADC	14 ADC	
F1	σ_n	104 keV	11 keV	
F1	s	1052 ADC MeV^{-1}	37 ADC MeV^{-1}	
F1	o	2272 ADC	16 ADC	
F2	σ_n	82 keV	12 keV	
F2	s	1417 ADC MeV^{-1}	34 ADC MeV^{-1}	
F2	o	1584 ADC	27 ADC	

Table 6.2: Final set of parameters for the plastic scintillators in the full model, used to do MSL AC forecasts. Values for the D channel are also given for completeness and as they are used in Chapter 7. For the DU channel, they have been calculated by scaling with the gain differences DU/DN and DN/DL from a muon and the PTB run (different VIRENA gain scales have been used). To compare the noise widths with those for FM2 in Tab. 3.3 in Sec. 3.5, scale by 3 (diode surface factor). Error bars are 1σ, statistical errors only.

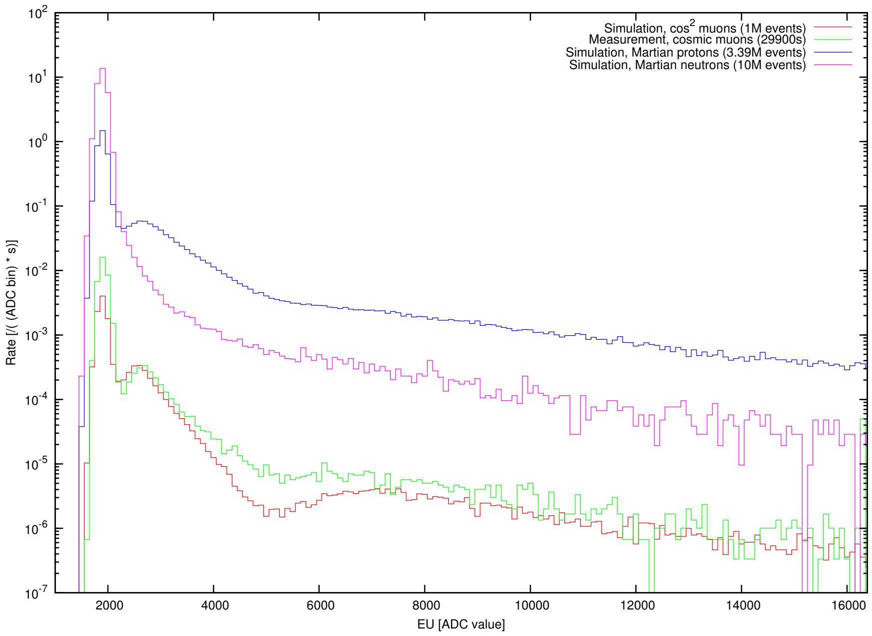

Figure 6.4: Simulated expected response of the *EU* diode for the Martian proton and neutron flux. The noise peak from triggers in other channels is visible to the left (at ADC pos. 1937). For reference, the cosmic muon response (measured and calculated) is also shown. No coincidence has been selected.

6.8 Martian Extrapolations

The main goal of this chapter is to give a more detailed estimate on the AC performance. To extend on the simple GAUSSian + exp fit done in Sec. 4.6, the selected parameter set can now be used to extrapolate the response of the instrument to Martian conditions using the input from B. Ehresmann, see App. D.1 for details. If not noted otherwise, the above parameter set is used for all further analysis in the context of the discussion of the full model.

In Fig. 6.4, the expected, simulated proton and neutron spectrum in the exemplary EU channel is shown when putting FM1/CalRAD on Mars. No additional trigger masks are applied. Also visible is the self-triggered readout from the cosmic muon measurement and the result of the model when assuming a rate of exactly $R = 1\,\text{cm}^{-2}\,\text{min}^{-1}$. Deviation between the $\cos^2$ simulation and measurement is visible for the untriggered EU channel, but this is expected due to the additional γ-background. Also, all shown noise peak heights depend on exact trigger settings and are therefore expected to vary by a large amount.

Completing this picture of protons and neutrons in the plastic scintillators on Mars is Fig. 6.5, which shows the expected response of the AC to Martian protons, given a trigger in D or E. Almost arbitrary (discretized) linear combinations of F1 and F2 can be formed onboard, but for simplicity, only the straight-forward sum is discussed further here.

It is of utmost importance that the shown neutron spectra do not include the effects from neutrons of the onboard RTG or any additional γ-background. Only the proton and neutron field as described in App. D.2 is considered here!

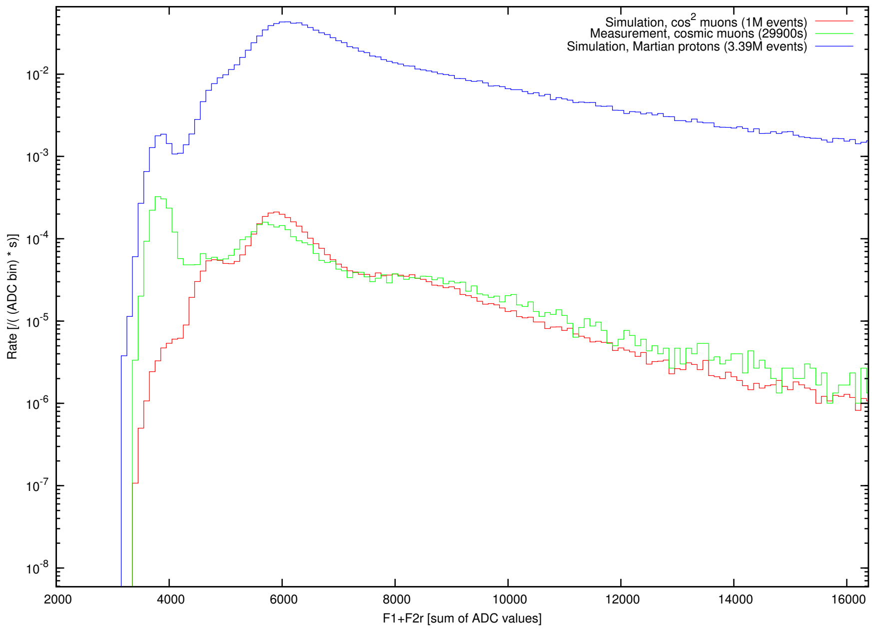

Figure 6.5: Simulated expected AC sum response (F1 + F2r) for proton events triggering D or E (any positive energy deposit). Note that for the measured data, the applied E-cut is closer to $E > 2.5 MeV$.

6.8.1 Anti-coincidence performance on Mars

As discussed in Sec. 4.4, the AC performance can be partially described using a leakage fraction $\bar{\eta}$. Given estimates for the neutron and proton fluxes, a simpler and more comprehensive value of the performance of the instrument is the ratio ρ of neutrons to protons seen in each the D and the E scintillator (signal-to-noise ratio). Done this way, it will also implicitly include effects of neutral particle suppression in the D or E channel due to recoils leaving the detector. As the total neutron flux is expected to be by a factor of about 10 higher than the proton flux in the energy ranges simulated (App. D.1), the value of $\hat{\rho}$ can be roughly calculated from ρ as

$$\hat{\rho} \approx \frac{\rho}{10}. \tag{6.16}$$

The AC detection threshold can be freely varied in the instrument, and thus it is helpful to look at the value of ρ depending on this threshold to see what can likely be achieved with the RAD instrument on Mars.

For a given AC trigger threshold (compare Sec. 4.6), the resulting values of ρ, for a trigger in the D and the E channel is plotted in Figs. 6.6, 6.7. To separate the effect of a change in ρ for different deposited energies, the energy seen in the D/E channel have been separated into three decadic energy ranges with a single curve each, for 1 MeV . . . 10 MeV, 10 MeV . . . 100 MeV and 100 MeV . . . 1 GeV. The selection is based on the energy deposit in the particular channel as given by the `GEANT4` output and the optical or readout effects are neglected for the cuts on the D and E channels. Their influence on the set of triggered events is deemed to be insignificant.

The line to the left of the plots mark the ADC value corresponding to $\Delta E = 0$ for F1+F2r ($\lambda = \frac{1}{2}$). The coloured areas denote the final error bars for the rate values. They are assumed to be a safe bet and are calculated by

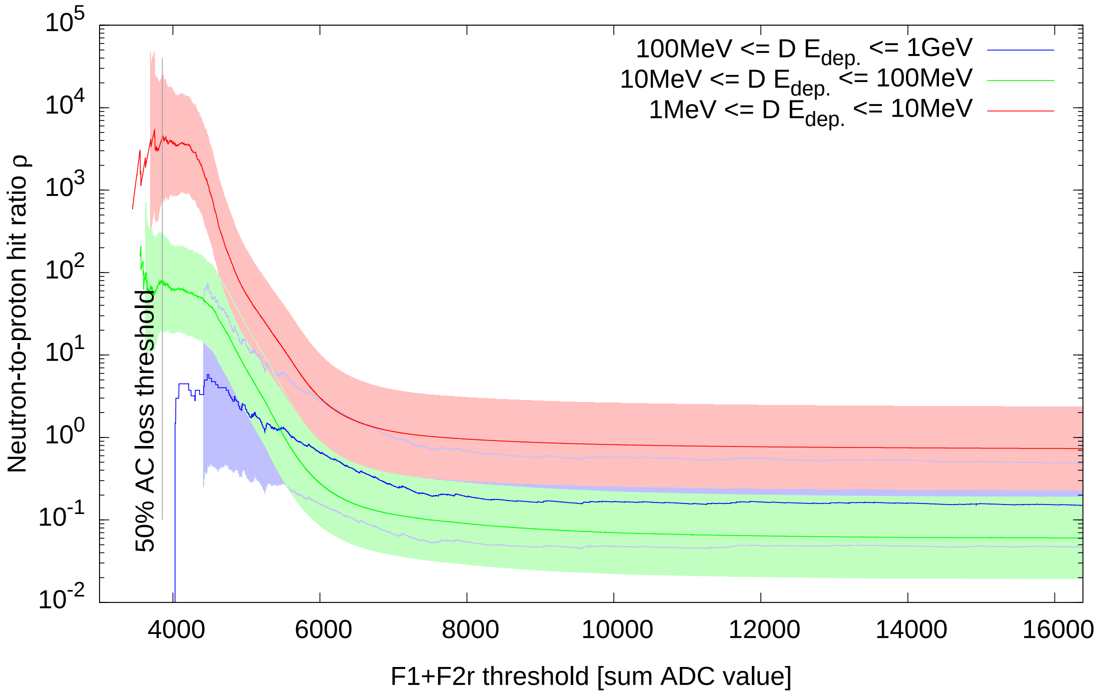

Figure 6.6: Simulated neutron-to-proton hit rate ratio for the D scintillator and variation of the AC threshold (sum AC). The marked areas show the error bars for the different energy ranges. The error bar has not been plotted if any of the MC error estimations failed to produce a meaningful ratio (low statistics).

1. Including 3σ of the statistical error calculation as described in Sec. 6.7.1
2. Additionally selecting a factor 2 due to possible systematic imbalances. The factor two has been selected, as it is the largest systematic deviation seen for a simulated spectrum when compared to a measurement (App. C, Fig. C.3).

The systematic error could possibly be reduced using a more detailed analysis of the deviations, for example by further investigating their dependency on selected energy ranges. This has not been done yet.

At last, it can be seen that the best separation is achievable on Mars in the range of 1 MeV . . . 10 MeV, which is unfortunately also the range in which a large amount of RTG neutrons are expected to enter the instrument. For the interesting range of 10 MeV . . . 100 MeV, good separation is expected to be possible, even assuming a worst case error. For the range $E > 100$ MeV, the neutrons will become very hard to distinguish from charged particles (due to escaping recoils).

6.9 Conclusions

The full model is set up and has been verified to explain muon data. The quality of the fits make it reasonable to use this model for further and other data analysis work. A major part of this work is done with the goal of giving an explanation of the workings of RAD's scintillators, with a special focus on the AC. To fulfill this goal and to give the needed hints on the AC configuration onboard the spacecraft, the value ρ as the most important factor

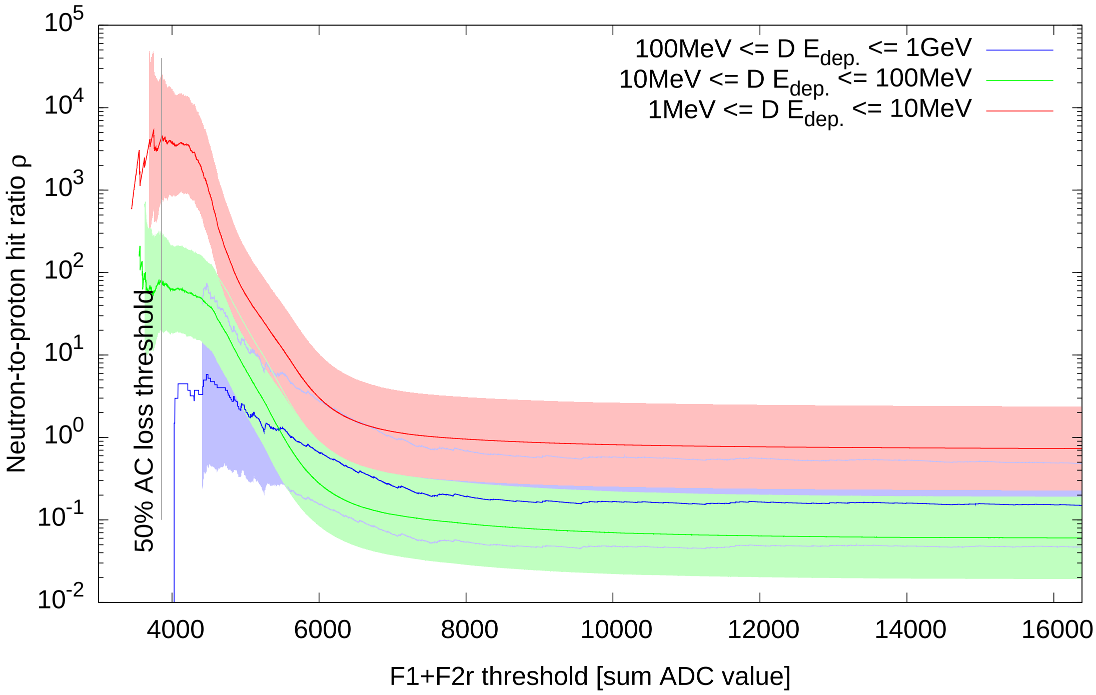

Figure 6.7: Simulated neutron-to-proton hit rate ratio for the E scintillator and variation of the AC threshold (sum AC), compare Fig. 6.6.

is forecasted to Martian conditions. The set of scintillator performance parameters that still need investigation is of considerable size. The full set of instruments (PF, FM1/2) needs to be cross checked for their AC performance, among other things to give hints on degradation and temperature effects, and to find out how much insights from possible further beam runs on FM1 can be applied to a remote FM2 RAD. A further discussion of this main result is given in Sec. 8.

Chapter 7

Neutral particles in RAD

In this section, a short overview of the neutral data taken with RAD so far is given. The main focus is on neutron data, as neutrons with a high Relative Biological Effectiveness (RBE) are very interesting in the context of dose rate estimation. The model that has been discussed in the last section is applied to the neutron data to see how much of RAD's neutron behaviour is understood and where a more thorough investigation is still necessary. It is now extended to include the effects of quenching in the E channel.

7.1 Neutral particles in the context of inversion

According to the *RAD Proposal* [2006], RAD's neutral detectors are designed to measure γ- and X-rays up to 1.5 MeV and to measure neutrons in the range 2 MeV ... 100 MeV. The task is roughly split such that γ-photons are detected in the high-z D scintillator crystal whereas neutrons will produce proton recoils in the hydrogen-rich plastic scintillator material of the E detector. Nonetheless, the D scintillator has a non-negligible response to neutrons and the E scintillator has an (albeit low) response to γ-photons.

For the analysis of flight data, inverse methods are therefore needed to be able to infer, from the energy loss spectra of the D and the E channel, the separate incoming neutron- and γ-spectra. Additional assumptions about the incoming particle fields have to be made, such as their intensity depending on azimuth and zenith angle. The inversion method relies on the fact that the energy loss spectra $r_{\mathrm{D}}(\mathbf{E})$ and $r_{\mathrm{E}}(\mathbf{E})$ in D resp. E for incoming energy $\mathbf{E}$ relate to the neutron $n(\mathbf{E})$ and γ-energy spectra $\gamma(\mathbf{E})$, by means of a linear map

$$L\left(n(\mathbf{E}), \gamma(\mathbf{E})\right) = \left(r_{\mathrm{D}}(\mathbf{E}), r_{\mathrm{E}}(\mathbf{E})\right). \tag{7.1}$$

A third term $r_{\mathrm{D,E}}(\mathbf{E}_{\mathrm{D}}, \mathbf{E}_{\mathrm{E}})$ may be additionally included on the right hand side, to describe combined D-and-E hits. The problem is discretized into energy bins[1] $\mathbf{E}_0, \ldots, \mathbf{E}_m$ such that the energy loss spectra result from the incoming particle spectra by multiplication with a matrix

$$M := \begin{pmatrix} \mathrm{D}-\mathrm{for}{-}n & \mathrm{D}-\mathrm{for}{-}\gamma \\ & \\ \mathrm{E}-\mathrm{for}{-}n & \mathrm{E}-\mathrm{for}{-}\gamma \end{pmatrix} \in \mathbb{R}^{(2m)\times(2m)} \tag{7.2}$$

---

[1] Additionally, there could possibly be different energy levels for each part of the equation, measured as well as reconstructed energy.

in the following schematic way:

$$M \bullet \begin{pmatrix} n(\mathbf{E}_0) \\ \vdots \\ n(\mathbf{E}_m) \\ \gamma(\mathbf{E}_0) \\ \vdots \\ \gamma(\mathbf{E}_m) \end{pmatrix} = \begin{pmatrix} r_D(\mathbf{E}_0) \\ \vdots \\ r_D(\mathbf{E}_m) \\ r_E(\mathbf{E}_0) \\ \vdots \\ r_E(\mathbf{E}_m) \end{pmatrix} \tag{7.3}$$

The left matrix can be found with a combination of comprehensive MC modeling of RAD and cross checks of those models with the neutral particle performance of MSL (which will be described below). It then needs to be inverted to solve for the desired

$$(n(\mathbf{E}_0), \ldots, n(\mathbf{E}_m), \gamma(\mathbf{E}_0), \ldots, \gamma(\mathbf{E}_m)) \,. \tag{7.4}$$

The size of the matrix M and the ill-posedness of the inversion due to partly similar behaviour of D and E makes finding a satisfactory matrix inverse difficult. The process is detailed in *Böhm et al.* [2007] and work is underway to build an inversion matrix for the problem of RAD neutrals [*Böhm and Kharytonov*, 2008]. This inverse estimation method for neutral rates is out of the scope of this work, but a calibrated MC model will form the input to the inversion process.

7.2 Gamma spectroscopy

Even though the light output of the CsI scintillator material is quite high with about 50 k photons/MeV [*de Haas et al.*, 2005] and the output optical spectrum approximately matches the sensitivity of photo diodes, doing the readout with diodes instead of a Photo Multiplier Tube (PMT) reduces the achievable resolution considerably. Early tests of the MSL CsI scintillator geometry in a separate laboratory setup independent of any sensor head indicated an achievable resolution of approx. 45 keV with a single attached diode [*Gooß*, 2006]. As it has been described in detail in Sec. 3.8, mainly due to the redundant readout of the D channel using different gain channels, this resolution could not be achieved in the final flight configuration and different photo peaks are hard to distinguish. An example test spectrum showing the signal of a ^{60}Co γ-source in the D scintillator for RAD RSH FM2 can be seen in Fig. 7.1. The direct sum reconstruction of the original light signal is deemed to be the best possible in this case. No distinct ^{60}Co γ-lines are discernible. The figure also shows the discretization of the DN/DL channel exemplarily for VIRENA gains $(g_H, g_M, g_L) = (8, 2, 2)$.

No exposure to high-energy γ-fields has yet been done with any RSH and it is also not part of the *RAD Proposal* [2006].

7.3 Neutrons

Neutrons are expected to have a significant contribution to the equivalent dose on the Martian surface, as they have been assigned a high RBE of 5 ... 20, depending on their energy. It has thus been deemed important for RAD to be able to measure the neutron rate on Mars. Additionally, at least a coarse energy resolution of the neutron spectra is needed to calculate the proper neutron dose quality factors. Neutron data acquisition is complicated by the fact that power will be supplied to the MSL rover by means of an RTG. The RTG is filled with a large amount of ^{238}Pu which produces the needed heat mainly through α-decay.

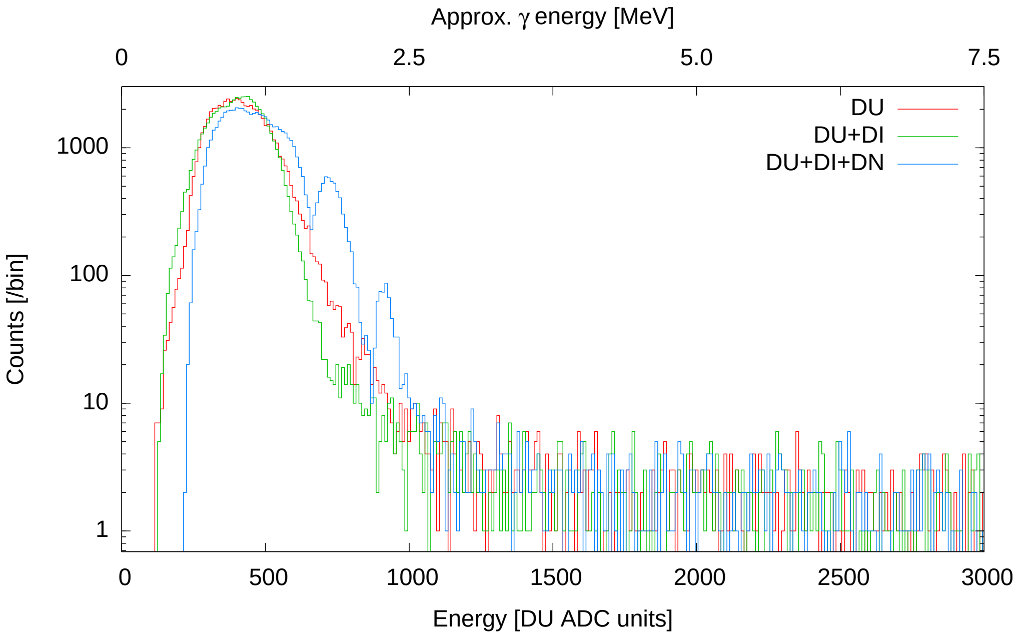

Figure 7.1: Measured energy loss spectrum in D (offset corrected sum signal DU+DI+DN) for a ^{60}Co source. Shown is the one, two and three-channel reconstruction. Note that what appears to be a photo peaks in the blue three-channel reconstruction curve are really *quantization effects in DN*. The VIRENA gain in the DN channel has been set to 2 and can be increased to a additional maximum factor of 8, which would make discretization features 4× smaller. Silicon hits have been removed by setting a cut of at most a 3.5 variation between any signal pair out of DN, DI or DU. The upper energy axis stems from a by-eye fit of the muon peak in D in FM2 and the scaling has been determined to be close to 400 DU ADC/MeV. Binning is done into bins of size 10 ADC units.

With a probability of 1.9×10^{-7}, decay half time of $t_{\frac{1}{2}} = 87.7\,\mathrm{y}$ [*BNL NuDat2*, 2006-2010], spontaneous fission of the plutonium occurs and this will produce a large background of fast neutrons up to about 19 MeV. The sensitivity of RAD to Martian neutrons below this value is therefore strongly reduced. Exact values for the rate of RTG neutrons seen in RAD can be calculated not before launch time, as the exact amount of radioactive material as well as the placement and shielding relative to RAD is not yet known. In Fig. 7.2, the expected rates due to RTG neutrons as well as those from the environment on Mars (compare also App. D.2), from an early RAD MC calculation [*Böhm*, 2006-2008] are shown. An approximate RTG spectrum has been estimated from measured data onboard the Ulysses spacecraft. At the high energy end ($\sim 100\,\mathrm{MeV}$) sensitivity of the neutron E channel is reduced (among other effects) by the escape of recoil protons, as it has been worked out in Sec. 6.8.1.

7.4 Available neutron measurements

Although disturbed by the RTG, understanding of the low energy neutron range $< 20\,\mathrm{MeV}$ helps in understanding the principal way neutrons interact with the instrument. This energy range $< 20\,\mathrm{MeV}$ for neutrons in RAD has been tested using the neutron fields available at PTB*Nolte et al.* [2004] and is the focus of the following discussion. The sensor head FM1, with REB readout electronics, has been irradiated with fast neutrons having $5, 14.8$ and 19 MeV at the main PTB facility.

Preliminary data on the response in the high energy range (up to 100 MeV) neutron part

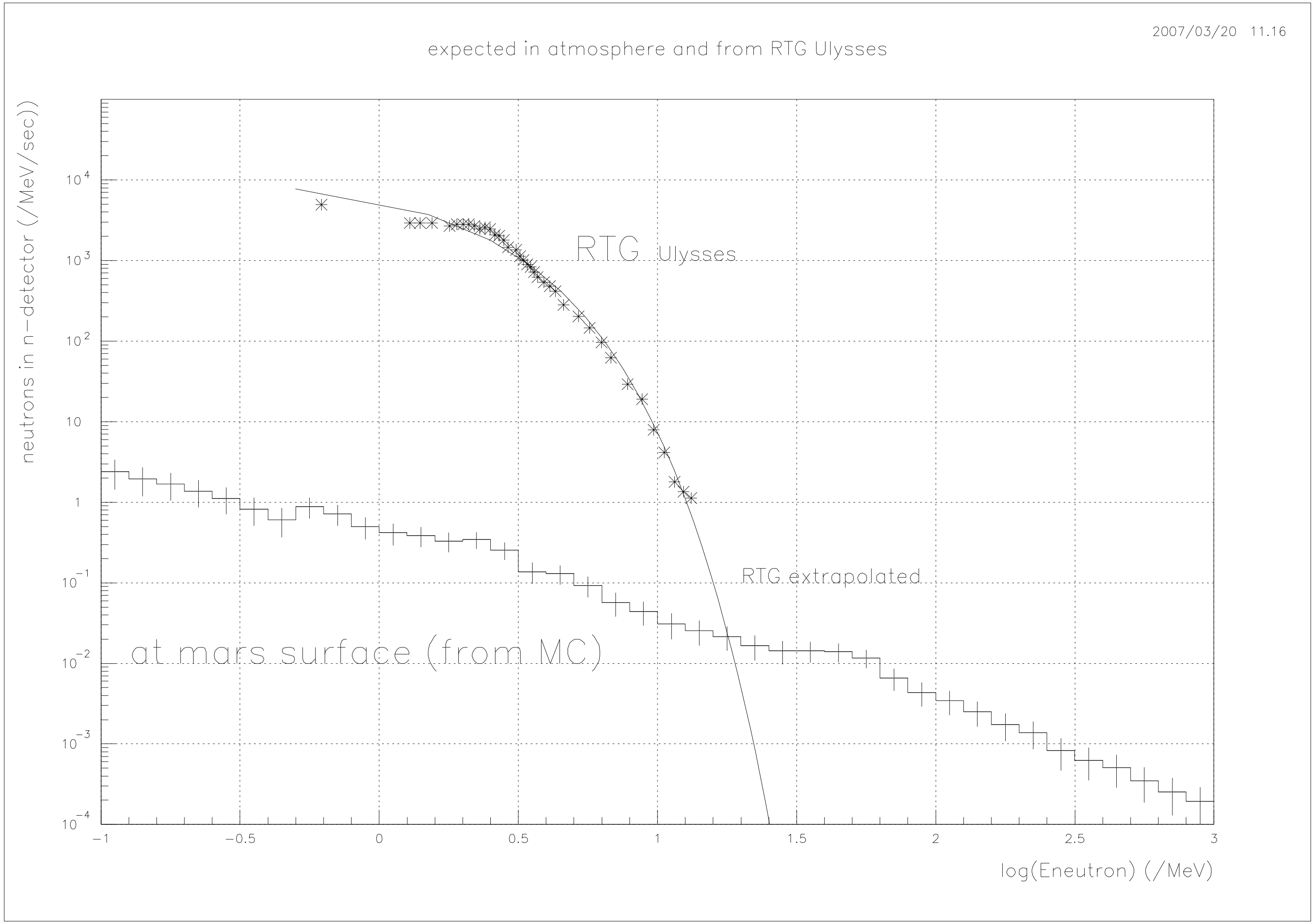

Figure 7.2: Estimated natural and RTG neutron spectrum on the Martian surface, taken from *Böhm* [2007]. MC-Simulations. The RTG input neutron spectrum is an estimate based on the RTG data acquired for the Ulysses mission. The x-axis is given in $\log_{10}(E \cdot \mathrm{MeV}^{-1})$ units.

of the CERF field [*Mitaroff and Silari*, 2002] is available for the PF RSH, using the DIRENA system for data acquisition. This limited the amount of useful neutron data for this run, as the high noise of the DIRENA system at that time prevented proper AC rejection of the charged particle background. Additionally, the PF sensor head has been tested with early REB prototype electronics at the 100 MeV neutron source at iThemba labs [*Nolte et al.*, 2004]. Both high-energy neutron runs are not yet fully modeled (esp. the electronics parts) and are not further discussed here.

For most of the existing neutron runs, the particles enter the instrument along its main axis and the angular response to neutrons needs to be extrapolated based on the `GEANT4` model of the sensor head.

7.5 Neutron modeling

To compare the response of the instrument to the theoretical expectations of its performance and to aid in developing adequate reconstruction algorithms and measurement schemes, a comprehensive model of the neutron behaviour of RAD is helpful. Like for the D scintillator charged particle optical model, the model of RAD's neutron behaviour splits into several parts. In the following, the main parts of the model will be detailed.

The extended `GEANT4` model with CAD data support has been used to produce the theoretical energy loss spectra, for which a simple quenching approximation is done (see below) and further post processing using the readout model as described in Sec. 6.3. Only plastic scintillator quenching has been implemented so far, as it is believed to be well understood in its effects in regard to RAD. The advanced empirical models of C. Martin for the D scintillator have not been implemented yet.

In Fig. 7.3, the pure calculated response (given in units of energy loss in the detectors), as it will be compared to the beam measurements is shown. In contrast to *Böhm and Martin* [2008], a wide neutron beam covering the whole instrument has been simulated. It can be seen that for neutron energies up to 19 MeV, a sharp edge results in the energy loss spectrum, whereas for high energy neutrons (e.g. 100 MeV), the recoil protons escape and no edge is visible at the high end of the energy loss spectrum anymore for any realistic integration time.

7.5.1 Quenching

Light production inside both the crystal as well as the plastic scintillator depends nonlinearly on the ionization density and thus the $\frac{dE}{dx}$ along the ionization path. Due to non-radiative recombination of excited states in the track regions with high ionization density, the light output is quenched compared to low-Linear Energy Transfer (LET) sections. This happens for both the plastic scintillators as well as the CsI crystal, but in different amounts and according to different laws. This introduces a single additional quenching parameter into the optical and readout model, which is otherwise taken unchanged, including parameter estimates, from Secs. 6.2, 6.3.

D scintillator. Especially in the D scintillator, a lot of work has been done by C. Martin and E. Böhm on quenching [*Martin*, 2008a; *Martin et al.*, 2008a,b]. The current model is a semi-empirical multi-parameter model and, as said above, has not yet been included in the full model. Because it is in the interesting dynamic range and has a trigger threshold set for the measurements, the DU channel has been used as a representative of the D channel in the measurement. For the readout model, the parameter c has been deemed to be the same as for the DN channel and is taken to be $c = 15.9$ MeV Si/MeV CsI (as in Sec. 3.5). The σ

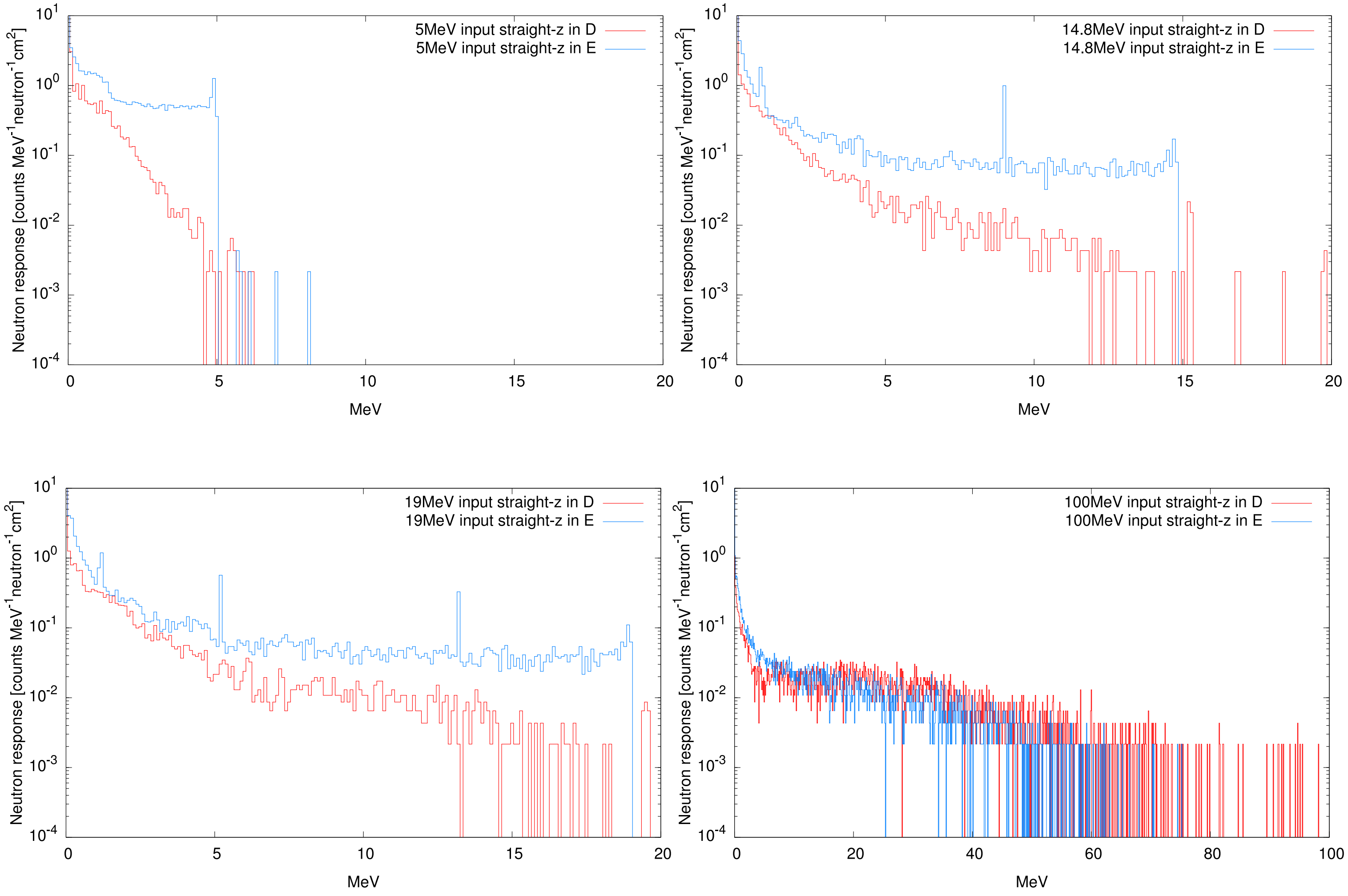

Figure 7.3: Simulated response to various monoenergetic neutron fields, as calculated by a `GEANT4`-based model, with physics list input from E. Böhm and S. Böttcher and using the RAD CAD geometry. A wide beam is entering the instrument front window perpendicularly. A total of 1 M neutrons are simulated impinging on a boundary disc with $r = 83\,\mathrm{mm}$. Shown is the expected response of the instrument to a given input rate of monoenergetic neutrons. Very visible is the suppression of high energy hits in the tail of the 100 MeV simulation (esp. the E channel), as the produced secondaries escape from the scintillators. No quenching and no optical effects are included in the simulation and only the bare energy deposit is shown. The resolution of the measurement does not allow to see the resonance peaks visible in the simulation.

and o parameters have been derived from a simple noise peak fit. The value of s has been determined by a cross-calibration of the DN/DU scales for the muon run [#8, μ-FM1-fREB] and representatively[2] the neutron run [#9, n-19-FM1-REB]. The parameters are given in Sec. 6.7.1, Tab. 6.2.

E scintillator. For detailed quenching studies, a quenching model has been implemented in `GEANT3` by C. Martin which applies the Birks quenching law at each step while navigating along a track in the particle physics model of the instrument. This is in principle able to handle any partial energy loss in a detector with possible entry and escape of the particle at any point in the track. This method has been transferred straight-forward to the full sequential model based on `GEANT4`. Only the simplified Birks formula using the single parameter kB has been implemented. The model has been deemed sufficient to explain the quenching effects on the neutron data in the E scintillator.

The quenching law by Birks, as detailed in *Craun and Smith* [1970], states that the light output per track length x, $\frac{dL}{dx}$ fulfils

$$\frac{dL}{dx} = S \cdot \left(\frac{-\frac{dE}{dx}}{1 - kB\frac{dE}{dx}} \right), \tag{7.5}$$

with the convention of $\frac{dE}{dx} < 0$. This formula is applied for each step-wise energy loss ΔE and step length Δx from the `GEANT4` tracking. It as assumed that the energy loss across a `GEANT4`-step is constant:

$$\frac{dE}{dx} = \frac{\Delta E}{\Delta x}. \tag{7.6}$$

The default cut values are used in `GEANT4`, as the $\frac{dE}{dx}$ is highest at the stopping part of the track, changing cut values may have an influence here. The scintillation efficiency S will be simply subsumed in the general energy calibration factor for the scintillator and $S = 1$ can be assumed here. C. Martin used [*Martin et al.*, 2008b] a value of[3]

$$kB = 1.31 \times 10^{-2}\,\mathrm{g\,cm^{-2}\,MeV^{-1}}. \tag{7.7}$$

This is also the kB-value given for NE-102 scintillator material in *Craun and Smith* [1970]. Here, the value is selected differently (see below).

Using a numerical integration of the energy loss of protons in the scintillator material according to Eq. 2.1, the quenching law as in Eq. 7.5 has been applied to give the light signal of *stopping* protons in plastic vs. the initial energy. The resulting function $L(E)$ and exemplary the effect of using only a scaling factor to account for quenching can be seen in Fig. 7.4. As two light 'arms' are visible in the `GEANT4` scatter data in this figure, there is no unambiguous relationship between energy seen and energy deposited any more. For this reason, no energy axis is drawn for the measured E data discussed below. A very rough energy scale can be derived from the maximum neutron energy loss edge.

If the entrance energy and exit energy is available when crossing the plastic scintillator from the particle physics model, integration of $L(E)$ can also be done for only the relevant parts of the $\frac{dE}{dx}$ curve and the step-wise quenching calculation can be replaced with a event-wise energy calculation in the simulations.

---

[2] The other discussed runs have no changed VIRENA gain scale parameters.

[3] In the quenching calculations by Birks, it is assumed that $\left[\frac{dE}{dx}\right] = \left[\mathrm{MeV g^{-1}\,cm^2}\right]$. For the plastic scintillator, the density is $\rho \approx 1.0\,\mathrm{g\,cm^{-3}}$, so the same numeric values apply here.

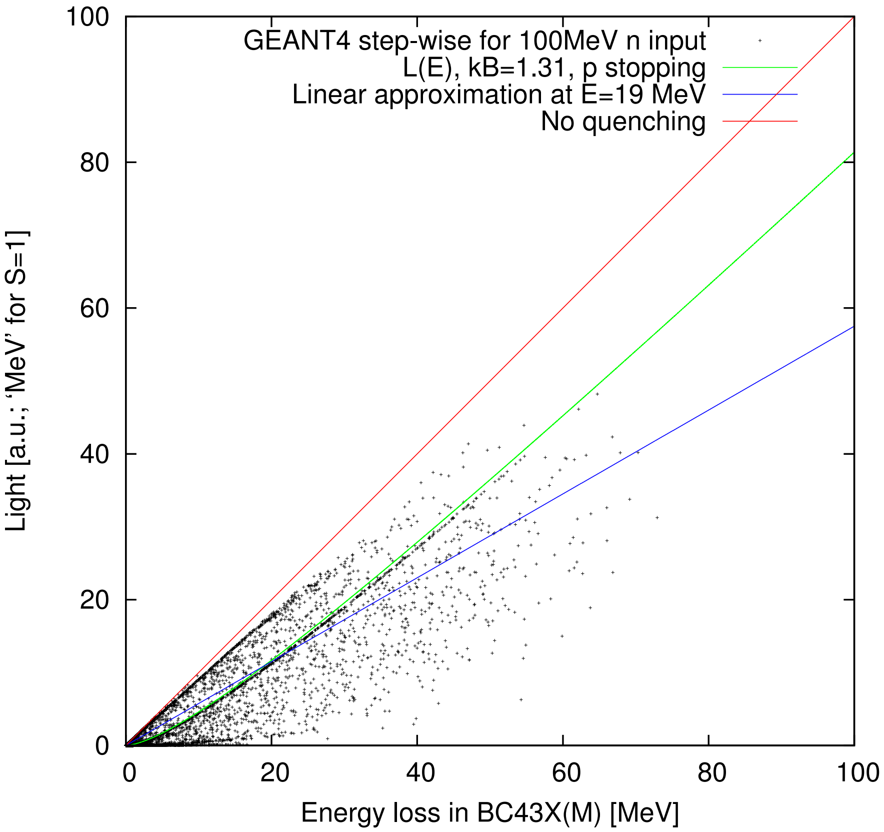

Figure 7.4: Example of a numerical integration of the quenched light output $L(E)$ for a given input energy E of stopping protons in approximately plastic scintillator material ($1\,\mathrm{g\,cm^{-3}}$), with C. Martin's kB of $kB = 1.31 \times 10^{-2}\,\mathrm{g\,cm^{-2}\,MeV^{-1}}$. $S = 1$ is assumed here. The blue curve shows a linearization of the quenching curve using a single calibration point at 19 MeV and thus illustrates the amount of error introduced by assuming only linear scintillator behaviour. The red curve shows the case $kB = 0$ without any quenching. The small black crosses in the background represent the output of the `GEANT4` simulation vs. the step-wise quenched values. Note that for producing the curves (but not the scattered data), no geometrical effects have been considered and all protons are assumed to be stopping. It can be seen that the `GEANT4` output divides into two arms, one for the penetrating, close to the red curve, and one for the stopping particles, close to the green curve. Nearly no quenching occurs for fast penetrating particles with low energy loss.

7.6 Data analysis

Cuts and reconstruction. As the full model simulation now covers most of aspects of the RAD instrument, as little amount of preprocessing as possible of the measured data has been done before it is compared to simulation results and only a single channel (DU/EU) is used for each scintillator. This way, most of the aspects of the model are included. It is important to note that if one wants to apply silicon hit rejection to the measurement, then this rejection would need to be applied in very much the same way to the simulated data for comparison.

For example, it is not a good idea to apply any cuts on the simulated data in the 'usual and efficient way', that is, before any effects of the readout model are included. In the case of the 5 MeV run, due to the relatively large amount of noise compared to the light signal, the silicon hit rejection using only the optical distribution model without the readout model will produce wrong results. Simply adding channels will also produce wrong results, as silicon hits are not accounted for. The only cut that is effective for the measurement is the trigger threshold, which has been set for both the DU and the EU channel. Triggers from other channels are not suppressed in any way and show up in the total height of the noise peak visible.

Background. A background of charged particles is expected for each neutron energy. Blank targets have been inserted into the beam at the PTB facility to account for this background field. Additionally, a shadow cone has been inserted in front of the instrument to just measure the field of scattered neutrons and induced γ-rays. By subtracting the shadow cone measurement from the actual one, approximately the net fluence of directed neutrons results. All MC simulations assume a 100% directed neutron field and the rates from the shadow cone measurements have been subtracted. The differential rate reduction due to subtraction of the shadow cone measurement is on the order of 10% for most energies and measurements.

Rate estimation. The reference for the neutron field is given as a neutron fluence and total dose [*Nolte*, 2008]. Debug mode operation and minor technical problems during data taking caused dropouts and additionally the inevitable reduction in the live-time of the instrument due to processing delays prevents that the total fluence is accumulated. This effect is accounted for by estimating the live-time of the instrument using the REB C1 counter value[4] and scaling the measured (actual and shadow cone) data with the quotient of reference length and C1 live-time. For the neutron field data used, the live-times are given in App. I. This method relies on the additional assumption that the neutron flux is constant for a run.

7.7 Results

As said above, the muon calibration of the full model from Sec. 6.5 has been applied as-is to the simulated neutron data $5 \ldots 19\,\mathrm{MeV}$, as the same VIRENA chip (albeit in a differently assembled REB unit, CalRAD vs. a FlatRAD) and the same sensor head have been used for both.

The quenching parameter of $kB = 1.31 \times 10^{-2}\,\mathrm{g\,cm^{-2}\,MeV^{-1}}$ has been deemed to be too high to properly explain the PTB neutron data. Instead, a value of

$$kB = 0.60 \times 10^{-2}\,\mathrm{g\,cm^{-2}\,MeV^{-1}} \tag{7.8}$$

has been selected from a by-eye fit of the 19 MeV neutron data. In Fig. 7.5, the effects of applying different quenching kB parameters to the simulation data (here the exemplary run with 19 MeV) can be seen.

The $\hat{y}$ value for scaling the rates from simulation to measurement have been matched by-eye in the low energy range (but above the noise peak) individually for each measurement to the data. When varying the values for $\hat{y}$ and kB for the E channel, no large correlation between the two parameter estimates is expected as the cleanly visible change in the slope at the upper 19 MeV-edge can be matched. The error for the kB value has been estimated (by-eye) as $\Delta kB = 0.10 \times 10^{-2}\,\mathrm{g\,cm^{-2}\,MeV^{-1}}$ and $\frac{\Delta\hat{y}}{\hat{y}} < 10\%$.

The results for the EU channel can be seen in Fig. 7.6 and those for the DU channel in Fig. 7.7.

For the EU channel, it can be seen that the full model explains the single-channel slope of all runs nicely, taking the light distribution between the diodes and losses into account. *This*

---

[4] To be more specific, the live-time counter value for the last minute-wise house keeping reading is used.

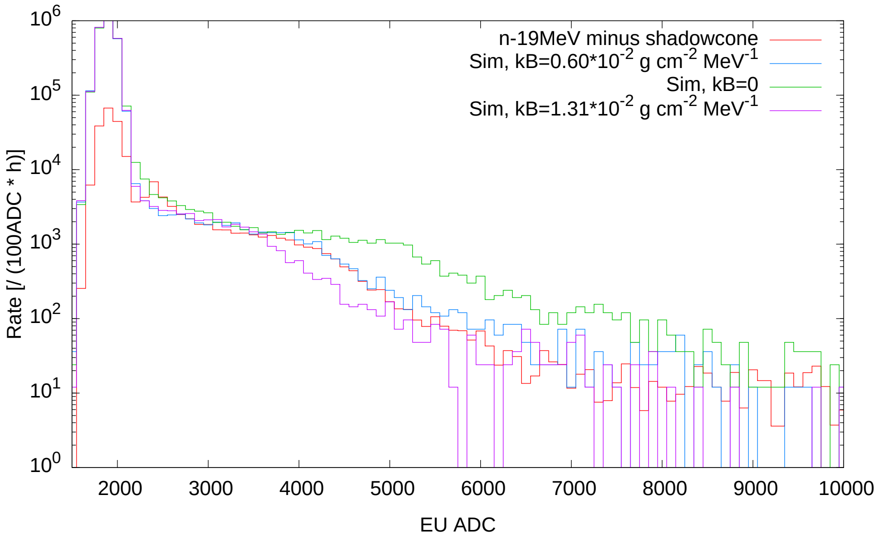

Figure 7.5: Measurement of 19 MeV neutrons in the E channel and the simulated response for different values of kB.

slope has not been reproduced without the optical model yet. For the 5 MeV run, a background of additional hits is visible, which are deemed to be mostly silicon hits from secondary γ-rays being produced in RAD's surroundings. This effect can also be slightly seen for the 14.8 MeV run.

For the DU channel, the picture is similar for the 14.8 and 19 MeV run. A large discrepancy appears for the 5 MeV run. No further investigations on this discrepancy have been done yet, but the discrepancy is, like for the EU channel, in the energy range where γ-hits could produce silicon hits.

A large deviation can be seen when comparing the $\hat{y}$ fluence scaling values for a single measurement between those derived from fitting DU resp. EU. The $\hat{y}$-values for the DU channel are always higher than those for the respective EU channel. No explanation for this behaviour is known yet. It can be speculated that this behaviour is due to either

- inaccuracy in the overall cross-section for neutrons in `GEANT4` either for CsI or for the plastic scintillator.
- or a larger γ-background visible in the DU channel that has a similar shape as the neutron energy loss spectrum.

7.8 Dose from neutral particles

From the simulation, the dose can be directly calculated. In Tab. 7.1, the simulated doses per given amount of forward neutrons is given. From this, energy deposit per fluence is calculated $\left(\cdot \frac{A}{N}\right)$ with area A and number of particles N. From this, dose per fluence is estimated by dividing by the scintillator mass. Let the unit n be the number of neutrons in this context.

The volume of the D scintillator is assumed to be $V_D = 29.9\,\mathrm{ml}$ with mass $m_D = 134\,\mathrm{g}$. For the E scintillator, it is assumed $V_E = 34.4\,\mathrm{ml}$ and mass $m_E = 34.4\,\mathrm{g}$. With the given bounding disc, $1 \times 10^6\,\mathrm{n}$ amount to $N/A = 4620.4\,\mathrm{n\,cm^{-2}}$.

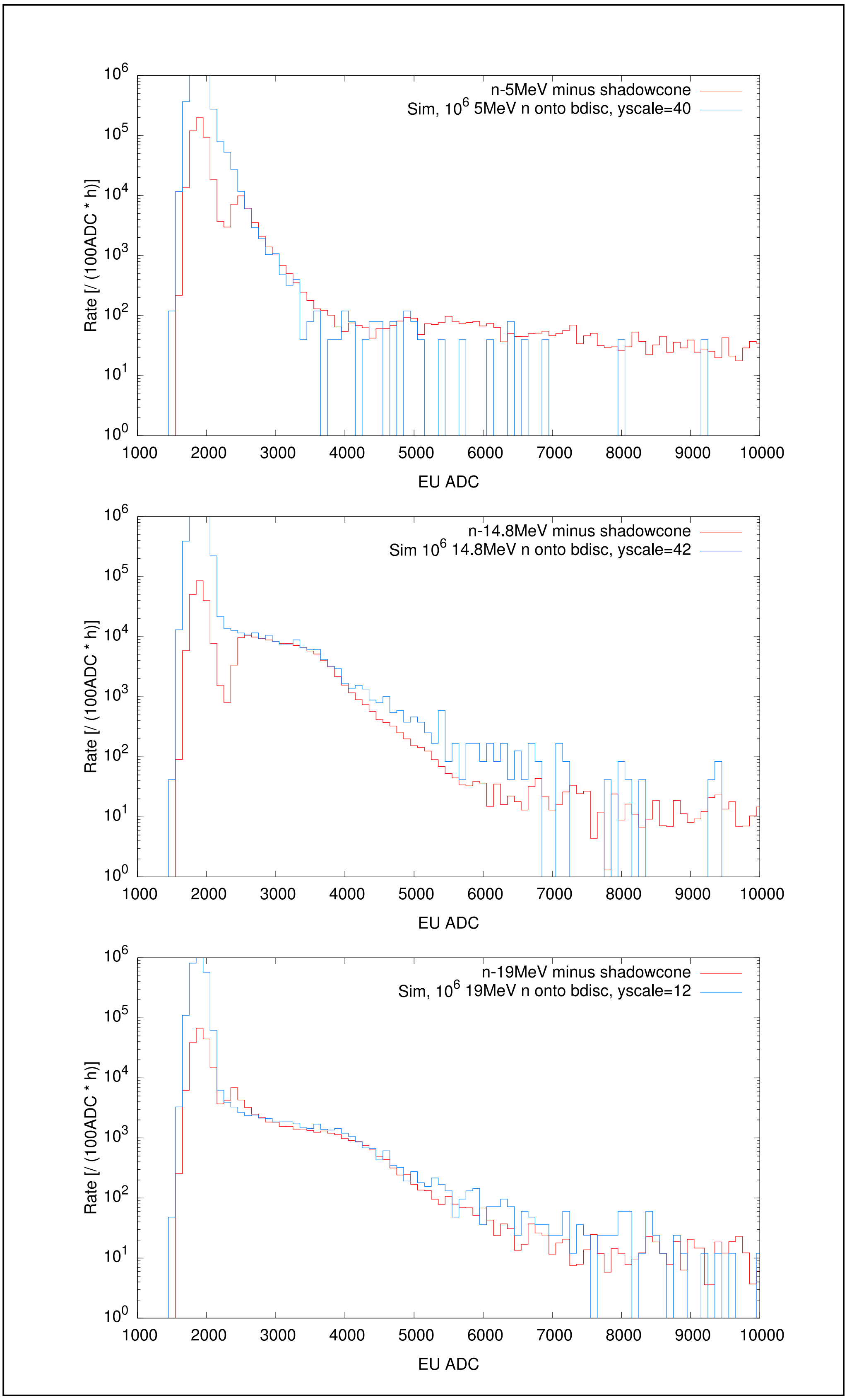

Figure 7.6: Response of the **EU** channel to 5, 14.8 and 19 MeV neutrons (from top to bottom), measured at PTB and simulation results of the full model for 10^6 neutrons onto the boundary disc. The different values of $\hat{y}$ are given in the plots. Data is binned into 100 ADC bins.

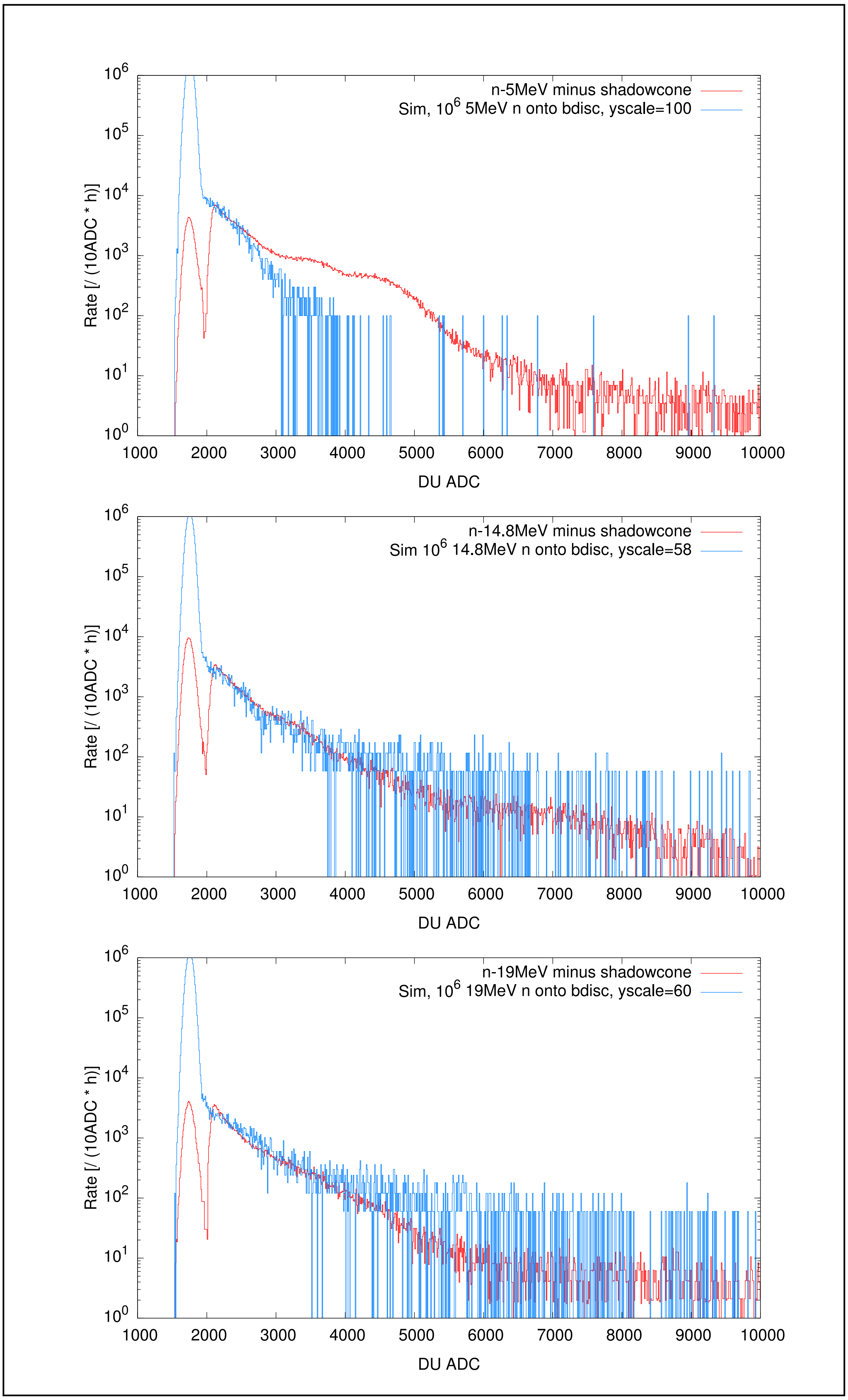

Figure 7.7: Response of the **DU** channel to 5, 14.8 and 19 MeV neutrons (from top to bottom), measured at PTB and simulation results of the full model for 10^6 neutrons onto the boundary disc. Again, the different values of $\hat{y}$ are given in the plots. Data is binned into 10 ADC bins.

E_n [MeV]	**Chan.**	E_{dep} / 1×10^6 n [GeV]	$\frac{A \cdot E_{\text{dep}}}{N}$ [MeV n^{-1} cm^2]	**Dose** [pGy n^{-1} cm^2]
5	D	5.72	1.24	1.47
5	E	36.4	7.88	36.7
14.8	D	8.83	1.91	2.27
14.8	E	48.5	10.5	48.8
19	D	11.7	2.53	3.02
19	E	50.8	11.0	51.2
100	D	91.3	19.8	23.5
100	E	58.0	12.6	58.4

Table 7.1: Simulated doses resp. total energy deposits in the D and E channel for given neutron fluences in $-z$-direction. The unit n means the number of neutrons.

E_n [MeV]	**Chan.**	$\hat{y}$	**R** F_{dir}[n cm^{-2}]	**S** F_{dir}[n cm^{-2}]	**R** H^*_{dir} [μSv]	**S** H [μSv]
5	D	100	4.641×10^5	4.62×10^5	188	6.8
5	E	40	4.641×10^5	1.85×10^5	188	68
14.8	D	58	1.977×10^5	2.68×10^5	54	6.1
14.8	E	42	1.977×10^5	1.94×10^5	54	95
19	D	60	1.121×10^5	2.77×10^5	65	8.3
19	E	12	1.121×10^5	0.56×10^5	65	32

Table 7.2: Measured and simulated fluences and equivalent doses. The letter **R** denotes the reference value and **S** the value derived from fitting the simulation to measurement. H is the equivalent dose, adjusted with a quality weighting factor of 10.

In Tab. 7.2, the directed fluences F_{dir} and the doses are compared to the reference values by PTB. It can be seen that the fluences are matching only within a factor of $2\times\ \ldots\ 3\times$. The dose is of the same order of magnitude for the calculated one for the E (but not the D) scintillator.

7.9 Conclusions

From the signals due to γ-rays in the final instrument, it can be easily seen that advanced γ-spectroscopy (direct identification and rate measurement of single γ-lines) will not be possible with the RAD instrument. Estimates of the γ-dose should be possible.

The neutron detection part in form of the E (and D) scintillator works mostly as expected and can be explained in its energy broadening behaviour quite well by the described model. Together with the AC results from Sec. 6.8.1 and assuming a working inversion method, one should be able to separate the neutrons out of Mars' expected mixed particle field. Missing is a further and more detailed investigation on the discrepancies between measured and reference fluence and dose to reduce the error bars on Martian fluence resp. dose estimations. Especially the large discrepancy between the D and E response warrants further investigation. It is not clear to us whether this effect is due to wrong or incomplete CsI neutron cross sections in the GEANT4 particle simulation of RAD.

Quenching effects in the D scintillator are still missing in the case of neutrons and, although the shape of the D scintillator response is reproduced well by the MC, the light yields need to be corrected for quenching, like for the other quenched data (heavy iron runs) to finally get one definitive response function of the D scintillator.

Chapter 8

Conclusions and outlook

In a set of different explorations of RAD's performance, it has been shown that RAD's scintillators should perform mostly as designed, and that neutral particle flux measurements in Martian conditions are feasible. Methods to estimate the important parameters for RAD have been developed and applied to various adequate subsets of the data processing chain and for a selection of the sensor heads.

Most importantly, it has been shown that the developed and implemented model of the optical propagation inside the complex-shaped scintillators of RAD is able to explain most features of the taken beam data qualitatively as well as quantitatively. An extensive set of tests of its capabilities has been done by comparing it to measurements of the D scintillator crystal. Parameter sets for the models have been found through lab testing and beam testing using a broad proton beam at BNL (D scintillator) as well as a manually set up scan using a collimated helium/proton beam at NIRS/HIMAC for the anti-coincidence and indirectly the E neutron channel. The optical model also gives a way to calculate limits on the achievable resolution when reading the light output of a single scintillator with multiple photo detectors. These resolution limits will influence the design of future scintillator based instruments and are crucial to the understanding and further modeling of the energy reconstruction onboard RAD.

The existing `GEANT4` simulation by E. Böhm and S. Böttcher has been extended to directly use existing CAD data of the sensor head. It has also been made to work in conjunction with the optical model. It further includes quenching effects in the plastic scintillator as well as another model implemented to describe the electronic processing chain of RAD. Quenching calculations have been compared to those by C. Martin and have been done both through Monte-Carlo- as well as a direct integration of the Bethe-Bloch relation and the Birks quenching law. A matching quenching parameter has been determined. The electronic model has been implemented and used to gather noise values from measurements on various levels, from a simple, coarse Gaussian noise description to the appended model dividing noise influences into their independent and common mode components between RAD and VIRENA.

In the context of the work on the full sequence of RAD models, an efficient software link between CAD and `GEANT4` has been implemented and is already in use for further instrument modeling in the Kiel work group. Efficient data structures and algorithms for the geometry implementation (BSP trees) have been appropriately taken from the field of computer graphics.

The optical model further describes the behaviour of the anti-coincidence scintillator, thus making neutron (and neutron dosimetry) measurements using the D/E channel possible. Incorporating the Martian particle field simulation data by B. Ehresmann, forecasts of RAD FM1 in Martian conditions are given. The signal-to-noise ratio of the anti-coincidence, crucial to all neutral particle measurements respectively separation of neutral and charged particles, is estimated and found to be acceptable in the energy range of interest.

As another byproduct of attending the whole RAD/MSL design process, data processing software and tests as well as filter software have been implemented. The tests have uncovered bugs in the electronics chain. Parts of the processing software are waiting, together with the combined models, for appropriate inclusion in the main RAD data processing chain.

Nonetheless, a multitude of further tasks remain in the coverage of RAD's performance. A major topic that is not covered by this work is a systematic application of all models to each sensor head. The selection of data has been made mostly depending on the availability for each sensor head at the given time of writing and was thus driven by the schedule of RAD's design and assembly as well as beam-time allocation. Also, the selection of beam data that has been analyzed in detail has been picked to just cover the basic cases (e.g. some further neutron runs such as a 90° sideways and 180° backwards run are yet to be evaluated). The optical model should be applied to the FM2 configuration and a detailed, systematic analysis of the gain scales for all settings and temperatures of FM2 needs to be done, incorporating the work on the electronics noise.

Before doing so, it appears worthwhile to include the final model for CsI-quenching from C. Martin as the one major missing effect into the sequential model, whilst extending it to include neutrons (which in itself may prove to be a major task) and attach the VIRENA noise model, in order to have a full chain available that can then give the appropriate onboard tables for the flight instrument. The inclusion of the quenching effects should be done based on the detailed set of data available by C. Martin and E. Böhm. The mismatch in the estimated quenching factors needs to be analyzed and the underlying reason need to be found to have a solid basis for quenching calculations in the plastic scintillator.

With the available, calibrated, sequential model, the small sets of forecasts already done can be easily extended to cover the performance of FM2 on Mars, and issues such as directional sensitivity of the anti-coincidence and the neutron detection can be approached. Freshly arrived (April 2010) data on tests of RAD in the vicinity of the MSL RTG needs to be incorporated into the given neutron signal-to-noise ratios.

The optical model has some visible systematic deviations from the data and additional work can be put into it to further reduce the errors on the parameter set. A mechanical setup for automatically moving a particle telescope on a grid over RAD exists and using this setup, one should be able to give more detailed scintillator readout maps when e.g. used in MIPs of the CERF field. The detailed scintillator maps could then be used to fine-tune the optical model as well exploring ways for further simplification, possibly exploiting the strong correlation of α and R. The known inaccuracies in the surface model can be addressed. Without FM2 available, both the PF and FM1 should be used in such a grid-scan setup to further investigate the possible effects of the separated glue layer in the FM1 model and to do more checks on the reproducibility of the scintillator behaviour.

In the more remote future, more details of the scintillators can be implemented (e.g. glue spots). More work can be done to work out the differences between the surface models in realistic cases such as the RAD scintillators. Additionally, the high amount of computer time needed for the current simulations can be reduced by implementing more sophisticated MC sampling techniques, possibly building on work from the computer graphics realm. Comparisons to further simplified models based on diffusion can be done.

Further possible applications of the photon model are timing studies for fast plastic scintillator studies, and for testing spatial resolution methods when using scintillators with multiple readouts.

The electronic noise model can be extended to include the frontend electronics properly.

In this context, a detailed analysis of crosstalk effects, including nonlinearities, should be done. With the data available on the VIRENA chip, it may be useful in modeling noise behaviour and possible reconstruction methods for future missions where it will be used.

Appendix A

Electronics

This chapter gives a more detailed look at the electronic noise figures visible through the REB/VIRENA configuration. A model which is able to distinguish between influences from the VIRENA and from the sensor head itself is described. An important focus of this model is to separate the amount of common mode noise from the independent noise for redundant VIRENA channels.

A.1 Electronic influence on data

The RSH as well as the analog part of the REB have been designed to cover the full expected energy ranges in the detectors and to be as low noise as possible, given the strict power limits for RAD. Still, imperfect behaviour and mangling of the energy loss readings from the detectors happens in RAD's electronics chain. In particular, the following sources of imperfections have been identified:

Noise The carrier generation inside the silicon involves shot noise and the electronic chain inevitably adds additional noise. In case of the high-gain channels, most of the additional electronics noise is produced in the charge sensitive amplifier, whereas for low-gain channels, the effects inside the REB dominate (see below).

Nonlinearities The most obvious nonlinearity in RAD's electronics chain is the saturation of the ADC or any of the amplifier stages. Without saturation effects, the readout electronics behaves quite linear.

Crosstalk Capacitive coupling between the parallel guided signal lines will cause crosstalk between the channels belonging to different detectors. Also, coupling through the power rails may cause crosstalk between the channels. Crosstalk can be nonlinear when saturation happens. In terms of reconstructed energy deposit, the most important crosstalk is a large signal in a high-gain channel affecting the readout of a low-gain channel (in respectively larger units of reconstructed energy). As the reconstruction methods (see also Sec. 3.8) tend to ignore low-gain values when the respective high-gain value is assumed to be correct, this effect is most visible for vastly different energy loss figures in different detectors. For such events, full PHA data will be stored and detailed offline corrections can be done. All other events will be put into histograms onboard the spacecraft without taking into account any crosstalk corrections.

A.2 Noise

It is very important to separate the broadening influence of electronics noise on the signals seen for any given channel from the above physical effects of straggling energy loss or, if the readout diode for a given channel is attached to a scintillator, the possibly uneven light distribution inside a scintillator.

Effects such as shot noise are also excluded. For the D channel, see Sec. 3.4.5. Just as for the D scintillator, no shot noise is assumed for the E scintillator, but sufficient information has not been collected for this detector. Shot noise for direct silicon energy deposits can be completely ignored due to the large numbers of charge carriers involved for even the hit of a MIPs[1].

Temperature dependency of the noise is not separately covered here and all measurements discussed here have been done at approximately[2] room temperature (20°C). Measurements of the noise behaviour of FM1/2 has been done independently from the REB and a total noise measurement for temperature variation of the complete instrument has been done. This data is not yet fully evaluated.

A.2.1 Model

The electronic noise contribution alone can be measured by looking at a given detector output A when the channel is quiet and no energy loss occurs in the detector. For a given RAD calibration run, this can be achieved by filtering for events where a different, independent channel C than the one to be looked at is producing triggers. Each trigger in C, which is not happening due to a particle also producing an energy deposit in A, will cause readout of a noise value from A. All expected processes that generate noise are assumed to generate white noise, producing a Gaussian shaped noise peak as the sum of all noise terms. In the following, all detector signals are assumed to be in quiet state with no energy deposits happening.

In RAD, most channels are duplicated inside the REB, just before entering the analogue signal VIRENA chip. This gives redundant readout for each channel. Step-wise adjustable gain scales inside the VIRENA allow to scale the incoming analogue signals differently before they are processed by the ADC.

A simple model has been conceived to analyse and capture the most important noise factors in the signal chain. The model does not make any assumptions about the exact source of noise from within the sensor head. It captures the signals from the RSH right at the interface to the VIRENA and includes the most important features of the VIRENA. In its present state, it should be comprehensive enough to feed the REB reconstruction algorithms with appropriate hints (for a given operating point with fixed temperature!). This is the main use of this model so far, as described in Sec. 3.8. It explains the noise data as a single noise value for each channel and a small set of global parameters.

In Fig. A.1, the overall scheme can be seen. The two signals from a common physical detector and CSA+Shaper combination are split into two VIRENA channels A and B and are then scaled by two individual scaling factors s and t for A and B, respectively.

The Detector+CSA+Shaper combination is assumed to produce common mode noise in both the A and the B input of the VIRENA with width σ_n. Additionally, a parameter φ is

---

[1] About 3.6 eV are per carrier as in *Leo* [1987, 1994], about 100 keV energy deposit $\Rightarrow \frac{\sqrt{N}}{N} \approx 0.6\%$.

[2] Regular temperature measurements are given by the REB's sensors when activated; such readouts are included in most of the measurements done with a REB.

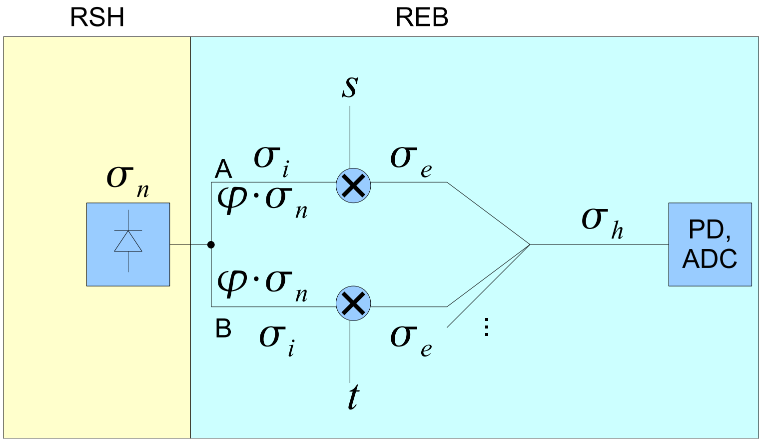

Figure A.1: Diagram showing the noise terms used for the simple noise model to distinguish between coherent RSH noise and VIRENA noise contributions.

introduced such that $\sqrt{\varphi}$ of this correlated noise couples independently into each amplifier chain.

Each input of the VIRENA is further assumed to have the same amount of independent noise with width σ_i. This models the input amplifier chain inside the VIRENA. The signal up to this point (and thus the noise) is scaled with s resp. t and a final noise term with width σ_e is added to each (modeling the noise in each amplifier chain after gain scaling), independently, before the signal is fed into the output buffer/ADC. There, an additional common mode noise term σ_h is added. The sources for the scaling factors s and t are assumed to be noise free, i.e. no multiplicative noise term is assumed to exist.

In the following, let $g_i(\sigma)$ be a random variable with GAUSSian pdf having variance σ^2. Let g_i, g_j be statistically independent for $i \neq j$. By exploiting the additive behaviour of the variances, one can now build a linear system of equations for the noise terms.

The signals seen in A and B amount to

$$A = s\,(g_0(\sigma_n) + g_1(\sqrt{\varphi}\cdot\sigma_n) + g_2(\sigma_i)) + g_3(\sigma_e) + g_4(\sigma_h). \tag{A.1}$$

and

$$B = t\,(g_0(\sigma_n) + g_5(\sqrt{\varphi}\cdot\sigma_n) + g_6(\sigma_i)) + g_7(\sigma_e) + g_4(\sigma_h). \tag{A.2}$$

Note that the same g_0 and g_4 is used both for A and B while $g_1 \neq g_5$, $g_2 \neq g_6$ etc. The variances of each individual channel can now be calculated as

$$\sigma_A^2 = s^2\left((1+\varphi)\sigma_n^2 + \sigma_i^2\right) + \sigma_e^2 + \sigma_h^2 \tag{A.3}$$

$$\sigma_B^2 = t^2\left((1+\varphi)\sigma_n^2 + \sigma_i^2\right) + \sigma_e^2 + \sigma_h^2. \tag{A.4}$$

These two equations allow to calculate the amount σ_e^2, σ_h^2 and σ_i^2 given a value for σ_n^2.

For simplicity, define now the following symbols:

$$d := \frac{1}{s^2} + \frac{1}{t^2}, \tag{A.5}$$

$$f := \left(\frac{1}{s} + \frac{1}{t}\right)^2 \tag{A.6}$$

and

$$g := \left(\frac{1}{s} - \frac{1}{h}\right)^2 . \tag{A.7}$$

Further information yielding σ_n can be squeezed out of the (A, B) signal by calculating the sum signal

$$S_+ := \frac{1}{s}A + \frac{1}{t}B \tag{A.8}$$

and difference signal

$$S_- := \frac{1}{s}A - \frac{1}{t}B, \tag{A.9}$$

with variances

$$\begin{aligned}
\sigma_+^2 := \sigma^2(S_+) &= \sigma^2(2g_0(\sigma_n)) && \text{(A.10)}\\
&\quad +\sigma^2\left(g_1(\sqrt{\varphi}\sigma_n) + g_5(\sqrt{\varphi}\sigma_n)\right) && \text{(A.11)}\\
&\quad +\sigma^2(g_2(\sigma_i) + g_6(\sigma_i)) && \text{(A.12)}\\
&\quad +\sigma^2\left(\frac{1}{s}g_3(\sigma_e) + \frac{1}{t}g_7(\sigma_e)\right) && \text{(A.13)}\\
&\quad +\sigma^2\left(\left(\frac{1}{s} + \frac{1}{t}\right) g_4(\sigma_h)\right) && \text{(A.14)}\\
&= (4+2\varphi)\sigma_n^2 + 2\sigma_i^2 + d\sigma_e^2 + f\sigma_h^2. && \text{(A.15)}
\end{aligned}$$

and

$$\begin{aligned}
\sigma_-^2 := \sigma^2(S_-) = &\quad \sigma^2(g_2(\sigma_i) + g_6(\sigma_i)) && \text{(A.16)}\\
&\quad +\sigma^2(g_1(\sqrt{\varphi}\sigma_n) + g_7(\sqrt{\varphi}\sigma_n) && \text{(A.17)}\\
&\quad +\sigma^2\left(\frac{1}{s}g_3(\sigma_e) + \frac{1}{t}g_7(\sigma_e)\right) && \text{(A.18)}\\
&\quad +\sigma^2\left(\left(\frac{1}{s} - \frac{1}{t}\right) g_4(\sigma_h)\right) && \text{(A.19)}\\
= &\quad 2\varphi\sigma_n^2 + 2\sigma_i^2 + d\sigma_e^2 + g\sigma_h^2. && \text{(A.20)}
\end{aligned}$$

The set of Eqs. A.3, A.4, A.15 and A.20 yield a system of linear equations relating the values $(\sigma_n^2, \sigma_i^2, \sigma_e^2, \sigma_h^2)$ to $(\sigma_+^2, \sigma_-^2, \sigma_A^2, \sigma_B^2)$, if considering φ as constant:

$$\left(\sigma_n^2, \sigma_i^2, \sigma_e^2, \sigma_h^2\right) \cdot \begin{pmatrix} 4+2\varphi & 2\varphi & s^2(1+\varphi) & t^2(1+\varphi) \\ 2 & 2 & s^2 & t^2 \\ d & d & 1 & 1 \\ f & g & 1 & 1 \end{pmatrix} = \left(\sigma_+^2, \sigma_-^2, \sigma_A, \sigma_B^2\right) \tag{A.21}$$

Because the matrix in Eq. A.21 does not have full rank, this system of equations is unfortunately not unambiguously solvable for one channel. By further assuming that each independent physical channel $i \in \{1, \ldots, N\}$ has an independent $(\sigma_n)_i$ but the noise terms σ_e, σ_h and σ_i are equal for all processed channels, a larger set of linear equations can be derived; define the $(4N) \times (N+3)$ matrix M to be

$$M := \begin{pmatrix}
4+2\varphi & 2\varphi & 1+\varphi & 1+\varphi & 0 & 0 & 0 & 0 & \ldots & 0 & 0 & 0 & 0 \\
0 & 0 & 0 & 0 & 4+2\varphi & 2\varphi & 1+\varphi & 1+\varphi & \ldots & 0 & 0 & 0 & 0 \\
 & & & & & & & & \ddots & & & & \\
0 & 0 & 0 & 0 & 0 & 0 & 0 & 0 & \ldots & 4+2\varphi & 2\varphi & 1+\varphi & 1+\varphi \\
2 & 2 & 1 & 1 & 2 & 2 & 1 & 1 & \ldots & 2 & 2 & 1 & 1 \\
d_1 & d_1 & \frac{1}{s_1^2} & \frac{1}{t_1^2} & d_2 & d_2 & \frac{1}{s_2^2} & \frac{1}{t_2^2} & \ldots & d_N & d_N & \frac{1}{s_N^2} & \frac{1}{t_N^2} \\
f_1 & g_1 & \frac{1}{s_1^2} & \frac{1}{t_1^2} & f_2 & g_2 & \frac{1}{s_2^2} & \frac{1}{t_2^2} & \ldots & f_N & g_N & \frac{1}{s_N^2} & \frac{1}{t_N^2}
\end{pmatrix} . \tag{A.22}$$

For clarity, the recurring sequence of $(4+2\varphi, 2\varphi, 1+\varphi, 1+\varphi)$ as the vector for the relation to the $(\sigma_n)_i$ values (as well as the φ parameter) has been marked in red here. For the given set of parameters s, t (and the case $\varphi = 0$), it can be numerically determined that this matrix finally has full rank (the minimum singular value is strictly positive).

Further, let

$$x := \left(\sigma_{n1}^2, \; \dots \; , \sigma_{nN}^2, \sigma_i^2, \sigma_e^2\right) \tag{A.23}$$

and

$$b := \left(\sigma_{+,1}^2, \sigma_{-,1}^2, \frac{\sigma_{A,1}^2}{s_1^2}, \frac{\sigma_{B,1}^2}{t_1^2}, \; \dots \; , \sigma_{+,N}^2, \sigma_{-,N}^2, \frac{\sigma_{A,N}^2}{s_N^2}, \frac{\sigma_{B,N}^2}{t_N^2}\right). \tag{A.24}$$

Solving

$$x \cdot M = b \tag{A.25}$$

for unknown x will give the particular noise terms in the above equations. As visible, scaling σ_A^2 and σ_B^2 by $\frac{1}{s^2}$ resp. $\frac{1}{t^2}$ is done for numerical reasons, to have all values in the same units. As the solution fulfilling the above equation is overdetermined (for example, for a set of 15 different channels with readout in RAD, $M \in \mathbb{R}^{60\times 18}$), an approximative solution needs to be found, done here by calculating x through minimizing $\|x \cdot M - b\|$,

$$c := \min_x \|x \cdot M - b\| \tag{A.26}$$

with minimum squared deviations c. The results of this model, essentially the coherent (common mode) and the incoherent (independent) noise contributions for each VIRENA channel, are needed in the assessment of the behaviour of the REB for different reconstruction patterns (See Sec. 3.8).

A.2.2 Results

The RSH/REB connection has been investigated for FM2, for two cases with different REB units used for each case. The first case is the analysis of the noise for FM2+KielREB, taken from cosmic muon sampling data in between runs at BNL, 2008 [#7, μ-FM2-KielREB]. In this case a longer cable has been used between RSH and REB, introducing additional EMI spikes. The data has been preprocessed as described in Sec. E.1 to get the noise performance of the setup during quiet operation.

The second case is a long cosmic muon run which followed thermal vacuum testing of the final flight configuration at SwRI [#6, μ-FM2-fREB].

The values for $\sigma_{+,-,A,B}^2$ and the error bars have been determined as described in App. E.1. The resulting parameter sets of the model are most sensitive to the parameters s and t. The values of s and t have not been determined from direct measurements. Instead, the ratio

$$r := \frac{s}{t} \tag{A.27}$$

is estimated by linear regression of the event data from a redundant channel pair (see Sec. E.3). The value of s is then calculated by assuming that t takes the perfect theoretical value of $t = 1$.

The error estimate Δr_f from the fit gives

$$\frac{\Delta r_f}{r} \leq 0.2\% \tag{A.28}$$

But comparing the set of measured r_i to their theoretical values gives a deviation Δr_t of about

$$\frac{\Delta r_t}{r} \approx 4.5\% \tag{A.29}$$

Although r is measured with quite good accuracy, the exact values of s and t are unknown yet. For error estimation, it is now assumed that each s and t vary independently with a GAUSSian pdf. around their measured value with

$$\frac{\Delta s}{s} = \frac{\Delta t}{t} = \frac{1}{\sqrt{2}} 4.5\%, \tag{A.30}$$

which would symmetrically reproduce the variation of r when comparing to theory. The factor $\sqrt{2}$ stems from the linearization of the error estimate around the measured value of r by assuming

$$\left(\frac{\Delta r}{r}\right)^2 = \left(\frac{\Delta s}{s}\right)^2 + \left(\frac{\Delta t}{t}\right)^2. \tag{A.31}$$

This does not account for systematic variations in the values of s and t. Such variations do exist, possibly due to inexact resistivity parameters during the production of the VIRENA chip. Assuming the above independent errors on s and t also clearly overestimates the measurement error of r, as it introduces an additional Δr term.

Given this set of error estimates and assuming an independent, normal distribution of all individual errors, the error of the parameter set x is determined by MC propagation. Values drawn from a GAUSSian pdf with appropriate widths are added to all input parameters and the least squares fit is repeatedly called to get the distribution of the output values.

Luckily, negative variances σ_N^2 resulting from the fit did not need to be handled specially, as they did not occur as the result of any fit. When they occurred during MC error estimation, they have been taken as-is into the calculation of the particular variance value.

Two cases, the model without the φ parameter (linear case) and the model including it will now be analyzed.

Linear. Assume the completely linear case with $\varphi = 0$ and looking at the final flight data. Let K denote the KielREB and F the flight-REB cases. The parameters σ_i^2 as well as σ_h^2 can be excluded, as they do not influence the fit results significantly. In the case including σ_i^2 and σ_h^2 it is

$$\chi_F^2 \approx 3.5,\ \chi_K^2 \approx 1.8 \tag{A.32}$$

and without, it is

$$\chi_F^2 \approx 3.4,\ \chi_K^2 \approx 1.9. \tag{A.33}$$

Thus, the two parameters σ_h and σ_i will be completely ignored from now on ($\sigma_h = \sigma_i = 0$). In Fig. A.2 one can see the result of fitting this simpler model.

To test whether the assumption of a common value for σ_e for all channels is correct, a test fit of a variation of the above model, modified to have independent values $(\sigma_e)_i$ for each channel i has been done[3].

This gives $\chi_F^2 \approx 2.0$ and $\chi_F^2 \approx 1.1$, but introduces another set of 15 parameters into the model when excluding the overall σ_e^2 term. Using the single φ parameter, this additional large set of parameters can be avoided.

---

[3] In this case, the rows describing σ_h^2 and σ_i^2 would be each linearly dependent on the rest of the rows of the matrix.

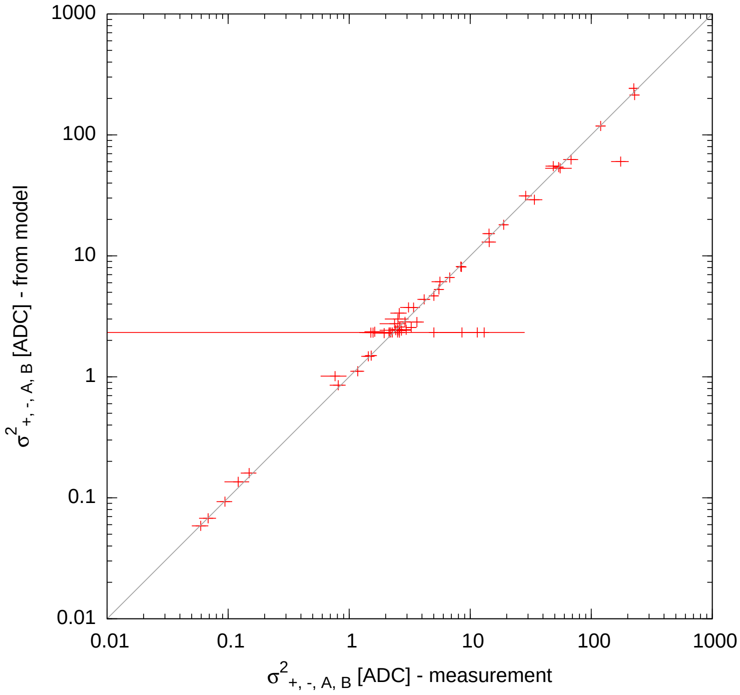

Figure A.2: Reproduction of the measured variance values by the linear model ($\varphi = 0$). The variances of all calculated noise widths are shown ($+, -, A, B$).

With φ parameter. When further splitting up the χ^2 into the parts belonging to $+$, $-$, A and B for the ($\varphi = 0$)-model without individual $(\sigma_e)_i$ values, one notices that the group of σ^2_- values are responsible for most of the deviation between model and data (see Tab. A.1). It is further observed that the σ^2_- values seem to depend on the corresponding preamplifier noise value σ^2_n. This is also visible as the horizontal bar of outliers all having a $\sigma^2 \approx 2$ from the model on the y-axis in Fig. A.2. The first thing that comes to mind which could explain wrong values of σ^2_- is an imbalance in s and t. As the errors for these are assumed to be already rather over- than underestimated, this idea has been rejected.

Noise parameter	**partial χ^2_F**	**partial χ^2_K**
$+$	0.9	1.2
-	**8.0**	**4.6**
A	1.8	0.5
B	2.8	1.3

Table A.1: χ^2 parts when assuming that $\chi^2_{\text{total}} = \frac{1}{4}\left(\chi^2_+ + \chi^2_- + \chi^2_A + \chi^2_B\right)$.

These outliers can be explained by the model by including the single φ parameter, as described above. Although the introduction of the φ parameter departs from a simple linear ‘noise matrix’ model, the obvious alternative would be the introduction of the above individual $(\sigma_e)_i$ values or a separate parameter $(\overline{\sigma^2_n})_i$ for each sensor head channel, describing the individual uncorrelated noise components, also shown to be completely unnecessary by the good fit of the model.

For this final case, it is

$$\chi_F^2 \approx 1.5 \tag{A.34}$$

and

$$\chi_K^2 \approx 1.1. \tag{A.35}$$

The final comparison between the modeled and the measured noise values can be seen in Fig. A.3. The corresponding noise figures can be seen in Tab. A.2 and A.3. The input data for this fit, which may be of interest, can be seen in Tabs. A.4, A.5.

The noise on the back end of the VIRENA can therefore be sufficiently described with a single parameter and it can therefore be concluded that additional noise processes apart from the large noise contribution from the CSAs in the RSH are either happening in equal magnitude in the VIRENA chip for each channel (or the variations are small compared to the noise from the preamplifiers), or that most of the noise in the later parts of the chain originate from the region between the ADC-multiplexer and the ADC itself.

The noise values in the KielREB are mostly larger than those of the FlightREB, with the single exception of the EN channel.

Fitting the model with the full set $\varphi, \sigma_e^2, \left(\sigma_n^2\right)_i$ thus gives a simple description of the behaviour of the analog chain, agreeing well with the measured data, without implementing a comprehensive model of the sensor head. It captures the data set which is relevant for configuring the analog frontend as well as the reconstruction algorithms for a selected measurement agenda.

Such an extended model could be used to further fix noise figures to the parts of the early amplification stages (CSA + Shaper) but would be unlikely to give any additional relevant information for set up of the instrument. Nonetheless, the figures provided here can be used for further investigation of sensor head effects.

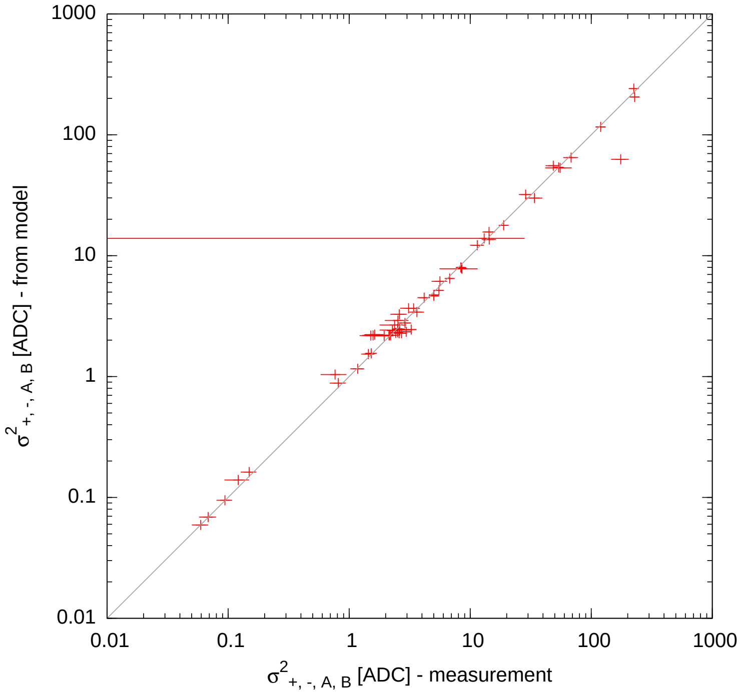

Figure A.3: Reproduction of the measured variance values by the full model including the φ parameter. The variances of all calculated noise widths are shown $(+, -, A, B)$.

φ	DU/DH	DI/DM	DN/DL	EU/EH	EI/EM	EN/EL	A1U/A1H	A1M/A1L	A2U/A2H	A2M/A2L	BU/BH	BM/BL	CU/CH	CM/CL	C2r/C2	σ_e	
0.10	56.75	0.68	0.04	48.30	3.60	0.47	12.28	0.06	1.36	0.03	1.02	0.03	1.38	0.02	27.08	2.16	variance [ADC^2]
0.01	4.02	0.09	0.02	3.80	0.28	0.09	0.80	0.01	0.13	0.01	0.09	0.01	0.11	0.02	1.92	0.07	error [ADC^2]
13	7	13	43	8	8	19	6	23	10	33	9	30	8	139	7	3	error [%]

Table A.2: Noise model fit results for FlightREB and FM2.

φ	DU/DH	DI/DM	DN/DL	EU/EH	EI/EM	EN/EL	A1U/A1H	A1M/A1L	A2U/A2H	A2M/A2L	BU/BH	BM/BL	CU/CH	CM/CL	C2r/C2	σ_e	
0.08	90.28	4.06	0.29	99.47	4.08	0.34	20.76	0.22	1.58	0.12	1.13	0.13	1.64	0.09	32.35	2.80	variance [ADC^2]
0.02	7.51	0.50	0.11	9.33	0.32	0.06	1.72	0.04	0.16	0.03	0.12	0.02	0.14	0.03	2.21	0.09	error [ADC^2]
20	8	12	36	9	8	18	8	17	10	20	11	19	9	38	7	3	error [%]

Table A.3: Noise model fit results for KielREB and FM2.

Channel	**Zero pos.** [ADC]	**Noise** σ [ADC]	**Base channel**	**Measured gain**	**Set gain**
A1H	1426	4.24			
A1L	1736	1.99			
A1M	1576	3.27	A1L	8.9	8.0
A1U	1592	29.09	A1H	7.9	8.0
A2H	1563	2.37			
A2L	1753	1.84			
A2M	1459	2.75	A2L	8.0	8.0
A2U	1981	10.18	A2H	8.3	8.0
BH	1681	2.11			
BL	1715	1.91			
BM	1303	2.74	BL	8.5	8.0
BU	1859	8.91	BH	8.0	8.0
C2	1579	5.65			
C2r	1756	44.03	C2	7.7	8.0
CH	1652	2.29			
CL	1345	1.99			
CM	1707	2.17	CL	4.2	4.0
CU	1758	9.84	CH	7.8	8.0
DH	1646	10.28			
DI	1841	3.75	DM	4.1	4.0
DL	1519	1.99			
DM	1813	2.05			
DN	1477	2.33	DL	4.3	4.0
DU	1755	52.14	DH	7.7	8.0
EH	1817	7.23			
EI	1568	4.48	EM	2.0	2.0
EL	1558	2.07			
EM	1879	2.77			
EN	2037	2.35	EL	2.0	2.0
EU	1914	57.14	EH	7.7	8.0
F1	2275	112.33			
F2r	1568	96.76			

Table A.4: Noise peak positions and widths, and gain scales for the FlightREB and FM2. The gain scales the ‘base channel’ units into units of the given particular channel.

Channel	**Zero pos.** [ADC]	**Noise** σ [ADC]	**Base channel**	**Measured gain**	**Set gain**
A1H	1423	5.18			
A1L	1732	2.00			
A1M	1570	4.30	A1L	8.0	8.0
A1U	1594	37.41	A1H	7.9	8.0
A2H	1560	2.46			
A2L	1752	2.05			
A2M	1458	3.12	A2L	8.0	8.0
A2U	1977	10.71	A2H	8.1	8.0
BH	1678	2.41			
BL	1713	2.28			
BM	1300	3.19	BL	7.6	8.0
BU	1854	9.43	BH	8.2	8.0
C2	1578	6.20			
C2r	1755	46.97	C2	7.8	8.0
CH	1649	2.51			
CL	1345	2.36			
CM	1706	2.35	CL	3.8	4.0
CU	1753	10.58	CH	7.8	8.0
DH	1636	7.23			
DI	1817	2.82	DM	2.0	2.0
DL	1518	2.08			
DM	1812	2.70			
DN	1453	2.44	DL	2.0	2.0
DU	1755	53.21	DH	7.8	8.0
EH	1816	7.76			
EI	1643	8.30	EM	3.9	4.0
EL	1557	2.19			
EM	1877	2.86			
EN	2145	3.09	EL	3.7	4.0
EU	1908	56.27	EH	7.8	8.0
F2r	1569	99.16			

Table A.5: Noise peak positions and widths, and gain scales for the KielREB and FM2.

Appendix B

HIMAC F1/F2 ratio details

As discussed in Sec. 5, the F1/F2 signal ratio is measured at the NIRS/HIMAC accelerator facility [*Takada et al.*, 2000] for a set of collimated 160 MeV proton and 180 MeV nuc^{-1} helium beams, entering the instrument from the `top` (protons) and `side` (helium). The runs are numbered chronologically. It should be noted that this chronological order is not related in a meaningful way to the positions on the instrument, as the runs have been optimized to reduce the number of beam place accesses and shifts that needed to be done and to exploit partial overlap with other experiments on RAD at HIMAC.

B.1 Rates

A top-level view of all 2D histograms for the measured positions can be seen in Figs. B.2 and B.3. The drawn line indicates the ratio that is selected as the best fit for the ratio of F1 to F2. The fits are done by-eye only. For all measurements discussed here, the noise peak zero-position o is assumed to be constant at

$$o(\mathrm{F1}) = 1922 \text{ and } o(\mathrm{F2}) = 1755.5. \tag{B.1}$$

Exact estimates of error bars on the ratios are omitted, as the ratios alone are deemed to be measured with sufficient precision. As discussed in Sec. 5.5, much larger errors occur due to positioning inaccuracies and model inaccuracies and alleviate the need for more exact estimates. An side and a top view of the instrument, annotated with these values, can be seen in Figs. B.4 and B.5. The integer values in square brackets denote the AC run number. A more intuitive 3D view of the positions, also showing the relative orientation of the D crystal and E scintillator, is visible in Fig. B.6.

B.2 Gain corrections

A minor correction could be applied to this data when assuming that calibration data taken during the assembly stages of the instrument gives the best insight available on the relative energy scales between F1 and the segments in F2. During assembly of the flight models, test data for all segments has been taken using a ^{207}Bi β-source and using the DIRENAv1 readout electronics. The relative responses of the four different silicon channels (the outer C part for F1 and the three individual bottom F2 diodes) can be seen in Fig. B.1. The peak positions of the 481.7 keV lines (the 553.8 keV line is hardly visible) are at about $x_{\mathrm{F1}} = 266\,\mathrm{mV}$, $x_{\mathrm{F2}_1} = x_{\mathrm{F2}_2} = 276\,\mathrm{mV}$ and $x_{\mathrm{F2}_3} = 296\,\mathrm{mV}$. When now assuming that the ratio is best

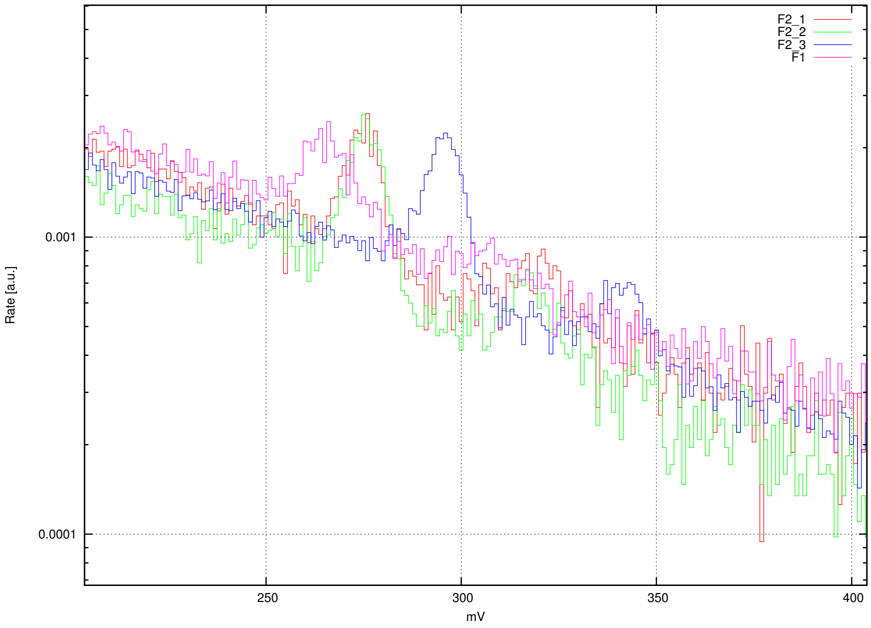

Figure B.1: FM1 F1 F2 gain scales from KT, taken with flight FEE but the DIRENAv1 readout electronics. F1 is the signal in the outer C segment and F2_x denotes the signal in the three independent bottom F2 detectors.

described by the mean peak position for F2 compared to the peak position for F1, this gives a ratio of F1 to F2 of

$$\frac{\mathrm{F1}}{\mathrm{F2}} = \frac{266\,\mathrm{mV}}{279.3\,\mathrm{mV}} \approx 0.95. \tag{B.2}$$

Thus any determined F1/F2 ratios would have to be multiplied by a factor g of

$$g \approx 1.05. \tag{B.3}$$

All data shown does not contain this minor correction and it is unclear whether the effects seen are shadowed or not by larger variations in the VIRENA input gain. A detailed gain scale analysis of the REB with VIRENA in flight configuration would settle this issue. Note also the discrepancy found in Sec. 6.5.4.

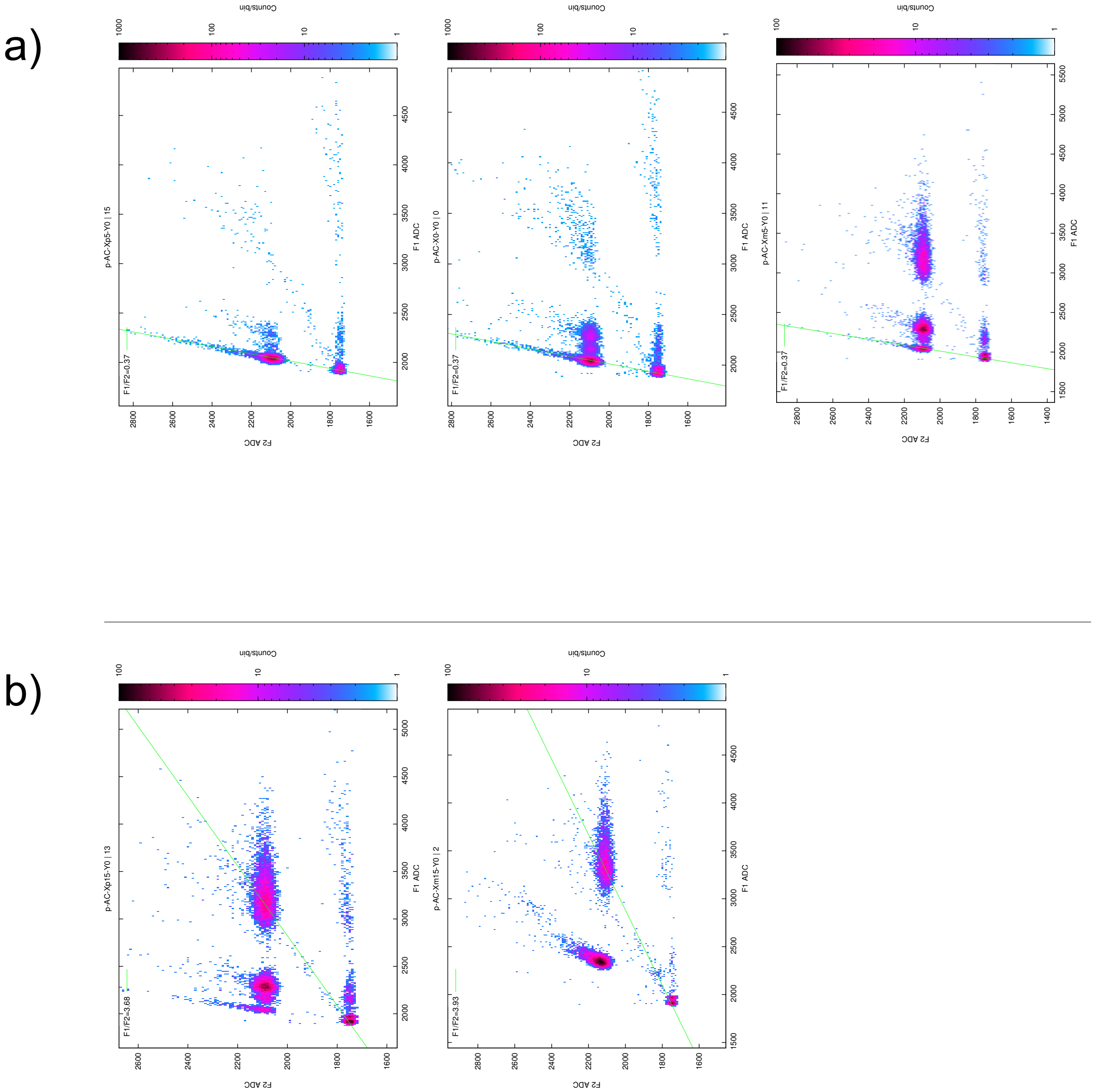

Figure B.2: Bird's eye view of the F1/F2 proton data that is used for determination of the optical model parameter(s) (R, α). Each plot shows a colour-coded 2D histogram of F1 vs. F2. The green line shows the fitted ratio estimate for the light signal between F1 and F2. The plots in line **a)** consist of the three proton positions close to the center of the instrument. The two figures below at **b)** show the runs where significant silicon-hit data has been taken (and the ratio fit has been put through the mixed optical+silicon peak) and are not processed further; they are shown just for reference. Some silicon hit data (esp. top right) can be seen in the center plots **a)** as well. They are assumed to be due to scattered protons and misalignment.

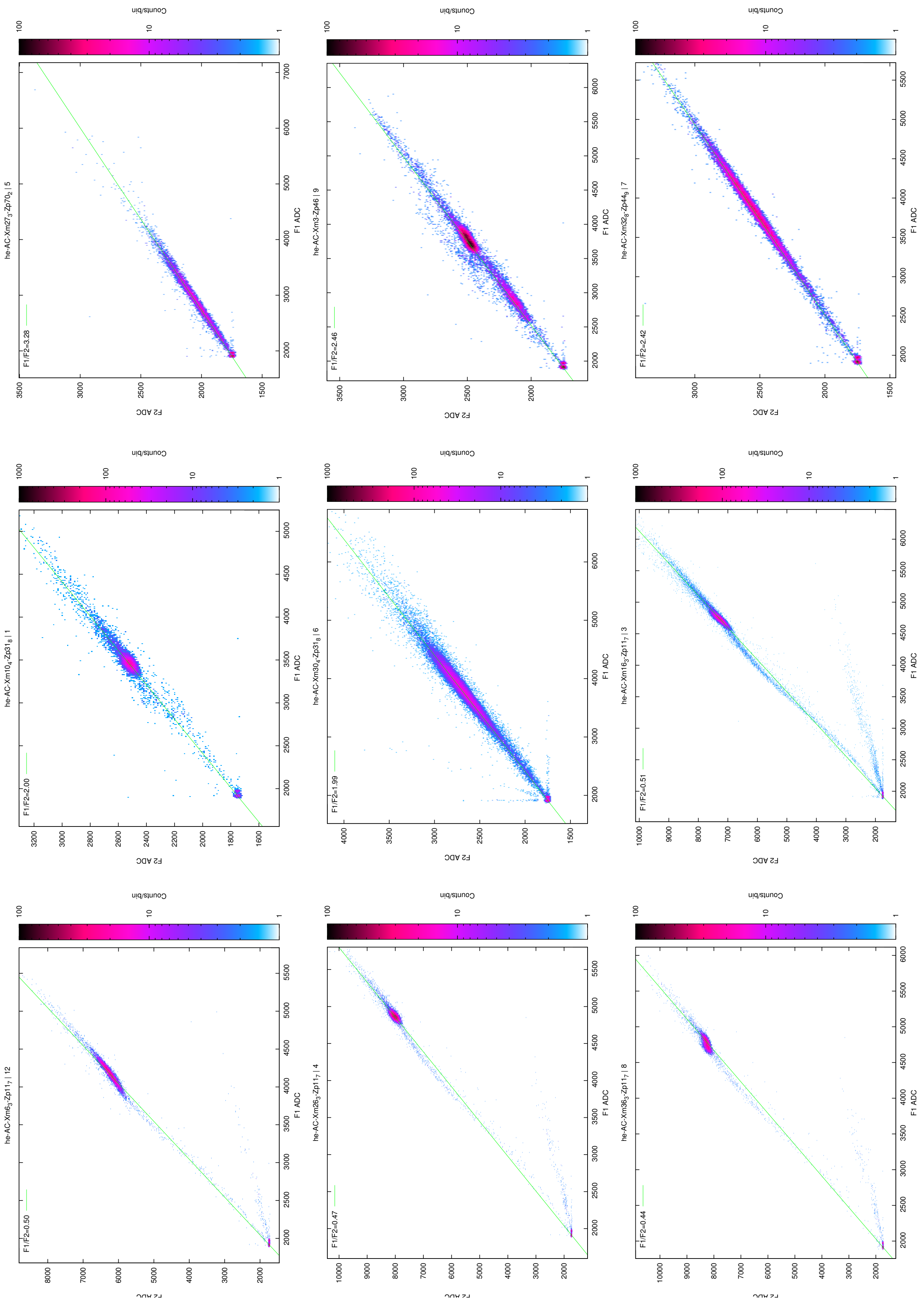

Figure B.3: Top-level view of the F1/F2 helium data that is used for determination of the optical model parameter(s) (R, α), compare also Fig. B.2 on the previous page.

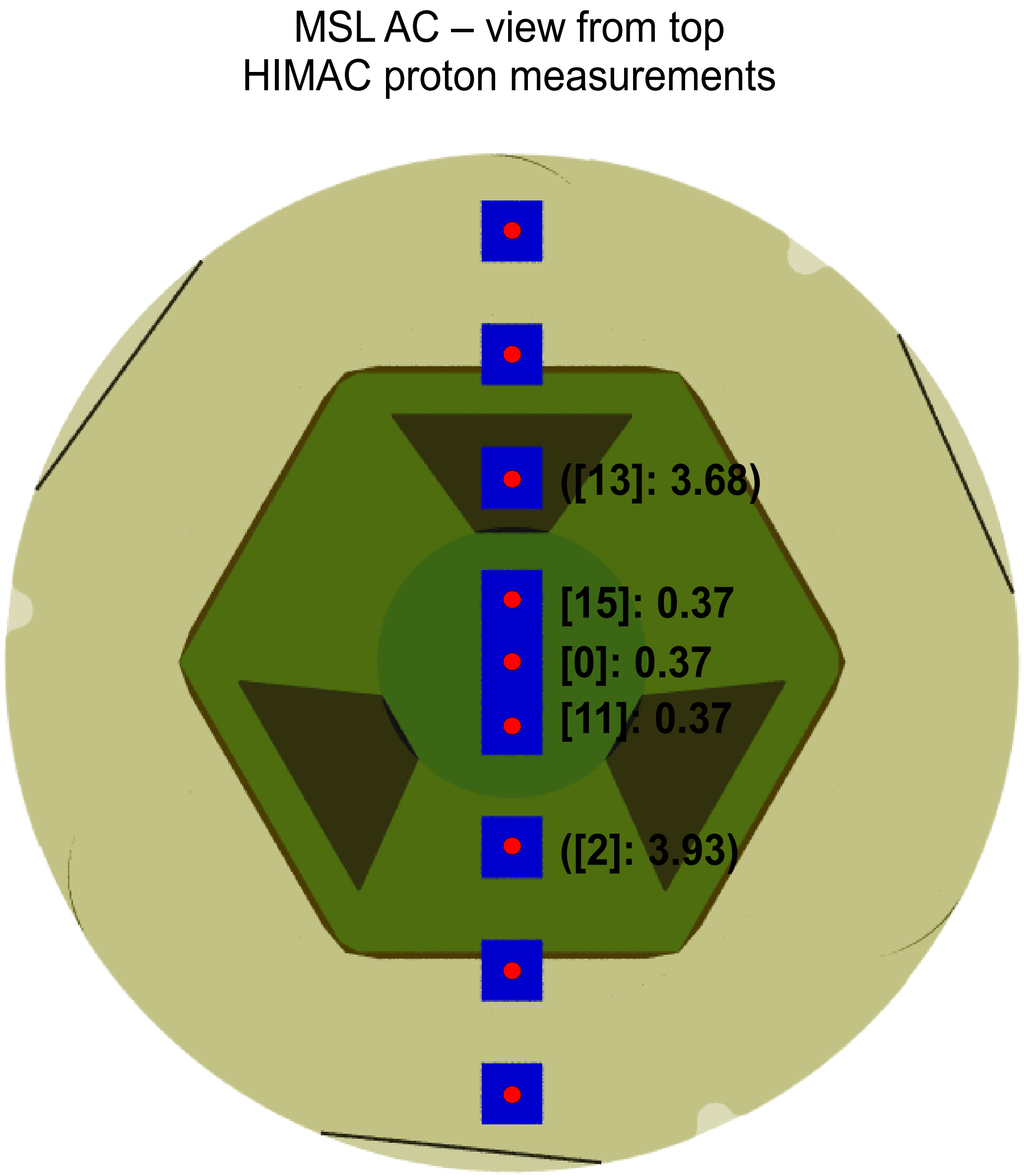

Figure B.4: Top view of the MSL/RAD F (light yellow) and D(, E) (green) detector, with the measured F1/F2 signal ratio. The red dots mark the beam positions, with the assumed 5 mm × 5 mm shape of the beam given by the blue squares. Gain scales are assumed to be equal for F1 and F2 in this plot. The outer two positions give the ratio when including silicon hits (compare also the respective line fit in Fig. B.2) and due to the geometry, no F1/F2 light ratio can be estimated for those positions. They are therefore not processed any further. Also the next outer two positions ([**2**], [**13**]) are not used, as many silicon hits are expected. Protons with an energy of 160 MeV have been used to produce this data. After exit from the vacuum window, the beam passes through a protective (against dust) thin Llumalloy cover foil before hitting the instrument.

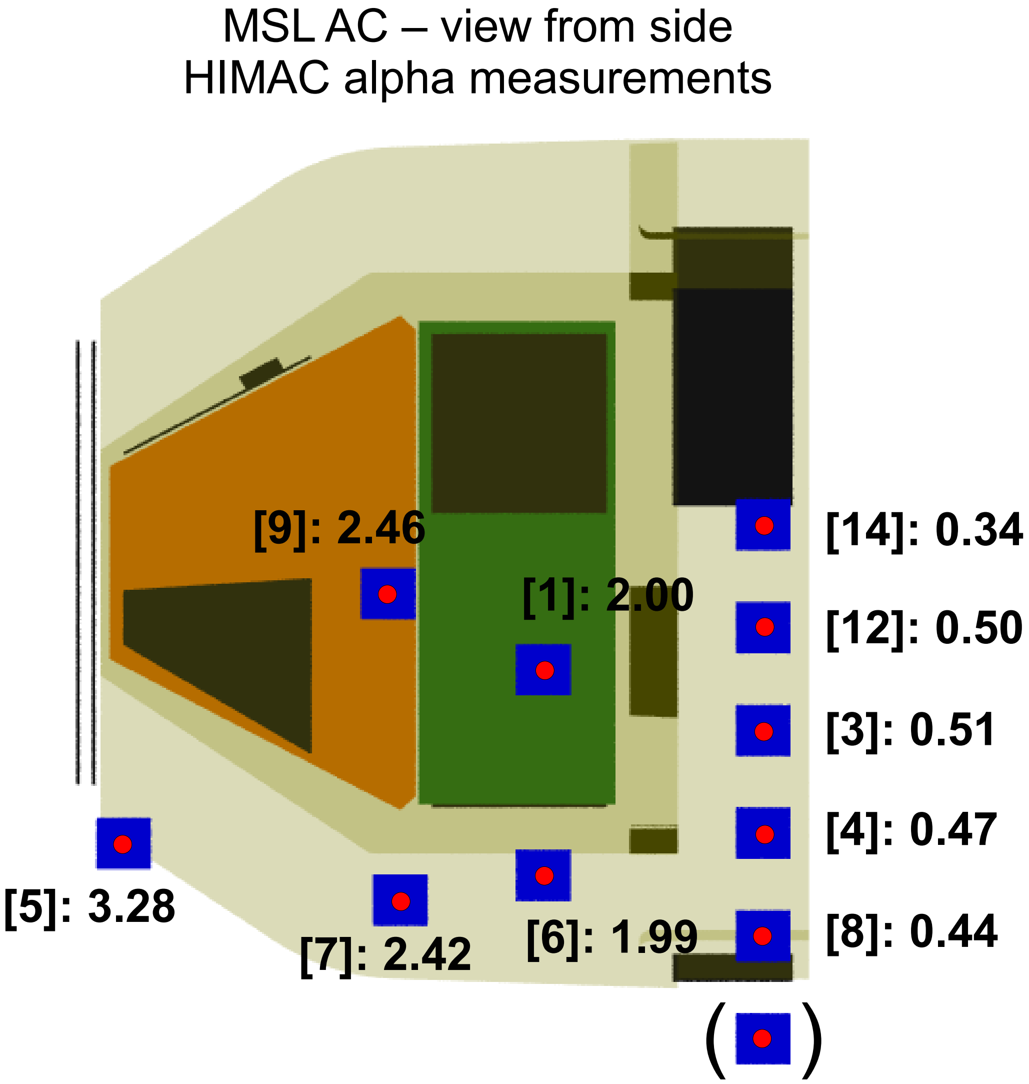

Figure B.5: Side view of the MSL AC (light yellow), with D (red) and E (green) detector visible and the positions of the run done. Like for Fig. B.4, the F1/F2 ratio for the different marked run positions is given. Again, equal gain of F1 and F2 is assumed here. Helium with 180 MeV nuc^{-1} has been used to produce this data. The housing and the protective Llumalloy covering is between the exit window of the beam and the scintillators. The position shown in brackets at the bottom right in the picture is an additional test position with the collimated beam outside of the instrument and is not further processed.

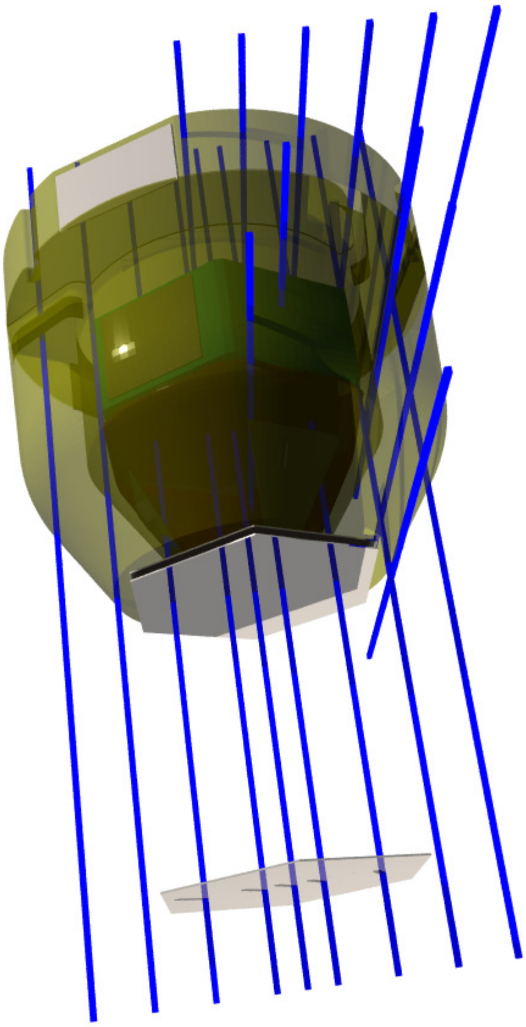

Figure B.6: 3D overview of the AC run positions in Figs. B.4, B.5, in respect to the AC.

Appendix C

Further details for the full model

This section covers details that are missing from the main explanation of the full model in Sec. 6. Further details on the selection of the final set of parameters are given and the calculation of the fit error bars is discussed in detail.

The fit ranges and bin widths are given in Tab. C.1, the noise values for fit error estimates in Tab. C.3, and in Fig. C.1, the reduced χ^2-distributions of doing the MC error bar estimation for the fit results of the final model can be seen. In Tab. C.2, the covariance matrix used as the noise input for the statistical error bar estimation of the forward calculations in Chapter 6. Further best fit results are given in Figs. 6.1, C.3, and C.4.

Channel	**Bin width**	$\mathbf{x}_{\min}$	$\mathbf{x}_{\max}$
CU	8	1500	3000
DN	2	1500	1700
EU	32	1500	4000
F1	16	2000	8000
F2	32	1300	6000

Table C.1: Bin widths and fit ranges $x_{\min}, \ldots, x_{\max}$ that are used for fitting the full model single-channel-wise to the data.

	c Opt/Si MeV	σ_n(F1) keV	s(F1) ADC MeV^{-1}	o(F1) ADC	σ_n(F2(r)) keV	s(F2(r)) ADC MeV^{-1}	o(F2(r))ADC
c Opt/Si MeV	1.6	0.0043	-38	6.9	0.0043	-38	6.9
σ_n(F1) keV	0.0043	0.000 12	-0.17	0.13	0	0	0
s(F1) ADC MeV^{-1}	-38	-0.17	1.4×10^3	-2.9×10^2	0	0	0
o(F1) ADC	6.9	0.13	-2.9×10^2	2.5×10^2	0	0	0
σ_n(F2(r)) keV	0.0043	0	0	0	0.000 14	-0.34	0.31
s(F2(r)) ADC MeV^{-1}	-38	0	0	0	-0.34	1.1×10^3	-7.5×10^2
o(F2(r))ADC	6.9	0	0	0	0.31	-7.4×10^2	7.3×10^2

Table C.2: Assumed covariance matrix for the statistical error estimation of the F1 and F2(r) behaviour. The units of the values in the matrix are appropriate products of the units given in the header row.

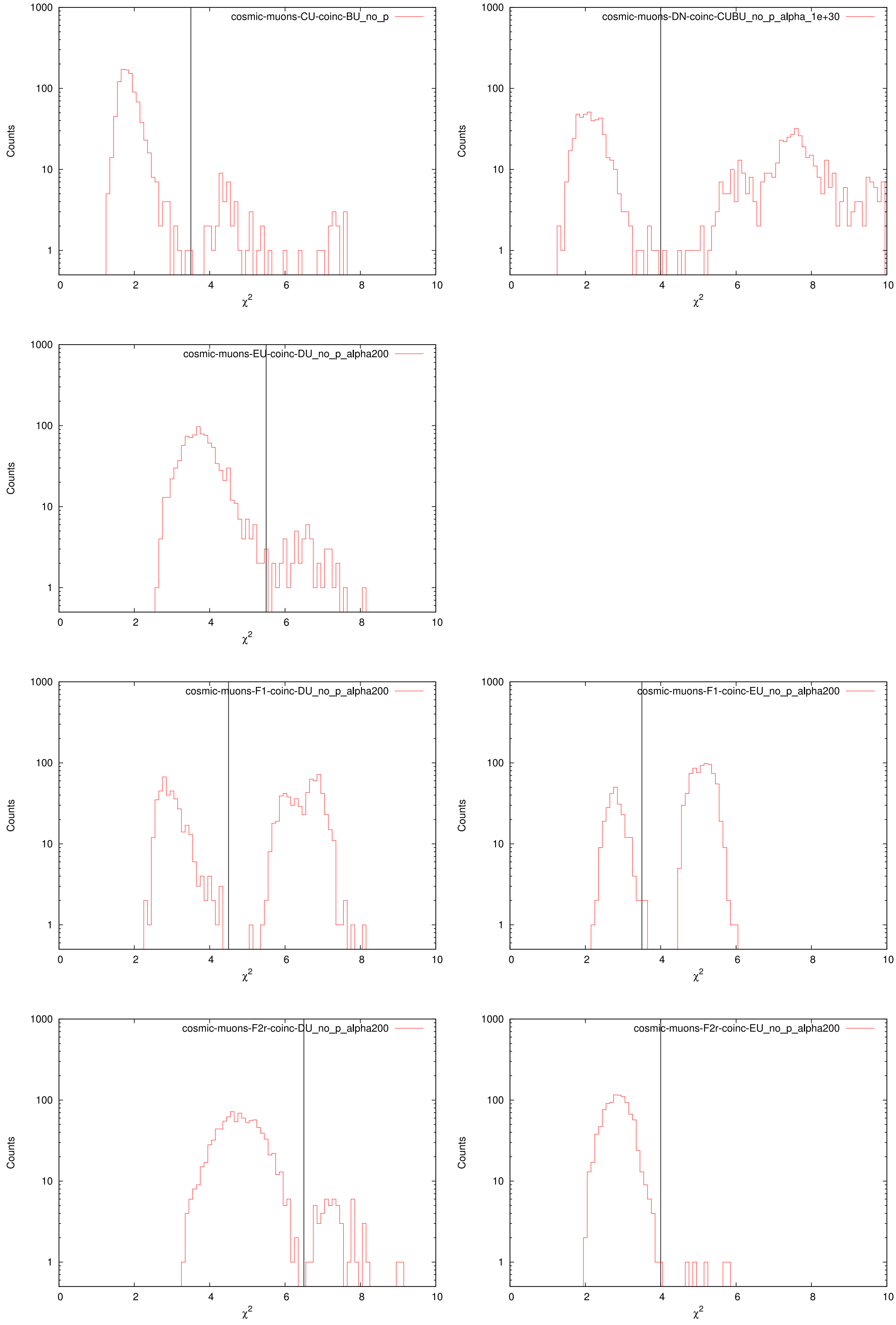

Figure C.1: χ^2 distribution from Monte-Carlo error estimation for the selected models, for each channel. The vertical bar denotes the cut that has been done on the χ^2 to remove outliers before calculating fit error bars.

Parameter	Rel. noise
$\hat{y}$	0.1
c	10
σ	1
z	0.25
s	0.1
o	0.05
m	10
p	2

Table C.3: This table gives the selected, relative amount of noise for each fit parameter (distributed according to log uniform distribution).

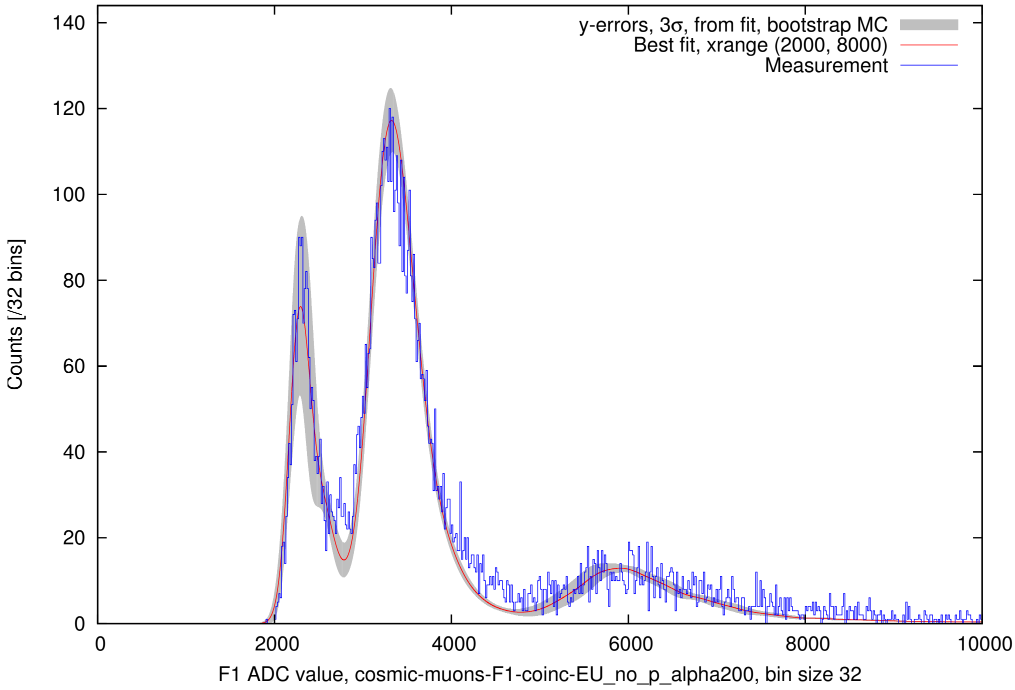

Figure C.2: Selected best single-channel fit for **F1** channel to cosmic muon input data. Coincidence selected with EU channel.

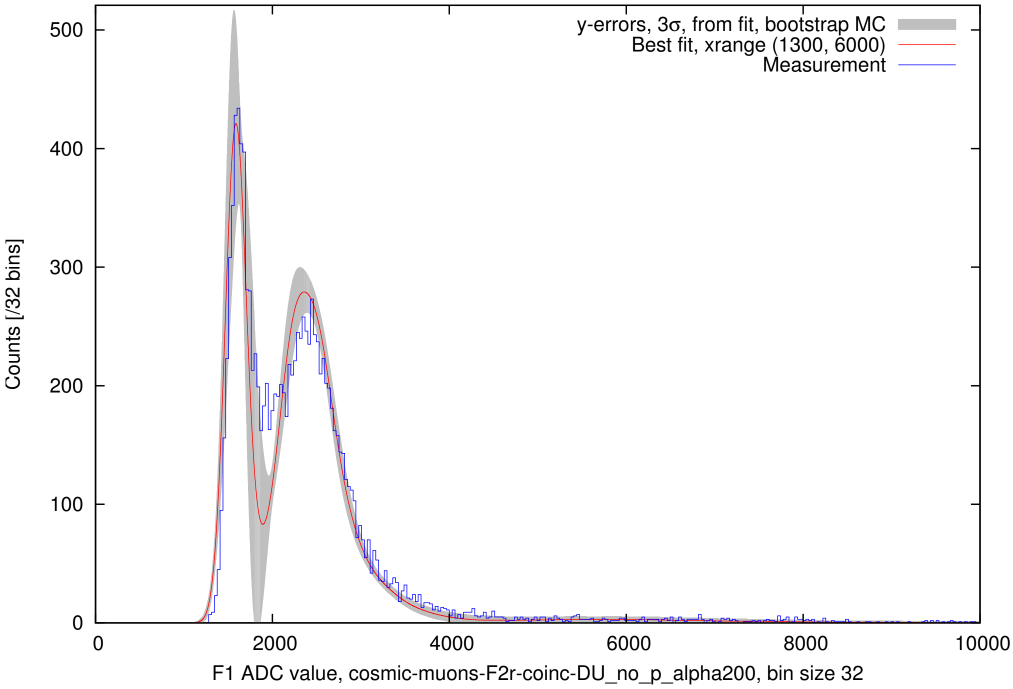

Figure C.3: Selected best single-channel fit for **F2r** channel to cosmic muon input data. Coincidence selected with DU channel. A larger difference between model and measurement can be found in the low energy range between noise and MIPs peak. This deviation is the reason for taking a factor 2 in systematical errors.

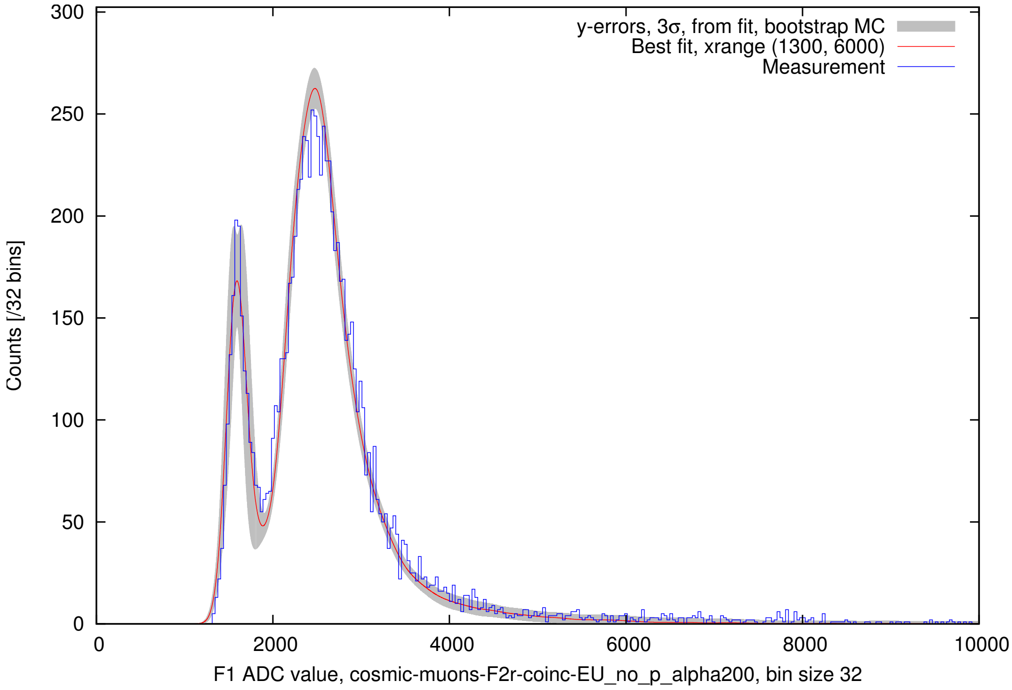

Figure C.4: Selected best single-channel fit for **F2r** channel to cosmic muon input data. Coincidence selected with EU channel.

C.1 Output of combined optical and `GEANT4` model

The output set of values from the combined optical and `GEANT4` model is a set of values for each event, from the following list:

sA, sB, sC The amount of energy deposit in the *whole silicon* of the A, B or C detector.

Ainner, Aouter, B,C,D,E,F Total energy deposits in the logical detectors B, C, D, E, and F. Without optical effects.

$D_{1,2,3}, E_{1,2,3}$ Direct silicon hit signals in the three readout diodes of D resp. E.

$F_{1,2,3}$ Direct silicon hit signals in the three bottom readout diodes of the F scintillator.

C_AC Direct silicon hit signals in the outer C ring reading out the top F scintillator.

B_C2, C_C2 B resp. C part of the C2 channel.

$oD_{1,2,3}, oE_{1,2,3}$ Light signal in the three readout diodes of D resp. E.

$oF_{1,2,3}$ Light signal in the three bottom F diodes.

oF_4 Light signal in the outer C top anti-coincidence diode. Please note that this is in reverse order to F1/F2 where F1 means top and F2 means bottom! The rationale for this order is to have the three symmetric bottom diodes at the same positions in data processing arrays as the D/E symmetric readout diodes.

Appendix D

Further Monte-Carlo results

A few selected additional results from the optical high-energy MC calculations of RAD are given here. In Fig. D.1, the response of the D crystal, as calculated by C. Martin with `FLUKA` can be seen. Fig. D.2 shows the neutron response as calculated with a pencil beam of neutrons. The angular distribution for $\cos^2$ cosmic muons assumed for simulations, binned in θ-bins is shown in Fig.D.3. This is followed by the description of the Martian particle field, as used for the AC forecasts (Sec. 6.8.1) and a basic rate estimate in RAD using these Martian particle fluxes. In Sec. D.3, the differences between the distinct `GEANT4`-based MC setups are listed.

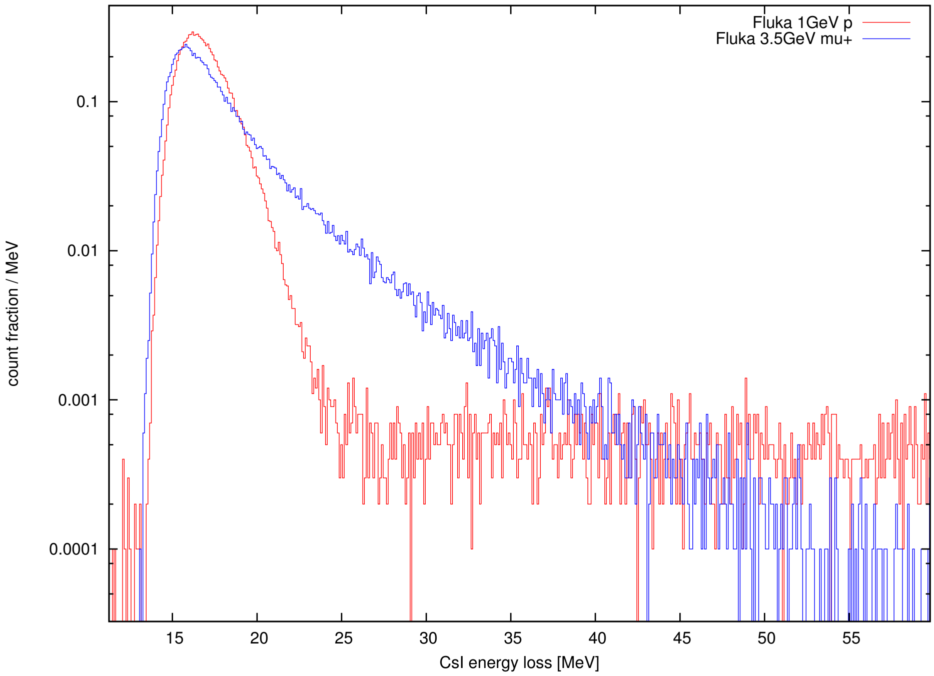

Figure D.1: `FLUKA` simulation by C. Martin of the energy loss in the MSL D detector for a pencil-shaped beam of μ_+ (blue) and a beam of p (red), coming from zenith. Simulated 100 k events. The energy loss MPV for muons is at 15.8 MeV, for protons at 16.3 MeV, with mean values of 18.2 MeV and 23.5 MeV respectively. This is the input curve to simulate the energy loss straggling in the E direction in Sec. 3.4.

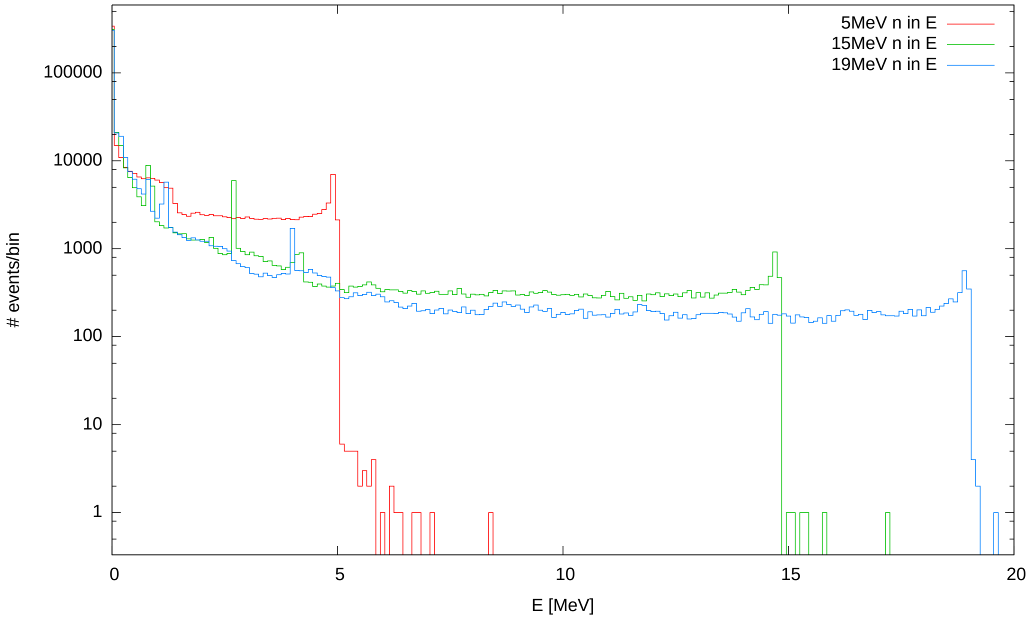

Figure D.2: Simulated energy loss (using the `GEANT4` model of RAD from E. Böhm and S. Böttcher) of PTB neutrons $(5, 15, 19\text{MeV})$ in the E channel. Neutrons are shot into the instrument from the front, in a thin beam through the center of the instrument. Simulated 10^6 incoming neutrons.

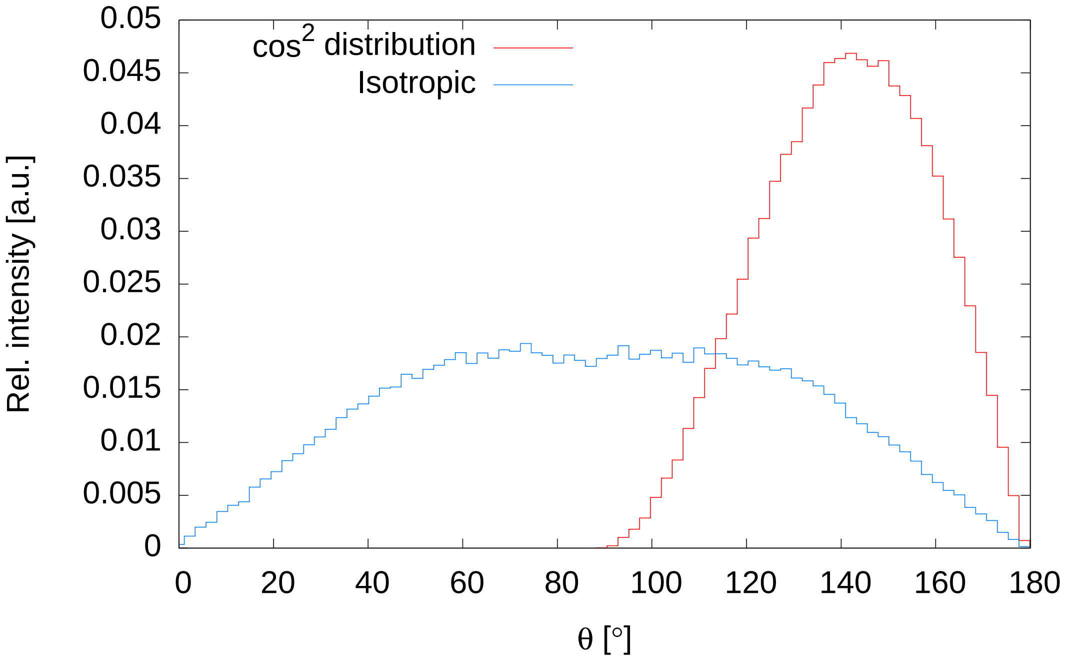

Figure D.3: Simulated distribution of θ-angles of events for the runs with $\cos^2$ angular and with isotropic distribution. Shown is the angle of the direction a primary particle is *going to*. The data is binned into equal sized $\Delta\theta$ bins. Shown is the output from MC distribution generation procedure *when requiring any hit in any of MSL's detectors* A . . . F (and thus projecting to the whole MSL detector area!). Note also that the detectors are aligned in the order A . . . F with decreasing z-position in the instrument's CAD model but θ is measured against $+z$.

D.1 Martian particle distributions

The following distributions have been calculated by B. Ehresmann using the `PLANETOCOSMICS` code (*Desorgher et al.* [2006]). For each simulation (protons and neutrons), a total of 100 k primary events has been simulated. So far, the primary events are assumed to be only due to protons. Solar minimum conditions and an energy range of 1 keV . . . 100 GeV are further assumed. The atmospheric level is placed at a height $h = -4.0884\,\mathrm{km}$ (and thus the rover sits in a valley). The geographic position on Mars is 45°N, 180°E. The data has been binned into equidistant bins in $\cos\theta$ direction and into logarithmic bins in energy. The proton distribution can be seen in Fig. D.4, the neutron distribution in Fig. D.5. The total rate of neutrons R_N and protons R_P hitting a sphere with radius r, as calculated by this simulation, are:

$$R_P = 4\pi r^2 \cdot 1.5\,\mathrm{cm}^{-2}\,\mathrm{s}^{-1} \tag{D.1}$$

and

$$R_N = 4\pi r^2 \cdot 11.2\,\mathrm{cm}^{-2}\,\mathrm{s}^{-1}. \tag{D.2}$$

The value of $\cos\theta$ has the following meaning in this context:

$$\cos\theta = 0 \quad \text{particle coming from horizon} \tag{D.3}$$

$$\cos\theta = 1 \quad \text{particle from zenith} \tag{D.4}$$

$$\cos\theta = -1 \quad \text{particle from martian regolith.} \tag{D.5}$$

Details on this and similar simulations will be part of an upcoming bachelor's thesis: Nils Janitzek, "Untersuchung der Winkelverteilung des Strahlungsfeldes am Marsboden", April - July 2010.

The total error of the total simulated rates is given by B. Ehresmann to be $< 10\%$. Assuming this happens independently for each the proton and the neutron rate, an approximate change of $< 15\% (\sim \sqrt{2} \cdot 10\%)$ can be expected to happen for the ratio of protons and neutrons. This error term is included in the error bars of the plots in Figs. 6.6, 6.7, Sec. 6.8.1.

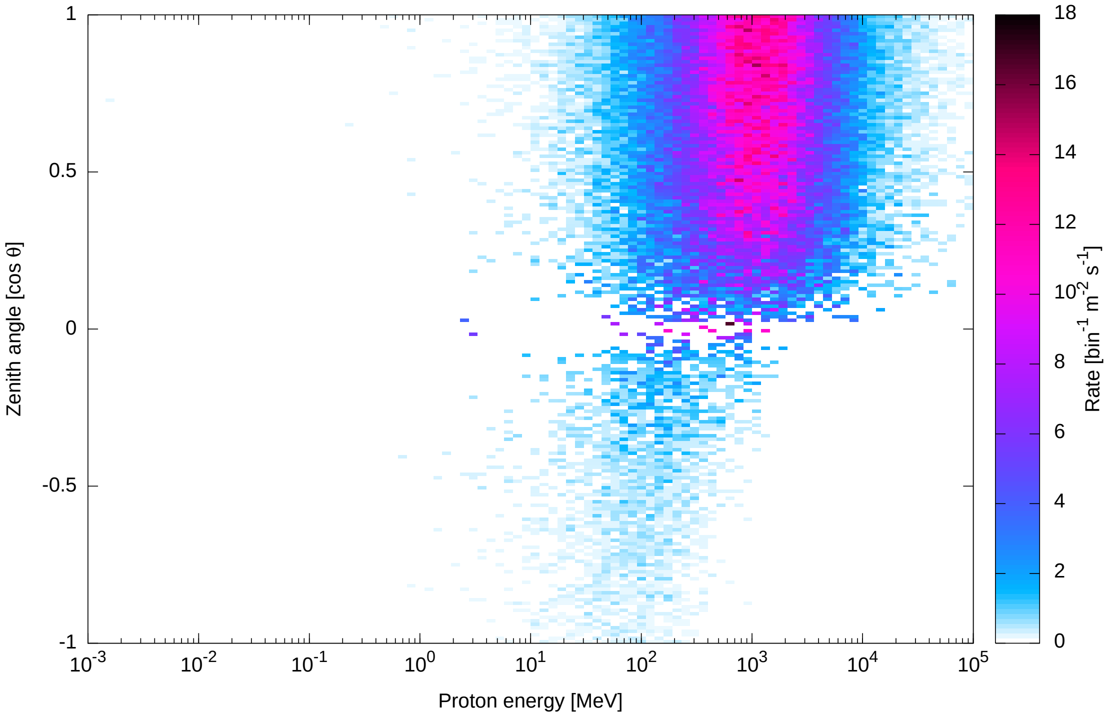

Figure D.4: 2D histogram of simulated angular and energy distribution of protons on Mars.

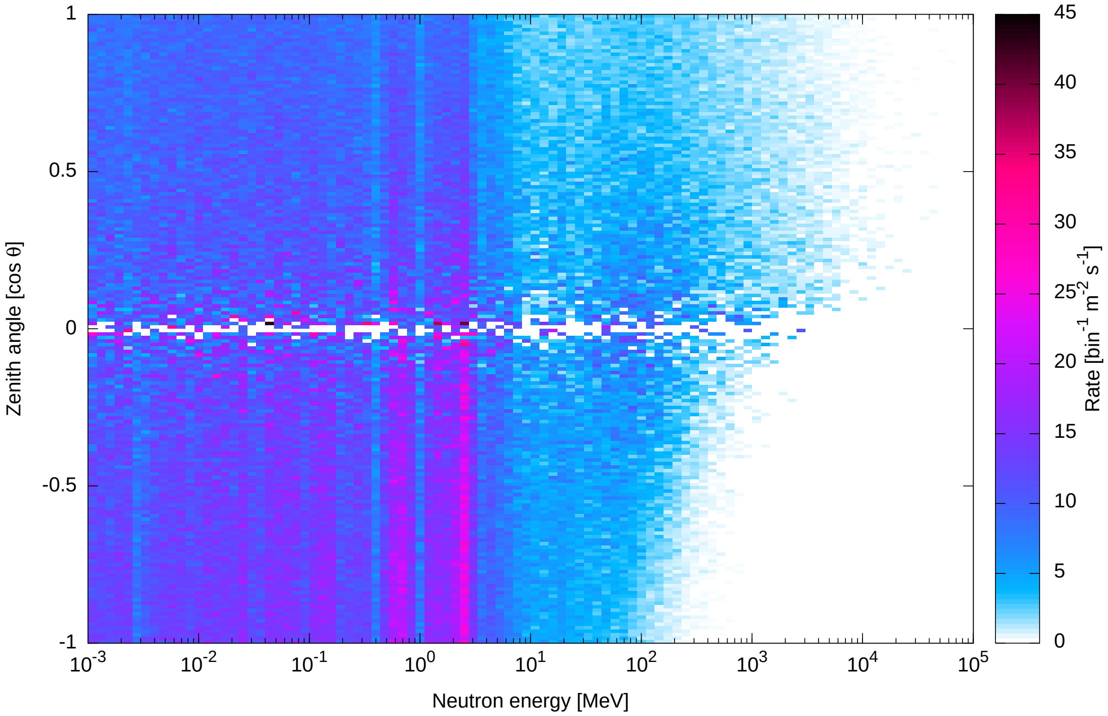

Figure D.5: 2D histogram of simulated angular and energy distribution of neutrons on Mars.

D.2 Expected Martian instrument response

Using the full model and the above input (App. D.1), several performance figures of the instrument on the Martian soil can be estimated. In Figs. D.6 and D.7, the expected count rates for (GCR generated) neutrons and protons can be seen, given a threshold on the x-axis.

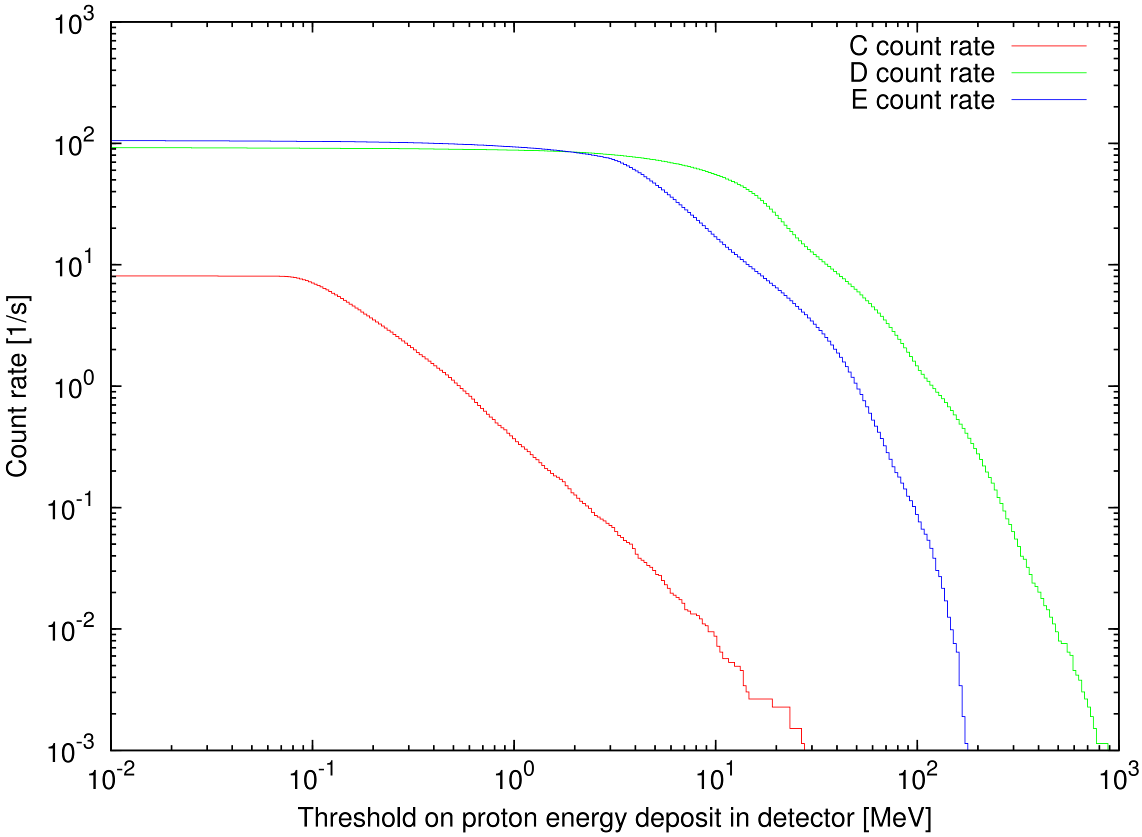

Figure D.6: Simulated integrated count rate of all expected protons in the detectors C, D, E on Mars, for a given energy threshold. This should approximate the proton count rate depending on the trigger selection. The full MSL model has been used with the input flux as shown in Fig. D.4, but no electronic noise or readout noise has been incorporated (as these effects are estimated to be negligible here). Data from MC run with 3.39×10^6 events onto the bounding sphere.

D.3 Differences between particle models of the RAD sensor head

Slight differences exist between the CAD based and the manually implemented model of the MSL geometry. This differences are mainly visible in a change of the coordinate system, but other slight changes are notable and the following list will cover most of the changed aspects, without covering *every* minor detail.

Whereas the manually implemented model is constructed from perfect mathematical shapes, the solids in the CAD model are split into a tessellated surface consisting of triangles. The CAD model covers more detail, but introduces an additional discretization error for the rounded surfaces.

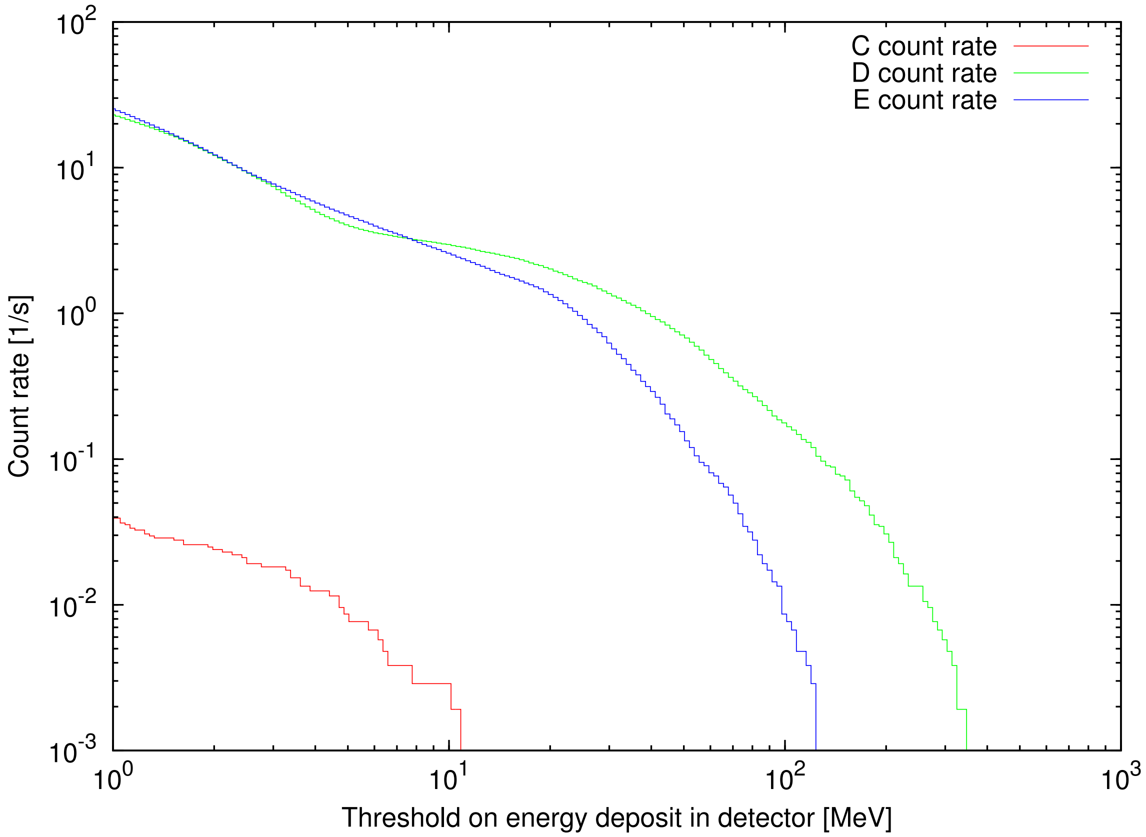

Figure D.7: Simulated integrated count rate of the expected neutrons due to GCRs in the detectors C, D, E on Mars, compare above Fig. D.6. *This simulation does not include the RTG neutrons.* Recently taken RTG data (April 2010) is still being processed. The full MSL model has been used with the input flux as shown in Fig. D.5, again without electronic or optical noise effects. Data from MC run with a total of 1×10^7 primary events onto the bounding sphere.

No unexpected deviations have been found so far when comparing to the old `GEANT4` model. The main visible difference are the expected slight changes in the shape of the scintillator single channel spectra. An example of this can be seen when comparing the Neutron results by E. Böhm in Fig. D.2 to those given in Sec. 7.5, Fig. 7.3.

AC detector. The AC has the largest changes. The top cone includes the curvature of the finally machined piece (instead of being a mathematical cone). The bottom of the top part includes the cable ducts from the D/E stack.

D crystal. The minor chamfered corners at the bottom of the crystal are included.

ABC SSDs. The SSD surface segmentation is taken from the final vendor chip mask, but the CAD geometry of a the SSD has a slight mismatch to the geometry of the chip mask (and the vendor chip mask has been scaled so that it fits the CAD geometry). In particular, in the vendor chip mask, the maximum diameter of the outer hexagon surrounding all active segments and the outer guard ring is 5.07 cm (see App. H, Fig. H.2), whereas the SSD in the CAD model has a maximum diameter of 4.98 cm, a change in surface area of $< 3.7\%$. SSD hit rates may be off by this amount.

Other SSDs. The SSDs are taken from the CAD model and therefore, for all scintillator readout calculations, the active surface area is slightly larger than the active surface area of the real detectors.

Housing. The manual geometry includes a simple description of the housing. This is missing from the CAD based geometry, as it has been neglected as insignificant for all of the work done with the new geometry.

D.4 Further optical simulation results

For the F scintillator simulation using the default surface model `fresnel` (2π) and parameters $\alpha = 200\,\mathrm{mm}, R = 1.0$ (just as described in Sec. 5.3), maps of the sum readout value for light generation at various points through its volume are given in Figs. D.8, D.9.

The most important result in this context is the determination of weak spots in the AC where its shielding is anticipated to be lowest against passing MIPs. In a possible future beam test, these areas should be given extra attention. Comparable to the findings in Sec. 3.9, the $R < 1$ cases looks quite similar to a corresponding one with $\alpha < \infty$.

The behaviour is mostly as expected. In the upper part of the AC, light from the part directly surrounding the E scintillator is most problematic to collect. In the bottom plate, the structure from the cable channels is visible and a ring-shaped modulation of the response due to the number of reflections changing with the radial position in the bottom plate.

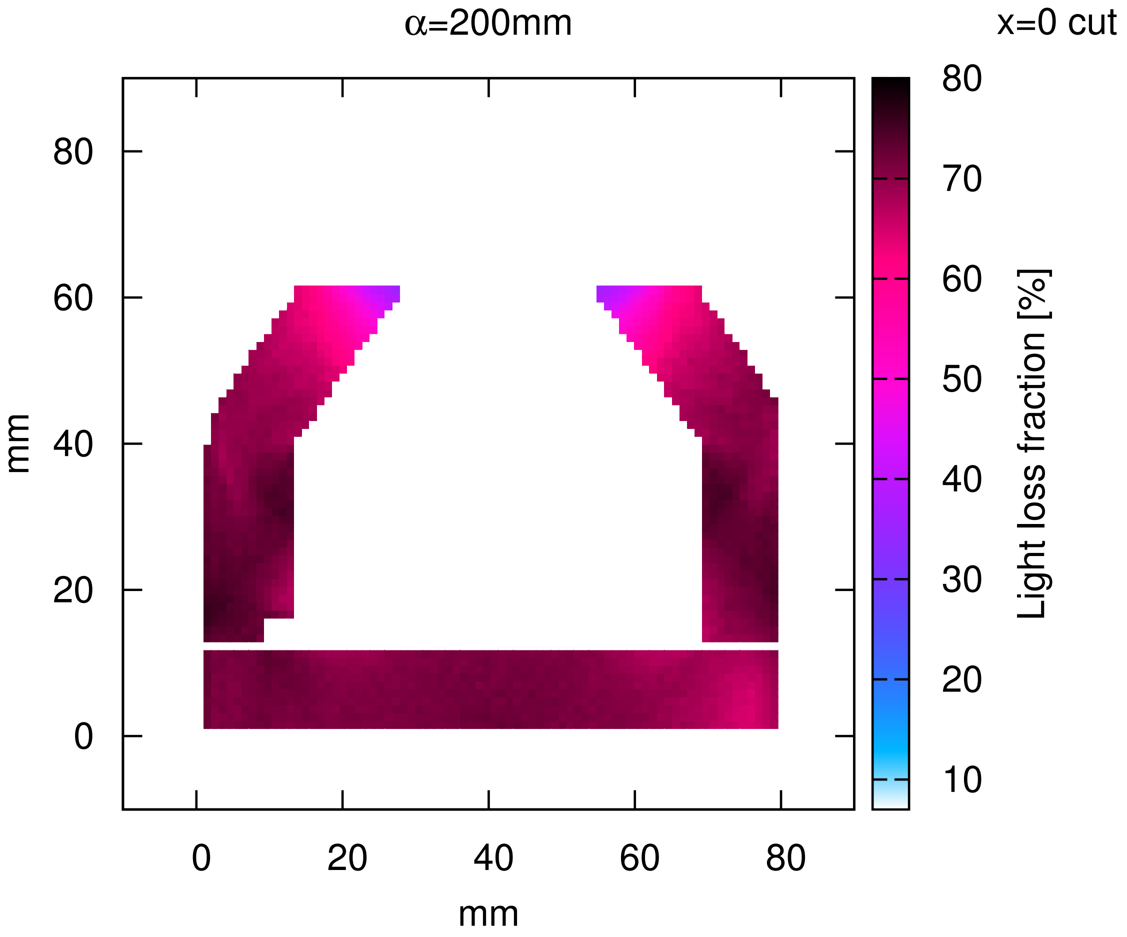

Figure D.8: Sideways cut of the simulated AC response. Fraction of light lost for no reflection losses but an absorption length of $\alpha = 200\,\mathrm{mm}$. The hole apparent in the bottom left part of the top AC is the projected shape of the cable duct through the AC to the E PCB below the E scintillator. As mentioned in Sec. 5.3, three such cable ducts, rotated by 120° each, exist.

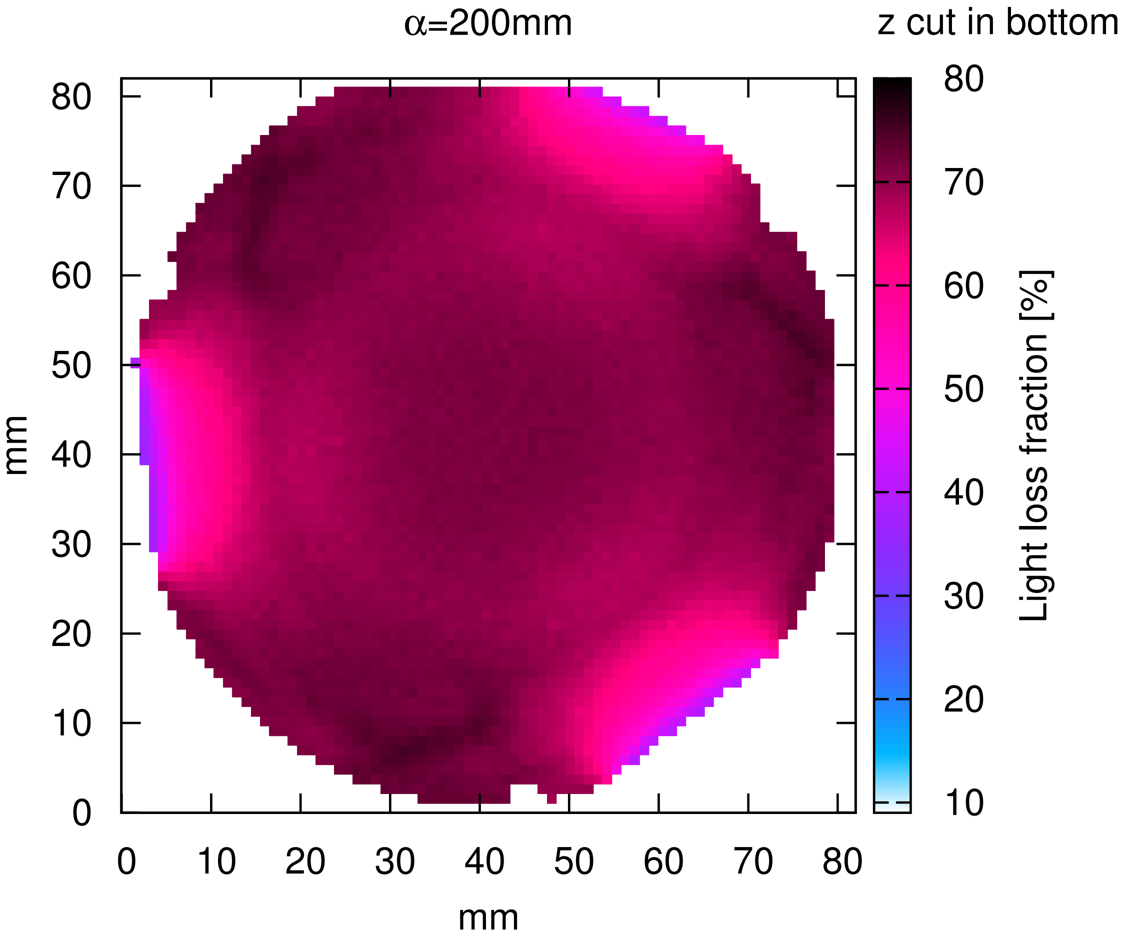

Figure D.9: Cut through the bottom of the simulated AC response. Fraction of light lost for $\alpha = 200\,\text{mm}$ and $R = 1.0$.

Appendix E

Further notes on REB data processing

A few selected notes on processing the REB data, especially some notes about the technical pitfalls encountered when processing earlier data from the REB are given here. The process of noise peak fitting, as done for the input to App. A is detailed next.

E.1 Noise peak fitting

Noise values are affected by temperature and may be affected by additional factors such as cabling between the RSH and the REB. To get the reliable noise figures for a given particle run, it is therefore a good idea to determine the noise peak width from the data in the run itself or a run with comparable parameters.

After filtering as described in App. E.2, the following sequence has been used to fit each noise peak in each channel C_1 for the REB data:

1. Find a suitable trigger condition in a different channel C_2 such that the data in C_1 consists mostly of noise events. To achieve this, it is usually best select C_2 to be physically far away from the considered C_1 such that only few particles produce coincidence events. This is of course only possible with particles such as muons having a large angular distribution, or a sideways run.

2. Select a range $(x_{\min}, x_{\max})$ for which there are almost no other events than noise.

3. Fit a Gaussian function with parameter set (μ, σ, s) (with mean μ and width σ, and with scaling factor $s =$ number of noise events) to the data to determine the best guess at the noise width in ADC values.

4. Error bars for the parameter set has been determined by doing repeated fits using data sampled with the bootstrap sampling MC method [*Press et al.*, 1988, 1992]. Note that to reduce computing time, at most 1 k events are bootstrap sampled from the total set of events. This may slightly overestimate the errors.

E.2 External Electromagnetic Interference

Unfortunately, most of the beam data for RAD+REB has been taken with a cable (some tens of centimeters in wildly varying configurations) connecting the RSH to the REB socket.

This creates additional issues as interference (assumed to be external EMI) couples into the cable and generates burst of events with doubtful contents. The source of this EMI has not been further investigated. Connecting the RSH to the REB in flight configuration, i.e. with the RSH firmly attached to the REB without an additional cable, strongly reduces the effects of external influence.

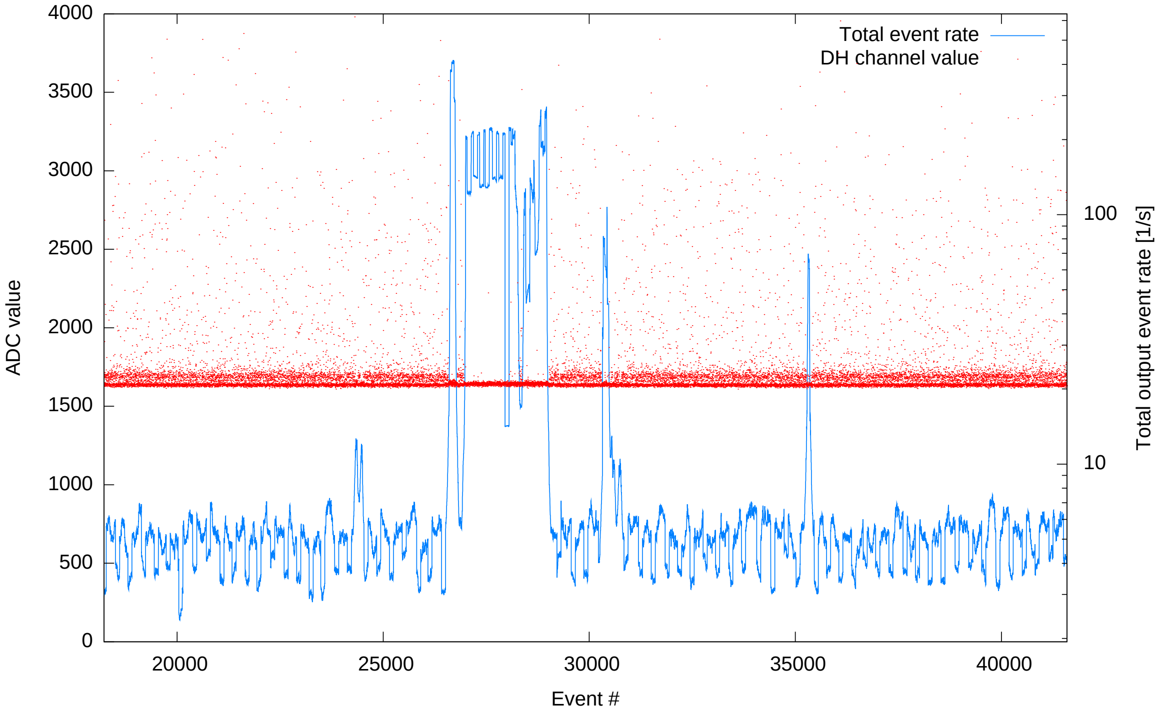

Figure E.1: EMI problem illustration. Shown is a part of the data of a muon calibration run taken in between beam calibration at BNL 05-2008. The red dots represent the ADC samples of the DH channel vs. event number. The blue curve shows the total rate of events received from the REB, for each particular event, calculated from the duration of 100 subsequent events around it. The periodic structure in the rate plot stems from FIFO queueing effects in the REB. It can be seen that there is a shift and change in the shape of the noise during the high rate conditions.

In Fig. E.1, one can see an example of this problem. In this case, muon data has been taken with the KielREB connected to FM2 using an additional cable. Most of the time, the instrument is taking particle data, but short intermittent bursts with a considerable number of events appear in between. For those events, the behaviour of the noise changes strongly.

This interference has been deemed to be a problem in the context of this work only for the determination of the noise peak widths for the model discussed in App. A and will only be discussed in this context in the following. The simplest and most straight-forward way to handle such effects is to ignore them by subsuming them in the overall noise figure and assume that their effect on the intrinsic noise figures is small. With the EMI-affected data included, the model in App. A still fits relatively well ($\chi^2 \approx 2 \dots 3$) - but the noise figures change considerably when excluding these effects.

The method which has been finally implemented is filtering the events by looking at the rate r, determined by averaging the rate over an interval of N_{int} events, as shown exemplarily in the blue curve in Fig. E.1. A maximum rate r_{max} is defined. When the particle rate exceeds this threshold rate, the affected events are thrown away. It is assumed, without further justification, that the events which do not exceed this rate cut are corresponding to quiet time measurements without EMI. As an additional safety margin, a certain number of events N_{cut} in each direction along the x-axis, is implemented such that events too close to events in the high rate region are also ignored. The parameters for this process, as applied, are given in Tab. E.1.

RSH	**REB**	$\mathbf{N}_{\mathrm{int}}$	$\mathbf{r}_{\max}$ [s^{-1}]	$\mathbf{N}_{\mathrm{cut}}$
FM2	Kiel	100	8	100
FM1	Flight	100	170	100

Table E.1: Rate cuts which have been applied before measuring noise peak widths for the two runs discussed in App. A. Note that these rate cuts have only been applied for the noise peak width determination. No cuts of this sort have been applied in any other data analysis cases discussed throughout this work. Currently, the selection of $r_{\max}$ has to be manually adapted to the baseline trigger rate, which is a weakness of this selection method. The large variation in $r_{\max}$ is easily explained by slightly different trigger threshold settings.

Note that such bursts are responsible for some (but far from all!) of the so-called ‘multiple lines problems’ seen in the data from the calibration REB runs. In a scatter plot of the events for a pair of redundant channels in the VIRENA, this problem manifests itself as multiple parallel lines of data, when only one is expected. In Fig. E.2, the scatter plot for the set of events deemed to be valid (blue and green) and the plot for those which are thrown away (red) before further analysis can be seen, here for the channel pair DN and DL, as this problem is most visible here.

According to E. Böhm [priv. comm.], most of the multiple lines can be selected (and thus excluded), by looking at the fast trigger bits of the VIRENA. This will do a corresponding cut on the data and direct cuts on the data values may give a similar effect. This has not yet been systematically analyzed. The mentioned multiple lines are considered to be at least partly due to non-linear crosstalk effects and appear mostly when looking at a low gain channel if any high gain channels saturates. This may demand corrected offset values for the energy calibration of low gain channels and has not been further investigated yet. Concerning the onboard reconstruction method (as described in Sec. 3.8), this may give an additional error term as trade-off values for the offsets have to be found which are satisfactory both for the saturated and the unsaturated energy reconstruction.

E.3 Determining gain ratios of related channels

Instead of doing a separate energy calibration for each single channel in a redundant VIRENA pair, it is easiest to do the energy calibration for one channel and then use the gain scaling factors to determine the behaviour for all other channels.

E.3.1 Silicon

In the case of the silicon channels, the energy calibration has only be done for one single channel and the relation to the corresponding redundant VIRENA channel is found by doing a simple linear regression. To get useable results, it is important that the regression should be done on a set of real energy deposits > 0 (not only noise triggers). Of such a set, a further selection is used for regression such that it does not contain any saturated ADC values in any channels as well as values large enough in each channel to stay clear of the region where

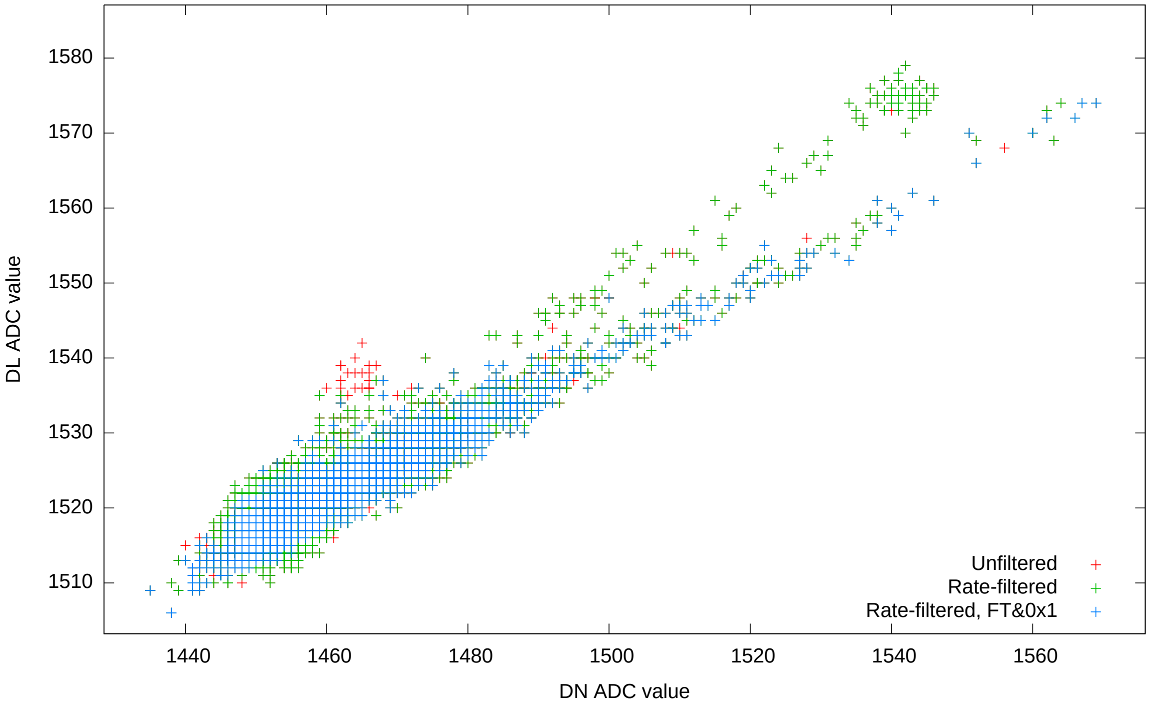

Figure E.2: EMI problems for a pair of redundant channels. Same data set as in Fig. E.1, but note the different channel selection. The red points represent the unfiltered, complete data set. The blue points denote the data after applying the rate filter, and exemplarily an additional condition on the fast trigger bits (FT & 0x01), leaving only the part unaffected by the multiple lines problem (in this case).

the multiple line problems may happen. It is important to keep the ADC saturation in mind here. For example, during muon runs, there may be only very few events saturating any given detector and they will thus be hard to notice in a scatter plot - but will nonetheless affect the fit result considerably. Also, for the silicon channels, the same method has been applied to redundant channels ending at the same physical detector but with different shaper stages in between. Slightly nonlinear behaviour has been seen in some channels, but this effect has not been further investigated yet.

E.3.2 Scintillators

The silicon gain determination can be applied for redundant readouts of a single photo diode attached to a scintillator exactly as above. For the calibration of the gain between different diodes attached to a single scintillator, the same method could be used. A complication is that any simple cut on the event data will bias the data much more strongly as above, as the spread of the signal between the scintillator diodes is much larger. Also, any silicon hit signals will influence the results strongly. Depending on the data set, manual fitting of visible peaks and/or edges in the data can be used to determine the scale. Or the following method can be applied, to avoid these bias effects and the exaggerated effects of silicon hits on the fit result (here, for a higher gain channel H and lower gain channel M):

1. An initial guess of the channel gain ratio $g = \overline{\left(\frac{H}{M}\right)}$ is done manually. A proper cut on the higher gain channel is selected.

2. ADC saturation events and noise signals are filtered out with the selected cut. To achieve symmetry, the approximate factor g is used to scale the ADC cut threshold as well as the noise threshold in H into units of M and apply it on this channel as well.

3. The factor g is determined by minimizing the sum of absolute deviations (as described in *Press et al.* [1988, 1992]).

4. The process is iterated at step 2. until no further change in g occurs.

Care must be taken that a sufficiently symmetric particle field is used for any scintillator inter-channel calibration. Another possibility is to fit single-channel spectra to MC results or against each other, see Chapter 6.

E.4 General processing of calibration data

As described in Sec. 2.7, the calibration data of RAD has been mostly taken through a special probe port on the engineering REB units. This high-speed mode gives access to the raw output of the L2 FIFO through a second serial link to the REB. The link is used in-flight as a redundant connection to the rover.

Picking the data at this point is necessary, as no calibration tables and/or functional and tested L3 software was available for the test and calibration runs. A major purpose of the test runs was to find values and constraints for this L3 processing software. The high-speed link allows to get a view of all RAD channels with acceptable statistics.

It is possible to make offset corrections as well as data prioritization with the L2 module. To have the most transparent view on the raw ADC values, these facilities have only been switched on for a few select runs. But each run should be checked for such settings, as for some tests, highly inconsistent settings have been used.

To be able to study the physical behaviour of the various detectors in the REB, it is necessary to perform several steps with the raw data, which are normally done in-flight. The result is akin, except for the data compression step, to the output of L3 processing.

1. Remove/mark data which is corrupted due to glitches in any of the data links.

2. Remove/mark spurious follow-up events by time-stamp and/or spill-phase filtering.

3. Perform offset correction and noise estimation per channel, crosstalk corrections if necessary and do linear energy calibrations per electronic channel. For MC comparisons including readout modeling, this step can be excluded.

4. For the silicon channels: Select the electronic channel that maximizes energy resolution.

5. For the scintillator readout channels: Remove/mark combined silicon+light hits, reconstruct total amount of light and apply an approximate inverse quenching curve[1]. This step can also be skipped when comparing with MC data that includes such effects.

6. Perform rate corrections if needed.

Details on these various steps for processing are given below. Except for those events which are obviously corrupted by data transmission problems, it is a good idea to only mark affected event rather than filtering it, in order to be able later to verify that the marked data is indeed to be removed and as the whole data chain of RAD has not been fully tested yet.

---

[1] Not knowing whether energy loss happened due to a penetrating or stopped charged particle, dequenching is possible only approximately as quenching according to Birks relates energy-loss non-injectively to light production in RAD, see Sec. 7.5.1, Fig. 7.4.

E.4.1 Data transmission errors

Older REB data was affected by various bugs in the L2 FIFO handling code of the onboard microcontroller in the REB. Certain events in the first fill of the FIFO got repeated in the output data and other events were corrupted with old data in regular intervals, corresponding to the sizes of software FIFOs in the 8051 core. Those have to be filtered out by exploiting their regular pattern. Additionally, there is corrupted data coming out of the L2 high speed link. For recent data taking, this happens very infrequently (on the order of one every 10 k events) and can be counteracted by doing plausibility checks on the decoded events, such as requiring all ADC fields (which are encoded as 16bit in the packet) not to exceed the 14-bit range of the ADC.

Some older REB data is affected by a bug in the VIRENA+ADC+EVIL combination. This bug caused the data being read back to contain zeros for some channels and some events. The events which are affected by this should be thrown away. It can be checked whether a given data set is affected at all by this bug, by looking at a set of channels for which events exist that have a 0 ADC value in that particular channel. If this matches exactly to the inverse of the selected readout mask in the L2 module, the data can be assumed not to be affected by this problem.

E.5 Crosstalk

The PCB traces in the RSH (the ‘Flex-board’) as well as on the REB analog board cause crosstalk between different detector channels. The multiple lines problem (as shortly described above) is assumed to be mostly due to non-linear crosstalk of saturated high gain channels onto the set of low gain channels. A linear crosstalk correction has been tried. This simple method has not been able to explain and correct for the multiple lines problem in the REB. The linear corrections are mostly $< 3\%$ and are thus below the energy resolution (see also Sec. 3.7.1) of the 8-bit PHA words.

E.6 Follow-up events and pileup

Pile-up. The VIRENA has a window of 5µs for the peak detectors to close after receiving a fast trigger. Any particle producing a second hit in any of the detectors will lead to pile-up. Pile-up as a source of bad data has been deemed especially a problem during the BNL runs with the flight REB. The accelerator time structure on the NSRL beamline has recently been changed. For the runs 2008, May and June, the particles arrive in approximately flat rate spills of 300 ms, with a total cycle time of 4 s, about 1000particles/spill. This gives a random coincidence rate in the spill interval of about

$$r_c \approx 2 \cdot 5\mu\text{s} \cdot 3000^2/\text{s} = 90/\text{s} \approx 30/\text{spill} \tag{E.1}$$

No good way to exclude events affected by pileup in this case has been found yet, but the spill structure can nonetheless be exploited (see below).

Follow-ups. When a high-energy deposit occurs in one of RAD’s detectors, it is possible for the REB electronics to detect a spurious second event following the first one. The reason has been determined to be long recovery times to baseline output for the preamplifier and the shaping stages in REB in combination with not fully understood behaviour of the VIRENA in such cases.

Removing these VIRENA events is possible for all runs made in 2008, as a time stamp facility has been introduced in the L2 module which allows to filter against events which have a small Δt. This facility stamps the incoming events with µs-resolution, although they can be delayed by the incoming FIFO. Usually, this filter is set such that events with $\Delta t < 512$µs are rejected.

E.7 Phase selection

For those runs which have a clean spill structure, such as all BNL runs, it is possible to reconstruct the spill phase from the time stamp data and use this reconstructed phase to filter the data for certain maximum rates and determine an in-place background.

E.8 Rate correction

Several correction steps are necessary to obtain real particle rates from the output of the instrument. For rate correction, events with different priorities have to be processed separately, indeed each trigger entry in the L2 table has to be processed separately. The instrument contains a multitude of counters, mostly to have a detailed view of the frontend of the instrument for each channel. For rate corrections, a total of five counters have to be used:

1. The frontend global live-time counter, let this be c_f. This counter is fed by the system clock as long as the VIRENA frontend is enabled.
2. The L2 readout counters for low and high priority, let them be $c_{r,l/h}$. Each readout of an event from the L2 FIFO increases the corresponding counter.
3. The L2 trigger counters for low and high priority, let them be $c_{t,l/h}$.

The total rate $r_{l/h}$ for a number of low- respective high-priority events $N_{r,l/h}$ is

$$r_{l/h} = n_{r,l/h} \frac{c_{t,l/h}}{c_{r,l/h} c_f}. \tag{E.2}$$

In the case that all triggered events are read out and rate reduction happens only due to the VIRENA being switched off regularly (housekeeping reading during a calibration run), only the L1 correction needs to be made.

Appendix F

Technical details of the photon Monte-Carlo

A few more rough details are given regarding the optical photon simulation code as it has been used to describe the scintillators in this work. For more details, refer to the technical documentation describing the code.

A flowchart of the photon model is given in Fig. F.1.

In Fig. F.2 an example of the resulting photon weights according to Eq. 3.7 (Sec. 3.1) is displayed. The 'oscillation' that is visible is due to the discrete reflections scaling the weight with the factor R each time. Also visible is the smearing $e^{-\frac{l}{\alpha}}$ of the discrete term R^{n_R} with a decrease in absorption length α.

In Fig. F.3, a full wireframe view of the triangle surface as it is used for the anti-coincidence part can be seen, to have an overview over the geometrical resolution used for scintillator modeling throughout this work.

F.1 Geometry handling

As it needs to be evaluated in the innermost loop of the photon tracing, the most complex part of the simulation infrastructure are the functions handling intersections with the triangle face list from the CAD system.

For computation efficiency reasons, the triangles are handled by a binary space partitioning tree structure, which allows to do ray-object intersection tests faster than traversing a linear list.

This tree structure recursively divides the space which contains the triangular faces into two half-spaces. Arbitrarily oriented planes are used for space subdivision.

The heuristics which has been used for finding appropriate splitting planes in the BSP tree mainly tries to balance the number of triangles in the left and right halves per splitting for a set of planes chosen randomly out of the set of triangle planes at the particular splitting point. The heuristics have only been optimized as far as being usable (acceptable runtime) for the wanted simulation parts.

F.2 Shortcomings

The model is as simple as possible while still taking into account the effects of the rather complex geometry of RAD's scintillators, which is especially of interest for the anti-coincidence part.

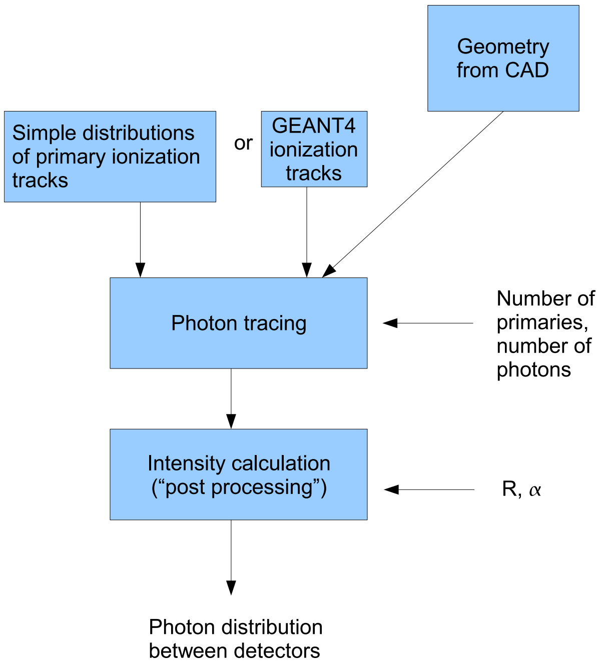

Figure F.1: Processing of simulation data in the described photon Monte Carlo model.

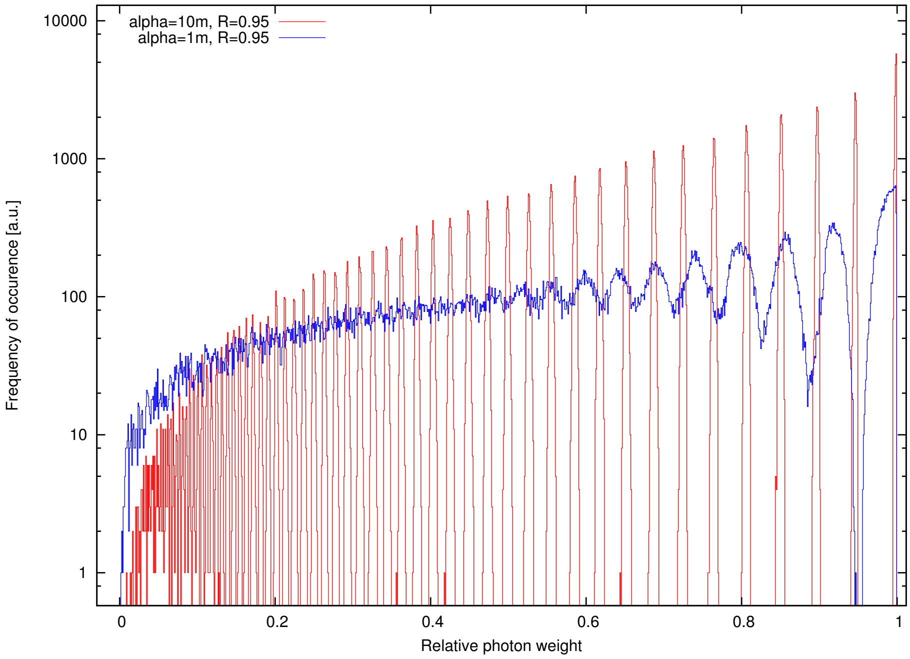

Figure F.2: Histogram of photon weights for photons randomly produced inside the D scintillator, for two different absorption lengths and same reflectivity of $R = 0.95$. Reflectance model is `fresnel`. 100 k simulated photon tracks.

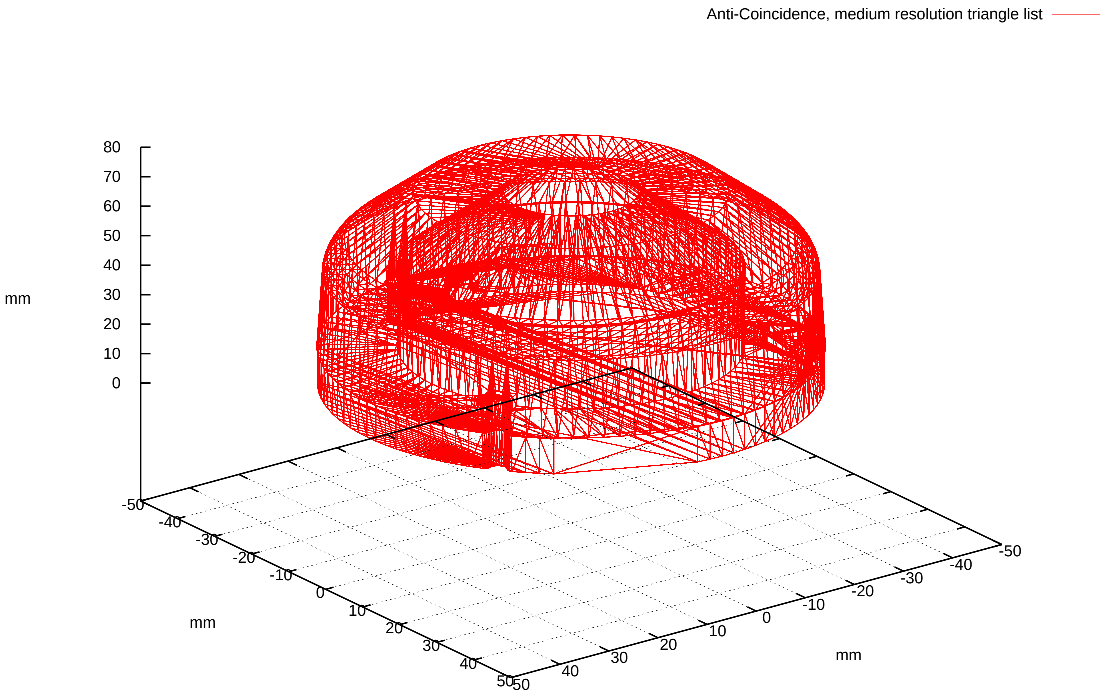

Figure F.3: View of the anti-coincidence, as used for photon simulations.

Fixing the parameters for a more detailed, exact model would at least need a lot of measurements of optical properties of the scintillators and the surrounding materials.

The several shortcomings of the model are, among other things:

Detector model Absorbing all photons in the detectors ignores the effects of the different refractive indices of the scintillator, glue layer, and the detector itself.

Bulk Wavelength-dependent effects in the scintillator, such as fluorescence of the material (such as by the wavelength shifting dye) are not modelled. Scattering is not modelled.

Surface The reflection model subsumes all interactions with the surface in a single reflectivity parameter R, although multiple reflections may occur. This is done to keep the ability to evaluate different (α, R)-combinations after a given surface model has been traced, but could be replaced with a physically correct implementation or a better tested simplification of the occurring processes. More systematic studies of all differences between the surface models and the accuracy of the modeling is needed.

F.3 Comparison to other models

Litrani. The special scintillator photon simulation Litrani as the time of this writing lacks support for complex geometric setups. This is the main reason why no further effort has been spent on using this framework for a scintillator simulation.

`GEANT4`. Considerable effort has been spent on implementing the geometry of RAD in `GEANT4` and using the model of *Gumplinger* [2002] to simulate the RAD scintillator behaviour [*Kortmann*, 2006]. The parameter set for the `GEANT4` simulation has been trimmed down to the same set as above, though the optical model of `GEANT4` supports much more detail such as optical photon polarity and more complex models for scintillator/wrapping surface interactions etc.

To use the `GEANT4` photon code, the surfaces of the objects taking part in optical photon processes have to be placed so that they are accurately attached to each other. Unavoidable inaccuracies (floating point precision, gaps in the CAD model, inaccuracies due to the tessellation of otherwise smooth and matching surfaces) in the case of modeling RAD can be partly overcome by adjusting one global constant named `kCarTolerance`, which unfortunately also affects the way photon intersections in the scintillator are made and therefore the effective shape of the simulated scintillator. The normal for surface interactions is determined in a separate step, which causes a larger slowdown.

The `GEANT4` optical photon processes have been tested both with the built-in object for triangle surfaces (`G4TessellatedSolid`) as well as with a BSP-tree based custom object type which initially was planned as a replacement of the linear-list based `G4TessellatedSolid`. The built-in G4TessellatedObject uses a simple linear list of triangles and the custom object is used only for the non-optical simulation part. For the optical simulations, the linear list model causes an unacceptable runtime of the `GEANT4`-based code for any complex triangle based object.

Appendix G

Additional single channel spectra

Some additional single channel spectra for FM1 with FlightREB, and with selected cuts applied, are given below. The C2 channel is visible in Fig. G.1, and the DU channel in Fig. G.2 and F2r for a D trigger in Fig. G.3.

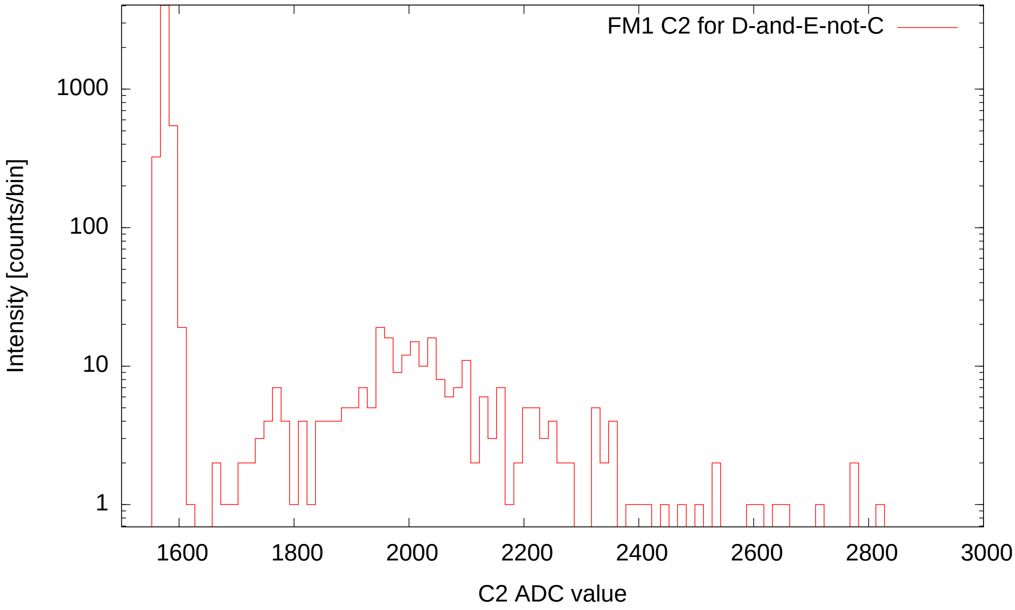

Figure G.1: Shape of the C2 energy loss distribution for a trigger D ∧ E ∧ ¬C. Cosmic muon data from FM1 [#8, μ-FM1-fREB] is used to produce this histogram. It is assumed that hits can be separated from non-hits perfectly. This neglects a small number of particles which may cross the guard ring dead areas.

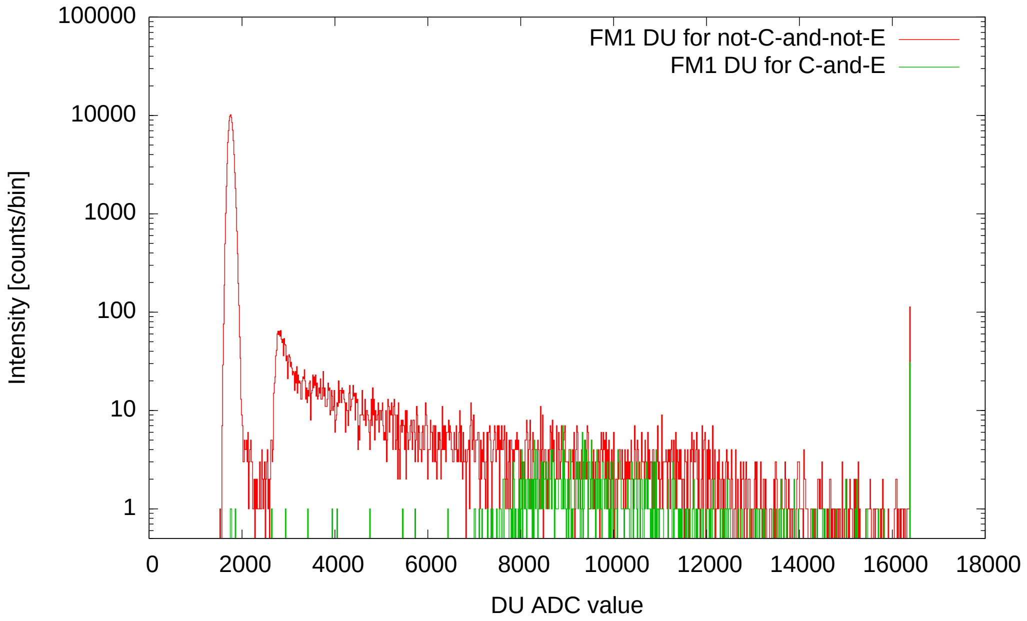

Figure G.2: Shape of the DU energy loss distribution for a trigger B ∧ C ∧ E. Same data set as underlying Fig. G.1. The data is binned into 100 ADC units.

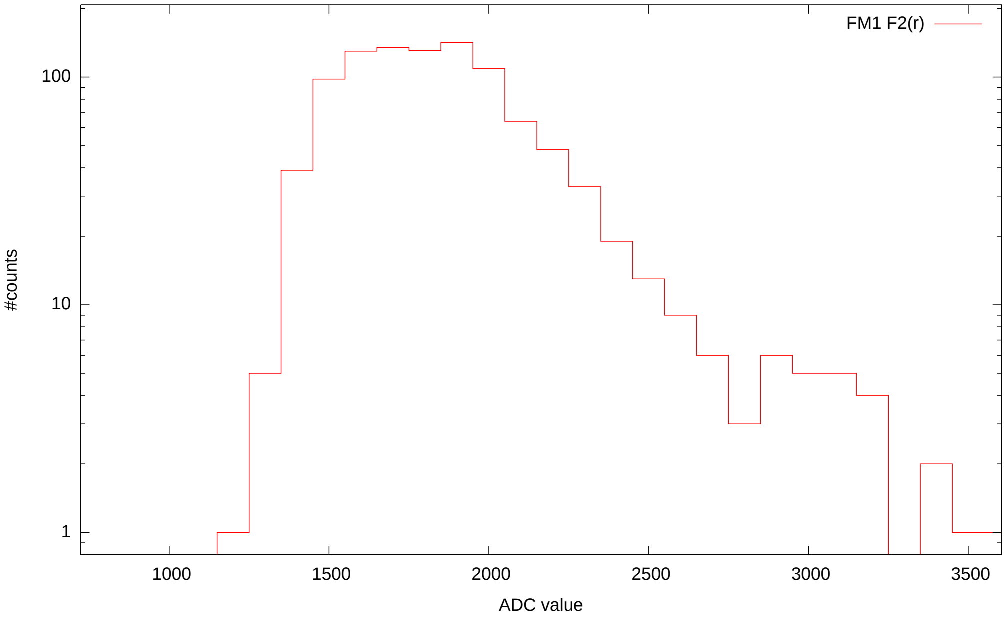

Figure G.3: FM1 F2r energy loss distribution for D triggers. Same data file as for above Fig. G.1.

Appendix H

Additional drawings

In H.1, a schematic view of the segments on the RAD ABC detectors can be seen. A guard ring surrounds each segment. The segments are connected to CSAs to form the MSL RAD detectors in the following way:

$$A_{\text{inner}} = S_C(A) + S_H(A) \tag{H.1}$$

$$A_{\text{outer}} = S_R(A) + S_S(A) + S_T(A) + S_U(A) \tag{H.2}$$

$$B = S_C(B) \tag{H.3}$$

$$C = S_C(C) + S_H(C) \tag{H.4}$$

$$C_2 = S_H(B) + S_R(B) + S_R(C) \tag{H.5}$$

$$\text{AC}_{\text{F1}} = S_S(C) + S_T(C) + S_U(C) \tag{H.6}$$

The letter in brackets denote the physical silicon detector the segment is placed on. Additionally, in Fig. H.2, the dimensions of the final ABC chip mask are given. For more information, see *Böttcher* [2008].

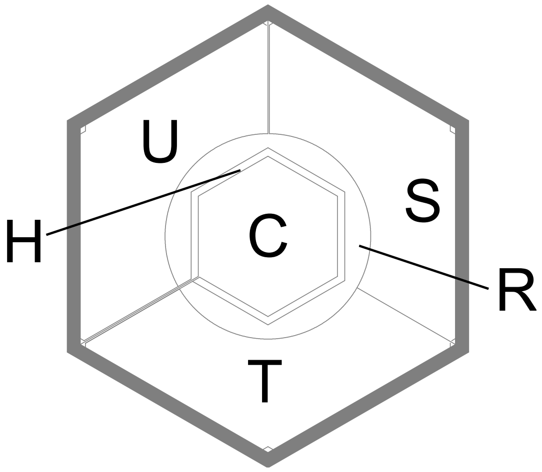

Figure H.1: Schematic view of the various segments on the RAD ABC detectors.

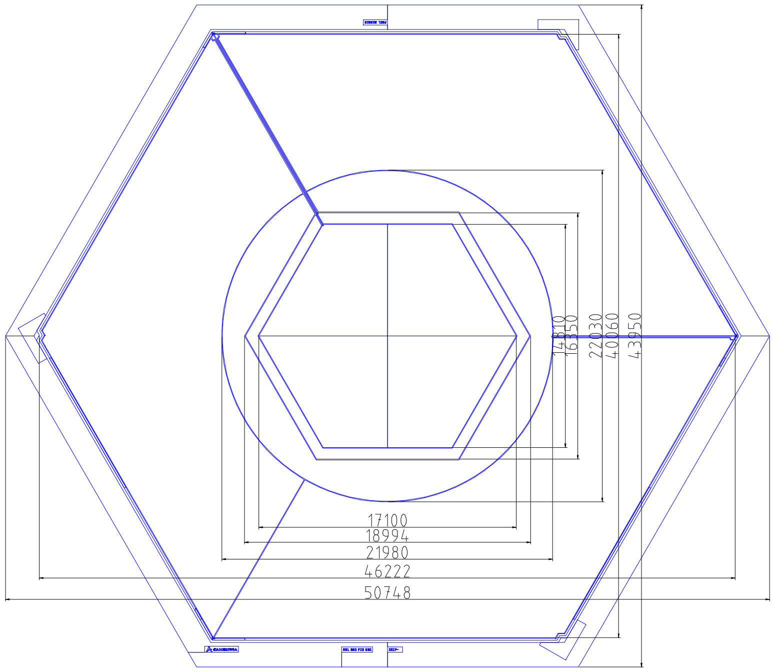

Figure H.2: Final layout of the SSD chip mask for the MSL/RAD ABC detectors. Adapted from a drawing by S. Böttcher and Canberra Industries Ltd. The drawing shown is approximately 2× the original scale.

Appendix I

List of measurement files

To aid in using the results of this work and to have an overview of the set of measurements that are used, a list of measurements is given below.

p-**PF**-1 GeV-0° **#1**
File name: *nsrl-protons-1GeV-0deg.dat*
Early measurement of the PF RSH with a DIRENAv1 at BNL(2007). Protons with an energy of 1 GeV are entering the instrument through the front window. The beam is wide and approximately homogeneous and penetrates the whole instrument.

p-**PF**-250 MeV-0° **#2**
File name: *nsrl-protons-250MeV-0deg.dat*
Like above, but with a proton energy of 250 MeV.

p-**PF**-1 GeV-0°-50 mV **#3**
File name: *nsrl-protons-1GeV-0deg-50mvD.dat*
In general like [#1, p-PF-1 GeV-0°], but for this run, the D threshold has been set higher (to 50 mV) in order to not be swamped with D triggers.

p-**PF**-1 GeV-25° $\circlearrowright_y$ **#4**
File name: *nsrl-protons-1GeV-25deg.dat*
Like above, the instrument that has been turned by 25° around $\circlearrowright_y$. The beam enters the instrument at approximately the edge of the view cone of the telescope.

p-**PF**-1 GeV-90° $\circlearrowright_y$ **#5**
File name: *nsrl-protons-1GeV-90deg.dat*
Like above, but with a rotation by 90° around $\circlearrowright_y$.

μ-**FM2-fREB** **#6**
File name: *fm2-post-tv-muons_20080404_03_04_0.bin*
A longer, upright $\cos^2$-muon run collected with FM2 and the flight REB after thermal vacuum testing.

μ-**FM2-KielREB** **#7**
File name: *bnl_muons_fm002_day2run2_20080520_16_00_0.bin*

Upright cosmic muon run during beam time testing at BNL, 2008. FM2 has been connected to the KielREB for this run.

μ-FM1-fREB **#8**

File name: *freb_fm1_muon_20080930_21_12_1.bin*
FM1 run with cosmic muons and the flight REB connected. The instrument is standing upright and events are taken as single events through the high speed streaming output.
Non-comprehensive set of offsets and scales:

$$\begin{aligned}
\mathrm{E} &:= (\mathrm{EU}-1945.3)+9.9\cdot(\mathrm{EI}-1648.6)+45.64\cdot(\mathrm{EN}-2150.0) && \text{(I.1)}\\
\mathrm{sel\ E} &:= \mathrm{E}>1590 && \text{(I.2)}\\
\mathrm{sel}\ \neg\mathrm{E} &:= \mathrm{E}<500 && \text{(I.3)}\\
\mathrm{sel}\ \neg\mathrm{C2} &:= \mathrm{C2}<1637 && \text{(I.4)}\\
\mathrm{sel}\ \neg\mathrm{CU} &:= \mathrm{CU}<1811 && \text{(I.5)}\\
\mathrm{sel\ DU} &:= \mathrm{DU}>8000 && \text{(I.6)}\\
\mathrm{sel}\ \neg\mathrm{DU} &:= DU<2500. && \text{(I.7)}
\end{aligned}$$

These selections have been used to arrive at the single channel spectra as discussed in Chapter 6.

n-19-FM1-REB **#9**

File name: *ptb_fm1_straightforward_19mev_t2_20080408_12_39_0.bin*
PTB run with a wide beam of 19 MeV neutrons entering the instrument along the z-axis through the entrance window. Apparently, the same VIRENA chip has been used for this measurement as it has been used for [#8, μ-FM1-fREB], but the VIRENA gain setting and readout table is different. The scales of EU, F1 and F2r are the same, but the DN channel has an input gain of 4 for the neutron runs, whereas it has an input gain of 8 for the above muon run. This also changes the pedestal position! The last frontend live-time counter c_f in the run is $c_f = 1713.11\,\mathrm{s}$. The reference duration is $T = 3600\,\mathrm{s}$, so the run contains about half of the total fluence. All described PTB runs here have been taken using the same VIRENA gain configuration table.

n-19-sk-FM1-REB **#10**

File name: *ptb_FM1_front_real1_shadowcone_20080408_14_22_0.bin*
Shadow cone run for the 19 MeV run above. The run has been started before particle data arrived and stopped after the beam has been stopped. Consequently, the live time is larger than the reference duration of $T = 1800\,\mathrm{s}$, it is $c_f = 2462.12\,\mathrm{s}$. The beam is live between events 2200 . . . 36700. The total number of events in the file is 43027. The effect of the seen extra counts on the correction of the D/E spectra is neglected and it is assumed (due to the low count rate) that no live-time reduction happens, except for housekeeping. As periodic 60 s-housekeeping takes about 6 s each, it assumed for shadow cone subtraction that the live-time is $90\% \cdot 1800\,\mathrm{s} = 1620\,\mathrm{s}$.

n-14.8-FM1-REB **#11**

File name: *PTB_FM1_15MeV_front_20080409_08_19_0.bin*
PTB neutron run with 14.8 MeV neutrons. Live time is $c_f = 3399.02\,\mathrm{s}$ and the reference run duration is $T = 3600\,\mathrm{s}$.

n-14.8-sk-FM1-REB **#12**

File name: *PTB_FM1_15MeV_front_shadowcone_20080409_09_26_0.bin*
Shadow cone run corresponding to the above run. Live time is $c_f = 1630.64\,\mathrm{s}$ and reference run duration is $T = 1800\,\mathrm{s}$.

n-5-FM1-REB **#13**

File name: *ptb_FM1_5mev_front_20080409_13_08_0.bin*
PTB neutron run, 5 MeV neutrons. $c_f = 3114.31\,\mathrm{s}$ and $T = 3600\,\mathrm{s}$.

n-5-sk-FM1-REB **#14**

File name: *PTB_FM1_5mev_front_shadowcone_20080409_15_24_0.fD.ehist_ac*
Shadow cone measurement for above 5 MeV run. Run times are $c_f = 2041.06\,\mathrm{s}$ and $T = 1800\,\mathrm{s}$. Like for the 19 MeV run (see above), live-time is therefore estimated to be 1620 s overall.

Bibliography

Agostinelli, S., and others, GEANT4 — a simulation toolkit, *Nuclear Instruments and Methods in Physics Research*, *A*(506), 250–303, 2003.

Battistoni, G., F. Cerutti, A. Fasso, A. Ferrari, S. Muraro, J. Ranft, S. Roesler, and P. R. Sala, The FLUKA code: description and benchmarking, in *AIP Conference Proceedings*, vol. 896, p. 31, 2007.

Bichsel, H., Straggling in thin silicon detectors, *Reviews of Modern Physics*, *60*(3), 663, 1988.

Bichsel, H., and R. P. Saxon, Comparison of calculational methods for straggling in thin absorbers, *Physical Review A*, *11*(4), 1286–1296, 1975.

BNL NuDat2, `http://www.nndc.bnl.gov/nudat2/`, 2006-2010.

Böhm, E., MSL Monte-Carlo model, *Tech. rep.*, Christian-Albrechts-Universität zu Kiel, 2006-2008.

Böhm, E., Estimated neutron spectra on the Martian surface, *Tech. rep.*, Christian-Albrechts-Universität zu Kiel, 2007.

Böhm, E., and A. Kharytonov, Statistical separation of neutrons and γ-radiation in RAD, *Tech. rep.*, Christian-Albrechts-Universität zu Kiel, 2008.

Böhm, E., and C. Martin, Neutrons run at PTB (Braunschweig), *Tech. rep.*, Christian-Albrechts-Universität zu Kiel, 2008.

Böhm, E., A. Kharytonov, and R. F. Wimmer-Schweingruber, Solar energetic particle spectra from the SOHO-EPHIN sensor by application of regularization methods, *A&A*, *459*, 673, 2007.

Born, M., and E. Wolf, *Principles of Optics*, Cambridge University Press, 1980.

Böttcher, S. I., The MSL RAD second level trigger algorithm, *Tech. rep.*, Christian-Albrechts-Universität zu Kiel, 2007.

Böttcher, S. I., Signal processing in the Radiation Assessment Detector for MSL, *Tech. rep.*, Christian-Albrechts-Universität zu Kiel, 2008.

Böttcher, S. I., and O. Kortmann, Science Impact for MSL RAD for the case of a missing medium gain CsI channel (draft), *Tech. rep.*, Christian-Albrechts-Universität zu Kiel, 2007.

Brose, J., G. Dahlinger, K. R. Schubert, et al., Properties of CsI (Tl) crystals and their optimization for calorimetry of high energy photons, *Nuclear Instruments and Methods in Physics Research*, *417*(2), 311–324, 1998.

Burmeister, S., Entwicklung eines Neutronendosimeters und Messung schneller Neutronen in der Verkehrsluftfahrt, Ph.D. thesis, Christian-Albrechts-Universität zu Kiel, 2006.

Canberra, Canberra datasheets for the RAD PIN detectors, *Tech. rep.*, Canberra Industries, 2007-7.

Craun, R., and D. Smith, Analysis of response data for several organic scintillators, *Nuclear Instruments and Methods in Physics Research*, *80*, 239–244, 1970.

de Haas, J., P. Dorenbos, and C. van Eijk, Measuring the absolute light yield of scintillators, *Nuclear Instruments and Methods in Physics Research*, *537*(1-2), 97–100, 2005.

Desorgher, L., E. O. Flückiger, and M. Gurtner, The PLANETOCOSMICS GEANT4 application, in *36th COSPAR Scientific Assembly*, vol. 36, p. 2361, 2006.

Dow Corning, Datasheet for Space-Grade Silicone Sealants, *Tech. rep.*, Dow Corning Corporation, 2005.

Gaisser, T. K., *Cosmic Rays and Particle Physics*, Cambridge University Press, 1990.

Gentit, F., Litrani: a general purpose Monte-Carlo program simulating light propagation in isotropic or anisotropic media, *Nuclear Instruments and Methods in Physics Research*, *486*(1-2), 35–39, 2002.

Gooß, M., Design and tests of a detector for MSL and Solar Orbiter, Diploma thesis, Christian-Albrechts-Universität zu Kiel, 2006.

Grieder, P. K., *Cosmic rays at Earth*, first ed., Elsevier, 2001.

Gumplinger, P., Optical photon processes in GEANT4, *Tech. rep.*, CERN, 2002.

Hancock, S., F. James, J. Movchet, P. Rancoita, and L. V. Rossum, Energy loss distributions for single particles and several particles in a thin silicon absorber, *Physical Review A*, 1983a.

Hancock, S., F. James, J. Movchet, P. Rancoita, and L. V. Rossum, Energy loss and energy-straggling of protons and pions in the momentum range 0.7 to 115 GeV/c, *Nuclear Instruments and Methods in Physics Research*, 1983b.

Hunter, W. G., and G. E. Box, Statistics for experimenters: An introduction to design, data analysis, and model building, *Wiley series in probability and mathematical statistics*, 2005.

Isaev, A. B., and V. I. Popov, Energy loss distribution of charged particles in thin absorbers, *Measurement Techniques*, *13*(3), 406–410, 1970.

Kortmann, O., Studies on the Radiation Assessment Detector, Diploma thesis, Christian-Albrechts-Universität zu Kiel, 2006.

Leo, W., *Techniques for Nuclear and Particle Physics Experiments, A How-to Approach*, second revised ed., Springer-Verlag, 1987, 1994.

Martin, C., Study on carbon ions for the MSL/RAD instrument, *Tech. rep.*, Christian-Albrechts-Universität zu Kiel, 2008a.

Martin, C., RAD GCR counting rate, *Tech. rep.*, Christian-Albrechts-Universität zu Kiel, 2008b.

Martin, C., and E. Böhm, Some aspects on the problem of the energy calibration for the MSL/RAD flight units, *Tech. rep.*, Christian-Albrechts-Universität zu Kiel, 2008.

Martin, C., E. Böhm, and R. F. Wimmer-Schweingruber, Comprehensive RAD calibration report, *Tech. rep.*, Christian-Albrechts-Universität zu Kiel, 2008a.

Martin, C., et al., Light-output response of the plastic scintillator for the Mars Science Laboratory (MSL) Radiation Assessment Detector (RAD), Poster, 2008b.

Meschede, D., *Gerthsen Physik*, 22nd ed., Springer-Verlag, Berlin, Heidelberg, New York, 2004.

Millipore Corporation, Datasheet for Millipore filter material, *Tech. rep.*, Millipore Corporation, 2005.

Mitaroff, A., and M. Silari, The CERN-EU High-Energy Reference Field (CERF) facility for dosimetry at commercial flight altitudes and in space, *Radiation Protection Dosimetry*, *102*(1), 7–22, 2002.

Moyal, J. E., Theory of ionization fluctuations, *Philosophical Magazine*, *46*, 263–80, 1955.

NASA Mars Science Laboratory web site, `http://marsprogram.jpl.nasa.gov/msl/index.cfm`, 2006-2010.

NASA photo journal, `http://photojournal.jpl.nasa.gov/`, 2006-2010.

Needham, M., Simulating energy loss in thin silicon detectors, *Tech. rep.*, CERN, 2003.

Nolte, R., PTB neutron fluences for RAD (run log sheet), *Tech. rep.*, PTB, 2008.

Nolte, R., et al., Quasi-monoenergetic neutron reference fields in the energy range from thermal to 200 MeV, *Radiation Protection Dosimetry*, *110*(1-4), 97, 2004.

Pauls, M., Entwicklung eines Neutronendetektors für Dosimetrie, Diploma thesis, Christian-Albrechts-Universität zu Kiel, 1998.

Press, W. H., S. A. Teukolsky, W. T. Vetterling, and B. P. Flannery, *Numerical Recipes in C - The Art of Scientific Computing*, second ed., Cambridge University Press, 1988, 1992.

RAD Proposal, RAD Radiation Assessment Detector Proposal by Southwest Research Institute and Christian-Albrechts-Universität zu Kiel, 2006.

Saint-Gobain Crystals and Detectors, BC-430 plastic scintillator datasheet, 2005-8.

Schorr, B., Programs for the Landau and the Vavilov distributions and the corresponding random numbers, *Tech. Rep. CERN-DD-73-26*, CERN, Geneva, submitted to Computer Physics Communications, 1973.

Stuart, A., and J. K. Ord, *Kendall's Advanced Theory of Statistics*, vol. 1. Distribution Theory, Griffin, 1987.

Takada, E., et al., Present status of HIMAC, *EPAC2000, Wien, June*, 2000.

Valentine, J., D. Wehe, G. Knoll, and C. Moss, Temperature dependence of absolute CsI (Tl) scintillation yield, in *Nuclear Science Symposium and Medical Imaging Conference, Conference Record of the 1991 IEEE*, pp. 176–182, 1991.

von Lány, C., Grundlegende physikalische Nachweiseigenschaften des Dosimetrie-Teleskops DOSTEL für Neutronen, Ph.D. thesis, Christian-Albrechts-Universität zu Kiel, 2001.

Wimmer-Schweingruber, R. F., MSL/RAD Critical Design Review 06 Instrument Performance Analysis, Talk, 2007.

List of Acronyms

AC Anti-Coincidence. 4

ADC Analog to Digital Converter. 14

ASIC Application Specific Integrated Circuit. 14

BNL Brookhaven National Laboratory. 19

BSP Binary Space Partitioning. 33

CSA Charge Sensitive (Pre-)Amplifier. 10

DIRENA Digital Readout Electronics for Nuclear Applications. 18

DLR Deutsches Zentrum für Luft- und Raumfahrt. 3

EMI Electromagnetic Interference. 19

EVIL Electronics for VIRENA Interface Logic. 19

FEE Frontend Electronics. 19

FIFO First In First Out. 20

FPGA Field Programmable Gate Array. 19

FWHM Full Width At Half Maximum. 39

GSE Ground Support Equipment. 21

GSEOS Ground Support Equipment Operating System. 21

HDPE High Density Polyethylene. 83

HIMAC Heavy Ion Medical Accelerator in Chiba. 83

IOR Index Of Refraction. 31

JFET Junction Field Effect Transistor. 13

JPL Jet Propulsion Laboratory. 19

KT Kayser-Threde GmbH. 4

L2 Level two. 57

LET Linear Energy Transfer. 109

LUT Look-Up Tables. 4

MC Monte-Carlo. 25

MER Mars Exploration Rover. 1

MPV Most Probable Value. 149

MSL Mars Science Laboratory. 1

NASA National Aeronautics and Space Administration. 1

NIRS National Institute of Radiological Sciences. 83

NSRL NASA Space Radiation Laboratory. 24

PCB Printed Circuit Board. 16

pdf probability density function. 8

PDS Planetary Data System. 21

PHA Pulse Height Analysis. 4

PIN Positive-Intrinsic-Negative. 9

PMT Photo Multiplier Tube. 106

PPT Primary Particle Track. 27

PTB Physikalisch-Technische Bundesanstalt. 24

PTFE PolyTetraFluoroEthylene. 13

RAD Radiation Assessment Detector. 1

RBE Relative Biological Effectiveness. 105

RTG Radioisotope Thermoelectric Generator. 2

VIRENA Voltage Input Readout Electronics for Nuclear Applications. 19

Danksagung

Zuallererst möchte ich Herrn Prof. Dr. Robert F. Wimmer-Schweingruber für die Vergabe dieser Arbeit und die sehr gute Betreuung danken. Er gab mir stets die Freiheit völlig selbstständig zu arbeiten, war aber bei den aufgetretenen Problemen immer bereit den Stand der Dinge zu diskutieren und neue Denkanstöße zu geben.

Weiterhin gilt mein Dank natürlich einer Vielzahl von Mitgliedern der Gruppe von Prof. Wimmer und der von Prof. Heber. Hier sind zuallererst meine (teils ehemaligen) Kollegen Dr. Muharrem Köten, Dr. Roland Rodde, Dipl. Phys. Jan Köhler und Dr. Lars Berger zu nennen. Neben vielen fachlichen Hinweisen, Berichtigungen und Diskussionen verschiedenster Art hat sich ein sehr angenehmes Arbeitsklima ergeben und es sind auch privat Freundschaften entstanden.

Die mit einem in jeder Hinsicht anspruchsvollen internationalen Projekt wie MSL/RAD einhergehenden, verschiedenen Schwierigkeiten und Probleme wurden in eben jenem direkten Arbeitsumfeld sehr angemessen ausgeglichen.

Einer Vielzahl Personen schulde ich weiterhin Dank für die fachliche Unterstützung. Hier ist zuerst Dr. Michael Stalder zu erwähnen, der mir durch tiefgehende Analyse meiner Ideen und Resultate Fehler aufgezeigt und sehr wertvolle Verbesserungsvorschläge geliefert hat. In diesem Kontext ist weiterhin Dr. Sönke Burmeister zu erwähnen, der mir bei Dosimetrie betreffenden Themen und auch vielen allgemeinen Fragen oft helfen konnte. Dr. Eckart Böhm und Dr. César Martin, in dieser Arbeit oft erwähnt, haben jederzeit viele Ratschläge nennen können und es wurden viele ertragreiche Diskussionen geführt. Dipl. Ing. Lars Seimetz hat mir neber der Bereitstellung der für diese Arbeit nötigen CAD-Daten viele technische Fragen zu RAD beantwortet und den nötigen kühlen Kopf bewahrt.

Nicht zu vergessen ist auch der wertvolle Beitrag von Dipl. Phys. Lauri Panitzsch, Christoph Terasa und Dipl. Phys. Bent Ehresmann in den Korrekturen dieser Arbeit, als auch für einige Anregungen und Diskussionen. Bent danke ich auch für die Bereitstellung der Teilchenflüsse auf dem Mars.

Across the Atlantic, I further thank, amongst others, Eddie Weigle and Dr. Cary Zeitlin for their endurance in integrating the very diverse science and data taking requests with the inevitable engineering, management and quality control needs. Further I thank for the fruitful discussions regarding the various aspects of RAD.

Ich danke ebenfalls dem Deutschen Zentrum für Luft- und Raumfahrt (Grant #50QM0501) und auch dem Land Schleswig-Holstein, die diese Arbeit finanziell ermöglicht bzw. unterstützt haben.

Last but not least danke ich meinen Eltern und meinen Geschwistern und auch Asja.

Zuallerletzt danke ich noch jedem, den ich in dieser Auflistung vergessen habe!